Radiofrequency Pulse Design for Robust Quantitative Spin-Lock MRI

Coletti, C.

DOI
10.4233/uuid:b48bef11-7b68-445c-ba99-4f2771b1c048

Publication date
2024

Document Version
Final published version

Citation (APA)
Coletti, C. (2024). *Radiofrequency Pulse Design for Robust Quantitative Spin-Lock MRI*. [Dissertation (TU Delft), Delft University of Technology]. https://doi.org/10.4233/uuid:b48bef11-7b68-445c-ba99-4f2771b1c048

Radiofrequency Pulse Design for Robust Quantitative Spin-Lock MRI

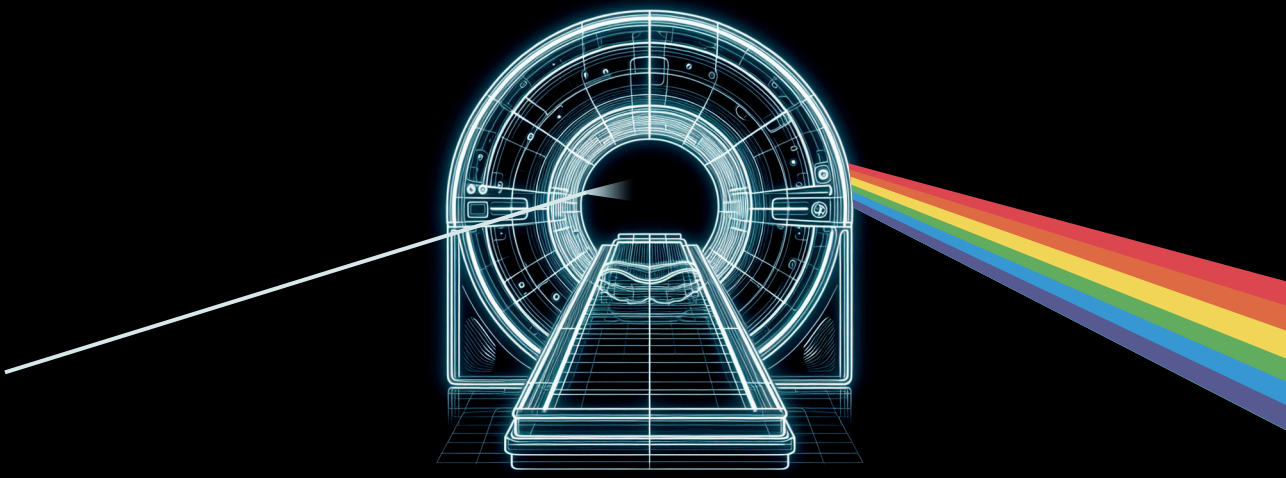

Chiara Coletti

Radiofrequency Pulse Design for Robust Quantitative Spin-Lock MRI

Radiofrequency Pulse Design for Robust Quantitative Spin-Lock MRI

Dissertation

for the purpose of obtaining the degree of doctor
at Delft University of Technology
by the authority of the Rector Magnificus,
prof. dr. ir. T.H.J.J. van der Hagen,
chair of the Board for Doctorates
to be defended publicly on
Friday 27th, September 2024 at 12:30 o'clock

by

Chiara COLETTI

Laurea Magistrale in Ingegneria Biomedica - Biomedical Engineering,
Politecnico di Milano & Politecnico di Torino,
Italy

born in Rome, Italy

This dissertation has been approved by the promotors.

Composition of the doctoral committee:

Rector Magnificus	chairperson
Dr. F.M. Vos	Delft University of Technology, *promotor*
Dr. S.D. Weingärtner	Delft University of Technology, *copromotor*

Independent members:

Prof. dr. J.A. Hernandez-Tamames	Delft University of Technology
Prof. dr. M. Garwood	University of Minnesota, USA
Dr. A. Phinikaridou	King's College London, UK
Dr. ir. P. van Ooij	Amsterdam UMC
Dr. M. Götte	Amsterdam UMC
Prof. Dr. B. Rieger	Delft University of Technology, *reserve member*

Keywords: Quantitative MRI, Spin-lock, Rotating-frame relaxation, Adiabatic RF, $T_{1\rho}$ mapping, $T_{2\rho}$ mapping

Printed by: Gildeprint

Cover by: Chiara Coletti, inspired by "*The Dark Side of the Moon*" album cover by Pink Floyd

ISBN 978-94-6384-636-3

An electronic copy of this dissertation is available at https://repository.tudelft.nl/.

Contents

Summary

Magnetic resonance imaging (MRI) is one of the most powerful tools currently available for diagnostic imaging and medical research. MRI can provide information about the composition, structure, and function of biological tissues and systems in a non-invasive way, with unsurpassed soft-tissue contrast and spatial resolution. While MRI images typically depict qualitative information, quantitative MRI techniques have emerged for their promise of enabling objective and intra-and inter-subject comparable quantification of tissue properties. Quantitative MRI techniques yield parametric maps, which are voxel-wise representations of physical properties of tissues, such as relaxation times. MRI relaxation times, conventionally T_1 and T_2, characterize the evolution of the excited MRI signal back to its equilibrium value and they are directly influenced by the molecular environment. Thus, T_1 and T_2 parametric maps yield useful insight into the normal state of biological tissues and eventual pathological remodeling.

Rotating-frame relaxation methods, like $T_{1\rho}$ or $T_{2\rho}$ mapping, have recently been proposed as complementary techniques to conventional T_1 and T_2 mapping. Rotating-frame relaxation times describe the signal relaxation during radio-frequency (RF) irradiation and they have shown increased sensitivity to slow molecular motion, which characterizes water interactions with macro-molecules in biological tissues. This way, rotating-frame relaxation parameters represent valuable endogenous contrast mechanisms, potentially reducing the need for contrast-agent administration in MRI-based tissue characterization.

Rotating-frame relaxation mapping relies on the use of specific signal preparation modules, called spin-lock preparations, during which moderately high RF pulses are applied for a relatively long time (in the order of tenths of ms) to induce $T_{1\rho}$ or $T_{2\rho}$ decay. The in vivo applicability of spin-lock techniques is currently limited by two main factors: the high specific absorption rate (SAR) burden of spin-lock preparations and their strong susceptibility to system imperfections, such as inhomogeneities in the main magnetic field and the RF field. The latter becomes more important at high field strengths, as inhomogeneities in both the main magnetic field and the RF field are stronger. For this reason, the successful application of rotating-frame relaxation mapping has been limited, so far, to lower field strengths or more homogeneous body regions.

The goal of this dissertation is to design and test novel RF preparations to enable robust, quantitative MRI at high field strengths. First,

we explore the use of adiabatic spin-lock preparations to achieve robust myocardial $T_{1\rho,adiab}$ or $T_{2\rho,adiab}$ mapping at 3T. We show that the use of amplitude-and frequency-modulated RF pulses in spin-lock preparations allows robust, artifact-free, and reproducible $T_{1\rho,adiab}$ or $T_{2\rho,adiab}$ quantification even in the presence of strong inhomogeneities. This is particularly important for cardiac applications at high field strengths. We also propose a modified version of adiabatic spin-lock preparations, combining slice-selective and non-selective RF pulses, to achieve intrinsic dark-blood contrast in myocardial $T_{1\rho,adiab}$ maps. At the cost of a moderate loss in precision, dark-blood $T_{1\rho,adiab}$ maps yield improved myocardium-to-blood contrast that could facilitate scar visualization in the endocardium.

Next, we investigate novel rotating-frame relaxation parameters, such as the sub-adiabatic relaxation along a fictitious field (RAFF), for contrast-free quantitative MRI at 3T. We introduce a framework for the optimization of RAFF pulses in order to maximize resilience to field inhomogeneities. We test the performance of the optimized generalized inhomogeneity-resistant RAFF (girRAFF) pulses for in vivo rotating-frame relaxation mapping of the calf muscle and knee cartilage. Significant improvements in robustness with respect to standard RAFF preparations are observed in both applications.

Moreover, we propose a theoretical derivation of $T_{1\rho}$ in liquids based on Redfield relaxation theory. We extend this framework to model $T_{1\rho,adiab}$ relaxation during amplitude-and frequency-modulated RF pulses, with the goal of designing adiabatic spin-lock preparations with minimized $T_{1\rho,adiab}$ dispersion in the presence of inhomogeneities in the main magnetic field.

Finally, we study an alternative application of spin-lock preparations, namely the direct detection of weak oscillatory magnetic fields induced by neuronal currents. Spin-lock-based direct detection of neural activity could represent an opportunity to perform functional MRI (fMRI) with very high temporal resolution, beyond the limits of blood-oxygenation-level-dependent (BOLD) contrast. We characterize the susceptibility of different spin-lock techniques to field inhomogeneities and their impact on the final sensitivity of neuro-currents fMRI. We also introduce a novel statistical analysis process based on signal variability to improve neuro-currents fMRI signal specificity.

In summary, we seek to improve the robustness of RF preparations with the ultimate goal of pushing the boundaries of their in vivo applicability at high field strengths and enabling their widespread use in clinical practice.

Samenvatting

Magnetische resonantiebeeldvorming (MRI) is een van de krachtigste hulpmiddelen die momenteel beschikbaar zijn voor diagnostiek en ander medisch onderzoek. MRI kan op een niet-invasieve manier informatie verschaffen over de samenstelling, structuur en functie van biologische weefsels en systemen. Daarbij levert het een groot contrast tussen zachte weefsels en een hoge resolutie. MRI-beelden geven doorgaans kwalitatieve informatie, maar sinds kort zijn er ook kwantitatieve MRI-technieken beschikbaar. Deze zijn veelbelovend omdat ze objectieve en reproduceerbare meting van weefseleigenschappen mogelijk maken. Een goed voorbeeld van kwantitatieve MRI-technieken is het afbeelden van parameters, dat wil zeggen van van fysieke eigenschappen, van weefsels zoals de relaxatietijden. Deze MRI relaxatietijden, bijvoorbeeld de T_1 en T_2 relaxatie parameters, beschrijven de evolutie van het ge MRI-signaal terug naar zijn evenwichtswaarde, na excitatie. Dit proces wordt direct beïnvloed door de moleculaire samenstelling van de biologische omgeving. De T_1 en T_2 parameter maps leveren nuttige inzichten op in de normale toestand van biologische weefsels en eventuele pathologische processen.

Zogenaamde roterende frame-relaxatie metingen, zoals $T_{1\rho}$ en $T_{2\rho}$, zijn onlangs geïntroduceerd als een techniek die complementair is aan het mappen van T_1 en T_2-parameters. Roterende frame-relaxatie tijden meten de signaalrelaxatie tijdens excitatie en hebben een verhoogde gevoeligheid voor langzame moleculaire bewegingen die de interacties van water moleculen met macromoleculen in weefsels karakteriseren. Daardoor leveren deze parameters waardevolle MRI contrasten, die misschien kunnen leiden tot verminderd gebruik van contrastmiddelen voor weefselkarakterisering.

Het roterende-frame relaxatie mappen is afhankelijk van het gebruik van specifieke signaal manipulaties, die spin-lock-voorbereidingen worden genoemd. Dit zijn RF-pulsen van matig-hoge intensiteit die gedurende een relatief lange tijd worden toegepast (in de orde van tienden van ms) om $T_{1\rho}$ of $T_{2\rho}$ relaxatie te induceren. De in vivo toepasbaarheid van spin-lock-technieken wordt momenteel beperkt door twee belangrijke factoren: enerzijds de hoge SAR-last van spin-lock preparatie en anderzijds hun sterke gevoeligheid voor systeemimperfecties, zoals inhomogeniteiten in het hoofdmagneetveld en in het RF-veld. Dit laatste wordt belangrijker bij hoge veldsterkten, omdat daaarbij de inhomogeniteiten in zowel het magnetische hoofdveld als het RF-veld sterker zijn.

Als gevolg hiervan is de toepassing van het roterende frame-relaxatie mappen tot nu toe beperkt gebleven tot lagere veldsterktes en meer homogene lichaamsgebieden.

Het doel van dit proefschrift was het ontwerpen en testen van nieuwe RF-pulsen om robuuste, kwantitatieve MRI bij hoge veldsterktes mogelijk te maken.

Uiteindelijk heeft dit onderzoek de robuustheid van spin-lock RF preparaties verbeterd, waardoor de grenzen van hun in vivo toepasbaarheid bij hoge veldsterktes is verlegd en hiermee wijdverspreid gebruik in de klinische praktijk mogelijk is gemaakt.

1

Introduction

Magnetic Resonance Imaging (MRI) constitutes arguably one of the most remarkable applications of physics in healthcare over the last century. Since its introduction, it has firmly established itself as a crucial part of imaging-based clinical diagnostic processes thanks to its non-invasive nature, flexibility, and rich soft-tissue contrast. MRI examinations are now an integral part of the clinical work-up for a multitude of diseases and MRI research is a bustling field with continuous innovations at the interface of physics, engineering, and medicine.

MRI has been conventionally used as a qualitative imaging tool. As such, visual interpretation of MRI scans relies on relative contrast differences among tissues and depends on the radiologist's reading. A paradigm shift arrived through the more recent introduction of quantitative MRI techniques, where MRI has started to be seen and used as an instrument to quantify, voxel-by-voxel, the physical properties of biological tissues. Quantitative MRI has enhanced the objective measurement of tissue characteristics, facilitating intra-and inter-subject reproducibility of MRI-based biomarkers.

Quantitative MRI yields parametric mapping of several physical properties, including voxel-wise measurement of MRI relaxation times. Relaxation is a fundamental phenomenon associated with nuclear magnetic resonance (NMR) that describes the return of an excited spin system to its thermal equilibrium state. T_1 and T_2 are the relaxation time constants that are conventionally used to characterize the longitudinal and transverse evolution of the signal, respectively. Since the relaxation process is caused by the interaction of nuclear spins with their molecular and physical environment, T_1 and T_2 times can be used as biomarkers to differentiate between tissue compositions. Normal T_1 and T_2 times for biological tissues have been experimentally determined over the years and the sensitivity of T_1 and T_2 mapping

to certain pathological processes is well documented [1–5]. However, for subtle changes in the tissue composition, the use of external contrast agents may be necessary to enhance contrast [6]. In cardiac tissue characterization, for instance, native T_1 maps show limited sensitivity to fibrosis in ischemic and non-ischemic myocardial diseases [7]. In these cases, T_1 maps acquired after gadolinium-based contrast injections display higher contrast between scar and remote myocardium. However, administration of external contrast agents during MRI has been associated with a risk of retention in brain tissues and, thus, limits the possibility of repeated examinations [8–10].

Recently, rotating-frame relaxation methods have gained prominence for their potential to provide insight into the macro-molecular environment of biological tissues without having to inject external contrast agents [11]. Rotating-frame relaxation refers to the relaxation processes measured during continuous redio-frequency (RF) irradiation, as opposed to conventional relaxation probed during free decay. Thus, rotating-frame relaxation reflects different physical interactions compared with conventional relaxation times. Specifically, it has shown higher sensitivity than native T_1 or T_2 to interactions between water and macromolecules. Compared with contrast-based techniques, rotating-frame relaxation mapping entails less risk, better cost-effectiveness, and the potential for repeated assessments over time. These advantages have led to a growing number of technical and clinical studies [11, 12].

Specific signal preparations, during which the RF field is kept at a moderately high value for long durations (usually 10-50 times longer than for RF excitation pulses) are used to induce rotating-frame relaxation. These RF pulses are called spin-locking pulses because they are not used to excite the magnetization but to lock it along their axis. Spin-locking effectively suppresses certain mechanisms that would conventionally induce relaxation under free-decay conditions. Thus, during spin-lock preparations, longitudinal and transverse relaxation are relative to the spin-locking RF pulse, instead of the main magnetic field, and are called $T_{1\rho}$ and $T_{2\rho}$, instead of T_1 and T_2.

The use of spin-lock preparations poses limitations in vivo. On the one hand, their high specific absorption rate (SAR) can cause heating-related patient discomfort or even tissue damage. On the other hand, their high susceptibility to inhomogeneities of the main magnetic field or the RF field hinders robust quantification. For these reasons, the successful application of rotating-frame relaxation mapping techniques has so far been limited to lower field strengths ($\leq$1.5 T) or regions of the body subjected to lower field inhomogeneities (brain, articular cartilage). Because of these limitations, the full clinical potential of rotating frame relaxation remains yet to be explored.

1.1. Research Goals

The works presented in this dissertation aim to design more robust RF preparations for in vivo quantification of rotating-frame relaxation at 3T. Our primary focus is on cardiac tissue characterization as it introduces additional challenges stemming from the strong difference in magnetic susceptibility between the heart and the lungs, the presence of flow effects, as well as the influence of cardiac and respiratory motion.

Our first objective is designing spin-lock preparations fulfilling three conditions. First, we want to improve the resilience of spin-lock preparations to inhomogeneities in the main magnetic field (B_0) and in the RF field (B_1^+). Second, we aim to develop spin-lock preparation with adequate SAR burden for in vivo application. Lastly, we want to achieve good sensitivity to pathological changes in tissue composition. To this end, we evaluate adiabatic spin-lock pulses for in vivo rotating-frame relaxation mapping at 3T.

Once novel RF preparations with the potential for robust rotating-frame relaxation mapping are identified, our goal is to define a framework for the optimization of RF pulse parameters, maximizing their resilience to both B_0 and B_1^+ inhomogeneities. To this end, we initially model the signal dynamics during adiabatic RF irradiation using Bloch simulations. In a second phase, we extend the optimization framework to include a relaxation theory-based component, characterizing rotating-frame relaxation during amplitude-and frequency-modulated RF pulses.

Next, the performance of the proposed techniques is evaluated in both phantoms, healthy volunteers, and clinical patients in order to assess their relevance for potential clinical use. The proposed techniques are compared to conventional rotating-frame relaxation methods both qualitatively, in terms of overall image quality and presence of artifacts, and quantitatively, in terms of precision and reproducibility.

Finally, we aim to explore different applications of spin-locking pulses in quantitative MRI, beyond rotating-frame relaxation mapping. Specifically, we target the translation of insights from the applications in rotating-frame relaxometry to the direct detection of oscillating neuronal currents.

Our ultimate goal is to propose novel techniques and contrast mechanisms for quantitative MRI that can significantly impact the applicability of non-invasive MRI imaging in clinical settings and positively transform the diagnostic processes.

1.2. Dissertation Outline

The main body of this dissertation is structured as follows:

- In Chapter 2 we introduce basic MRI physics principles necessary to understand the techniques introduced in this dissertation. We

introduce the concepts behind nuclear magnetic resonance (NMR), which explains the origin of MRI signals, the principles of spatial encoding that allow the acquisition of multi-dimensional images, and how all of this is combined into complete MRI sequences. Finally, we also briefly describe the functional parts of clinical MRI scanners.

- Chapter 3 contains a targeted overview of MRI sequences and techniques commonly used for cardiac MR (CMR), which is the primary application for most of the following chapters. Basic anatomy and functional processes of the human heart are also described to better understand how cardiovascular diseases can be captured by CMR imaging. Finally, techniques to enable the acquisition of spatial, temporal, and parametric dynamics of the cardiac cycle are presented, with a special focus on mitigating cardiac and respiratory motion effects.
- In Chapter 4 we propose a novel technique, based on adiabatic spin-lock preparations, to achieve robust $T_{1\rho,adiab}$ mapping in the human myocardium at 3T. Simulations are performed to optimize the preparation design in terms of robustness to B_0 and B_1^+ field inhomogeneities. The proposed sequence is tested in phantoms and healthy volunteers and compared to a conventional non-adiabatic $T_{1\rho}$ mapping technique. $T_{1\rho,adiab}$ mapping is also performed on a proof-of-principle cohort of patients with suspect cardiovascular diseases and compared to standard clinical protocols to assess its potential clinical feasibility and value.
- In Chapter 5 we modify the proposed $T_{1\rho,adiab}$ preparations to obtain intrinsic dark-blood contrast and potentially improve myocardial scar visualization at the blood-to-myocardium interface. We study the influence of preparation parameters on blood suppression and myocardial thickness for the proposed dark-blood $T_{1\rho,adiab}$ mapping sequence through simulations, phantom, and in vivo experiments. We also compare the dark-blood $T_{1\rho,adiab}$ mapping with the reference bright-blood method in terms of precision and reproducibility both in phantoms and in vivo. Finally, we test both dark-and bright-blood $T_{1\rho,adiab}$ mapping on a small cohort of patients referred for CMR examination.
- In Chapter 6 we propose adiabatic preparation to quantify myocardial $T_{2\rho,adiab}$, providing complementary information to $T_{1\rho,adiab}$. $T_{2\rho,adiab}$ mapping is compared to $T_{1\rho,adiab}$ and conventional T_2 mapping in terms of precision and reproducibility in phantoms and a small cohort of healthy subjects.
- In Chapter 7 we explore relaxation along a fictitious field (RAFF) pulses, operating in the sub-adiabatic regime. We propose

a simulations-based framework to optimize RAFF preparations for rotating-frame relaxation by generalizing them to arbitrary duration, starting phase, and adiabaticity. The resulting optimal girRAFF preparation is tested for phantom and in vivo mapping in the calf muscle and knee cartilage. Performance is compared to conventional RAFF in terms of precision, reproducibility, and robustness to field inhomogeneities.

- In Chapter 8 we investigate rotating-frame relaxation during adiabatic pulses from a theoretical point of view. Based on Redfield relaxation theory, we propose a framework to derive $T_{1\rho,adiab}$ relaxation during adiabatic pulses with variable amplitude-and frequency-modulation functions. We use this framework to derive optimal pulse parameters to minimize $T_{1\rho,adiab}$ dispersion in the presence of field inhomogeneities to potentially improve in vivo applicability at high field strengths.

- In Chapter 9 we study an alternative application of spin-lock preparation for quantitative MRI: directly sensitizing the MRI signal to weak magnetic field fluctuations caused by neuronal currents. Based on simulations, we compare the performances of two spin-lock schemes in terms of sensitivity and resilience to field inhomogeneities. Additionally, we propose a novel post-processing framework to extract statistical maps of neural activation patterns from neuro-currents functional MRI.

- In conclusion, in Chapter 10 we discuss the relevance of the work presented in this dissertation in the context of the wider research field and contrast it with other current research developments. This chapter offers a perspective on the future challenges to address in order to reach the full technical and clinical potential of rotating-frame relaxation techniques.

2

Brief Introduction to MRI Physics

Joao Tourais[†], **Chiara Coletti**[†], Sebastian Weingärtner

Adapted from: Magnetic Resonance Image Reconstruction: Theory, Methods, and Applications. Ed. by M. Akçakaya, M. Doneva, and C. Prieto. Vol. 7. Advances in Magnetic Resonance Technology and Applications. Academic Press, 2022. Chap. 1, pp. 3–36.
doi: https://doi.org/10.1016/B978-0-12-822726-8.00010-5.

[†]These authors contributed equally

Abstract

Magnetic resonance imaging (MRI) is one of the most fascinating applications of advanced physics in modern society. MRI combines multiple physical concepts to enable non-invasive imaging based on a magnetization signal that forms within the subject. An unparalleled wealth of contrast mechanisms can be achieved with MRI, making it integral to many areas of diagnostic radiology. In this chapter, we set out to explain the basics of MRI physics, to provide the background necessary to understand advanced MRI reconstruction techniques. We will look at the theory of nuclear magnetism and introduce the basic concepts required to generate the nuclear magnetic resonance (NMR) signal. Subsequently, the process of spatial localization of the NMR signal that allows for image formation is explained. With this knowledge, we will discuss basic MRI pulse sequences. To conclude, we lay out the basic characteristics and hardware components of modern MRI machines.

2.1. A Brief History of MRI

In the 1970s, the State University of New York decided against supporting a patent application, with the rationale that a resulting patent would be unlikely to cover the necessary expenses. The patent application in question was written by Paul C. Lauterbur, describing his technique of creating an image from nuclear magnetic resonance (NMR) using field gradients. Some 30 years later, this invention would be recognized by the Nobel Committee as fundamental for the development of what is now known as magnetic resonance imaging (MRI) - and by the State University of New York as a huge missed opportunity. Since Lauterbur created his early predecessor to MR images by rotating a probe with deuterium and water in an NMR spectrometer [13], MRI has come a long way. With nearly 100 million scans performed each year worldwide, MRI is one of the backbones of modern image-based diagnosis. A plethora of key innovations by brilliant minds has facilitated the techniques that now enable unique insight into the human body.

MRI is based on the phenomenon of NMR, which was first described by Isidor I. Rabi in the 1930s [14] and later followed by experimental validation in 1938 [15]. The next step was taken by Felix Bloch and Edward M. Purcell, who independently demonstrated NMR in liquids and solids in 1946 [16, 17]. These discoveries marked the beginning of NMR spectroscopy, which in the following years proved to be a transformative technique for the study of molecules. However, further leaps were required to enable the formation of images.

The first step in this direction was taken by Hermann Y. Carr, who reported in his Ph.D. thesis from 1952 the use of spatially varying magnetic fields, so-called gradient fields, to encode the spatial location of magnetization in NMR experiments [18]. In his landmark paper from 1973, Lauterbur built on this idea to create a two-dimensional image, introducing the fundamental concept of image formation used in modern MRI machines [13]. Following Lauterbur's seminal work, Sir Peter Mansfield in Nottingham, UK, introduced the mathematical characterization of the newly formed imaging methodology [19]. The contributions of Paul C. Lauterbur and Sir Peter Mansfield that enabled the development of MRI were honored with the Nobel Prize for Physiology and Medicine in 2003. These developments sparked the rapidly evolving field of MRI research, which remains an active area of research to date.

In this chapter, we describe the basic physical principles that underpin MRI and that are necessary to understand the properties of MR images, data acquisition techniques, and reconstruction methods. We take an explorative approach to derive six principles that aim at enabling the reader to follow in-depth discussions of MRI: 1) The formation of a magnetization based on nuclear magnetism; 2) The dynamics of this magnetization in an external magnetic field; 3) The use of rotating magnetic fields to create a detectable magnetization component; 4)

The use of induction to measure this component; 5) The evolution of this signal in the presence of relaxation mechanisms, and finally 6) The use of gradient fields to enable image formation. By the end of this chapter, the reader will hopefully have attained a basic understanding of an MRI experiment and the different components involved. This forms the foundation necessary to understand and discuss advanced MRI reconstructions.

2.2. Nuclear Magnetism

The signal in MRI originates from magnetization that forms within the sample or the subject that is being imaged. The source of this magnetization can be found in the nuclei of certain atoms within the sample, due to a physical phenomenon, termed nuclear magnetism. To understand nuclear magnetism and the resulting MRI signal, the basic properties giving rise to this phenomenon, and the physical principles describing its behavior are laid out in this section.

2.2.1. Spin

Particles and nuclei are described by several characteristics, for example, their mass or their charge. Similar to mass or charge, *spin* also describes a fundamental property intrinsic to particles and nuclei. As hinted to by its naming, a spin is related to an angular momentum, similarly to the rotational momentum of a spinning top. However, unlike the classical angular momentum of the spinning top, the spin angular momentum is quantized, i.e., it can only occur in certain discrete states.

Think of this as the difference between a bicycle wheel compared with a fortune wheel: a classical angular momentum can align in any direction, similar to the bicycle wheel that can stop at any angle. A spin angular momentum, however, has only a discrete set of directions, similar to the stopping position of the fortune wheel. The number of possible directions, also known as spin states, is characterized by the *spin quantum number*, s. By conventional definition, s is a half or full integer number ($s = 0, 1/2, 1, 3/2 \ldots$). Using the spin quantum number, the number of different spin states is given by $2s + 1$. The spin quantum number is a constant property that does not change over time and cannot be altered without modifying the particle or the nucleus. The spin state, on the other hand, can change over time and may be different for otherwise identical particles or nuclei.

Going back to our analogy of the spinning top, if additionally an electric charge is placed on the edge of the spinning top, it rotates due to the rotational momentum of the spinning top. Classical electrodynamics tells us that the rotation of the charge gives rise to a magnetic moment oriented along the rotational axis. Similarly, nuclei with nonzero spin

develop a magnetic moment. This nuclear magnetic moment is mostly a magnetic dipole moment, which means its magnetic field is comparable to the one created by an infinitely small bar magnet. Thus, a useful analogy of nuclei for the understanding of MRI is the picture of a spinning bar magnet as illustrated in Figure 2.1. However, the analogy has certain limitations. For example, nuclei with asymmetric charge distribution also exhibit weak quadrupole moments, associated with different resulting magnetic fields. These effects can have relevant consequences on the signal when imaged with MRI.*

2.2.2. Net Magnetization

When a nucleus that exhibits a nuclear magnetic moment is placed into an external magnetic field **B**, different orientations of the magnetic moment are associated with different magnetic potential energies. For the discrete spin states, this entails an energy gap between the various states. This splitting of the energy levels is called the *Zeeman effect*. The gap between the energy states depends on the strength of the external magnetic field B, the magnetic moment (μ), and the spin (s). A useful quantity to describe the behavior of nuclei in external magnetic fields is the gyromagnetic ratio which is obtained as the ratio between the magnetic and the angular momentum $\gamma = \mu/(s\hbar)$, where $\hbar$ is the reduced Planck constant. The energy gap between the spin states can then be expressed as

$$\Delta E = \frac{\mu}{s} B = \gamma \hbar B. \tag{2.1}$$

When placing a multitude of nuclei into the external magnetic field, distribution across the spin states will naturally arise, following the principles of thermodynamics. This distribution can be described using Boltzmann statistics as a function of the energy gap ΔE and the temperature T as

$$\frac{N^+}{N^-} = e^{-\frac{\Delta E}{kT}}, \tag{2.2}$$

with N^+ and N^- being the number of nuclei in the higher and lower energy spin state, respectively. Here, k denotes the Boltzmann constant. The uneven distribution of the orientations of the magnetic moments entails that, when summing all magnetic moments in a volume, a nonzero magnetization is formed.

MRI most commonly focuses on the hydrogen nucleus ^1H which comprises only a single proton. A proton is a Fermion, which means it has a half-integer spin, in this case, $s = 1/2$. Accordingly, the hydrogen

*For more details, the reader is referred to [20, 21].

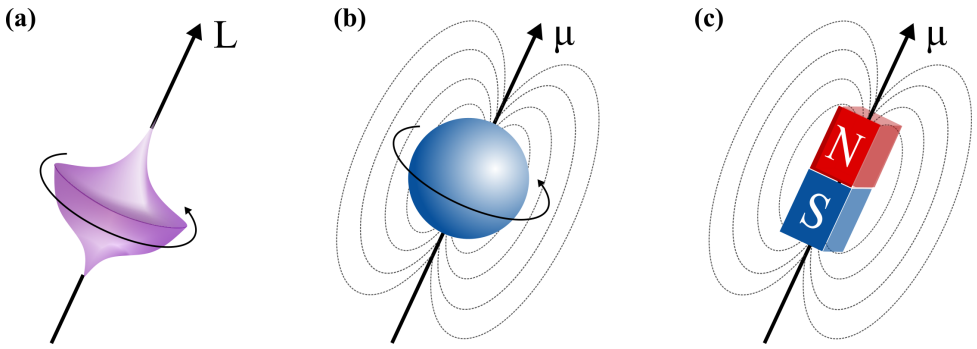

Figure 2.1 : (a) Spinning top with angular momentum L, (b) hydrogen nucleus (proton) with magnetic moment μ, and (c) spinning bar magnet with magnetic dipole moment μ.

nucleus has only $2s+1=2$ spin states, which are often referred to as *spin-up* and *spin-down*, respectively (Figure 2.2). In this case, the net magnetization is easily derived by subtracting the anti-parallel (spin-down) magnetic moments from the parallel magnetic moment (spin-up).

$$M_0 = N^+\mu - N^-\mu = N^-\mu\left(e^{-\frac{\Delta E}{kT}} - 1\right) \tag{2.3}$$

$$= N\mu\frac{e^{-\frac{\Delta E}{kT}} - 1}{e^{-\frac{\Delta E}{kT}} + 1} = N\mu\tanh\left(\frac{\Delta E}{2kT}\right) \tag{2.4}$$

$$\approx \frac{N\mu\Delta E}{2kT} = \frac{N\mu\gamma\hbar B}{2kT}. \tag{2.5}$$

Here, $N^- = N/(e^{-\frac{\Delta E}{kT}} + 1)$ with $N = N^+ + N^-$, was used in Eq. (2.4), which can be easily derived from Eq. (2.2). Further, $\tanh(x) \approx x$ was approximated under the assumption of $x \ll 1$. Eq. (2.5) can be similarly derived for other spin values and is known as Curie's law. As illustrated in Figure 2.3, this describes the first fundamental step in forming a magnetization that can later be used for imaging.

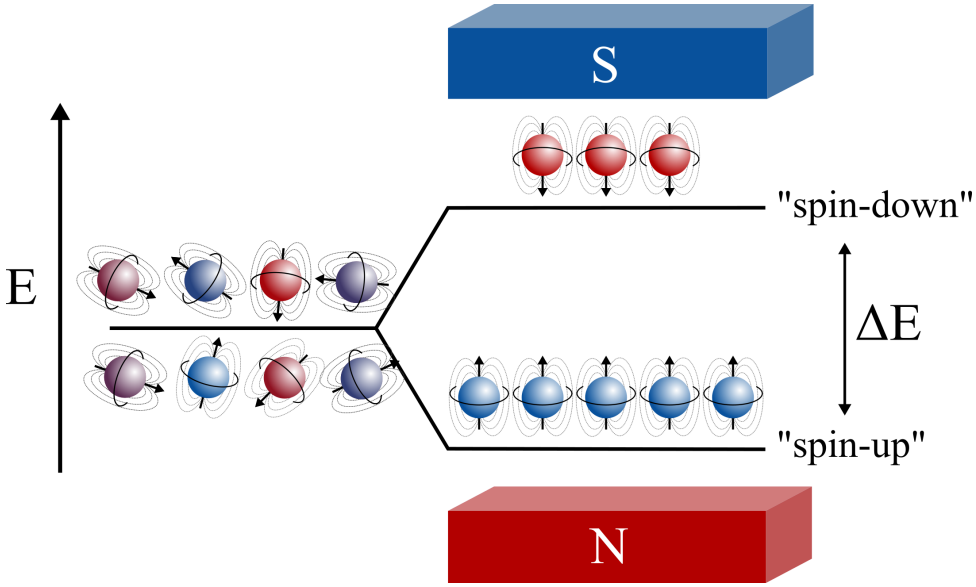

Figure 2.2 : Zeeman splitting effect: when no external magnetic field is present, spins with randomly distributed magnetic moments are characterized by the same energy level. In presence of an external magnetic field, the spin-up and spin-down states are separated by a potential energy gap.

Principle 1: Net Magnetization
If samples containing nuclei with nonzero spin s are brought into a magnetic field $\mathbf{B}$ a net-magnetization $\mathbf{M}_0$ forms. This magnetization is formed parallel to the external field ($\mathbf{M}_0 \parallel \mathbf{B}$) and its magnitude is characterized as

$$\mathbf{M}_0 = \frac{N\gamma s(s+1)\hbar^2}{3kT}\mathbf{B}, \tag{2.6}$$

with the gyromagnetic ratio γ, the spin quantum number s, the number of nuclei per volume N, the temperature T, and the Boltzmann constant k.

2.2.3. Magnetization Dynamics

Forming a magnetization along the external magnetic field proves to be not very fruitful by itself. Instead, it helps to consider the magnetization dynamics over time. Any sample with a magnetic dipole moment $\mathbf{M}(t)$ experiences a torque $\mathbf{T}(t)$ in the presence of a static external field $\mathbf{B}$:

$$\mathbf{T}(t) = \mathbf{M}(t) \times \mathbf{B}. \tag{2.7}$$

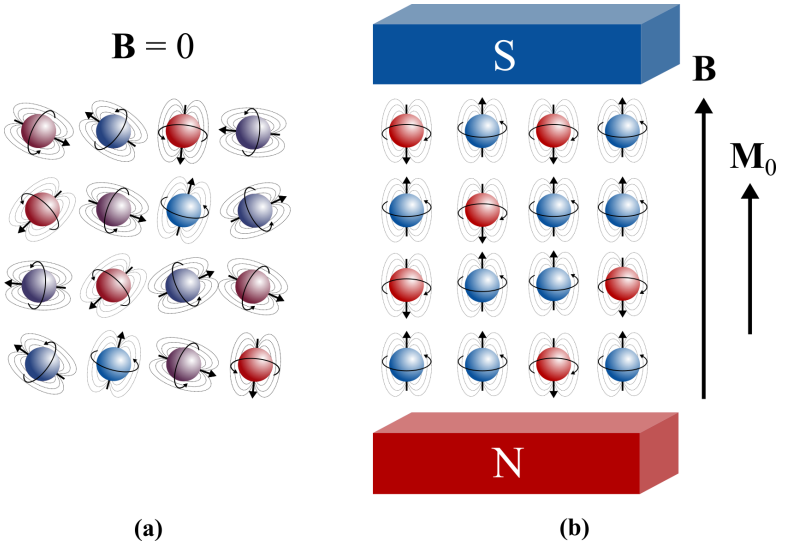

Figure 2.3 : (a) Spins and corresponding magnetic moments are randomly oriented in the absence of an external magnetic field ($\mathbf{B} = 0$). (b) In the presence of an external magnetic field $\mathbf{B}$, however, the majority of the spins occupy the lower energy configuration, the spin-up state, generating a net magnetization $\mathbf{M}_0$ aligned with the magnetic field.

Accordingly, the same happens to a sample with nonzero spin nuclei. However, as initially explained, the spin is also associated with an angular momentum. Thus, this torque affects the cumulative angular momentum $\mathbf{L}_s$ of the sample as[†]

$$\dot{\mathbf{L}}_s(t) = \mathbf{M}(t) \times \mathbf{B}. \tag{2.8}$$

The gyromagnetic ratio γ links the magnetic and the angular moment of our spin ensemble. Hence, we can link the dynamics of the angular momentum to that of the net magnetization as presented in the following principle.

Principle 2: Larmor Precession
The net magnetization $\mathbf{M}(t)$ described in Principle 1 undergoes the following dynamics in a static external magnetic field $\mathbf{B}$.

$$\dot{\mathbf{M}}(t) = \gamma \mathbf{M}(t) \times \mathbf{B} + \text{relaxation terms}^{\ddagger}, \tag{2.9}$$

with the gyromagnetic ratio γ. These dynamics are known as Larmor precession [22].

[†]For convenience, we use Newton's notation for differentiation throughout this chapter. If f is a function of t, then the derivative of f with respect to t is denoted as $\dot{f}$.

This enables us to gain some important insights into magnetization. First, if the magnetization is parallel to the external magnetic field, no dynamic behavior is observed in the magnetization:

$$\mathbf{M}(t) \parallel \mathbf{B} \implies \mathbf{M}(t) \times \mathbf{B} = 0 \implies \dot{\mathbf{M}} = 0 \implies \mathbf{M}(t) = \mathbf{M}(0). \tag{2.10}$$

However, if the magnetization is skewed away from the external field by an angle θ, Principle 2 dictates that the gradient direction is tangential to a circle around the main magnetic field, and its magnitude is found as

$$\|\dot{\mathbf{M}}(t)\| = \gamma \sin(\theta) M B, \tag{2.11}$$

with the (static) magnitude of the magnetization $M = \|\mathbf{M}(t)\|$ and the field strength $B = \|\mathbf{B}\|$.

Thus, the magnetization vector describes a cone around the external magnetic field, with the tip lying in a circle. This type of motion is called precession and can again be likened to our spinning top. If the spinning top is nudged so that its rotational axis is angled with respect to the gravitational force, it precesses around this axis comparably.

The circle prescribed in this motion has radius $\sin(\theta)M$. Thus, the frequency of the rotation can be obtained as

$$\frac{\gamma \sin(\theta) M B}{\sin(\theta) M} = \gamma B = \omega. \tag{2.12}$$

This field-dependent angular frequency is also known as the *Larmor frequency* and will prove important for our understanding of the MRI signal.

2.3. NMR/MRI Signal

2.3.1. Signal Creation and Reception

There is little use in knowing the magnetization dynamics if we cannot manipulate or detect them. We will now explore how the resonance phenomenon can be employed to change the magnetization and how this can be read out into a detectable signal.

Radiofrequency Pulses

In MRI, a signal can only be created if the magnetization is nutated away from the external magnetic field. For this purpose, the special case of

[‡]The relevant relaxation terms will be introduced in subsection 2.3.2.

rotating external magnetic fields is particularly relevant. To this end, we start by defining the overall magnetic field $\mathbf{B}_{tot}(t)$ as

$$\mathbf{B}_{tot}(t) = \begin{pmatrix} B_1 \cos(\omega_1 t) \\ B_1 \sin(\omega_1 t) \\ B_0 \end{pmatrix}, \tag{2.13}$$

with a stationary magnetic field with strength B_0 along the z-axis and a secondary magnetic field with amplitude B_1 rotating in the transverse plane with angular frequency ω_1, i.e., the plane orthogonal to the $\mathbf{B}_0$ field.

To better understand the effects of rotating magnetic fields, it is useful to consider a rotating frame of reference (RFR). RFRs are a familiar concept. The reader is likely observing this chapter in an RFR: in a galactic reference frame, this book would rotate around the axis of the globe. However, the reference frame we observe is spinning with the globe and makes the book appear stationary. Similarly, we can define an RFR to rotate with the rotating magnetic field (an extensive explanation can be found in [23]). For the stationary or laboratory frame of reference (x, y, z) and the RFR (x', y', z'), we can define the following reference frame transformation

$$\begin{pmatrix} x \\ y \\ z \end{pmatrix} \mapsto \begin{pmatrix} x' \\ y' \\ z' \end{pmatrix} : \mathbf{R}(t) = \begin{pmatrix} \cos(\omega_1 t) & \sin(\omega_1 t) & 0 \\ -\sin(\omega_1 t) & \cos(\omega_1 t) & 0 \\ 0 & 0 & 1 \end{pmatrix}, \tag{2.14}$$

with $\mathbf{R}(t)$ being a proper rotation matrix, i.e., $\mathbf{R}(t)\mathbf{R}^T(t) = \mathbf{I}$ and $\det(\mathbf{R}(t)) = 1$.

Observing the magnetization dynamics of a magnetization $\mathbf{M}'(t) = \mathbf{R}(t)\mathbf{M}(t)$ in an RFR in the presence of a rotating dynamic magnetic field $\mathbf{B}_{tot}(t)$ such as defined in Eq. (2.13) yields

$$\dot{\mathbf{M}}'(t) = \frac{d}{dt}(\mathbf{R}(t)\mathbf{M}(t)) = \dot{\mathbf{R}}(t)\mathbf{M}(t) + \mathbf{R}(t)\dot{\mathbf{M}}(t) \tag{2.15}$$

$$= \dot{\mathbf{R}}(t)\mathbf{R}^T(t)\mathbf{M}'(t) + \mathbf{R}(t)\gamma\mathbf{M}(t) \times \mathbf{B}_{tot}(t). \tag{2.16}$$

By multiplying out the matrices, it can quickly be concluded that

$$\dot{\mathbf{R}}(t)\mathbf{R}^T(t)\mathbf{M}'(t) = -\omega_1 \mathbf{M}'(t) \times \begin{pmatrix} 0 \\ 0 \\ 1 \end{pmatrix} \tag{2.17}$$

and

$$\mathbf{M}(t) \times \mathbf{B}(t) = \mathbf{R}^T(t)\mathbf{M}'(t) \times \mathbf{B}_{tot}(t), \tag{2.18}$$

due to the rotation properties of the cross product. It follows

$$\dot{\mathbf{M}}'(t) = -\omega_1 \mathbf{M}'(t) \times \begin{pmatrix} 0 \\ 0 \\ 1 \end{pmatrix} + \mathbf{R}(t)\gamma\mathbf{R}^T(t)\mathbf{M}'(t) \times \mathbf{B}_{tot}(t) \tag{2.19}$$

$$= \gamma \left(\mathbf{B}'_{tot}(t) - \begin{pmatrix} 0 \\ 0 \\ B_0 \frac{\omega_1}{\omega_0} \end{pmatrix} \right), \tag{2.20}$$

with the Larmor frequency $\omega_0 = \gamma B_0$ and

$$\mathbf{B}'_{tot}(t) = \mathbf{R}(t)\mathbf{B}(t) = \begin{pmatrix} B_1 \\ 0 \\ B_0 \end{pmatrix}. \tag{2.21}$$

This yields the following principle.

Principle 3: Rotating Frame Excitation
For a magnetic field with a rotational component in the xy-plane $\mathbf{B}_{tot}(t) = \begin{pmatrix} B_1\cos(\omega_1 t) & B_1\sin(\omega_1 t) & B_0 \end{pmatrix}^T$, the net magnetization $\mathbf{M}'(t)$ in a RFR rotating about the z-axis with frequency ω_1 can be described as

$$\dot{\mathbf{M}}'(t) = \gamma \mathbf{M}'(t) \times \mathbf{B}_{\mathbf{eff}}(t) + \text{relaxation terms}, \tag{2.22}$$

with the gyromagnetic ratio γ, the Larmor frequency $\omega_0 = \gamma B_0$ and

$$\mathbf{B}_{\mathbf{eff}}(t) = \begin{pmatrix} B_1 \\ 0 \\ B_0 \left(1 - \frac{\omega_1}{\omega_0}\right) \end{pmatrix}. \tag{2.23}$$

Again, this principle allows us to derive some important properties. Namely, if the secondary magnetic field $\mathbf{B}_1$ is applied at the resonance frequency, i.e., $\omega_1 = \omega_0$, the magnetization vector in the RFR rotates only about the secondary magnetic field, as shown in Figure 2.4. The speed of this rotation is determined by the strength of the secondary magnetic field. Hence, the angle accumulated by the secondary magnetic field of time-varying amplitude $B_1(t)$ can be computed as

$$\alpha = \int_0^\infty \gamma B_1(t) dt, \tag{2.24}$$

and is called the *flip angle*. Accordingly, for the simple case of a constant magnetic field B_1 applied during a time τ, the flip angle $\alpha = \gamma B_1 \tau$. A flip angle of 90° tips the magnetization into the transverse plane and

yields the strongest magnetization component orthogonal to the main magnetic field. The application of $\alpha = 180°$, returns no transverse magnetization, essentially inverting the magnetization.

On the other hand, for $\omega_1 \neq \omega_0$ the magnetization precesses around an angled effective field, where the angle between $\mathbf{B}_{eff}$ and the z-axis amounts to $\theta = \operatorname{atan}(B_1/(B_0(1-\omega_1/\omega_0)))$. In MRI, the field strength of the secondary magnetic field is much smaller than the main magnetic field ($B_1 \ll B_0$), thus, to induce a precession that rotates the magnetization away from the z-axis, it is important to closely match the resonance frequency.

On clinical MRI systems, the field strength is often around $B_0 = 1.5T$. At this field strength, resonance is achieved at the Larmor frequency of $\omega_0/(2\pi) \approx 63.9\,\text{MHz}$ (for the hydrogen nucleus). As these frequencies are in the range of radio waves, the rotating magnetic field $\mathbf{B}_1$ may be referred to as radiofrequency (RF) field. Because the B_1 field is employed for a short duration, it is also often commonly referred to as an RF pulse. An RF pulse creating a flip angle of 90° is (conveniently) called a 90° pulse.

Signal Detection

To better understand how to create a detectable signal from the magnetization $\mathbf{M}$ in MRI, it is useful to consider the individual magnetization components

$$\mathbf{M}(t) = \begin{pmatrix} M_x(t) \\ M_y(t) \\ M_z(t) \end{pmatrix}. \tag{2.25}$$

$M_z(t)$ describes the magnetization component along the z-axis, which is aligned with the external magnetic field $\mathbf{B}_0 = \begin{pmatrix} 0 & 0 & B_0 \end{pmatrix}^T$, and is called the longitudinal magnetization. The vector $\mathbf{M}_{xy} = \begin{pmatrix} M_x & M_y \end{pmatrix}$ is referred to as the transverse magnetization which lies in the xy-plane, orthogonal to the main magnetic field $\mathbf{B}_0$.

Using this notation, the net magnetization $\mathbf{M}$ that is formed, following Principle 1, is aligned with the external magnetic field $\mathbf{B}_0$

$$\mathbf{M}(0) = \begin{pmatrix} 0 \\ 0 \\ M_0 \end{pmatrix}. \tag{2.26}$$

Using Principle 3, we can calculate the effect of an RF pulse played along the y'-axis with a duration τ and strength B_1 chosen to achieve a flip angle $\alpha = \gamma\tau B_1 = 90°$. When neglecting the relaxation terms, it

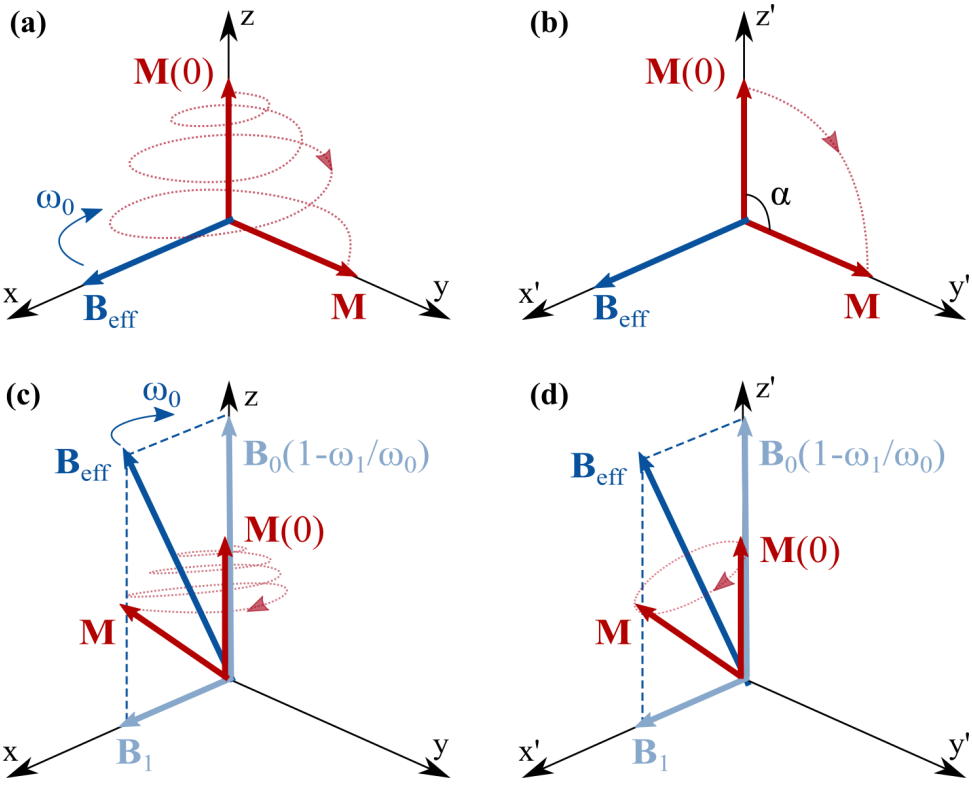

Figure 2.4 : On-resonance 90° excitation pulse ($\mathbf{B}_{eff} = \mathbf{B}_1$, $\omega_1 = \omega_0$) tipping the magnetization to the transverse plane, as viewed in the (a) laboratory and (b) rotating frame of reference (RFR). (c, d) Off-resonance excitation pulse ($\omega_1 \neq \omega_0$), causing $\mathbf{B}_{eff}$ to be strongly angled towards the z-axis, preventing full excitation.

follows for the magnetization:

$$\mathbf{M}'(\tau) = \begin{pmatrix} M_0 \\ 0 \\ 0 \end{pmatrix} \Longrightarrow \mathbf{M}(\tau + t) = \begin{pmatrix} \cos(\omega_0 t) M_0 \\ \sin(\omega_0 t) M_0 \\ 0 \end{pmatrix}, \tag{2.27}$$

in the RFR and the stationary frame, respectively.

This means that a time-varying magnetization component has been created on the transverse plane. The time-varying magnetic field originating in the precession of the magnetization vectors can be picked up using an inductive coil near the sample. In its most simplistic form, this coil is an individual loop of wire. Faraday's law of induction declares that a time-varying magnetic flux through a wire loop produces a current in the loop and induces a voltage ϕ over the edges of the loop.

Principle 4: Faraday's Law of Induction
If a coil is placed such that a magnetic field has a temporally varying component normal to the coil area, a voltage is induced in the coil. The produced voltage E is proportional to the negative of the rate of temporal variation of the flux ($d\phi/dt$), which in turn is proportional to the magnetic field strength normal to the coil ($\phi \propto \mathbf{M}_{xy}$):

$$E \propto -\frac{d\phi}{dt}. \tag{2.28}$$

The demand for a time-varying magnetic flux is the reason solely precessing magnetization in the xy-plane yields an increase to an NMR signal: the z-component does not precess and, hence, generates no voltage. At greater strengths of the $\mathbf{B}_0$ field, the magnetization precesses at a higher frequency, and so the value of $d\phi/dt$ rises. Thus, stronger magnetic fields yield better signal strength not only because of the larger nuclear polarization (Principle 1) but also because of the additional increase in magnetic flux.

2.3.2. Signal Relaxation and Decay

When researchers first created NMR signals from the principles above, such as Erwin Hahn with his pulsed NMR experiments in 1950 [24], they had to make the sobering observation that the carefully created signal would quickly decay. It was Felix Bloch, who phenomenologically concluded that the created NMR signal is subject to multiple relaxations and decay processes, which prevent a transverse magnetization from indefinite signal induction [25].

To create a detectable signal, following Principle 3, an RF pulse needs to be applied at the Larmor frequency. Note that this frequency corresponds to the energy gap between the spin states

$$\Delta E = \omega_0 h = \gamma h \mathbf{B}_0, \tag{2.29}$$

where h is the Planck's constant. Thus, when a secondary magnetic field is applied, energy is transmitted into the system. This excess energy excites the system above the thermal equilibrium, to which it naturally relaxes back. In the vector model, the M_z component has been lowered from its equilibrium value of M_0, and the M_x and/or M_y components may have a nonzero value. Each of the magnetization components M_z, M_x, and M_y returns to the thermal equilibrium value over time. To better understand this relaxation, it is useful to consider two different processes: 1) The recovery of the M_z component to the thermal equilibrium value M_0, also known as longitudinal relaxation, and

2) The decay of the transverse magnetization towards zero, also known as transverse relaxation.

Longitudinal Relaxation

During the recovery to thermal equilibrium, the spin system dissipates energy to the surrounding lattice. Thus, the recovery of the longitudinal magnetization is also known as spin-lattice relaxation. The closer the system gets to thermal equilibrium, the closer the longitudinal magnetization is to the equilibrium magnetization M_0. The rate of recovery depends on the excess of energy in the spin system, as well as a sample-specific constant T_1. This allows us to describe the dynamics of longitudinal magnetization, including magnetization recovery, as

$$\dot{\mathbf{M}}_z(t) = \gamma(\mathbf{M}(t) \times \mathbf{B}(t))_z - \frac{M_z(t) - M_0}{T_1}, \tag{2.30}$$

where $(\mathbf{x})_z = x_z$, for $\mathbf{x} = \begin{pmatrix} x_x & x_y & x_z \end{pmatrix}^T$.

In MRI, observing the longitudinal magnetization following an RF pulse of flip angle α is of particular interest. Following Principle 3 we see that promptly after the application of the RF pulse, the longitudinal magnetization M_z can be described by $M_0\cos(\alpha)$. For a time t after the RF pulse, Eq. (2.30) gives the value of M_z as

$$M_z(t) = M_0\cos(\alpha) + (M_0 - M_0\cos(\alpha))\left(1 - e^{-\frac{t}{T_1}}\right). \tag{2.31}$$

For instance, following a 90° pulse, the value of M_z is given by

$$M_z(t) = M_0\left(1 - e^{-\frac{t}{T_1}}\right). \tag{2.32}$$

This and an example of longitudinal magnetization regrowth following a 180° pulse can be seen in Figure 2.5.

Transverse Relaxation

The physical basis for the second relaxation mechanism, the transverse magnetization decay, differs from the T_1 relaxation process. A coherent magnetization in the transverse plane can only be maintained, as long as all magnetic moments contributing to the transverse magnetization precess at the same frequency. However, even in a perfectly homogeneous magnetic field, magnetic moments precess at marginally different frequencies. This is due to the magnetic moments of neighboring nuclei, which influence the observed net magnetic field strength at any location and in a time-varying manner, due to the molecular motion. Transverse magnetization decay is caused by losing

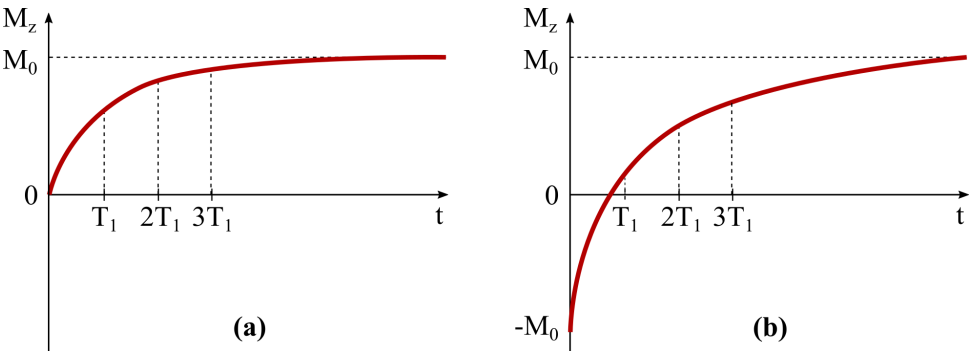

Figure 2.5 : Exponential regrowth, over time, of the longitudinal component of the magnetization $M_z(t)$ to the equilibrium value M_0 after a 90° (a) or 180° (b) excitation pulse.

the *phase coherence* among the magnetic moments. As a result, the net magnetization decays over time (Figure 2.6): the magnetic moments fan out, and consequently, the magnitude of the net sum decreases. Thus, the transverse magnetization unwinds back to the thermal equilibrium value of zero with a sample-specific time constant called the spin-spin relaxation time, or T_2:

$$\dot{M}_x(t) = \gamma(\mathbf{M}(t) \times \mathbf{B}(t))_x - \frac{M_x(t)}{T_2}, \tag{2.33}$$

$$\dot{M}_y(t) = \gamma(\mathbf{M}(t) \times \mathbf{B}(t))_y - \frac{M_y(t)}{T_2}. \tag{2.34}$$

Together these relaxation processes constitute the Bloch Equations, one of the most important tools for MRI researchers.

Principle 5: Bloch Equations
The time evolution of M_z, M_x, and M_y can be described by differential equations, recognized as the Bloch equations:

$$\dot{\mathbf{M}}(t) = \frac{d}{dt}\begin{pmatrix} M_x \\ M_y \\ M_z \end{pmatrix} = \gamma(\mathbf{M}(t) \times \mathbf{B}(t)) - \begin{pmatrix} \frac{M_x(t)}{T_2} \\ \frac{M_y(t)}{T_2} \\ \frac{M_z(t)-M_0}{T_1} \end{pmatrix} \tag{2.35}$$

Two mechanisms that contribute to the loss of phase coherence of the transverse magnetization can be differentiated. The first mechanism is the “real” T_2 decay originating in spin-spin interaction, as described before. The second mechanism derives from the spatial disparities of the magnetic field strength inside the body. There are, in turn, two

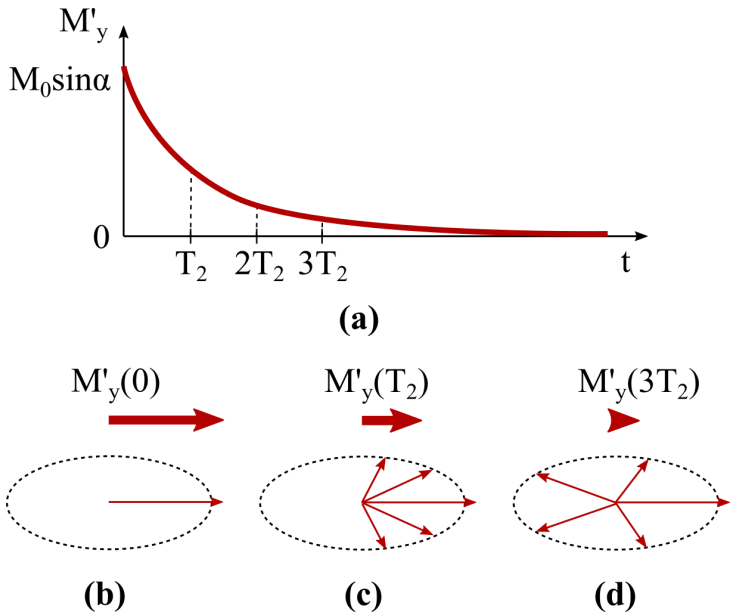

Figure 2.6 : (a) Exponential decay of the transverse component of the magnetization ($M'_y(t)$) in the RFR over time. The transverse component recovers to the equilibrium value zero after excitation with an arbitrary flip angle α. The coherence loss of magnetic moments precessing in the transverse plane and the corresponding net transverse magnetization M_y is shown right after the excitation pulse (b) and after one (c) or several (d) spin-spin relaxation periods T_2.

notable causes for these differences. The first is the inherent magnet design: it is impracticable to design a magnet generating a perfectly homogeneous magnetic field throughout the whole subject. The second cause is given by regional changes in the magnetic field due to the distinct magnetic susceptibilities of different tissues. This effect is particularly pronounced at the air/tissue and bone/tissue boundaries. Collectively, these effects create a decline in phase coherence, which is described by a relaxation time T_2'. The effective relaxation time that characterizes the decay of transverse magnetization is a combination of signal loss due to T_2 and T_2' effects. This is defined by T_2^*, and it can be expressed by

$$\frac{1}{T_2^*} = \frac{1}{T_2'} + \frac{1}{T_2}. \tag{2.36}$$

Considering these decay mechanisms, the detectable magnetization in the transverse plane from Equation (2.27), which is formed after the

application of a 90° RF pulse, can be described as

$$\mathbf{M}(t) = \begin{pmatrix} \cos(\omega_0 t) \\ \sin(\omega_0 t) \\ 0 \end{pmatrix} M_0 e^{-\frac{t}{T_2^*}}. \tag{2.37}$$

In high-resolution NMR spectroscopy for chemical examination, the sample is small and spatially uniform. Thus, there are only small field inhomogeneities leading to long $T_2^{'}$ times. In this case, the value of T_2^* is adequately approximated by T_2, and Principle 5 is accurate for representing the decay of transverse magnetization in the entire sample. In MRI, however, the value of $T_2^{'}$ can be up to 10-100 times lower than that of T_2. Thus, $T_2^{'}$ is the main driver of T_2^* decay.

In practice, it is often important to discriminate between T_2 and T_2^*. The field variations contributing to T_2 are temporally variant, but the effects contributing to T_2^* are static over time. Fortunately, a mechanism can also be used to recover the signal loss due to temporally invariant causes. If at a time τ, following the 90° pulse, a 180° pulse is applied, the magnetization is flipped, and the phase dispersion is re-wound. Thus, this pulse is also known as *refocusing pulse*. At the time point *echo time* ($TE = 2\tau$), when the phase coherence is maximally restored, a *spin-echo* is formed and T_2 can be measured [24, 26]. This effect is illustrated in Figure 2.7.

2.3.3. Signal Relaxation During RF Irradiation: Spin-Lock MRI

Generally, MRI relaxation is neglected during the application of RF pulses to excite, invert, or refocus the magnetization. The duration of these RF pulses is rarely longer than a few ms, while relaxation time constants T_1 or T_2 range from tens to thousands of ms in vivo. Thus relaxation contributions to the MRI signal evolution during RF irradiation can be discarded. However, there is a specific class of MRI techniques in which this approximation fails: the so-called spin-lock experiments. Spin-locking is performed when a moderate amplitude RF pulse is applied for longer times up to tens or hundreds of ms, following conventional excitation. If the spin-lock pulse is applied with a 90° phase offset with respect to the RF pulse used to excite the signal ($\mathbf{B}_{SL}(t) = \begin{pmatrix} B_{SL}\cos(\omega_{SL}t) & B_{SL}\sin(\omega_{SL}t) & 0 \end{pmatrix}^T$), the resulting effective field in the RFR can be expressed as:

$$\mathbf{B_{eff}}(t) = \begin{pmatrix} 0 \\ B_{SL} \\ B_0\left(1 - \frac{\omega_{SL}}{\omega_0}\right) \end{pmatrix}, \tag{2.38}$$

where B_{SL} and ω_{SL} represent the spin-lock pulse strength and frequency, respectively. When a spin-lock pulse is applied immediately after

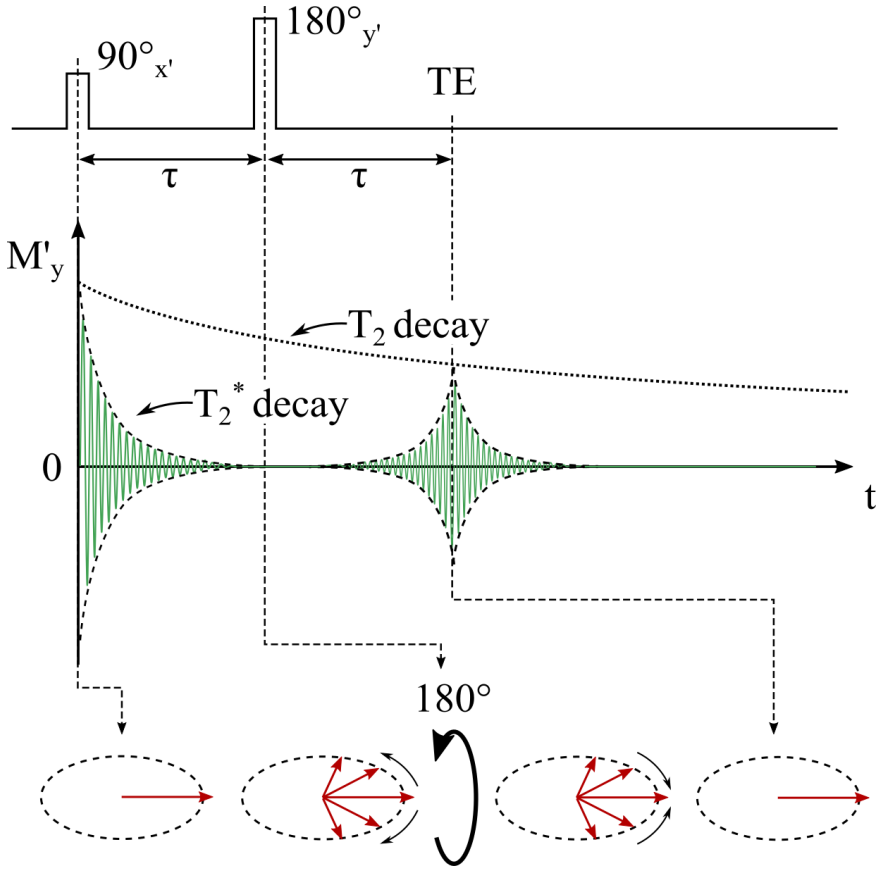

Figure 2.7 : Signal evolution during a spin-echo experiment in the RFR (green) and the laboratory frame of reference (gray). After the first 90° pulse, spins start dephasing, generating the FID signal, characterized by the T_2^* decay. The application of a 180° pulse inverts the process and generates an echo at $TE = 2\tau$, recovering T_2' losses. Overall, the spin echo signal follows a T_2 decay.

excitation, the magnetization rotates around the effective field vector $\mathbf{B_{eff}}$ instead of relaxing back to its equilibrium value under free decay conditions.

The Bloch equations in (2.35) can be adapted to describe the time evolution of the magnetization with a few precautions. Relaxation components can not be neglected during spin-lock pulses because of their significant duration. At the same time, T_1 and T_2 relaxation constants defined in Section 2.3.2 for free decay do not reflect the conditions of relaxation during RF irradiation. The spin-lock pulse constitutes an additional source of energy stimulating the relaxation process, in addition to the molecular motion processes introduced in

Section 2.3.2. Consequently, the longitudinal and transverse relaxation time constants during RF irradiation assume different values from conventional T_1 and T_2 and are called $T_{1\rho}$ and $T_{2\rho}$. The letter ρ stands for the rotating frame of reference, since $T_{1\rho}$ and $T_{2\rho}$ are derived in a double RFR where $\mathbf{B_{eff}}$ is aligned with z''. Thus, $T_{1\rho}$ describes the longitudinal magnetization along the orientation of the effective field, while $T_{2\rho}$ describes the transverse relaxation in the plane orthogonal to the orientation of the effective field.

While T_1 times are mostly sensitive to molecular motion processes at the Larmor frequency ($\omega_0 = 127.74$ MHz for a 1.5 T MRI system, or 127.74 MHz for a 3 T scanner, for instance), $T_{1\rho}$ is also sensitive to interactions at the spin-lock frequency (γB_{SL}). In clinical systems, due to technical constraints in the RF amplifiers, RF pulses can reach up to $\sim 15\mu$T, corresponding to a maximum frequency of ~ 650 Hz, a few orders of magnitudes lower than the Larmor frequency. The lower frequencies are characteristic of molecular motion phenomena such as chemical exchange or diffusion, which are important factors determining the interactions between macromolecules and water in biological tissues. Thus, rotating-frame relaxation induced by spin-lock experiments exhibits sensitivity to interesting dynamic processes that would normally be obscured in T_1 or T_2 relaxation.

2.4. Image Formation

The NMR signal defined so far is the gross summation of all net magnetic moments in the sample. It was not before 1973 when the contributions of Paul C. Lauterbur enabled to make spatial sense of the signal [13]. The key innovation was the introduction of *gradient fields*, magnetic fields whose strength is a function of the spatial location. It was discovered that in the presence of a gradient field, the spatial distribution of the protons gives rise to a variety of proton resonant frequencies, each dependent upon the location of the proton in the sample.

To understand image formation using magnetic field gradients, consider the most common form, linear field gradients. Let $\mathbf{G} = \nabla \mathbf{B}$ denote the *gradient* of the magnetic field strength of this gradient field. The total magnetic field strength at a position $\mathbf{r}$ can then be obtained as

$$B(\mathbf{r}) = B_0 + \mathbf{G}^T \mathbf{r}. \tag{2.39}$$

It should be noted that the orientation of the gradient fields (but not the direction of change) is always parallel to the static field, in order to alter the longitudinal component of the overall magnetic field.

In the presence of a field gradient, the Larmor frequency of the magnetization becomes a function of its spatial location,

$$\omega(\mathbf{r}) = \gamma \mathbf{G}^T \mathbf{r} \tag{2.40}$$

In other words, the gradient fields allow linking the Larmor frequency to the spatial location inside the magnet.

To see how the difference in precession frequency can be used for encoding, consider the application of gradient fields after a transverse magnetization has been created. For this purpose, the transverse magnetization is best described as a complex function of the time and the location $M_{xy}(t, \mathbf{r}) = M_x(t, \mathbf{r}) + iM_y(t, \mathbf{r})$. With this definition, the complex plane of $M_{xy}(t, \mathbf{r})$ coincides with the xy-plane. Following Principle 2, and assuming no relaxation effects due to $t \ll T_2^*$, it is easily verified that the precession can be described as

$$M_{xy}(t, \mathbf{r}) = e^{-i\gamma B(\mathbf{r})t} M_{xy}^0(\mathbf{r}). \tag{2.41}$$

Combining Equations (2.41) and (2.39), yields

$$M_{xy}(t, \mathbf{r}) = e^{-i\gamma B_0 t} e^{-i\gamma \mathbf{G}^T \mathbf{r} t} M_{xy}^0(\mathbf{r}). \tag{2.42}$$

The MRI signal can then be obtained as the spatial sum across the imaging volume

$$S'(t) \propto \int e^{-i\gamma B_0 t} e^{-i\gamma \mathbf{G}^T \mathbf{r} t} M_{xy}^0(\mathbf{r}) d\mathbf{r} \tag{2.43}$$

$$= e^{-i\omega_0 t} \int e^{-i\gamma \mathbf{G}^T \mathbf{r} t} M_{xy}^0(\mathbf{r}) d\mathbf{r}. \tag{2.44}$$

After demodulation of the signal with the Larmor frequency ω_0

$$S(t) \propto \int e^{-i\gamma \mathbf{G}^T \mathbf{r} t} M_{xy}^0(\mathbf{r}) d\mathbf{r}. \tag{2.45}$$

The versed reader might recognize the resemblance to a Fourier transform. Indeed, to connect to the Fourier transform, consider a gradient $\mathbf{G} = \begin{pmatrix} G_x & G_y & G_z \end{pmatrix}$ after time t. The gradient moments can be defined as $m_x = G_x t$, $m_y = G_y t$ and $m_z = G_z t$ and wavenumbers as $k_x = \gamma m_x$, $k_y = \gamma m_y$ and $k_z = \gamma m_z$ to yield

$$S(k_x, k_y, k_z) \propto \int \int \int e^{-i(k_x x + k_y y + k_z z)} M_{xy}^0(x, y, z)\, dx\, dy\, dz. \tag{2.46}$$

It follows that the Fourier transform of the signal S recovers the spatial information of the magnetization.

Principle 6: Gradient Encoding
If gradient fields with gradient moments m_x, m_y and m_z are applied after the creation of a transverse magnetization $M^0_{xy}(x, y, z)$, the resulting signal can be described as

$$S(k_x, k_y, k_z) \propto \int\int\int e^{-i(k_x x + k_y y + k_z z)} M_{xy}(x, y, z)\, dx\, dy\, dz. \quad (2.47)$$

using the wavenumbers $k_x = \gamma m_x$, $k_y = \gamma m_y$, and $k_z = \gamma m_z$, and the gyromagnetic ratio γ.
Of note, the Fourier transform of this signal recovers the spatial information about the magnetization

$$\mathbf{F}(S)(x, y, z) \propto M^0_{xy}(x, y, z). \quad (2.48)$$

In the remainder of this section, it will be explored how this principle can be used to encode an image in MRI. Commonly, three steps can be differentiated in this process: frequency encoding, phase encoding, and slice selection. Principle 6 is commonly considered in a stationary reference frame aligned with the image orientation to ease notation. Thus, we can assume that frequency encoding is performed along the x-axis, phase encoding along the y-axis, and slice selection along the z-axis.

2.4.1. Frequency Encoding

Frequency encoding is the most straightforward way to apply Principle 6 for spatial encoding. In frequency encoding, a gradient G_x is turned on and the signal is continuously sampled, while the gradient is applied. The acquired signal can thus be described as

$$S(\gamma G_x t, 0, 0) \propto \int e^{-ik_x x} \int\int M_{xy}(x, y, z)\, dy\, dz\, dx. \quad (2.49)$$

Accordingly, one spatial dimension can be fully characterized using frequency encoding.

As the frequency encoding gradient G_x remains turned on, the spins precess at different frequencies, while the signal is acquired. Thus, the received composite signal is a summation of the contributions at many frequencies. This situation can be compared to a glass harp (Figure 2.8a). Each spin is a different wine glass, and the filling line that determines the frequency is a function of the position along the frequency encoding direction. In this analogy, frequency encoding is obtained by playing all glasses at the same time, and a frequency analysis can be used to recover the position of the individual glasses.

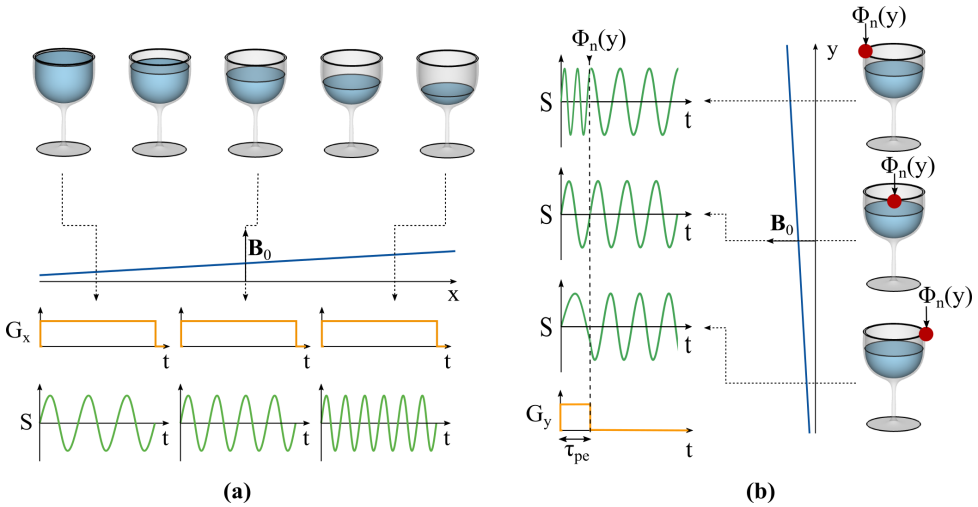

Figure 2.8 : (a) Frequency encoding: when G_x is applied, it induces a spatially dependent shift in the B_0 field and causes spins, at different locations along the x-axis, to precess at different frequencies. This enables signal localization in the x direction, similar to playing glass harp, with wine glasses filled with different water levels: the higher the water level, the lower the pitch. (b) Phase encoding: when G_y is applied for a duration τ_{pe}, the spins accumulate a spatially dependent phase value ϕ, precessing with the same frequency but different phases once the G_y is turned off. This can be compared to water-filled glasses, with identical water levels, being played at different initial phases.

2.4.2. Phase Encoding

In order to encode additional spatial dimensions, phase encoding can be applied. In phase encoding, a gradient is turned on and off *before* frequency encoding and data acquisition begins. A number N_y of distinct values of this phase encoding gradient with stepwise amplitude increment ΔG_y are used for a fixed duration τ_{pe}, to obtain different gradient moments $m_y(n) = n\Delta G_y \tau_{pe}, -N_y < n \leq N_y$.

In combination with frequency encoding, we obtain the following signal

$$S(\gamma G_x t, \gamma n \Delta G_y \tau_{pe}, 0) \propto \int\int e^{-ik_x x + k_y y} \int M^0_{xy}(x, y, z)\, dz\, dy\, dx. \quad (2.50)$$

During the application of G_y with moment $m_y(n)$, spins accumulate a spatially dependent phase shift $\phi_n(y) = \gamma m_y(n) y$. So while all spins along the phase encode dimension precess at the same frequency, the phase between the signals is shifted. Since only one phase shift can be obtained in the phase encoding direction, the application of many gradient amplitudes is necessary to spatially resolve this information. In the glass harp analogy, phase encoding is represented by glasses with the same filling line, thus producing the same frequency, but they are played with a different phase, as illustrated in Figure 2.8b.

Phase encoding, as described above, can be applied along multiple dimensions. For example, additional phase encoding can be used in the slice dimension, to enable the acquisition of a 3D image. To this end, a second phase encoding gradient is applied such that for each gradient step in the new axis, a whole set of phase and frequency encoding steps are obtained. However, the number of phase encoding steps required grows exponentially with the number of dimensions encoded. As phase encoding is the major time-limiting factor in MRI, 3D imaging is often time-consuming and the acquisition of (multiple) 2D slices remains standard in clinical use.

2.4.3. Slice Selection

To acquire a 2D slice in MRI, slice selection can be accomplished by a frequency-selective RF pulse employed together with a magnetic field gradient G_z. During the application of G_z, the Larmor frequency varies as a function of the location along the slice encoding direction. Thus, if the selective RF pulse is administered at a frequency ω_{sl} with an excitation bandwidth of $\pm\Delta\omega_{sl}$ (Figure 2.9), then following Principle 3 only protons precessing at frequencies between $\omega_{sl}+\Delta\omega_{sl}$ and $\omega_{sl}-\Delta\omega_{sl}$ are flipped into the transverse plane; those with resonant frequencies outside this range are not effectively nutated and remain largely aligned with the z-direction. In combination with frequency and phase encoding, slice selection enables two-dimensional imaging of the slice of interest, as follows

$$S(\gamma G_x t, \gamma n \Delta G_y \tau_{pe}) \propto \int_{slice} \int \int e^{-ik_x x + k_y y} M^0_{xy}(x, y, z)\, dx\, dy\, dz. \quad (2.51)$$

The thickness δ_{sl} of the acquired slice can be characterized by the bandwidth of the RF pulse, $2\Delta\omega_{sl}$, and the value of the slice-selection gradient:

$$\delta_{sl} = \frac{2\Delta\omega_{sl}}{\gamma G_z}. \quad (2.52)$$

The slice thickness can thus be increased, either by reducing the strength of G_z or by broadening the frequency bandwidth of the RF pulse, as illustrated in Figure 2.10. The ideal slice excitation profile of an RF pulse would cause the magnetization to be excited with the target flip angle inside the slice thickness and with a zero flip angle outside. This corresponds to a rectangular slice profile. For small flip angles, the achieved slice profile can be approximated by the frequency spectrum of the RF pulse. Thus, the commonly chosen RF pulse shapes are an approximation to sinc pulses, whose frequency spectrum is rectangular (Figure 2.9a-b). However, to obtain a perfectly rectangular slice profile, an infinitely long RF pulse would be required. In practice, truncated sinc

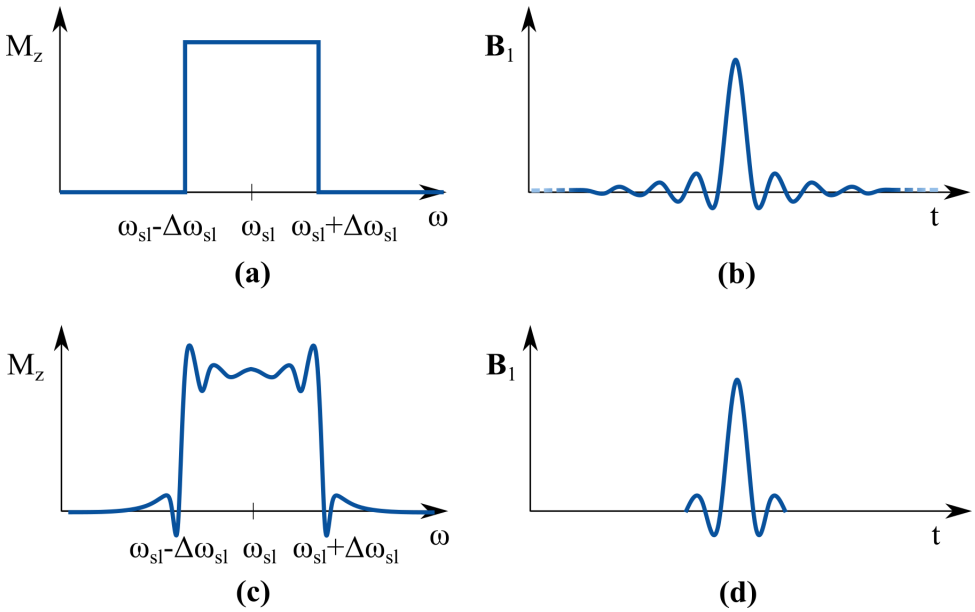

Figure 2.9 : (a) Ideal slice profile of an excitation RF pulse centered at frequency ω_{sl}, with an excitation bandwidth $\pm\Delta\omega_{sl}$, and (b) its corresponding temporal profile, an infinitely long sinc pulse. (d) Example of a time-limited RF pulse, obtained by truncating a sinc pulse with a rectangular window. This causes ripples at the edge of the slice profile, the so-called Gibbs ringing (c).

pulses are employed (Figure 2.9c-d). For a fixed pulse shape, increasing the pulse duration results in a narrowing of the frequency bandwidth and, consequently, smaller slice thickness. Shifting the center frequency ω_{sl} of the RF pulse, on the other hand, alters the slice position. Thus, the excitation pulse properties can be used to select the volume of interest.

The application of a slice selection gradient also induces a shift of Larmor frequency within the excited slice. Hence, after slice selection, the phase is spatially inhomogeneous across the slice thickness, which results in signal loss. To reduce this undesired loss of phase coherence, a rephasing gradient with opposite polarity is employed for half the duration to match the gradient moment. The area of the rephasing lobe is half of the slice selection gradient lobe since dephasing only affects the transverse magnetization M_{xy}. A viable approximation is to assume that, during the RF excitation, the magnetization is instantaneously tipped into the transverse plane at the center of the pulse, thus dephasing only occurs during the second half of the RF pulse duration.

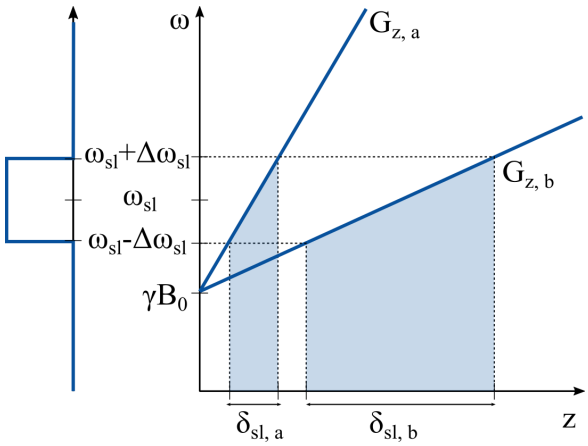

Figure 2.10 : Illustration of two different gradient strengths, $G_{z,a} > G_{z,b}$, and their effect on slice selection. Considering an RF pulse with an excitation bandwidth of $2\Delta\omega_{sl}$, the slice thickness δ_{sl} can be varied by changing the gradient strength G_z.

2.4.4. Sequence Diagram

So far, all encoding steps were considered in the image reference system. However, if frequency, phase, or slice encoding is angled with respect to the laboratory frame, multiple physical gradient coils are employed for each of the encoding steps. The three standard orientations, sagittal, coronal, and axial (Figure 2.11) can be obtained by performing slice selection along with the laboratory frame x, y, or z gradient axis, respectively. To acquire an oblique slice, two or three of the gradients are employed concurrently with suitably weighted strengths to achieve slice selection.

Figure 2.12 depicts a simple MRI pulse sequence diagram. At this point, the reader should be equipped with all the tools required to interpret the sequence diagrams. The imaging process starts with the application of an RF pulse with a flip angle α. The shape of the RF pulse is chosen as a truncated sinc, as illustrated in Figure 2.9. At the same time, a gradient for slice selection G_z is applied, followed by the slice rewinder. Next, the phase encoding gradient G_y is played with one of many stepwise incremented amplitudes. To readout the frequencies along one line, a prewinder is played before the frequency encoding, such that during frequency encoding, k_x is sampled from $-k_{x,max}$ to $k_{x,max}$. Finally, the frequency encoding gradient G_x is applied concurrently with the image readout, where the analog-to-digital converter (ADC) is switched on and the signal induced by the transverse magnetization M_{xy} is captured. As denoted in the sequence diagram, the most basic form of gradient field has a trapezoidal shape over time. The duration of the ramp is called rise time τ_{rt}, and describes how long

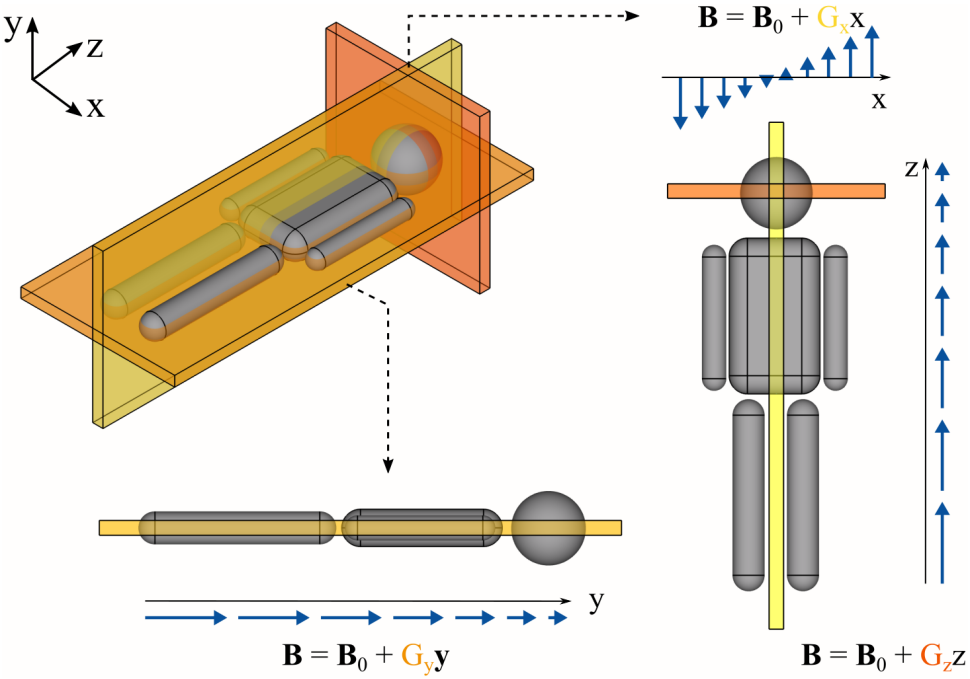

Figure 2.11 : Sagittal, coronal and axial slices acquired by choosing the slice-selection direction along the x, y, or z-axis (in the laboratory frame), respectively. Gradients induce spatially dependent shifts in the magnetic field strength B_0 along the direction of their application, allowing the excitation of narrow bands of spins in this direction.

it takes for the gradient field to be ramped up to its maximum value G, as shown in Figure 2.12b.

When characterizing pulse sequences, two timing parameters are particularly useful: 1) The duration between the creation of the transverse magnetization and the time point when the sampling along the frequency encoding direction accumulates zero moment from the pre- and rewinding. This time is commonly known as echo time or TE. 2) The time between the application of two excitation RF pulses in the same slice selection. This time is known as repetition time or TR. TE and TR are illustrated in Figure 2.12a.

2.4.5. k-space Formalism

Due to the naming of the wavenumbers k_x, k_y, and k_z, MRI is often considered to collect image data in "k-space". Following Principle 6 it is easily seen that k-space is indeed the Fourier domain of the MR image. The concept of k-space formalism is thoroughly discussed in [27, 28].

For 2D imaging, in practical terms, k-space is a data matrix of size $N_r \times N_{pe}$. It can be derived from the properties of the Fourier

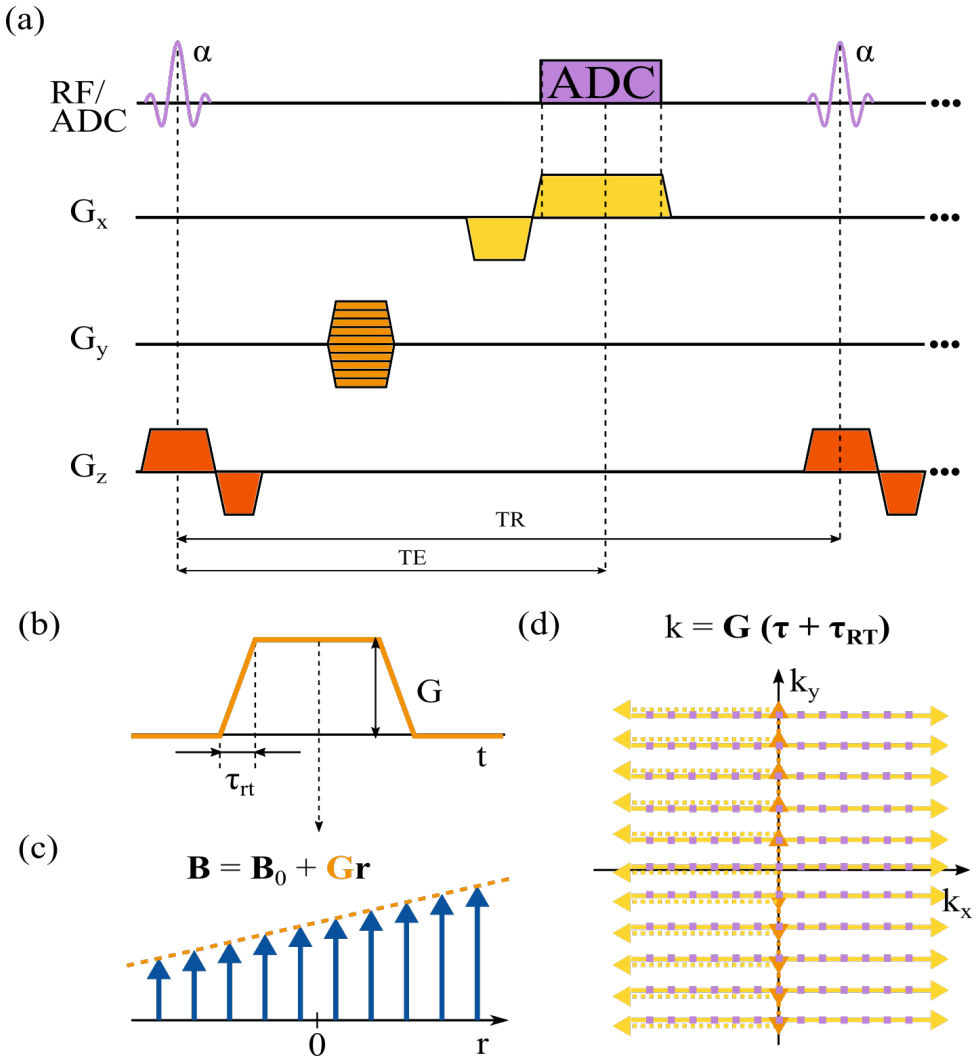

Figure 2.12 : (a) Pulse sequence diagram example, showing an α-RF excitation pulse and a simultaneous slice-selection gradient with subsequent refocusing lobe, followed by a phase encoding step and, finally, the frequency encoding gradient applied during signal acquisition. (b) Trapezoidal gradient shape, highlighting rise time τ_{rt}. (c) B_0 dependence on spatial location, with gradient strength determining the field intensity slope. (d) k-space trajectory of the pulse sequence. Every time the pulse sequence snippet in (a) is executed, a single line in k-space is acquired (yellow). Multiple repetitions with different phase encoding steps (orange) allow the sampling of the 2D k-space in parallel lines. This sampling trajectory in k-space is known as Cartesian sampling.

transform, that the distance between the k-space points determines the field-of-view (FOV) of the image, which describes the extent of the

object to be imaged:

$$FOV_x = \frac{1}{\Delta k_x} \tag{2.53}$$

$$FOV_y = \frac{1}{\Delta k_y}. \tag{2.54}$$

In a dual principle, the extent to which k-space is sampled determines the image resolution

$$\Delta x = \frac{1}{2k_{x,max}} \tag{2.55}$$

$$\Delta y = \frac{1}{2k_{y,max}}. \tag{2.56}$$

2.4.6. k-space Trajectories

The k-space can be traversed in multiple ways to acquire sufficient data for image reconstruction. k-space trajectory refers to the path along which this data is acquired. Most imaging sequences in clinical MRI sample k-space using a *Cartesian* sampling scheme (Figure 2.12d and Figure 2.13b). Here, a rectangular grid with equidistant k-space sampling in each of the two directions (k_x and k_y) is filled. In Cartesian sampling, one row of k-space is acquired at a time using frequency encoding, before navigating to the next row employing phase encoding. By collecting data in this fashion, high and low spatial frequencies are sampled uniformly. After the acquisition of all rows required to achieve the desired FOV and resolution, the k-space can be converted to an image using the Fourier transform.

Echo-Planar Imaging

A particular example of Cartesian k-space sampling is the so-called echo-planar imaging (EPI) [29]. In EPI, the collection of all the data necessary to reconstruct an image is performed after a single excitation of the magnetization, in one set of echoes, commonly referred to as echo train. Following the creation of the transverse magnetization, multiple k-space lines are sampled using frequency encoding. These are separated by a short phase encoding gradient pulse to traverse along the phase encoding direction. To allow for symmetric k-space readouts, this echo train is preceded by frequency and phase encoding prewinders. EPI is one of the fastest imaging pulse sequences, allowing image acquisition in the order of a few tens of milliseconds. Thus, it plays an essential role in many advanced MR applications, such as diffusion, perfusion, neuro-functional, and dynamic imaging. However,

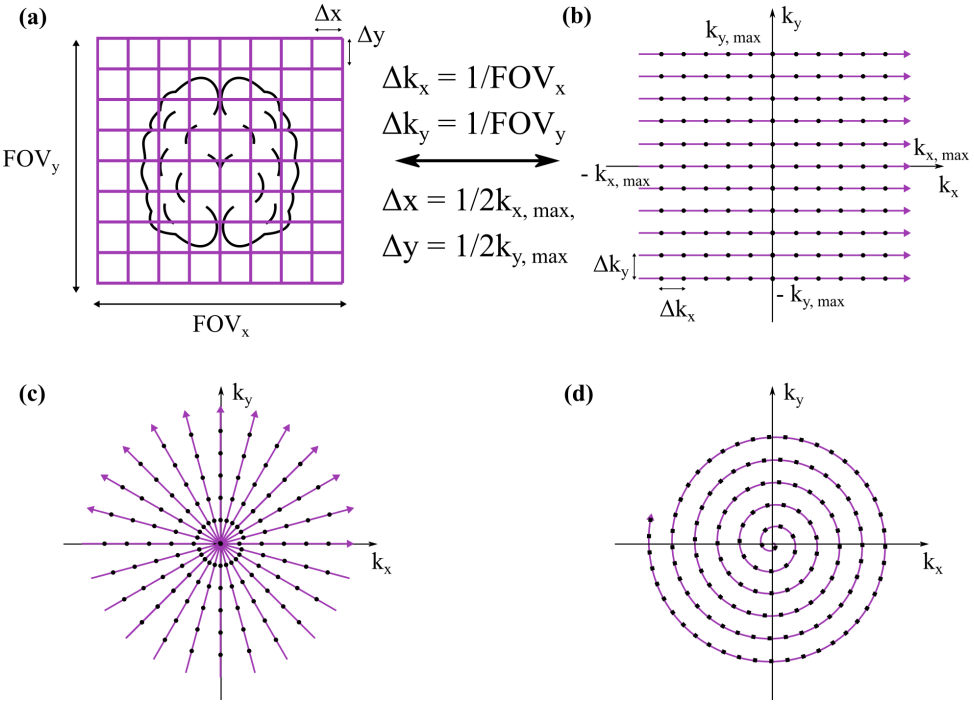

Figure 2.13 : Image-space representation, illustrating the concepts of resolution ($\Delta x, \Delta y$) and field of view (FOV) (a) and their relationship with k-space for the example of Cartesian sampling (b). Examples of radial (c) and spiral (d) trajectories for k-space sampling.

EPI sequences are prone to artifacts due to T_2^* decay, eddy currents, flow, and off-resonance spins.

Non-Cartesian Trajectories

There are advantages in collecting data using non-Cartesian (non-rectangular) k-space trajectories. Radial imaging, or projection reconstruction (PR), was the original MR k-space trajectory used by Paul C. Lauterbur to make the first MR image [13]. To perform the radial projection pattern, frequency encoding is employed together on multiple axes (e.g. x and y for transverse slices) with different amplitudes to attain a rotational pattern of radial spokes (Figure 2.13c) [30].

Another imaging trajectory is commonly known as spiral imaging (Figure 2.13d) [31, 32]. In spiral imaging, long readout trains allow frequency encoding of a spiral arm. This bears potential advantages. First, as in radial imaging, low spatial frequencies are sampled more densely because the spiral density is highest near the origin of the k-space axis, leading to a higher image signal-to-noise ratio (SNR) and

intrinsic robustness against motion. Second, the gradient *slew rate*, the rate at which the gradient strength has to be altered, is low for spiral scanning. However, errors in the gradient accuracy can lead to deviations from the prescribed non-Cartesian trajectories, with the risk of deteriorating the image quality.

Since the radial and spiral *k*-space samples do not lie on a regular grid, it is not possible to directly employ the fast Fourier transform, and advanced reconstruction methods are necessary.

2.4.7. Pulse Sequence Types

In most cases, numerous excitations are necessary to harvest sufficient information for image reconstruction, as described above. Thus, to allow for efficient imaging, while creating strong magnetization signals with the desired contrast, several pulse sequence schemes such as the one shown in Figure 2.12a have been devised. In this subsection, we will introduce the most commonly used pulse sequences, divided into two main families: *spin echo* and *gradient echo*. For an in-depth discussion about MRI pulse sequences, the reader is referred to [26].

The difference between *spin echo* and *gradient echo* sequences is most easily explained when considering how a strong signal is being attained: In *spin echo* (SE) sequences the transverse magnetization M_{xy} is being retained, while in *gradient echo* (GRE) sequences, the strong longitudinal magnetization M_z is preserved, as explained in more detail below.

Spin Echo

In spin echo (SE) sequences, the idea is to keep the transverse magnetization for as long as possible, by refocussing the magnetization dephasing incurred due to the reversible signal decay (T_2', see Section 2.3.2). Thus, for an SE experiment, at least two RF pulses are used for echo generation. First, the transverse magnetization is created with a 90° pulse, which then decays due to dephasing. After time τ a 180° pulse is played to recover the signal losses incurred due to reversible dephasing, such as those related to inhomogeneities in the main magnetic field. This leads to maximum rephasing at time point 2τ, creating the so-called *spin-echo*. SE sequences are characterized by an excellent image quality precisely because the effects of static field inhomogeneities are eliminated. The trade-off is long scan times, which makes the sequence highly sensitive to motion artifacts. For a review of spin-echo basic concepts, the reader is referred to [33].

Fast spin echo (FSE) sequences have been introduced to considerably shorten the scan times. This is accomplished by delivering several 180° refocusing RF pulses after a single magnetization excitation, as depicted in its sequence diagram in Figure 2.14a [34]. Multiple phase

encoding gradients with different amplitude enable the readout of multiple *k*-space lines for each excitation. This series of spin echoes is called an echo train and the number of echoes sampled is the echo train length. FSE sequences have a longer TR to deliver as many refocusing pulses as allowed before the transverse magnetization is considerably decayed due to T_2 relaxation. FSE sequences find use for a broad spectrum of MRI applications and are a workhorse in today's clinical MRI.

Gradient Echo

In gradient echo (GRE) imaging, the idea is to only use a part of the longitudinal magnetization to generate a transverse magnetization. This leaves substantial longitudinal magnetization, which can then be used to quickly generate a new transverse magnetization.

In GRE, a single RF pulse is used and gradient encoding is applied during the free induction decay. The time point when the gradient prewinder and rewinder amount to a zero moment is often referred to as the *gradient echo* [35, 36]. Every RF excitation chips away from the longitudinal magnetization that can be used for the following TRs. Simultaneously, T_1 relaxation during this time leads to the rebuilding of the longitudinal magnetization. This way, a steady-state magnetization (M_{ss}) is being approached after a number of TRs.

As no rephasing of the transverse magnetization is applied in GRE sequences, the signal intensity decays much faster than in SE sequences and the TE has to be much shorter to yield sufficient signal intensity.

The main advantage of GRE sequences is the ability to achieve short TR and, therefore, faster image acquisition. With very short TRs, however, part of the signal will be "left over" from cycle to cycle. This residual magnetization needs to be accounted for to avoid image artifacts. Two basic concepts are often used for this purpose: 1) Destroying (described below) or 2) recycling (described in 2.4.7) the left-over magnetization.

The purposeful destruction of the residual MR signal is called spoiling. Spoiling can be accomplished by turning on additional gradients, often along the slice encoding direction, to dephase the magnetization before the next RF pulse is applied. Alternatively, cycling of the RF phase, i.e., the direction of the B_1 field in the RFR, can be used to achieve spoiling [37]. Both yield a T_1-weighted image as the transverse magnetization decay does not contribute to the steady-state magnetization. Spoiled GRE sequences are widely used in the clinical setting, but small flip angles, typically much less than 45°, need to be applied for sufficient SNR.

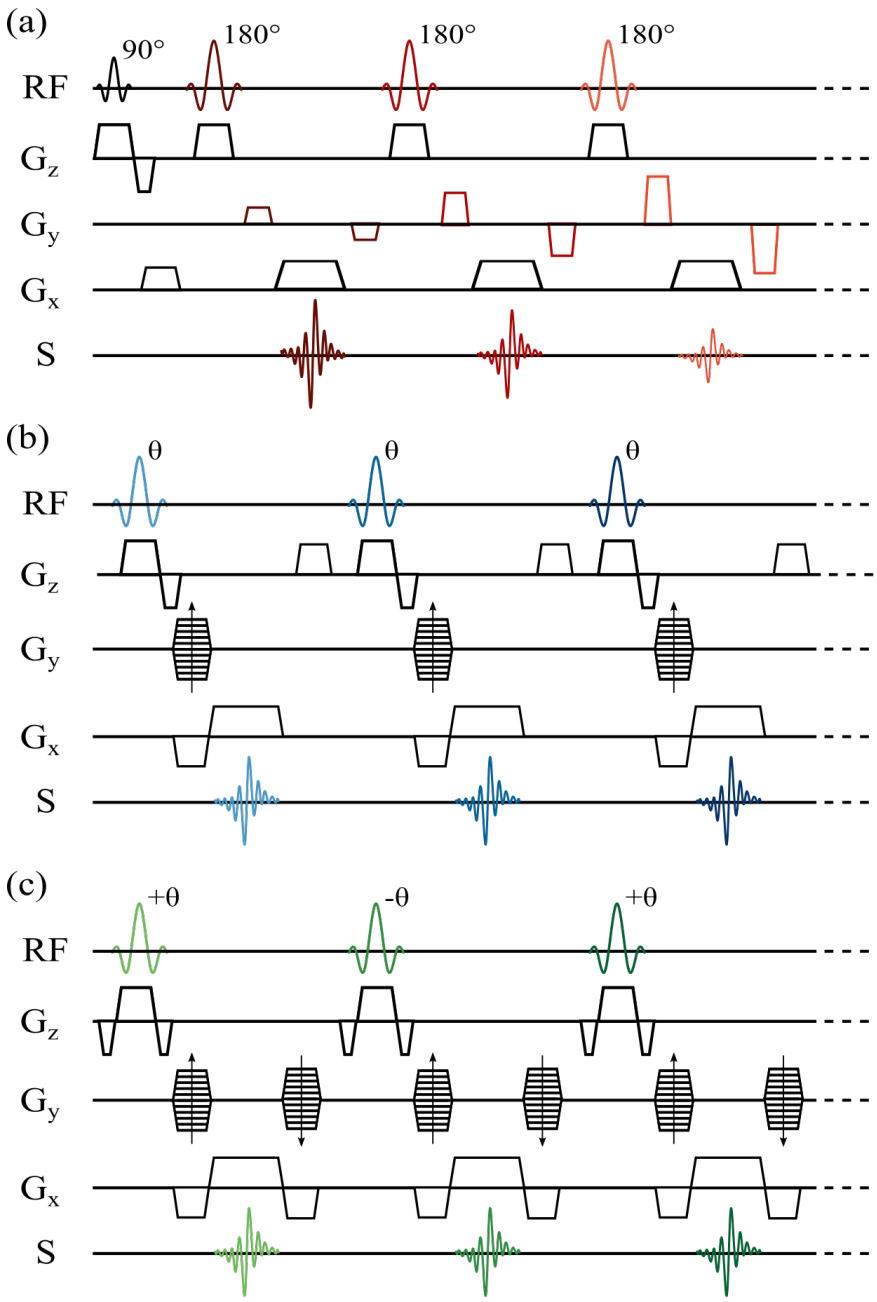

Figure 2.14 : Pulse sequence diagrams of (a) a fast spin echo (FSE), (b) a fast gradient echo, and (c) balanced steady-state free precession (bSSFP) sequence.

Balanced Steady-state Free Precession

The idea of recycling the transverse magnetization in a GRE sequence is called a balanced steady-state free precession (bSSFP) sequence [38]. In bSSFP sequences, it is ensured that, at the end of each cycle, the phase incurred by all gradients is fully rewinded. This is achieved by a symmetric pulse sequence diagram as shown in Figure 2.14c, with identical gradients before and after the gradient echo. This way, a second gradient echo is created at the time point of the RF pulse. Additionally, the RF pulses are played with alternating polarity. In the steady-state, this leads to alternating periods of dephasing and rephasing. As such, in an in-depth analysis, bSSFP sequences can be considered a hybrid between GRE and SE sequences, as both the longitudinal and the transverse magnetization are retained. For more intuition on this, the reader is referred to [39, 40].

In bSSFP, the generated contrast is determined by the T_2/T_1 ratio (e.g. blood has a high T_2/T_1 ratio and therefore appears bright on bSSFP images). Due to the recycling of the transverse magnetization, bSSFP images have a higher SNR than spoiled GRE images with comparable TRs. bSSFP sequences are characterized by very short scan times and are thus well suited for vascular imaging and real-time imaging of moving organs, such as the heart. However, the recycling of the transverse magnetization is prone to differences in the precession frequency of the spins and, thus, off-resonance artifacts are common at high field strengths.

2.5. Components of an MRI Scanner

Modern MRI systems can be described by three major components, corresponding to three integral parts of the image formation:

1. The superconducting magnet, responsible for the main magnetic field $\mathbf{B}_0$ that facilitates the formation of the net magnetization [41, 42];
2. Radiofrequency (RF) coils, placed around and/or on the subject, inducing secondary magnetic fields to create and detect transverse magnetization [43];
3. Three sets of magnetic field gradient coils, enabling spatial encoding of the signal [44, 45].

Figure 2.15 contains a schematic representation of these components.

2.5.1. Magnet

The design of a magnet has to consider several factors to create a magnetic field $\mathbf{B}_0$ with maximal spatial homogeneity and temporal stability in the subject. These factors are important to avoid

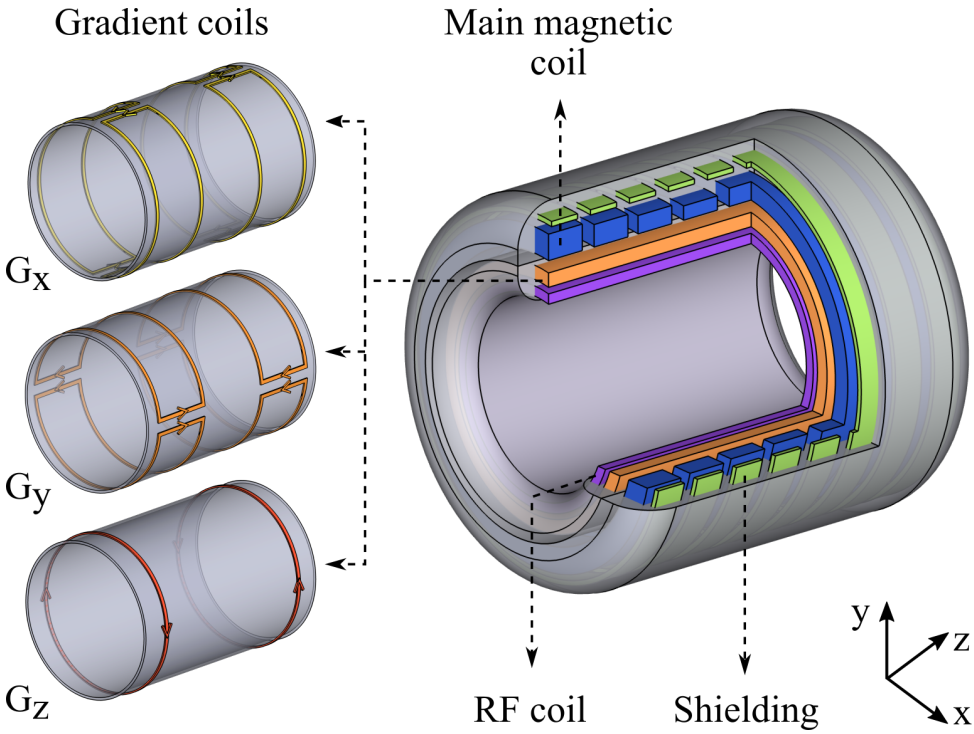

Figure 2.15 : 3D cross-sectional view of a conventional clinical MR scanner, with the different major components. The scanner bore is comprised of a transmitting body coil (RF coil), gradient coils, surrounded by a superconducting magnet, responsible for the main magnetic field. The shielding procedure is achieved by placing permanent magnets and shield coils. On the left, the three different gradient coils are depicted.

inhomogeneity-related artifacts and to achieve the best possible SNR. Over the years, magnet design has developed, allowing for stronger and more homogeneous magnetic fields. A wide variety of designs is available for a vast range of field strength (0.02-10.5T, for whole-body magnets). The magnets can be divided into three types: resistive, permanent, and superconducting.

Resistive magnets are no longer used for clinical MR scanners because the resulting magnetic field is greatly temperature-dependent and the maximum attainable field strength is very low (about 0.2T). In resistive magnets, the magnetic field is created by the passage of an electric current through an inductive loop (typically copper wire or aluminum band) and is proportional to the magnitude of the current. However, due to the electrical resistance in the loop, a large amount of electrical power is dissipated in the form of heat, requiring active water cooling systems with high power consumption to lower the temperature of the magnet.

Permanent magnets are typically employed in the so-called *open bore* systems, which reduce the subject's stress caused by claustrophobia and have lower costs for the installation and maintenance of the system. These magnets use rare earth alloys (like samarium-cobalt and neodymium-iron-boron) in which large magnetic fields are induced during manufacturing. However, the maximum achievable field strength is lower than 1T. The magnetic field is generally vertically oriented with reduced stray fields. However, the field homogeneity and stability are also temperature-dependent, for example, a 1 °C increase, will cause a 1000 ppm decrease in the magnetic field strength of neodymium-iron.

In clinical scanners, which generally operate at a field strength of 1.5T or 3T, superconducting magnets are employed. These magnets use the properties of superconductive materials (like those made from niobium-titanium). Superconductors have zero electrical resistance below a certain material-dependent critical temperature (e.g. -263.96°C, 9.2 *K* for niobium-titanium) and an associated critical magnetic field (e.g. 10T for niobium-titanium). Thus, once a current is fed into a loop of superconducting wire, it will circulate indefinitely. In comparison with other common types of magnets, superconducting magnets can achieve a much higher field strength (up to 10.5T whole-body, currently) and feature excellent field uniformity.

The superconducting material, which is designed as a conducting copper matrix with multi-stranded filaments, is surrounded by liquid helium at an extremely low temperature (4.2 K). Heat transfer slowly boils off helium, making regular refills necessary (commonly 3 to 18 months). Modern MRI scanners use increasingly effective cryogenic cooling of the helium chamber with the effect of minimizing the boil-off.

To further improve the magnet homogeneity and to minimize any field distortions, fixed shimming can be performed. Permanent magnets and shim coils, an arrangement of independently wired coils, can be employed either passively, actively, or as a combination of both. A more thorough discussion of MRI magnets can be found in [41].

2.5.2. Gradient Coils

As discussed in Section 2.4, to spatially encode the MRI signal in three spatial dimensions, three linear magnetic field gradients are used. In reality, these are generated by using *magnetic field gradient coils* or in short *gradient coils*. The gradient coils are placed inside the bore of the magnet, on a cylindrical former. By design, the center of the gradient coils, and also the center of the magnet, is placed at the *isocenter* ($z = 0$, $y = 0$, $x = 0$).

The design of the gradient coils needs to balance four major objectives: good linearity over the imaging field-of-view (FOV), maximum achievable amplitude, minimal rise time, and minimization of eddy current effects

induced in the magnet.

Contrary to the magnet design, where the goal is to obtain a uniform magnetic field, the magnetic field produced by the gradient coils should be as linear as possible. Although the method of producing the magnetic field is the same - current passing through conducting wires - the chosen material, the cooling system, and the geometrical configuration differ from the main magnet. For the selected material of the three gradient coils, copper at room temperature produces a sufficiently strong gradient (40-80 mT/m for clinical scanners). To minimize the heat losses in this resistive coil design and to maintain the desired temperature, water cooling is used. Although the gradient coils are placed in a cylindrical form inside the bore of the magnet, the geometrical configuration is different for the longitudinal (z) and the transverse (x and y) fields as seen in Figure 2.15. The z gradient is typically arranged in a *Maxwell pair*, where a pair of wire loops with counter-rotating currents are separated by $r\sqrt{3}$, with r being the coil radius. The x and y gradients use a different layout known as the *saddle coil* arrangement or the *Golay* configuration. However, the coil configuration in x is rotated by 90° with respect to y. With those design considerations, all three gradient fields are approximately parallel to $\mathbf{B}_0$.

For gradient design, as important as the gradient linearity, is the minimization of the gradient slew rate, which relates to the time at which a gradient can be turned on and off. The slew rate is commonly defined as the maximum gradient strength of the gradient divided by the rise time. When the gradients are rapidly turned on and off, eddy currents will be induced in the nearby conducting components of the scanner and may manifest in the final images as specific artifacts and/or signal loss. To reduce the eddy currents, clinical MRI scanners make use of active shielding, where additional coils are placed in the surroundings of the gradient coils, to minimize the stray gradient fields. This, however, results in reduced bore space and additional power consumption. For an in-depth discussion on gradient coils design, the reader is referred to [42, 44, 45].

2.5.3. Radiofrequency Coils

Radiofrequency (RF) coils are the components responsible for generating the rotating magnetic field $\mathbf{B}_1$ and for picking up the signal induced by the rotating magnetic fields in the sample. The RF coils can be divided into two types: *transmit* and *receive*.

Transmit Coils In most clinical scanners, the principal transmitting coil is known as the body coil, which encompasses the full subject volume and is built into the scanner bore. This coil typically uses a saddle or birdcage design, with the latter generally being able to create a

more homogeneous distribution of the transmitted energy throughout the object. The transmit RF coils are commonly built on a large area to optimize the uniformity of the $\mathbf{B}_1$ field and to cover a substantial volume. As a disadvantage, if used as a receiver, such coils will have low sensitivity to the MR signal. When scanning certain anatomies, for instance, the head or the knee, specifically designed coils are used for transmission where less power is required, often at the expense of less uniform fields.

At high field strength, the wavelength of the transmit field approximates the size of the object, which can lead to inadvertent energy distribution, e.g. due to the formation of standing waves. Therefore, in modern MRI systems at high (3T) and, in particular, ultra-high (7T and above) field strengths, multiple transmit channels are used simultaneously to circumvent this problem. In a process called B_1^+ shimming, those transmit channels are combined to create optimal homogeneity in the transmit field amplitude throughout the object and are essential to achieve reliable image quality.

Receive Coils In contrast to transmit coils, dedicated receive coils are designed to best match the anatomy of interest and are placed close to the sample of interest. This will result in increased sensitivity and noise minimization. Generally, two types of receive coils can be differentiated: *volume* and *surface* coils.

Volume coils, which are typically combined transmit and receive (Tx/Rx), cover the full area of interest. In contrast, surface coils are placed on top of the patient's anatomy of interest (e.g. a flexible surface coil is positioned on the chest when imaging the cardiac or abdominal region) to detect signals from a limited anatomical region of the patient. Generally, surface coils are only used for signal reception, as the RF field response with this coil design is highly inhomogeneous.

To circumvent the limited FOV, an array of multiple surface coils can be combined and used simultaneously to receive the MR signal, while maintaining the high sensitivity of each element. To eliminate the interaction from the different individual elements, these elements need to be decoupled. Most commonly, the coil elements are coupled by design (i.e., there is a geometrical overlap between neighboring elements). Since each element acts as an independent receiver, the coil noise[§] is uncorrelated with the other elements in the coil. Images from multiple coil elements are then combined in the reconstruction to yield a coverage of the entire imaging volume. In-depth analysis of MRI RF coils can be found in [43].

[§]Unfortunately, this is only one of two types of noise, as elaborated in the next section.

2.5.4. Noise Properties

As with any measurement, the quality of the MRI signal and the resulting images are curtailed by noise in the measurement process [46]. Multiple sources of noise taint the signal quality. The overall measurement is usually characterized by the dimensionless signal-to-noise ratio (SNR). To maximize SNR, either the signal strength needs to be improved or the noise contributions need to be mitigated.

Even though the MR signal is complex, most commonly the magnitude images are used for clinical diagnosis (Figure 2.16). The mapping from real and imaginary components to their magnitude is nonlinear. Therefore, even though noise in the real and imaginary components can be assumed to follow a Gaussian distribution, noise in the magnitude images is non-Gaussian. For the simplest case of receiving the signal with one channel, and without using advanced reconstruction methods, the noise distribution for the measured pixel intensity M is given by

$$p_M(M) = \frac{M}{\sigma^2} e^{\frac{-(M^2+A^2)}{2\sigma^2}} I_0\left(\frac{A \cdot M}{\sigma^2}\right), \tag{2.57}$$

where A is the image pixel intensity without noise, I_0 is the modified zeroth-order Bessel function of the first kind and σ is the standard deviation of the Gaussian noise in the real and imaginary images, which can be assumed to be identical [47]. This corresponds to the Rice distribution and can be obtained by taking the square root of the sum of squares of two independent and identically distributed Gaussian variables [48].

With Rician noise, the SNR can be defined as the ratio of A over σ. For high SNR (≥ 3), the noise distribution can be well approximated with a simple Gaussian distribution [47]. However, for SNR values ≤ 1, the noise distribution is substantially skewed. In regions where only noise is presented (i.e., $A = 0$ in Eq. (2.57)), $p_M(M)$ simplifies to a Rayleigh distribution. Note that multi-coil reconstructions or nonlinear reconstructions further influence the noise distribution and can lead to different noise properties.

As described in Eq. (2.5), the MRI signal is proportional to the value of the static magnetic field $\mathbf{B}_0$, as stronger $\mathbf{B}_0$ fields lead to an increase in the nuclear polarization and, thus, an increase in signal. Also, at higher field strength, higher voltage is produced in the coil by the precessing magnetization, which further improves the signal strength. However, when $\mathbf{B}_0$ increases, the value of T_1 increases and T_2^* decreases, resulting in a decreased signal strength. Thus, the choice of an optimal field strength remains highly application-dependent.

Besides the signal strength, two important sources of noise need to be considered. Firstly, the human body, which is conducting and, thus, produces thermal noise. This is picked up by the receiving RF coil during imaging. Secondly, random voltage variations in the copper conductors

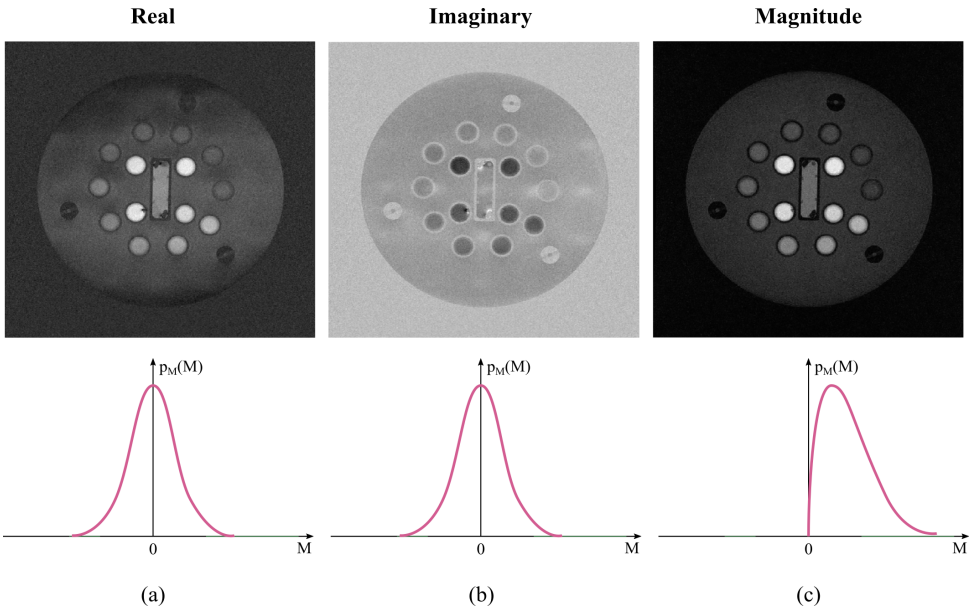

Figure 2.16 : Real (a), imaginary (b), and magnitude (c) images of the NIST/ISMRM system phantom, with their corresponding noise distributions.

in the RF coil itself will also increase the received noise. The SNR can be considered proportional to the sensitivity of the RF coil.

Several other imaging parameters affect the SNR. If multiple images are obtained using equal parameters, averaging can be performed to enhance the SNR at the cost of extra scan time. Since the MRI signal is coherent, but the noise is incoherent, the SNR increases with $\sqrt{N_a}$, where N_a is the number of signal averages. Also, as the imaging signal is proportional to the number of hydrogen nuclei per voxel, an increase in voxel size proportionally increases the SNR. Accordingly, for a given FOV, if the amount of phase encoding steps N_{pe} is doubled, then the image SNR is decreased by a factor of two. Similarly, if the number of points collected in the frequency-encoding direction N_r is doubled for a given FOV, the SNR decreases by a factor of two. If frequency-encoding is performed with twice the bandwidth, the SNR is decreased by a factor of two, leading to shorter readouts but more noise in the signal. Finally, increasing the slice thickness yields a proportional improvement in the image SNR as the imaging volume and the number of protons in the volume are increased.

2.6. Summary

This chapter has introduced a basic understanding of MRI physics and the basic aspects involved in image acquisition. This will hopefully enable the reader to understand advanced MRI methods and image reconstruction techniques as described in the remainder of this book. The physics of MRI has been described around six central principles.

1. *Origin of the net magnetization*: Certain nuclei are characterized by a physical property, a nonzero spin, that causes them to form a magnetic moment when placed into an external magnetic field. Many of these nuclei together form a net magnetization, which is the basis of all MRI signals.
2. *The dynamics of this magnetization in an external magnetic field*: The net magnetization is related to both a magnetic and angular momentum. Thus, if the net magnetization is angled with respect to the external effective field, it prescribes a precession motion around the axis of the effective field, with a characteristic field strength-dependent resonance frequency, the so-called Larmor frequency.
3. *Using rotating magnetic fields to create a detectable magnetization component*: While a strong static magnetic field is necessary to create net magnetization, a much weaker rotating magnetic field can be used to change the orientation of the effective field. Specifically, when this second magnetic field is applied near the resonance frequency, the net magnetization can be tipped away from the direction of the main magnetic field.
4. *Using induction to measure this component*: A magnetization component orthogonal to the main magnetic field precesses and can be used to create a signal. Specifically, this temporally varying magnetic field induces a current in the nearby receiver coils via induction, which can be recorded as the imaging signal.
5. *The evolution of this signal in the presence of relaxation mechanisms*: If the net magnetization is altered from its equilibrium state, e.g. by nutating away from the main magnetic field, multiple recovery processes are at play to return the magnetization back to the thermal equilibrium. The longitudinal magnetization, i.e. the component along the axis of the main magnetic field, undergoes an exponential recovery. The transverse magnetization, which is the component orthogonal to the main magnetic field, experiences an exponential decay.
6. *Gradient fields to enable image formation*: To spatially locate the acquired signal, gradient fields are used to create a spatially dependent phase in the signal. The signal is then acquired in the so-called k-space. To fully resolve the signal in all spatial

dimensions, frequency, phase, and slice encoding gradients can be used.

Based on these basic principles, a wide variety of pulse sequences that allow for acquisitions with different properties can be designed. Most fundamentally, gradient echo and spin echo sequences have been introduced along with variations of those to allow for fast imaging. Image acquisition can also be performed by sampling various trajectories in k-space to further speed up the scan.

For the practical realization of the imaging process, several hardware components relating to the physical principles above are necessary. Superconducting electromagnets are most widely used to create the main magnetic field. Different coil arrangements enable spatially varying gradient fields and the creation of a secondary magnetic field to excite the magnetization. Anatomy-specific coil arrays are used to receive the signal with maximum strength.

The basic properties of the magnetization signal, its dynamics, and relaxation help to understand the limitations in MRI pulse sequence design. The fundamental spatial encoding principles and the related hardware further explain the bottlenecks in the image acquisition speed. In recent years, advanced reconstruction methods have been taking center stage in the acceleration of MRI scans. Craftily reducing the number of samples, or supplementing the acquired information with a-priori knowledge has enabled unprecedented acquisition times. However, in MRI, the development of reconstruction techniques, as described throughout the remainder of the book, goes hand in hand with a thorough understanding of the physical principles of the magnetization signal. This chapter aims to serve as a reference for understanding limitations and opportunities in the signal properties of MRI that are relevant for image reconstruction.

3

Cardiac MR: from theory to practice

Tefvik F. Ismail[†], Wendy Strugnell[†], **Chiara Coletti**[†], Maša Božić-Iven[†], Sebastian Weingärtner[†], Kerstin Hammernik[†], Teresa Correia[‡], Thomas Küstner[‡]

Adapted from: "Cardiac MR: from Theory to Practice", Frontiers in Cardiovascular Medicine, Vol. 9 (2022): p.826283, doi: https://doi.org/10.3389/fcvm.2022.826283.

[†]These authors share first authorship
[‡]These authors share last authorship

Abstract

Cardiovascular disease (CVD) is the leading single cause of morbidity and mortality, causing over 17.9 million deaths worldwide per year with associated costs of over $800 billion. Improving prevention, diagnosis, and treatment of CVD is therefore a global priority. Cardiovascular magnetic resonance (CMR) has emerged as a clinically important technique for the assessment of cardiovascular anatomy, function, perfusion, and viability. However, the diversity and complexity of imaging, reconstruction, and analysis methods pose some limitations to the widespread use of CMR. Especially in view of recent developments in the field of machine learning that provide novel solutions to address existing problems, it is necessary to bridge the gap between the clinical and scientific communities. This review covers three essential aspects of CMR to provide a comprehensive overview ranging from CVDs to CMR pulse sequence design, acquisition protocols, motion handling, image reconstruction, and quantitative analysis of the obtained data. 1) The basic MR physics of CMR is introduced. Basic pulse sequence building blocks that are commonly used in CMR imaging are presented. Sequences containing these building blocks are formed for parametric mapping and functional imaging techniques. Commonly perceived artifacts and potential countermeasures are discussed for these methods. 2) CMR methods for identifying CVDs are illustrated. Basic anatomy and functional processes are described to understand the cardiac pathologies and how they can be captured by CMR imaging. 3) Imaging acceleration and reconstruction techniques are presented that enable the acquisition of spatial, temporal, and parametric dynamics of the cardiac cycle. The handling of respiratory and cardiac motion strategies as well as their integration into the reconstruction processes is showcased.

3.1. Introduction

Over the past 40 years, cardiovascular magnetic resonance (CMR) has evolved from an esoteric research tool found in the confines of large academic supraregional tertiary referral centers to being an indispensable clinical tool that routinely changes patient management across the breadth of modern cardiovascular practice [49]. Increasing clinical recognition of the transformative role this technology can play in patient care has led to its growing availability in secondary care settings too, although significant barriers remain to its greater adoption world-wide.

CMR is a versatile non-invasive and radiation-free imaging modality that provides a comprehensive assessment of multiple parameters of cardiac function and anatomy in a single examination. CMR plays a major role in the diagnosis and management of cardiovascular disease. However, aside from cost, there remain major obstacles for the widespread usage of this technique like: (i) complex underlying physics and technology, (ii) data analysis and interpretation, (iii) large number of pulse sequences and parameters to choose from, (iv) challenges from the inherent cardiac and respiratory motion and (v) duration of examination. The recent hype around artificial intelligence algorithms designed to overcome these hurdles has raised new questions around the reliability, accuracy, and stability of this technology. Therefore, to help shape the future of CMR, it is essential to bridge the gap between theory and practice, and thus, to promote a bridge of scientific knowledge between the research and clinical communities by improving (maintaining or updating) their knowledge of CMR technical principles and clinical applications.

This review provides an overview of three essential aspects of CMR which have been covered separately in-depth in other review papers [50–59]. We address: 1) data acquisition sequences and common artifacts, 2) clinical applications, 3) image acceleration, reconstruction, and motion handling. In addition, this review provides hands-on tutorials and videos that can be found at `ismrm-mit-cmr.github.io`. More specifically, Section 3.2 describes the key physical principles of CMR, most common pulse sequences and preparation pulses, and the physics behind the most common artifacts. Section 3.3 covers the clinical application of CMR in the diagnosis of a spectrum of cardiovascular diseases. Finally, Section 3.4 provides an overview of scan acceleration acquisition and image reconstruction methods while also describing current solutions to overcome challenges from cardiac and respiratory motion.

3.2. The Physics behind Cardiovascular MR

In this section we aim to provide a brief overview of the physical principles and basic mathematical concepts behind magnetic resonance imaging (MRI) targeted to create the necessary background to understand modern CMR methods. Basic building blocks of MRI are introduced, and common cardiac MR sequences are described, along with possible sources of artifacts.

3.2.1. Sequence Building Blocks

By manipulating the timing and strength of RF-pulses and gradients, a plethora of MR sequences can be constructed. Different pulse sequences differ in their acquisition speed, encoded image information, or to which degree image contrast is affected by differences in proton density, T_1, T_2^*, or other properties. CMR sequences are typically described by components for actual image acquisition and components for preparing the magnetization. These elements can be understood as building blocks of MRI sequences. The schematic design of the most common building blocks is shown in Figure 3.1.

Image acquisition methods

Spin echo (SE): After RF excitation the net magnetization is subject to T_2^* relaxation. Fortunately, part of the dephasing of the transverse magnetization can be recovered with a so-called spin-echo (SE) sequence. In this sequence a second RF pulse is applied, where the simplest form comprises a 90° excitation and 180° refocusing pulse. After the first excitation, the spins dephase and fan out in the transverse xy-plane. Dephasing caused by temporally invariant field inhomogeneities, however, can be reversed via the second refocusing pulse [24]. Its effect is often described as a pancake-flip: The fan of spins is flipped by 180° around the x- or y-axis, such that the faster spins now move towards instead of away from the slower rotating spins. After a so-called echo time TE, corresponding to twice the time between the two RF pulses, all dephasing caused by static inhomogeneities is rephased and an echo of the signal is created, as depicted in Figure 3.1. This gives the name to the SE sequence. Consequently, the contrast in SE, is driven by the T_2 time, which captures the residual dephasing caused by temporally variable factors, such as spin-spin interaction.

Spoiled Gradient echo (spGRE): As opposed to SE, the so-called gradient echo (GRE) sequences retain not the transverse but the longitudinal magnetization. They typically require only one RF excitation pulse after which the frequency encoding gradient is applied (see Figure 3.1). In GRE, however, the positive FE gradient lobe is preceded by an additional negative lobe.

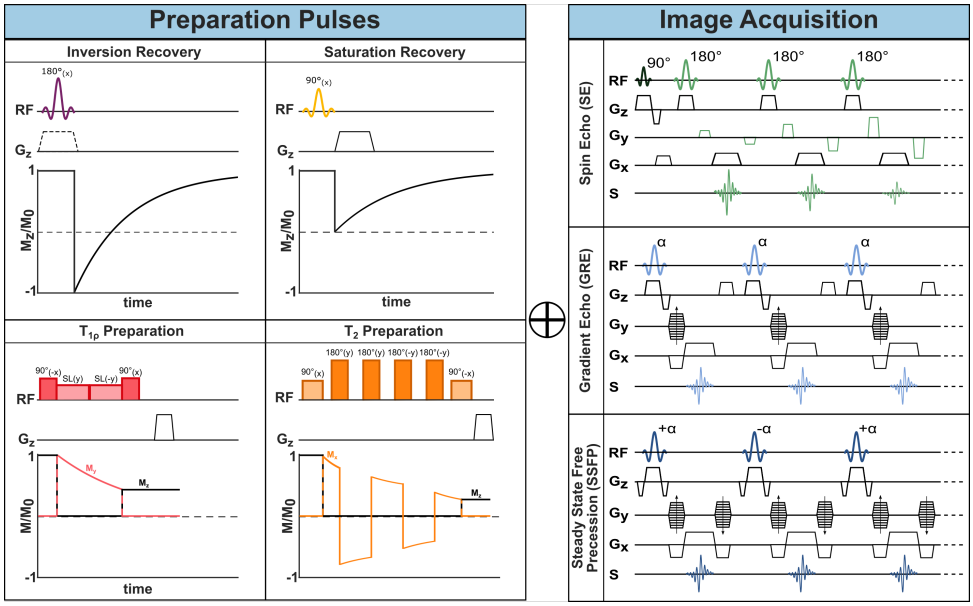

Figure 3.1 : MR sequence building blocks. One or more preparatory pulses (left) can be combined with different acquisition sequences (right) to encode the desired information into the imaging data and achieve different image contrasts.

When the areas of the positive and negative lobe are equal, the initially evoked dephasing of spins is reverted - except for T_2^* decay. This creates a signal which is referred to as a gradient echo and gives name to the GRE sequence [60]. In the so-called spoiled GRE, remaining transverse magnetization is destroyed at the end of each TR cycle. This can be achieved with strong gradients at the end of the TR and results in T_1 weighted imaging [61]. As no additional RF pulses are required, shorter TE and TRs can be achieved in GRE compared to SE allowing for faster image acquisition. In GRE, the echo signal is subject to T_2^* decay as no rephasing of field inhomogeneities is achieved. Therefore, GRE sequences are less robust in the presence of field inhomogeneities.

Balanced Steady-state free precession (bSSFP): A third common image acquisition sequence in CMR is the so-called Balanced Steady-State Free Precession (bSSFP). It can be understood as a hybrid between SE and GRE. Starting from a GRE sequence, a train of RF pulses is applied with very short TR ($\ll T_2$) such that the magnetization never fully recovers between two consecutive RF pulses and a non-zero net magnetization is present at the next RF pulse. This residual magnetization contributes to the signal of the following TR. Characteristically for bSSFP, the flip angles are alternated every TR between $+\alpha$ and $-\alpha$ causing the net magnetization to flip around the

z-axis between TRs [39, 62]. This further means that each RF pulse has both an excitation and refocusing effect on the spins and explains the SE nature of bSSFP sequences. For effective refocusing of the magnetization, the gradient moments on all three axes (SS, FE, PE) need to be zero at each TR. This means that the areas of positive and negative gradient lobes on each axis must be equal, as shown in Figure 3.1, which is referred to as balanced gradients. The alternating magnetization progresses through a transient state and after a certain number of TR cycles $\overrightarrow{M}$ reaches a steady state, that is a stationary amplitude. For TR$\ll T_2$ the contrast in bSSFP sequences is determined by the T_2/T_1 ratio [39]. The main advantage of bSSFP lies in the improved signal to noise ratio (SNR) compared with spGRE, due to the recycled transverse magnetization. However, the scheme is highly sensitive to off-resonances making it a less common choice for high field strength and rarely useful for ultra-high fields [62].

3.2.2. Preparation pulses

Inversion pulses: So-called inversion pulses are 180° RF pulses which can be applied before image acquisition to flip the initial magnetization along the B_0 axis [63]. During the time between inversion and the first imaging RF pulse (inversion time, TI), the longitudinal magnetization recovers along the B_0 axis towards its equilibrium state as depicted in Figure 3.1. At image acquisition, the degree to which $\overrightarrow{M}$ has recovered determines the image contrast and, thus, induces T_1 weighting. This enhances the image contrast based on T_1 properties, which is of interest in many imaging applications. By adjusting TI, imaging can also be timed to the point when the magnetization of specific tissues is crossing the zero point, leading to effective signal suppression [63]. For instance, in double inversion black blood imaging [64], a global and slice-selective inversion pulse are applied immediately one after the other such that only the blood outside of the imaging slice is inverted. With an appropriate TI, the signal of blood flowing into the slice can be nulled at image acquisition.

Saturation pulses: Intentionally suppressing tissue signal can also be achieved through so-called saturation pulses. These RF pulses flip the magnetization to the transverse plane. Subsequent spoiler gradients dephase the magnetization, thereby nulling the signal from the "saturated" spins. The subsequent recovery of longitudinal magnetization is shown in Figure 3.1. Saturation pulses can be made spatially selective, such that regions in or outside of the image are cancelled out. For instance, artifacts due to through-slice flow can be reduced by applying a saturation pulse upstream, parallel to the imaging slice. Furthermore, saturation pulses can be made selective to specific chemical species by adjusting the resonance frequency. The

most common example is fat saturation, where RF pulses with carrier frequencies specific to ω_L of fat are applied close to the imaging sequence such that only fat but not water signal is nulled. Creating uniform saturation with common rectangular RF pulses is hindered by their high sensitivity to B_0 and B_1 inhomogeneities. To overcome this limit, adiabatic saturation modules - such as composite [65] or B_1 insensitive rotation (BIR) pulses [66]- have been proposed.

T_2 preparation: T_2 contrast can be induced using the so-called T_2 preparation pulses [67, 68]. In a T_2 preparation, a first 90° excitation pulse is followed by a series of refocusing pulses and, finally, by a 90° flip-back pulse. To induce robust refocusing, the refocusing pulses are separated by a 2τ interval, whereas the interval between the 90° pulses and the refocusing pulses is equal to τ. The total T_2 preparation time is varied to achieve different echo times. During this time, the refocusing pulses compensate for T_2^*-decay, resulting in a transverse magnetization decay effectively characterized by the T_2. The final 90° flip-back pulse brings the remaining transverse magnetization back to the z-axis, encoding T_2 contrast in the longitudinal magnetization, which is then imaged during acquisition. Several strategies, such as phase cycling following Malcolm Levitt (MLEV) schemes or using composite pulses, are employed in order to make T_2 preparations more robust to field inhomogeneities [69, 70].

$T_{1\rho}$: The relaxation constant in the rotating frame of reference, $T_{1\rho}$, is an additional property of tissues, besides T_1 and T_2 times. $T_{1\rho}$ contrast can be achieved through spin-lock preparations. A spin-lock module consists of a 90° tip-down pulse followed by a continuous wave RF pulse applied for a certain time τ_{SL}. During this time the magnetization is locked on the spin-lock axis, and it relaxes back to its equilibrium value following an exponential $T_{1\rho}$ decay. Finally, a 90° tip-up pulse is applied after the spin-lock to restore longitudinal magnetization. Spin-lock pulses show high susceptibility to field inhomogeneities. Several compensated schemes, as well as adiabatic spin-lock modules, have been proposed to make $T_{1\rho}$ preparation more robust to B_0 and B_1^+ variability [71–73].

3.2.3. Common CMR Sequences

The sequence building blocks introduced in the previous sub-sections can be combined to design tailored sequences to assess, for example, cardiac function and viability. These sequences represent powerful tools for the non-invasive characterization of congenital or acquired cardiovascular diseases, including ischemia, valvular diseases and ischemic and non-ischemic cardiomyopathies, as described in Section 3.3. Here, we will discuss the physics principles governing the main CMR sequences and introduce some emerging techniques.

Cine bSSFP: Cardiac function is commonly assessed using bSSFP

sequences in cine mode. The structure of bSSFP sequences, described in Section 3.2.1, allows very short TR values to be achieved and increasing the number of k-space lines acquired in a single heartbeat. At the same time, bSSFP sequences maintain high intrinsic myocardial/blood contrast [74]. These characteristics enable the fast acquisition of a single slice across multiple cardiac phases (typically 10-30 phases, also referred to as *frames*). This allows the reconstruction of movies of the beating heart. To achieve good spatial resolution for every frame, the acquisition of each frame is divided among different cardiac cycles, using the so-called segmented acquisition (see Section 3.4.1). During each heartbeat, in fact, only a limited number of k-space lines (or a *segment*) is acquired for each cardiac phase. Therefore, several heartbeats are necessary to acquire all the k-space segments. The acquired images are then assigned to the corresponding heart phases using retrospective gating (see Section 3.4.1). Full heart coverage is achieved by repeating the acquisition of each cine image set for different locations and orientations.

Late gadolinium enhancement (LGE) CMR: Cardiac viability studies traditionally rely on the use of gadolinium-based contrast agents (see Section 3.3.2). These cause enhancement of tissue contrast, with respect to native T_1 contrast. Gadolinium-based contrast agents have the effect of shortening the T_1 of both healthy and diseased myocardium, resulting in their enhancement right after injection. However, healthy and diseased tissues are characterized by different contrast wash-out times: at a certain time point after injection, gadolinium has largely washed out of healthy tissues but is still retained in pathological areas where the extracellular space is expanded.

LGE imaging is most commonly performed with an inversion-prepared segmented GRE sequence, where the inversion time (TI) is chosen so as to null the signal from healthy myocardium and maximize the contrast. This technique, however, shows high sensitivity to a correctly chosen TI, which is often based on a quick scout acquisition [75]. Alternatively, Phase-Sensitive Inversion-Recovery (PSIR) sequences can be used to mitigate the effects of an incorrect TI on the resulting image contrast [76]. Unlike traditional IR sequences, PSIR retains the information on the longitudinal magnetization polarity by incorporating the signal phase in the image reconstruction. The reconstructed PSIR images exhibit enhanced contrast between healthy and diseased myocardium. PSIR sequences, however, require the acquisition of a reference image, in addition to the inversion-recovery image, to extract the signal polarity. Nevertheless, the total scan time can be kept constant by acquiring the reference scans during the T1-recovery heartbeats.

First Pass CMR: First pass perfusion CMR is the clinical gold-standard for measuring myocardial blood flow (MBF) and detecting myocardial ischemia [77], as described in Section 3.3.2. In this technique, images

are acquired during the first passing of a bolus of contrast agent, which increases the blood signal as described above. To this end, saturation prepared single-shot GRE (1.5T/3T) or bSSFP (1.5T) sequences in multiple slices are usually performed. In consequence, myocardial regions with low perfusion and, hence, low gadolinium concentration, will exhibit lower signal intensities. Moreover, if perfusion data is acquired under stress conditions, myocardial perfusion reserve can be obtained as the ratio of MBF at stress and at rest. Recent first pass perfusion methods can even yield quantitative MBF values by taking the temporal dynamics of the signal into account [78]. In clinical practice, first pass and LGE images are often evaluated alongside each other. This provides additional information on cardiac viability.

3.2.4. Quantitative CMR techniques

The methods described in the previous section offer powerful tools for the qualitative assessment of cardiac function and viability. Nevertheless, new quantitative MRI biomarkers have recently been introduced, significantly enhancing the diagnostic capabilities of CMR. Here, we provide a general overview of these techniques.

T_1 mapping: While T_1-weighted LGE images provide good qualitative characterization of focal myocardial infarction, it becomes less sensitive in the presence of diffused scarring. An emerging alternative is the pixel-by-pixel quantification of T_1 relaxation times [79]. By obtaining a healthy reference range, several pathologies can be characterized without the need for healthy reference areas within the image. T_1-mapping can be performed with or without contrast injection. In the latter case, it is referred to as *native* T_1-mapping, as opposed to *post-contrast* T_1-mapping.

T_1-mapping sequences are traditionally based on the Look-Locker technique, which consists in measuring the signal at multiple time points following an inversion preparation pulse [80] (see Figure 3.2). The collected data points, sampling the longitudinal magnetization recovery, are then fit to an exponential curve to derive the T_1 estimates for each pixel. The most commonly used method for myocardial T_1-mapping is the Modified Look Locker Inversion recovery (MOLLI) sequence. Single-shot bSSFP images are each acquired in the end-diastole phase of consecutive heart beats following the application of an inversion pulse [81]. A typical MOLLI pattern is the 5(3s)3 scheme [82], where the first inversion preparation is followed by 5 bSSFP acquisitions in separate heart beats, then 3 seconds of rest are inserted to allow for T_1 recovery and, finally, a second inversion pulse is followed by the last 3 bSSFP measurements. MOLLI enables precise T_1-mapping in a single breath-hold.

Saturation recovery has been proposed as an alternative to inversion-

recovery techniques. The SAturation recovery single-SHot Acquisition (SASHA) sequence [83] acquires nine consecutive saturation-prepared single-shot bSSFP images, with variable saturation recovery times, in consecutive hearth beats. Saturation recovery-based sequences have the advantages of not requiring rest periods and of acquiring each image independently. As a result, the T_1-mapping will be less susceptible to biases introduced by T_2, magnetization transfer, inversion pulse efficiency and magnetic field inhomogeneities, however at the expense of a reduced dynamic range and, thus, reduced precision. Hybrid inversion, saturation recovery sequences have also been proposed to mitigate some loss in precision [84].

T_2/T_2^* mapping: T_2 relaxation time in the myocardium can be used as a marker for the presence of edema, as mentioned in Section 3.3.4. T_2-mapping is most often performed using a T_2-prepared bSSFP sequence [69], as shown in Figure 3.2. Commonly, the acquisition of each image is interleaved with rest periods to allow for T_1 recovery. Alternatively, T_1 recovery periods can be omitted introducing a saturation pulse at the end of the R wave in every heartbeat [85]. The signal is sampled at different TEs by varying the echo time of the T_2-preparation. Acquired data are then fit to an exponential decay curve to estimate T_2 values.

T_2^*-mapping can also be performed and is used for the identification of iron accumulation [70, 86]. T_2^*-mapping is commonly achieved with multi-echo GRE sequences, with a number of equally-spaced echo times. The resulting signal is then fit to an exponential decay curve to estimate T_2^* values.

$T_{1\rho}$ mapping: Myocardial $T_{1\rho}$-mapping has been recently introduced as a promising method for assessment of myocardial fibrosis without the need for exogenous contrast agents [87]. $T_{1\rho}$-mapping is performed through spin-lock-prepared bSSFP sequences acquired for different spin-lock times and interleaved with T_1 recovery periods (Figure 3.2). The sampled signal is then fit to an exponential decay curve to estimate the relaxation constant $T_{1\rho}$. The *in-vivo* applicability of $T_{1\rho}$-mapping, however, is hindered by the susceptibility to field inhomogeneities, especially at high field strengths.

Cardiac magnetic resonance fingerprinting (MRF): Obtaining T_1/T_2 values with the techniques described above requires the acquisition and subsequent fit of multiple high-resolution images to exponential decay models. Unfortunately, high-resolution scans can be impractically long, particularly if multiple parameters need to be estimated. On the other hand, magnetic resonance fingerprinting (MRF) offers the possibility to simultaneously quantify multiple tissue parameters in a single scan [88]. By varying sequence parameters such as TR and FA throughout the acquisition of highly undersampled images, information on tissue parameters is encoded in the temporal signal of each pixel. These so-called fingerprints are unique to the underlying

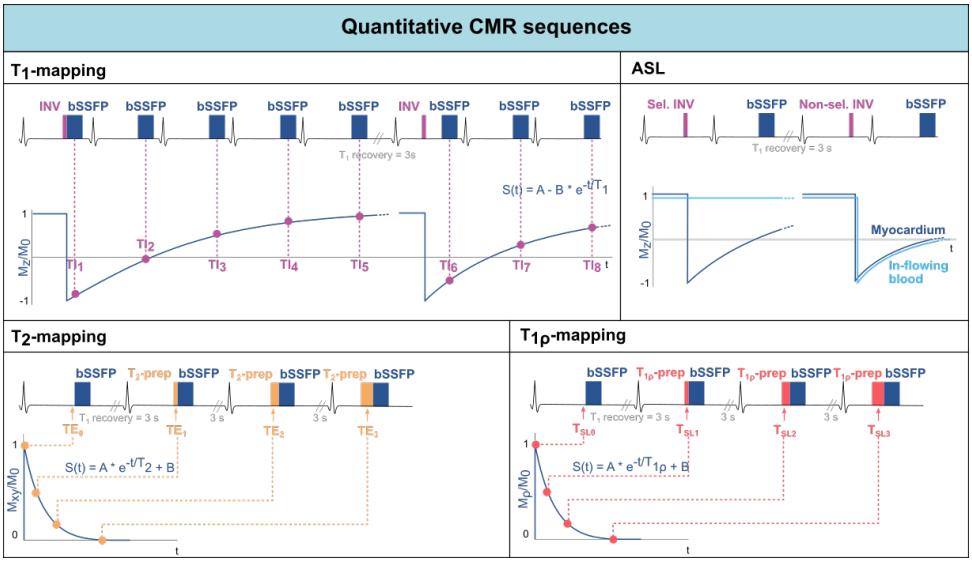

Figure 3.2 : Acquisition schemes for quantitative CMR techniques: T_1-mapping, Arterial Spin Labeling (ASL), T_2-mapping, and $T_{1\rho}$-mapping. For each technique, the sequence scheme is represented along with the data sampling and reconstruction strategies.

tissue parameter configuration and can be compared to previously generated dictionaries to infer the model parameters of interest. The dictionary contains simulated time signals for the chosen sequence parameters for a range of model parameter values. While MRF is well established for studies of the brain, non-static organs such as the heart pose challenges due to high respiratory and cardiac motion [89, 90]. Therefore, cardiac MRF is performed in breath-held acquisitions which are ECG triggered to the quiescent, end-diastolic phase of the cardiac cycle [91]. More recently, free-breathing cardiac MRF sequences have also been proposed [92]. However, since the heart rate varies over time, multiple dictionaries which are simulated with the actual heart rate, are required. To further increase sensitivity to T_1/T_2, inversion or saturation pulses can be added [91]. Although clinical validation is still in its early stages due to complex acquisition and reconstruction as well as relatively long breath-holds, cardiac MRF remains a promising technique for fast multi-parametric mapping.

Blood flow: Cardiovascular flow is typically measured through phase contrast methods that are sensitized to through-plane velocities [93]. Flow velocity values are obtained by adding bipolar flow-encoding gradients in the slice-selection direction, after the excitation but before read-out. Flow encoding is based on the principle that moving spins, contrary to stationary spins, accumulate a net phase shift proportional to their velocity when subject to bipolar gradients. By toggling the

bipolar gradients, the other contributions to the phase shift, such as those cause by field inhomogeneities, can be neutralized and the blood flow velocity can be quantified.
2D-phase contrast imaging only resolves though-plane flow in 2 spatial dimensions. However, more recently, 4D-flow imaging has been proposed, which combines 3D spatial encoding with 3D directional velocity encoding [35, 94]. As a result, 4D-flow MRI offers the possibility to visualize the temporal evolution of complex flow patterns in a 3D volume.

Arterial Spin Labelling: Myocardial perfusion imaging is the clinical non-invasive gold standard for detecting of myocardial ischemia [78]. However, current techniques are based on first pass perfusion imaging which requires the use of contrast agents and, thus, limits the repeatability and clinical applicability. Arterial spin labelling (ASL), on the other hand, relies on endogenous contrast in the form of magnetically labelled blood. The general idea behind ASL is to acquire two images, one with and one without labelled blood. Subsequently, these images are subtracted to obtain the perfusion related signal only. For cardiac applications of ASL, the most commonly used tagging method is Flow-Alternating Inversion Recovery ASL (FAIR-ASL) [95, 96], depicted in Figure 3.2. In FAIR-ASL, spatially selective and non-selective inversion pulses are applied alternately: The selective pulse serves as a preparation for the control image. During image acquisition after the non-selective pulse, however, in-flowing inverted spins reduce the longitudinal magnetization proportionally to the perfusion rate. During reconstruction, the subtracted images are first normalized to the baseline intensity, i.e., an image without any preparation pulse. This difference is then multiplied with the inversion efficiency, the blood water-tissue partition coefficient, and an exponential factor accounting for T_1-decay to obtain the MBF [97].

3.2.5. Common CMR Artifacts

The complexity of cardiac anatomy, as well as the presence of respiratory motion, cardiac motion, and blood flow, constitute a unique set of challenges for CMR examinations. In this section we recount the most common artifacts in cardiac MR and strategies for mitigating them (see Section 3.4). A comprehensive guide to cardiac MR artifacts can be found in [98].

Respiratory motion can cause inconsistencies between different segments of the acquisition. As a result, ghosting artifacts may appear on the reconstructed images. Two approaches are commonly used to avoid breathing-related artifacts: breath-holding and respiratory navigators (both will be described in Section 3.4.1). On the other hand, cardiac motion can cause blurring for long imaging blocks, when

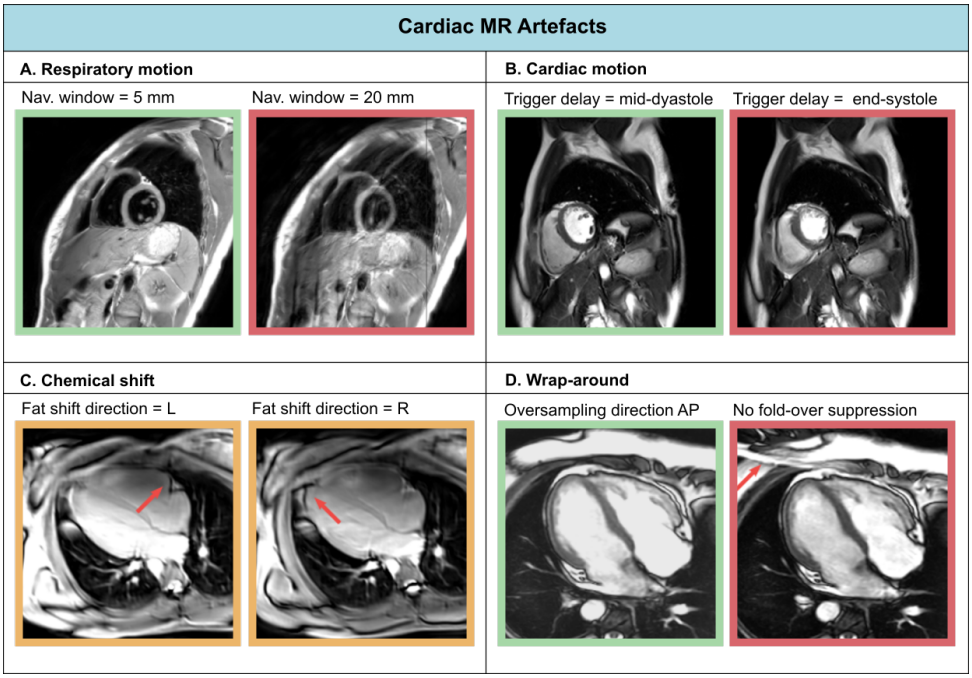

Figure 3.3 : Experienced CMR image artifacts of (A) respiratory motion, (B) cardiac motion, (C) chemical shift, and (D) wrap-around.

the acquisition window includes phases of rapid motion. This effect is commonly tackled by introducing cardiac triggering, which synchronizes the acquisition with the cardiac cycles. Choosing relatively long trigger delays from the R peak of the electrocardiogram (ECG) signal enables acquisition during quiescent cardiac phases, such as mid-diastole.

Blood flow can also be a cause of artifacts in CMR. As already discussed in the blood flow imaging paragraph of Section 3.2.4, motion-induced phase shifts occur in presence of blood flow, corrupting the spatial phase encoding. Flow-compensated gradient can be employed to minimize these alterations, by nulling the higher-order gradient moments. For instance, 1^{st} order flow compensation consists of nulling the gradients 1^{st} order moment, minimizing constant flow velocities contributions.

Aliasing artifacts are very common in MRI and specifically in CMR, where the strict time constraints often limit the FOV dimensions. These artefacts manifest as wrap-around ghosts, which can overlap to the anatomical structures under investigation. While aliasing in the frequency-encoding direction can be avoided through oversampling, this is not feasible in the phase encoding direction without increasing scan time. In this case, the FOV must be enlarged at the expense of lower resolution.

Finally, chemical shift artifacts can manifest in the presence of pericardial fat. These arise because of the different molecular environment of protons in fat and water, whose resonant frequencies differ by approximately 420 Hz (at 3T) as a result. This difference results in a misregistration of fat and water tissues along the frequency encoding direction. Chemical shift artifacts become more evident, for example, when changing the frequency encoding direction. They can be reduced by increasing the signal bandwidth, albeit at the cost of lower SNR.

3.3. Clinical Cardiovascular MR

This section will outline the contributions CMR can make within each of the major cardiovascular subspecialties and set the scene for the remaining articles in this manuscript which focus on image acquisition, reconstruction, and the burgeoning impact of artificial intelligence on all these areas. Where relevant, reference is made to international diagnosis and treatment guidelines and the levels of supporting evidence underpinning recommendations.

3.3.1. Basic Principles and Advantages of CMR

CMR is widely recognized as the gold-standard for the non-invasive quantification of left ventricular (LV) ejection fraction which remains a cornerstone parameter that guides decision making in various scenarios ranging from the diagnosis of heart failure to determining the need for primary prevention implantable cardioverter defibrillators (ICDs) and the timing of surgical intervention in patients with valvular heart disease [99, 100]. For many of these applications, echocardiography remains a first-line investigation, but CMR is particularly valuable for evaluating cardiac structure and function in patients with poor acoustic windows. This is recognized in the recent ESC heart failure guidelines as a class I indication for CMR (Class I: evidence and/or general agreement that a given treatment or procedure is beneficial, useful, or effective) with level of evidence C (consensus opinion of experts and/or small studies, retrospective studies, registries) [99]. The ability to non-invasively acquire high spatial and temporal resolution images in any plane using bSSFP sequences which have high intrinsic T_1 and T_2 contrast affords high endocardial definition enabling chamber volumes and function to be quantified with high accuracy and precision [101]. This is achieved by acquiring a contiguous short-axis stack parallel to the atrioventricular groove and planned with two and four chamber cine sequences [53, 102].

A key feature of CMR is its ability to non-invasively characterize tissue by exploiting intrinsic differences in nuclear magnetic relaxation

characteristics of hydrogen nuclei which are found in abundance in the human body in different chemical environments in the form of water but also bound in large macromolecules such as triglycerides and proteins. This enables different anatomical structures and pathology to be readily appreciated and differentiated without the need for exogenous contrast. However, the administration of the latter, in the form of large macromolecular chelates of the paramagnetic element gadolinium, augments our ability to detect pathology even further by highlighting the presence of myocardial fibrosis, infiltration, or areas of infarction [103]. Gadolinium contrast agents shorten T_1 relaxation times in proportion to their local concentration. As large positively charged macromolecules, they are unable to penetrate the intact cell membrane and so remain entirely extracellular. As such, in tissues where the extracellular space has been expanded by the presence of fibrosis or infiltrated by exogenous proteins such as for instance in cardiac amyloidosis, gadolinium can accumulate to higher local concentrations. If imaged ~10 minutes after contrast administration using an appropriate inversion recovery prepared T_1-weighted sequence with an inversion time set to null the signal from healthy myocardium, such areas are illuminated as gadolinium washes out of healthy tissue but remains at higher concentrations in diseased areas, causing faster recovery of signal. Infarcted or non-viable areas of myocardium can be similarly delineated as they are rich in extracellular matrix and proteins, but cell-poor or in the case of acute myocardial injury, may be populated by necrotic cells with disrupted cell membranes [104]. The LGE imaging technique (see Section 3.2.3) plays a pivotal role in phenotyping patients with heart failure, particularly differentiating patients with ischemic from non-ischemic heart failure (Class IIa: conflicting evidence and/or divergence of opinion about the usefulness/efficacy of the given treatment or procedure but weight of evidence/opinion is in favor of usefulness or efficacy) with level of evidence C [99].

3.3.2. Ischemic Heart Disease

In patients with ischemic heart disease, occlusion of an epicardial coronary artery tends to cause injury and necrosis of endocardial cells first as these are furthest away from the blood supply, evolving to a wavefront of necrosis that gradually spreads centrifugally towards the epicardium (Figure 3.4A). Areas of LGE extending from the sub-endocardium, particularly if they are regional or in a coronary distribution, denote areas of ischemic infarction. In contrast, non-ischemic pathologies such as dilated cardiomyopathy or myocarditis tend to be associated with LGE in an epicardial or mid-wall distribution, allowing ischemic and non-ischemic etiologies of heart failure to be readily distinguished (Figure 3.4B). CMR is regarded as a class I indication

for evaluating acute chest pain or myocardial injury in patients with unobstructed coronary arteries (level of evidence B: moderate quality evidence from one or more well designed, well-executed non-randomized studies, observational studies or registry studies or meta-analyses of such studies) [105]. As well as being diagnostically valuable, it is increasingly being recognized that the presence and/or extent or pattern of LGE may have prognostic significance [106–110].

In patients with ischemic heart disease, the distribution of LGE can localize infarcts to specific coronary territories (Figure 3.4A), and the transmural extent can determine the likelihood of underlying myocardial viability [111]. By imaging the first pass of contrast through the myocardium under conditions of vasodilator stress (typically achieved with adenosine or regadenoson), myocardial perfusion abnormalities may be identified which may signify myocardial ischemia [112]. When the epicardial coronary arteries are unobstructed, contrast arrives synchronously and homogeneously in all supplied myocardial segments. However, where there is a hemodynamically significant stenosis in a given coronary artery, that vessel will already be maximally vasodilated at baseline. The administration of a vasodilator will thereby augment blood flow (and so the arrival of contrast) to unobstructed coronary arteries, allowing areas of hypoperfusion to be delineated by the delayed and reduced arrival of contrast to the already maximally dilated stenosed vessel [112]. This technique can therefore be used to diagnose the presence of coronary disease [113] or where this is already known, determine the functional significance of a given stenosis identified using an anatomical imaging technique such as invasive coronary angiography or CT coronary angiography. As mentioned previously, this technique is frequently used in tandem with LGE imaging to assess for myocardial ischemia and viability and thereby determine the need for or to guide revascularization [112]. Recent US chest pain guidelines now regard this as a class I indication for stress CMR (level of evidence B) [105]. Advances in sequence design, image processing, and quantification techniques now enable myocardial blood flow to be measured at the voxel level with high in-plane spatial resolution [114–119]. The latter allows microvascular dysfunction to be elucidated non-invasively [115, 120, 121] (Figure 3.4C-D), and for ischemic burden to be accurately calculated [117, 122]. Quantification techniques also appear to improve the ability to correctly identify multivessel coronary disease [123].

3.3.3. Non-ischemic Cardiomyopathies

The ability to quantify tissue characteristics has enabled various MR relaxation parameters to be used as biomarkers for diagnosis and to guide therapy [79, 124]. The seminal example of this is the development of T_2^* imaging (Figure 3.4E-F), which has enabled non-invasive hepatic

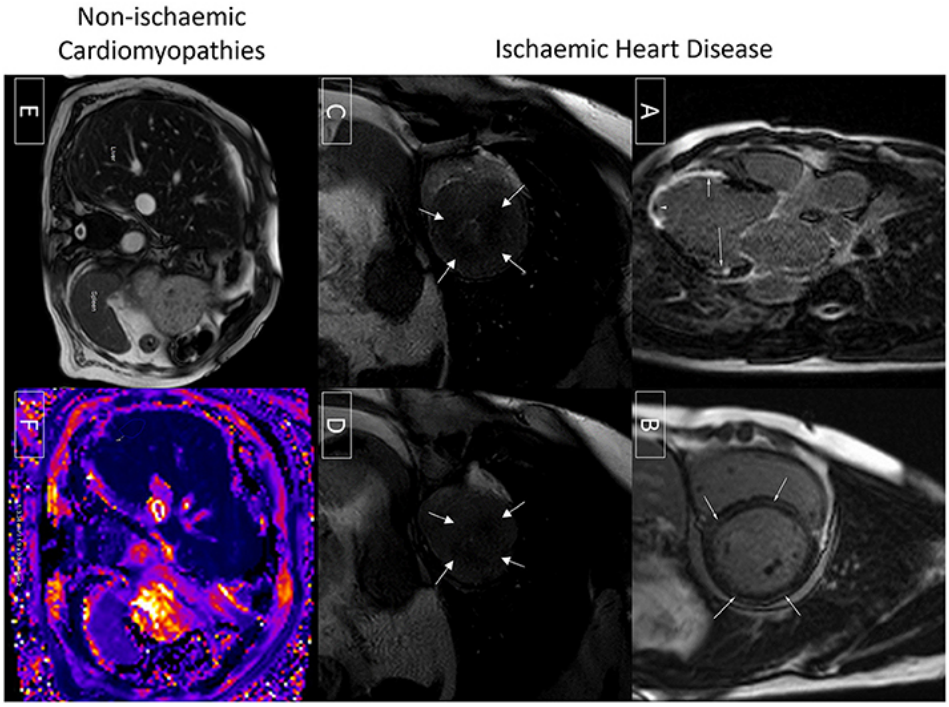

Figure 3.4 : Ischaemic and non-ischaemic heart disease. (A) Late gadolinium enhancement sequence in the 3-chamber view. There is near transmural sub-endocardial enhancement of the mid-apical septum and apex (short arrow, mid-left anterior descending coronary artery territory). A signal void focus is also seen adherent to the apex (arrowhead). This represents a left ventricular thrombus. In addition, there is focal partial thickness sub-endocardial enhancement of basal inferolateral wall (long arrow, circumflex coronary artery territory), which spares the sub-epicardium (denoting an ischaemic etiology). The presence of infarcts in two different coronary territories alludes to the potential presence of multivessel coronary disease. (B) Late gadolinium enhancement sequence demonstrating a ring or circumferential pattern of non-ischaemic enhancement. The areas of enhancement involve the mid-wall or sub-epicardium, sparing the sub-endocardium. (C,D) Stress perfusion scan from a patient with hypertrophic cardiomyopathy. There is widespread circumferential sub-endocardial delayed arrival of contrast (hypoperfusion) at mid-ventricular level (C) and apex (D), typical of microvascular dysfunction. (E,F) Bright blood axis scout at upper abdominal level (E). The normal liver should have signal characteristics similar to the spleen (marked). However, in this patient with hepatic iron overload, the spleen appears almost black due to accelerated dephasing of spins brought about by the increasing field inhomogeneity generated by intrahepatic iron stores. This T_2^* effect can be used to quantify liver iron levels (F). Here, the liver T_2^* is ~1.9 ms, denoting moderate hepatic iron overload (normal > 6.3ms) equivalent to ~5–10mg iron/g dry weight.

and myocardial iron quantification [86]. By allowing the early diagnosis of iron overload cardiomyopathy and timely initiation and titration of chelation therapy, this has been credited with significantly reducing the risk of death from heart failure in patients with thalassemia [125]. The development of T_1 mapping techniques (see Section 3.2.4) has found applications in detecting interstitial fibrosis, and by measuring post-contrast T_1 together with the knowledge of the patient's hematocrit, the estimation of extracellular volume fraction (ECV) has made it possible to track pathologies such as cardiac amyloidosis [79]. This is of growing relevance as these conditions are increasingly amenable to novel therapeutics which can stabilize or even potentially partially reverse cardiac amyloid deposition [126]. Thus, CMR is regarded as a class I indication for the evaluation of infiltrative disease and suspected iron overload (level of evidence C) [99].

CMR also plays a vital role in the evaluation of patients with heart failure or suspected non-ischemic heart muscle disease. It can be used as a gatekeeper for invasive coronary evaluation [127] but also to accurately evaluate areas of the heart that are difficult to clearly visualize by echocardiography such the LV apex or the right ventricle. This can be invaluable for the diagnosis of particularly the apical variants of hypertrophic cardiomyopathy [128] and arrhythmogenic right ventricular (RV) cardiomyopathy [129].

3.3.4. Myocardial Inflammation

The ESC guidelines regard CMR as a class I indication (level of evidence C) for the evaluation of patients with suspected myocardial inflammation [99]. Acute inflammatory processes and tissue injury can increase tissue water content and increase the mobility of tissue water protons [130]. This can be exploited with T_2-weighted imaging techniques and quantitative mapping methodologies (see Section 3.2.4) to diagnose the presence and distribution of myocardial inflammation (Figure 3.5) [124, 130, 131]. Myocarditis can be diagnosed when in the appropriate clinical context, there is evidence of tissue oedema and inflammation/injury on one T_2-based (T_2-weighted-imaging or T_2-maps) and one T_1-based criterion (native T_1 map, LGE imaging, or ECV maps) respectively, in a non-ischemic distribution [132].

3.3.5. Cardiac Electrophysiology

Within the sphere of cardiac electrophysiology, not only is CMR playing a vital role in the identification of patients at increased risk of arrhythmia [106, 108–110], but it is increasingly being used to plan invasive arrhythmia ablation procedures [133]. Atrial fibrillation is the commonest sustained cardiac arrhythmia and an important cause of morbidity and mortality [134]. In most patients, the arrhythmia

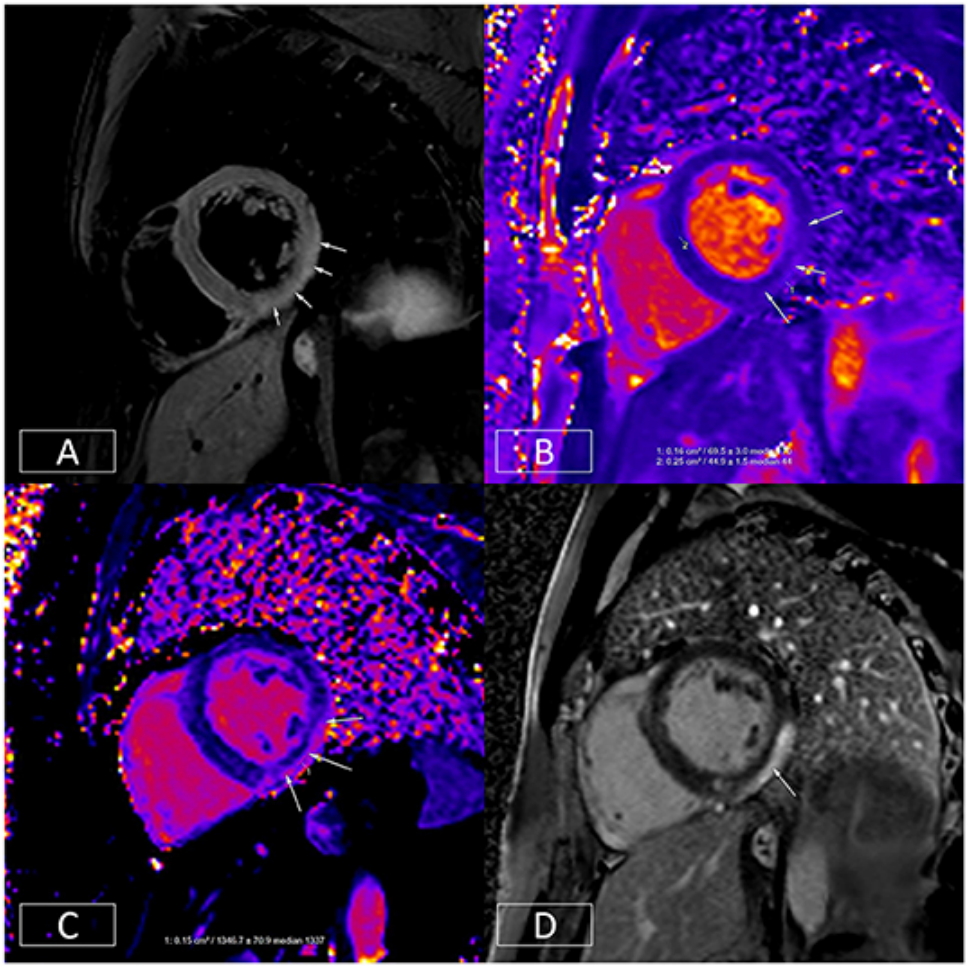

Figure 3.5 : Multiparametric evaluation of a patient with acute myocarditis. (A) Depicts increased T_2 signal in the mid-inferior and lateral walls in an epicardial to mid-wall distribution. The absolute T_2 time in the inflamed area is increased to ~70 ms (B) whereas the remote myocardium in the septum has a normal T_2 time of 45 ms (normal < 55 ms). (C) depicts increased native T_1, another marker of tissue injury. This is raised at 1347 ms in the epicardium of the mid-inferior and lateral walls (normal range: 890–1035 ms on this platform at 1.5T). (D) illustrates epicardial to mid-wall enhancement of the mid-inferior and lateral walls, which spares the sub-endocardium (typical of myocarditis).

is triggered by electrical activity from the pulmonary veins which can be treated by electrically isolating these through ablation [134]. 3D-anatomical and fibrosis imaging sequences can help to define the number of pulmonary veins and the degree of fibrotic remodeling of the atrium which may influence procedural success (Figure 3.6) [135].

For patients with malignant ventricular arrhythmias, identifying the precise origin of arrhythmic foci often requires prolonged and tedious pace-mapping of the electrical substrate increasing procedure times and thereby risk to patients [136]. This can be considerably facilitated by pre-procedural CMR which can identify areas of scar tissue and help target electrical interrogation of the diseased myocardium [136].

3.3.6. Congenital Heart Disease

CMR has also revolutionized the care of patients with congenital heart disease, which occurs at a frequency of 6-8 per 1000 live births [137]. Advances in care now mean that more patients are surviving to adulthood and so are forming an important cohort of patients who require regular clinical and imaging evaluation [137–139]. The complexity of disease can range from minor anomalies such as a small restrictive ventricular septal defect through to patients with complex cyanotic heart disease with cardiac malformations that require often multiple complex surgeries to correct or palliate. The imaging assessment of such patients requires the ability to image in multiple planes, in 3D, and to quantify blood flow, particularly to diagnose the presence and severity of any intracardiac shunts [137, 139]. Importantly, this is achieved without the need for any ionizing radiation (which would have a greater impact on this younger cohort of patients who need frequent serial imaging) and unfettered by limitations imposed by acoustic windows as echocardiography often is. This is particularly true for structures such as the right ventricle that are more challenging to image with echocardiography [140]. The high accuracy and precision of the measurements of ventricular size and function as well as blood flow enable these parameters to be used to guide the timing for surgical intervention, for instance, pulmonary valve interventions in patients with repaired tetralogy of Fallot [139, 141]. The broad utility of CMR in congenital heart disease has been recognized in recent international guidelines [142]. The presence of RV scar detected by LGE-CMR has been highlighted as a risk factor for sudden cardiac death and its use for risk stratification is recommended as a class IIa indication (level of evidence C). These guidelines also recognize CMR with physical stress as a class I indication (level of evidence C) for the evaluation patients with coronary anomalies to confirm/exclude myocardial ischemia [142].

3.3.7. Valvular Heart Disease

While Doppler echocardiography is rightly considered the modality of choice for the evaluation of patients with valvular heart disease, phase-contrast velocity mapping is particularly adept at quantifying regurgitant lesions such as aortic and pulmonary regurgitation [143]. It can play a role in corroborating echo findings or in providing accurate

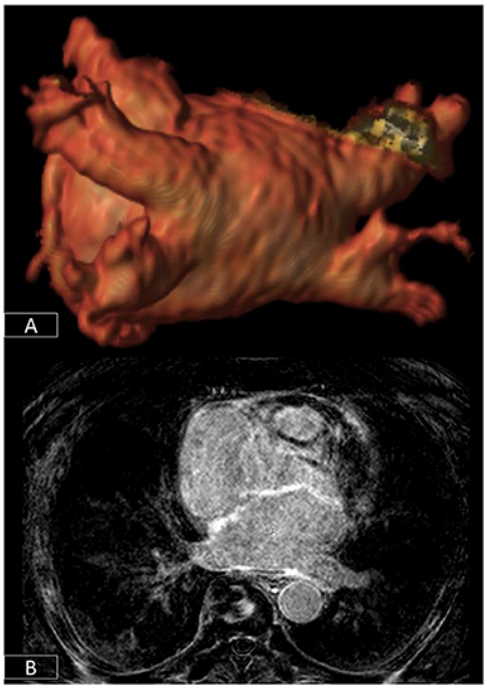

Figure 3.6 : 3D-segmentation of the left atrium depicting left atrial anatomy and four pulmonary veins and their tributaries (A). There is extensive fibrosis of the left atrial wall (B) on 3D late enhancement sequences which may reduce the likelihood of successful ablation.

quantification where unfavorable echo windows preclude this, or jet eccentricity can result in underestimation of jet severity [100, 144]. As in many other spheres of cardiovascular medicine, an accurate quantification of ventricular ejection fraction may be vital in determining the timing of any intervention [144].

3.3.8. Angiography and Vascular Disease

CMR also has the added advantage of enabling visualization of the aorta and great vessels which can often need intervention in patients with aortic valve disease, particularly if this is associated with aortopathy such as patients with bicuspid aortic valves. This can be achieved using time-resolved angiographic approaches [145], as well as with 3D-sequences acquired in free-breathing that can increasingly be combined with multiple tissue contrasts [146–148]. The former can enable the visualization of multiple vascular beds and structures (systemic venous, pulmonary arterial and venous, and systemic arterial) with a single dose of contrast (Figure 3.7)[145]. This has a range of applications from the

evaluation of vascular disease itself to planning interventions.

Advances in rapid imaging techniques, catheter technology, and the development of interventional imaging suites now allows actual invasive procedures to be performed under MR-guidance [149, 150]. This brings the principal benefit of minimizing the need for x-ray fluoroscopy particularly in younger patients who require frequent serial evaluation.

There is also growing interest in leveraging the tissue characterization capabilities of CMR to evaluate coronary plaque characteristics [151, 152]. Specifically, T_1-weighted non-contrast coronary imaging can be used delineate the presence of methemoglobin, a marker of coronary thrombosis or intraplaque hemorrhage, which has been associated with vulnerable plaque morphology and angina severity [152].

3.3.9. Cardiac Tumors

Another area where CMR has made significant indispensable contributions to patient care is the evaluation of cardiac tumors [153]. While these are thankfully rare, the ability of CMR to provide full-spectrum non-invasive characterization can help to refine the diagnosis and, in many instances, can type specific lesions. Anatomical and cine sequences can localize a lesion and define its geometry and relationship with surrounding structures [153]. Sequences with different T_1 and T_2 weighting with and without fat-saturation can be used to delineate tissue characteristics. Imaging of the tumor during the first pass of contrast can depict its vascularity and perfusion [154]. Imaging in the early phase after contrast administration can differentiate thrombus from neoplasia or reveal the presence of superadded thrombosis. Imaging in the late phase can provide information on the contrast uptake characteristics of the lesion which again can be valuable in differential diagnosis [153, 154]. Such data can increasingly be combined with FDG-PET and other radiotracer uptake data in hybrid CMR-PET imaging platforms to provide truly multimodal comprehensive evaluation that encompasses tumor metabolic activity [155].

In summary, CMR has found applications within every sphere of cardiovascular medicine and has often had a positive disruptive effect – improving diagnosis and in many cases, changing patient outcomes. In a single comprehensive study, it is now possible to assess and reliably quantify cardiovascular anatomy, function, tissue T_1, T_2, T_2^*, ECV, perfusion at stress and rest, late gadolinium enhancement, and blood flow. While many of the necessary sequences are ECG-gated and have been done with breath holding, recent advances now make it possible to acquire most data using free-breathing techniques making CMR more accessible and tolerable for patients with cardiovascular disease who often suffer from breathlessness (see Section 3.4.1). However, although the ability to acquire more and more data has grown over

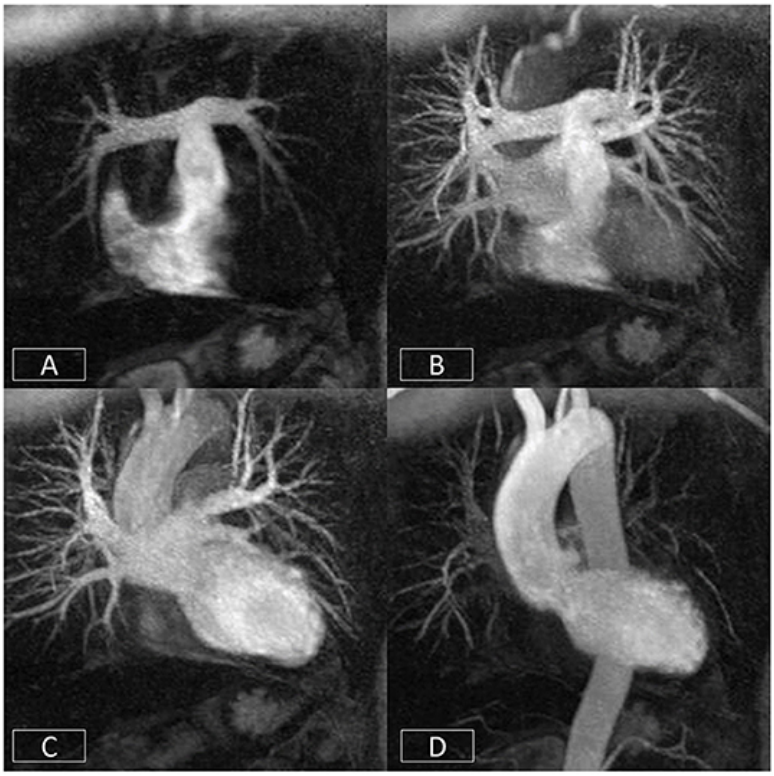

Figure 3.7 : Cardiovascular time resolved 3D-angiography. The bolus of contrast is imaged progressively as it passes from the right side of the heart (A) into the pulmonary arteries (B), left atrium/ventricle (C), and thoracic aorta (D). This obviates the need to precisely time the contrast volume and enables the rapid visualization of different parts of the circulation with a single bolus of contrast.

the years, the time available to scan patients (typically 1 hour) and report the voluminous imaging data sets that are generated has not. This requires careful protocolling and efficient image acquisition to harness the true benefits of this technology in a value-conscious and efficient way. Advances in the application of artificial intelligence to both image reconstruction and interpretation may help offset some of these challenges.

3.4. CMR image quality

When setting up and optimizing a clinical CMR protocol to obtain the best images possible, the inherent trade-off between spatial and temporal resolution, scan time and signal-to-noise ratio (SNR) must be taken into consideration. For example, imaging at higher spatial resolution will

result in lower SNR or longer scan times. Thus, a compromise in this triangle needs to be found in terms of image quality and acquisition time. Moreover, CMR can be impacted from image degradation due to cardiac and respiratory motion. Physiological motion induces aliasing along the phase-encoding direction and/or blurring of the image content (see Section 3.2.1), where the appearance depends on the imaging trajectory. Therefore, CMR acquisitions generally require synchronization or handling of the cardiac and respiratory cycles as depicted in Figure 3.8. In CMR, to avoid artefacts related to cardiac motion, it is usually desirable to freeze the heart motion, using gated/triggered acquisitions with <100ms temporal resolution. Unfortunately, this comes at the expense of spatial resolution and/or coverage adding further constraints to CMR.

3.4.1. Handling motion

Motion artifacts can be mitigated by (a) avoiding motion, *i.e.* training the patient to perform breath-holds or applying anesthesia and sedation to freeze respiratory motion; (b) reducing motion, i.e. signal averaging to smooth out motion, performing fast imaging to become less sensitive to motion [156–160] or suppressing motion outside the field of view using saturation bands; (c) triggering or gating motion, *i.e.* monitoring the motion cycle (using, for example, MR navigators [161–165], cameras [166], field probes [167], pilot tone [168], respiratory belts or electrocardiogram [169]) and either prospectively trigger on the respective motion [170, 171], meaning only acquiring within a small portion of the motion cycle, or retrospectively gate the motion [172–175], meaning sorting the data into distinct motion states for reconstruction. Motion avoidance (case (a)) requires, however, patient compliance and reduces patient comfort. For highly non-compliant patients (for example pediatric patients), moderate sedation or general anesthesia can be given which does however require the use of a lung respirator, increasing scan time and costs, and could have potential side effects and complications. Motion reduction (case (b)) can require longer scan times, increases induced radio frequency energy on patient (*i.e.,* tissue heating) and residual motion artefacts can remain in the image. Motion triggering and gating (case (c)) capture only a fraction of the entire dynamic respiratory and cardiac cycle or periodic assumptions of the dynamic cycle are made which may not hold in practice. Thus, a varied range of strategies has been proposed to avoid CMR image degradation due to cardiac and/or respiratory motion, some of which are summarized in Figure 3.9.

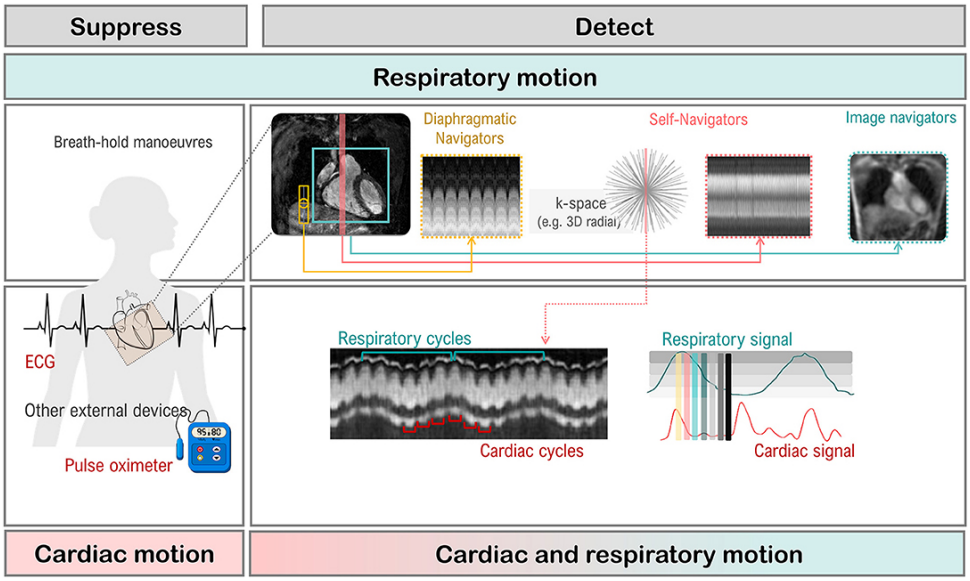

Figure 3.8 : Cardiac and respiratory motion monitoring. Motion can either be suppressed (e.g., breath-holding) or monitored with MR navigators or external devices like electrocardiogram (ECG). From the monitored signal, one can extract the respiratory, and cardiac cycles which are needed for triggering (prospective) or gating (retrospective).

Respiratory motion

Breath-holding techniques are commonly used to reduce respiratory motion artefacts. If the patient complies with the breathing instructions this provides a 10-15s window where artefact-free images can be obtained. A CMR examination requires multiple breath holds [176], which can lead to patient discomfort and fatigue, resulting in poor breath-holding and, consequently, motion artefacts that can impact the downstream analysis [177, 178]. In addition, breath-holding can be challenging or impossible for pediatric, critically ill, or uncooperative patients [179]. Moreover, some CMR protocols, such as CMRA and other 3D CMR applications, require acquisition times that are too long for a breath-hold. Free-breathing alternatives that use respiratory triggering or gating based on *diaphragmatic navigators* (that monitor the superior-inferior motion of the diaphragm) are available on most CMR scanners [180–182]. Unfortunately, this approach has low scan efficiency, since only data within a small predefined respiratory gating window is used to generate an image, which leads to long and unpredictable scan times (due to irregular breathing patterns). External respiratory monitoring devices, such as bellows around the chest or abdomen, are also often used. More recently, novel tracking devices like pilot tone [168, 183] are being investigated for the usage of a sequence-independent motion

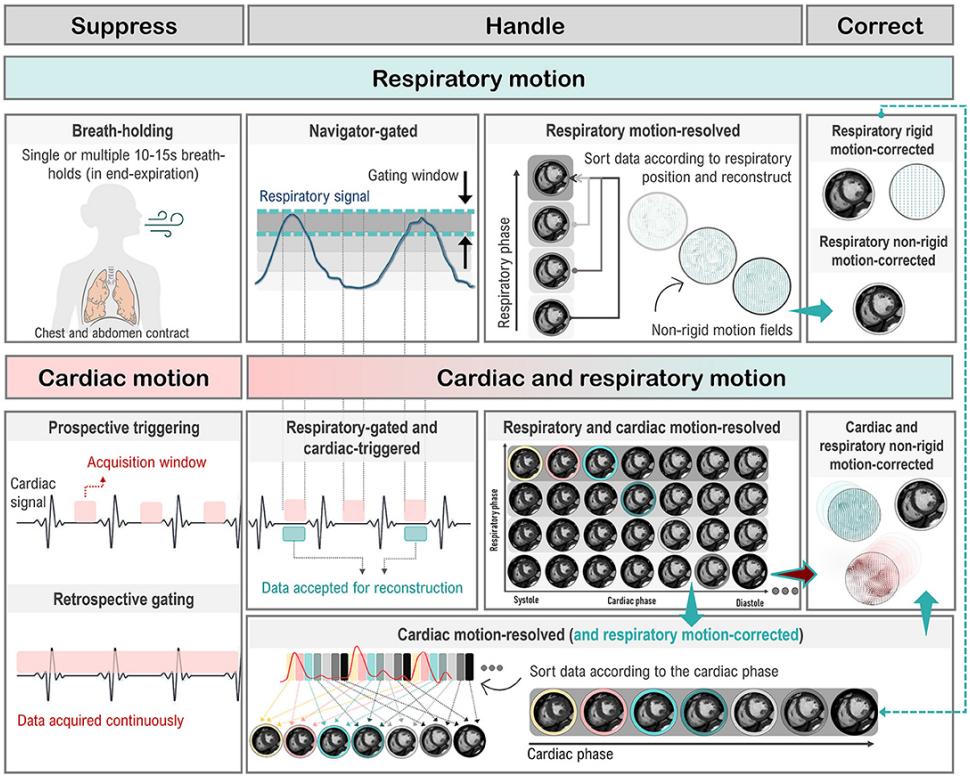

Figure 3.9 : Cardiac and respiratory motion handling. Motion can either be suppressed (left column), handled prospectively or retrospectively (middle columns) or corrected/compensated (right column). Different strategies exist to deal with respiratory-only (top), cardiac-only (bottom left), and respiratory and cardiac (bottom right) motion. Prospective triggering: motion can be triggered to shorten the acquisition window to a specific motion state. Retrospective gating: motion is resolved by gating which can be performed exclusively on either respiratory/cardiac motion or on the joint respiratory and cardiac motion (central gating matrix) to yield respiratory/cardiac motion-resolved data. Data between individual gates/motion states can furthermore be compensated by registering them with a rigid or non-rigid motion field along the respiratory or cardiac motion direction.

monitoring solution.

Free-breathing CMR techniques based on *self-navigation* [184–188] or *image navigators* [163, 189–191] have been proposed to achieve 100% respiratory scan efficiency (no data rejection), by correcting all data for respiratory motion. Thus, allowing for shorter and more predictable scan times. Respiratory self-navigation techniques derive the respiratory-induced motion of the heart directly from the imaging data. Self-navigation is achieved by periodically imaging the central points in k-space and thus do not require any additional interleaving of navigators into the sequence. Typically, self-navigation approaches

extract the respiratory signal from 1D projections of the field of view (in one or more directions). However, signal from static structures, such as chest wall, is also included in 1D self-navigators, which can lead to motion estimation and correction errors. Image-based navigators, which allow separation of static structures from the moving heart, have been proposed as an alternative to 1D self-navigation to reduce motion estimation errors. These methods use low spatial resolution images acquired with sequence interleaved imaging blocks at periodic intervals, prior to the CMR data acquisition, to estimate and correct for 2D or 3D respiratory motion. Free-breathing single shot CMR sequences often rely on retrospective motion correction using image registration methods to correct for respiratory motion between time frames.

Once the respiratory signal has been estimated, image degradation caused by respiratory motion can be reduced by: (a) correcting for translational motion (directly in k-space) [92, 163, 183, 191–195], (b) separating (or binning) the data into multiple respiratory states to generate respiratory motion-resolved images [196–215], and (c) (using the latter for) correcting for more complex non-rigid motion [148, 190, 216–234].

Cardiac motion

CMR acquisitions are usually synchronized with heart motion though an ECG (with electrodes attached to the chest) to minimize imaging artifacts caused by cardiac motion. Two approaches are typically used: prospective ECG triggering and retrospective ECG gating. *Prospective triggering* uses the R wave from the ECG signal to trigger the data acquisition (and "freeze" the heart) at a specific phase or certain number of phases of the cardiac cycle [182, 193, 235–239]. In *retrospective gating*, data are acquired continuously throughout the cardiac cycle and the ECG signal is recorded simultaneously [173, 176, 177, 240–246]. Subsequently, data are reordered and grouped into different cardiac phases according to the ECG signal. However, the ECG can be unreliable in CMR (as described in Sections 3 and 4), particularly in the case of arrhythmias and ectopic hearts. Finger pulse oximetry can be used as an alternative to ECG, but its signal is delayed relative to the ECG R wave. To overcome these challenges, cardiac *self-gating* approaches have been proposed to estimate an ECG-like signal directly from the acquired data [174, 175, 199, 203]. The signal is then used for cardiac gating. More recently, contactless external sensors like pilot tone have also been used to track motion during CMR exams.

Cardiac and respiratory motion

Several solutions have been developed to eliminate the need for ECG synchronization and breath-holding altogether. This allows continuous

acquisition of CMR data, known as *free-running CMR* [92, 199, 201, 202, 211, 230, 247]. After acquisition, data is then sorted into multiple cardiac phases (with the desired temporal resolution) and multiple respiratory motion phases based on the cardiac (ECG, self-navigation, pilot tone, etc.) and respiratory (self-navigation, belt, etc.) motion signals to generate a multidimensional dataset for reconstruction. Moreover, the (self-navigation) respiratory signal or, for each cardiac phase, the bin-to-bin (affine) respiratory motion can be estimated and used to correct for respiratory motion directly in k-space (by applying the corresponding phase-shifts in k-space), before the image reconstruction, to generate respiratory motion-corrected cardiac phase-resolved CMR images [202, 214]. In addition, these images can be used to generate cardiac motion-corrected images by selecting the cardiac phases with the smallest intra- and interphase motion and then correcting for non-rigid motion [233]. The obtained respiratory and/or cardiac motion-gated k-spaces are usually sparsely sampled. During reconstruction, the spatio-temporal information can be exploited by either regularizing the motion dimensions [203, 248], correcting for the motion [249–251] or exploring the low-rankness (see Section 3.4.4) of the dynamic processes [252, 253].

Retrospective gating assumes a periodicity of the temporal motion evolution which is however not a given for patients with arrhythmias or irregular breathing patterns [254, 255]. In these cases, real-time CMR which is based on fast imaging sequences, like spGRE or bSSFP, can provide a viable solution [187, 190, 217, 256–261]. Imaging with high (sub-second) temporal resolution makes acquisitions robust to motion, and thus, images can be obtained without gating or binning [253]. In combination with efficient sampling trajectories and reconstruction techniques, 2D and 3D imaging with high spatio-temporal resolution can be performed.

3.4.2. Fast CMR

Several approaches have been proposed to speed up CMR acquisitions by reducing the amount of data required for accurate reconstruction, including parallel imaging [158, 159], *k-t accelerated imaging* [205, 206, 261, 262], or pseudo-random sub-Nyquist sampling [156, 157, 263]. Besides more efficient sampling trajectories, fast imaging sequences like fast low angle shot magnetic resonance imaging (FLASH) [264], bSSFP [39], fast spin-echo imaging (RARE) [34], echo planar imaging (EPI) [29] have enabled fast CMR imaging. Accelerated scans can be used to shorten the imaging time, to shorten breath-holds and improve patient comfort, but can also be used to collect more information (within the same imaging time), to increase temporal or spatial resolution and/or volumetric coverage.

Parallel imaging methods, such as (the image-based) SENSitivity Encoding (SENSE) [159] and (k-space-based) GeneRalized Autocalibrating Partial Parallel Acquisition (GRAPPA) [158], are used worldwide for CMR applications, but are limited by the number of receiver coils and in practice typically to 2- to 3-fold acceleration. K-t accelerated imaging [205, 206, 261, 262] extends these concepts along the dynamic temporal direction. It uses a regular undersampling pattern that is shifted over time. Images are reconstructed using a linear reconstruction approach, which relies on information extracted from low spatial resolution calibration data (with high temporal resolution) to minimise fold-over artefacts.

Simultaneous multi-slice (SMS) imaging [155, 242, 265–267] has the potential to acquire multiple slices, *i.e.*, increasing cardiac coverage without sacrificing in-plane spatial resolution. However, pre-calibration scans are required to calibrate the unfolding during reconstruction which increase overall scan time.

On the other hand, reduced spatial coverage but increased dynamic resolution can be obtained with *real-time CMR* (158, 161, 189, 227-233)[187, 190, 217, 254–260]. It relies on fast imaging sequences and trajectories to provide respiratory and cardiac motion-resolved images. Data acquisition is performed under free-breathing with sufficiently fast enough trajectories to capture whole field of view with minimal motion impact.

High acceleration factors can be achieved if the compressibility (or sparsity in a transform domain) of images is exploited as proposed in *Compressed Sensing* (CS) [157] or *Low-Rank* methods [210, 263]. In these cases, we seek a (pseudo-) random sub-Nyquist sampling (*i.e.*, undersampling) of the data. The applied sampling induces incoherent noise-like aliasing artefacts in the sparse domain. Thus, to satisfy the incoherence criterion, (pseudo-) random Cartesian or non-Cartesian undersampling schemes are used to accelerate scans.

3.4.3. CMR trajectories

The k-space undersampling patterns to accelerate CMR acquisitions in combination with the selected reconstruction method determine the obtainable image quality. A few exemplar trajectories are shown in Figure 3.10. In parallel imaging, the number of k-space lines is usually reduced using regular Cartesian undersampling (*i.e.* sampling below the Nyquist-Shannon sampling limit) [158, 159]. In dynamic CMR, the Cartesian sampling patterns can be extended along the dynamic motion direction as used in k-t imaging [205, 206, 261, 262]. A different k-space undersampling should be used for each time frame to introduce incoherence along the temporal dimension, and to thus enable exploitation of both spatial and temporal sparsity, as for example

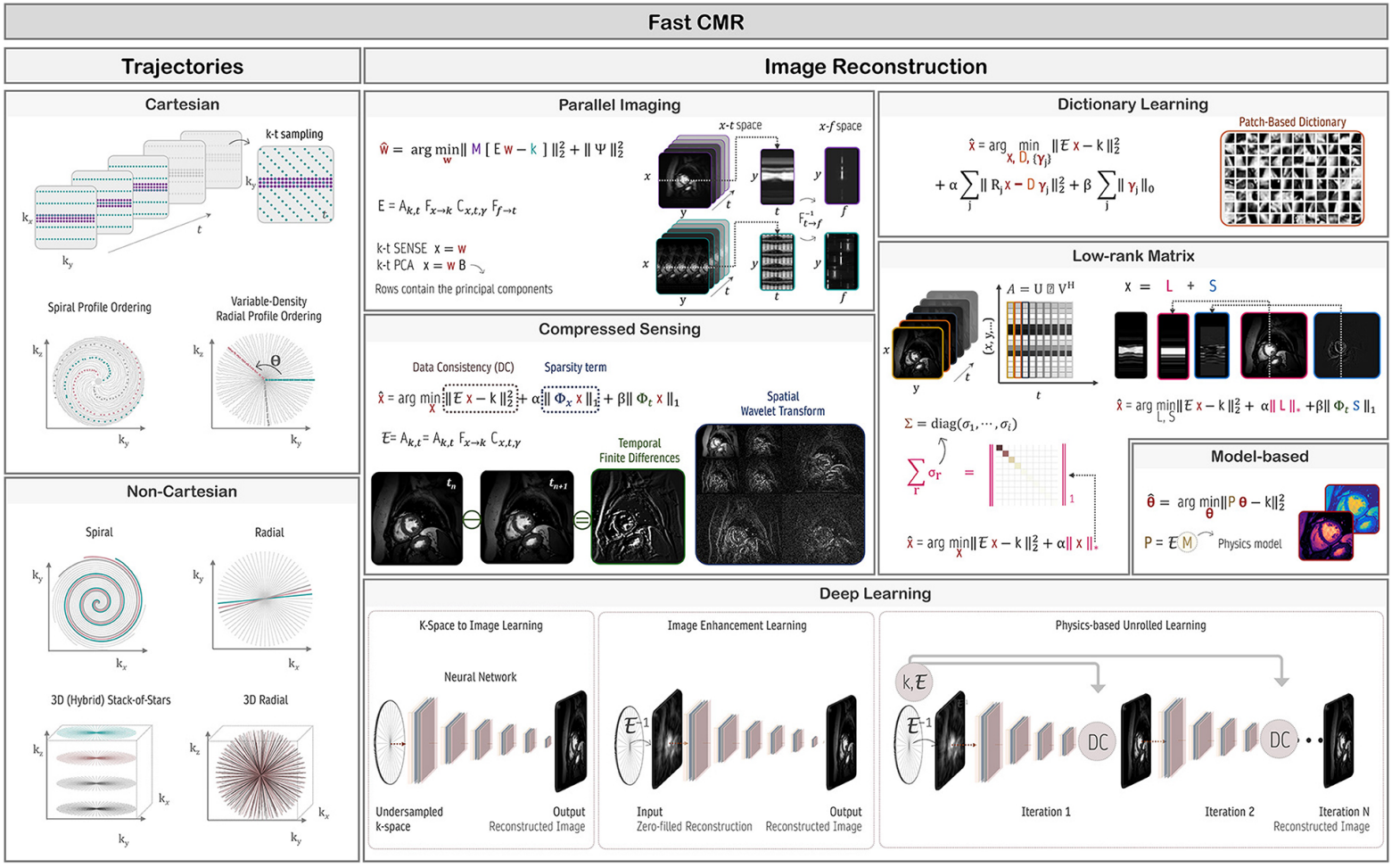
Fast CMR
Trajectories
Cartesian
k-t sampling
Spiral Profile Ordering
Variable-Density Radial Profile Ordering
Non-Cartesian
Spiral
Radial
3D (Hybrid) Stack-of-Stars
3D Radial
Image Reconstruction
Parallel Imaging
x-t space
x-f space
k-t SENSE x = w
k-t PCA x = w B
Rows contain the principal components
Compressed Sensing
Data Consistency (DC)
Sparsity term
Spatial Wavelet Transform
Temporal Finite Differences
Dictionary Learning
Patch-Based Dictionary
Low-rank Matrix
Model-based
Physics model
Deep Learning
K-Space to Image Learning
Neural Network
Undersampled k-space
Output Reconstructed Image
Image Enhancement Learning
Input Zero-filled Reconstruction
Output Reconstructed Image
Physics-based Unrolled Learning
DC
Iteration 1
Iteration 2
Iteration N
Reconstructed Image

Figure 3.10 : Fast cardiovascular MR techniques to enable high spatial and/or temporal resolved data acquisition. Cartesian or non-Cartesian undersampling trajectories (left column) can be used to accelerate acquisitions. Depending on the CMR application and acquired trajectory, various image reconstruction techniques (right column) like parallel imaging, compressed sensing, dictionary learning, low-rank, model-based, or more recently deep learning methods can be used. These reconstructions handle and exploit the spatial, temporal, and/or parametric dimensions. In CMR, the forward model, commonly given by k = Ex, maps the unknown (MR signal intensity) image series x to the k-space data k. The forward operator E contains the coil sensitivity maps C (enabling parallel imaging), Fourier operator F and sampling pattern A. If data are undersampled, dynamic images can be estimated using, for e.g., compressed sensing, by minimizing an objective function with a data consistency term (to enforce consistency between the measured data and model prediction) and a regularization term, with sparsifying transform Φ (e.g., spatial wavelet or total variation) and regularization parameter λ. Alternatively, a dictionary learning-based method can learn the sparsifying transform (dictionary, D), and reconstruct the image simultaneously from undersampled k-space data. The low-rank plus sparse (L + S) decomposition model enables the reconstruction of undersampled dynamic k-space data. In this case, the low-rank (L) component captures the temporally correlated background, and the sparse (S) component captures the dynamic information. Model-based reconstruction methods include the physics model in the forward model to directly estimate quantitative parameter maps from fully-sampled or undersampled k-space data.

performed with a variable-density incoherent spatiotemporal acquisition (VISTA) sampling [268].

Non-Cartesian sampling schemes may be preferred because they are less sensitive to motion [156, 184, 195, 201, 203, 204, 213, 231, 235, 242, 243, 256, 262, 269–279], due to a densely sampled low-frequency range and the repeated sampling of the k-space centre enables the extraction of motion signals (self-navigation). Unfortunately, non-Cartesian sampling requires resampling of the acquired data onto a Cartesian grid, which is computationally expensive.

Several Cartesian trajectories that acquire data using a radial or spiral-like pattern on a Cartesian grid have been proposed to overcome the computational complexity of non-Cartesian trajectories, such as Variable-Density sampling and Radial view ordering (VDRad) [216], CIRcular Cartesian UnderSampling (CIRCUS) [207], (Variable-Density) Cartesian acquisition with Spiral Profile ordering (VD-CASPR, CASPR) [233, 238, 280], GOlden-angle CArtesian Randomized Time-resolved (GOCART) [281], rotating Cartesian k-space (ROCK) [282], centric reordering [243] or Enhancing Sharpness by Partially Reduced Subsampling Set (ESPReSSo) [282, 283] sampling.

For 3D CMR imaging, non-Cartesian trajectories can be combined with Cartesian sampling, as in, for example, radial stack-of-stars [156, 207, 245, 284, 285] or stack-of-spiral [286] sampling schemes. Alternatively, 3D whole-heart CMR can be achieved using 3D Cartesian trajectories [199, 235, 241, 243], or 3D non-Cartesian sampling patterns, such as radial 'koosh-ball' [201, 214, 242] or spiral phyllotaxis [202, 213].

Moreover, acquisitions often use a golden-angle ordering scheme for which consecutive k-space spokes are incremented by the golden angle ($\theta \approx 111.25°$) [287, 288], to achieve nearly uniform k-space coverage (also optimal for retrospective binning) and incoherence along both spatial and temporal dimensions.

3.4.4. CMR reconstruction

The undersampled data requires appropriate reconstruction techniques to recover an aliasing-free image, as illustrated in Figure 3.10. The raw data is linked with the image via the forward model as stated in the equation from Sermesant et al. [59]. CS relies on non-linear reconstruction algorithms to reconstruct images from randomly (or pseudo-randomly) undersampled data [157]. In CS, the undersampling trajectory should lead to incoherent, noise-like aliasing artefacts which can be corrected for if images can be sparsely represented in a set transform domain (*e.g.* wavelets). In contrast to fixing the transform domain, dictionary learning techniques [289] seek to find the sparsest image representation by learning the sparsifying transform specific to each type of application. CS has the advantage that it does not require any training data and can achieve high accelerations. It can also be combined with parallel imaging methods [290, 291]. However, it depends on application specific hyperparameter optimization, and the iterative algorithms result in long reconstruction times.

Low-rank matrix completion methods have extended the idea of CS to matrices [210, 263]. These explore the global or local (patches) correlations within CMR images *e.g.* along the temporal or multi-contrast dimensions [148, 210, 211, 221, 263, 292–302]. For dynamic CMR, locally low-rank methods can act as an implicit motion compensation for any residual motion (after prior triggering/gating) [199, 209]. Some methods simultaneously enforce low-rank and sparsity constraints to separate the temporally correlated background and dynamic information in various CMR applications, such as dynamic contrast-enhanced CMR [263, 299, 302]. Moreover, low-rank tensor imaging has been proposed for multi-dimensional CMR imaging [201, 228, 230, 251, 252, 297, 303, 304]. These methods explore the spatio-temporal correlations in all dimensions (spatial, contrast, cardiac and respiratory motion) to generate multi-parameteric and motion-resolved CMR images, *e.g* cardiac- and respiratory-resolved T_1 and T_2 maps. In addition, motion can be handled implicitly in the low-rank decomposition instead of performing a prior motion gating.

Model-based reconstruction approaches have also been proposed to accelerate quantitative CMR imaging [275, 276, 305–308]. These methods incorporate the physics of the MR signal into the image reconstruction problem allowing for the direct reconstruction of quantitative

maps from the undersampled CMR data, bypassing the intermediate steps of image reconstruction and pixel-wise model fitting. Furthermore, in model-based reconstructions the underlying respiratory and cardiac motion model can be accounted for. Explicit motion compensation can be performed by mapping image data along the temporal direction with the underlying motion model extracted from image registration [219, 248, 249, 307].

Fast reconstruction is essential in a clinical setting. However, non-standard and iterative reconstruction methods often suffer from high computational demands, long computational times and require careful tuning of the algorithm (regularization) parameters. Recently, deep learning-based solutions have been proposed to address some of these shortcomings.

3.5. Challenges and Conclusions

The plethora of CMR sequences available and information offered makes the technique attractive, but also very challenging, particularly for a beginner. This review has provided an overview of the main CMR concepts and techniques, including recent technical advances, which should be useful for anyone wanting to improve, update, or maintain their knowledge and understanding of CMR. Ultimately, the dialogue between the scientific and clinical communities should improve if all users understand CMR terms and use a common language. This review has described the key physical principles underlying the most commonly used (quantitative) CMR sequences and preparation pulses and causes of common image artefacts. This review has explained how and why CMR can (and should) be used for diagnosis and guiding clinical decision making in a range of cardiovascular disease scenarios, such as ischemic heart disease, myocarditis, atrial fibrillation, valvular heart disease, vascular disease, congenital heart disease, and cardiac tumors. The challenges of CMR associated with acquisition time, SNR, spatial and temporal resolution, cardiac and respiratory motion have been discussed. In addition, popular and recently developed methods of suppressing and handling motion have been described. Finally, this review has explained how to speed up CMR scans by acquiring less data (than needed by conventional methods) using (pseudo-)random sampling trajectories and non-linear reconstruction algorithms, such as compressed sensing and low-rank completion, model-based or DL reconstruction approaches.

4

Robust cardiac $T_{1\rho}$ mapping at 3T using adiabatic spin-lock preparations

Chiara Coletti, Anastasia Fotaki, Joao Tourais, Yidong Zhao, Christal van de Steeg-Henzen, Mehmet Akçakaya, Qian Tao, Claudia Prieto, Sebastian Weingärtner

Magnetic Resonance in Medicine, Vol. 90.4 (2023): pp. 1363-1379,
doi: https://doi.org/10.1002/mrm.29713.

Abstract

Purpose To develop and optimize an adiabatic $T_{1\rho}$ ($T_{1\rho,\,\mathrm{adiab}}$) mapping method for robust quantification of spin-lock (SL) relaxation in the myocardium at 3T.

Methods Adiabatic SL (aSL) preparations were optimized for resilience against B_0 and B_1^+ inhomogeneities using Bloch simulations. Optimized B_0-aSL, Bal-aSL and B_1-aSL modules, each compensating for different inhomogeneities, were first validated in phantom and human calf. Myocardial $T_{1\rho}$ mapping was performed using a single breath-hold cardiac-triggered bSSFP-based sequence. Then, optimized $T_{1\rho,\,\mathrm{adiab}}$ preparations were compared to each other and to conventional SL-prepared $T_{1\rho}$ maps (RefSL) in phantoms to assess repeatability and in thirteen healthy subjects to investigate image quality, precision, reproducibility and inter-subject variability. Finally, aSL and RefSL sequences were tested on six patients with known or suspected cardiovascular disease and compared with LGE, T_1 and ECV mapping.

Results The highest $T_{1\rho,\,\mathrm{adiab}}$ preparation efficiency was obtained in simulations for modules comprising 2 HS pulses of 30ms each. In vivo $T_{1\rho,\,\mathrm{adiab}}$ maps yielded significantly higher quality than RefSL maps. Average myocardial $T_{1\rho,\,\mathrm{adiab}}$ values were 183.28±25.53ms, compared with 38.21±14.37ms RefSL-prepared $T_{1\rho}$. $T_{1\rho,\,\mathrm{adiab}}$ maps showed a significant improvement in precision (avg. 14.47±3.71% aSL, 37.61±19.42% RefSL, $p<0.01$) and reproducibility (avg. 4.64±2.18% aSL, 47.39±12.06% RefSL, $p<0.0001$), with decreased inter-subject variability (avg. 8.76±3.65% aSL, 51.90±15.27% RefSL, $p<0.0001$). Among aSL preparations, B_0-aSL achieved the highest inter-subject variability. In patients, B_1-aSL preparations showed the best artifact resilience among the adiabatic preparations. $T_{1\rho,\,\mathrm{adiab}}$ times show focal alteration colocalized with areas of hyperenhancement in the LGE images.

Conclusion Adiabatic preparations enable robust in vivo quantification of myocardial SL relaxation times at 3T.

4.1. Introduction

Cardiac MRI is the clinical gold standard for the assessment of scar and fibrosis in ischemic and non-ischemic heart diseases [111, 309–311]. Late gadolinium enhancement (LGE) imaging can be used to differentiate between scar and healthy myocardium based on retention of gadolinium-based contrast agents (GBCA) [312]. However, GBCAs injection is contraindicated in patients with severe renal impairment due to the risk of necrotic systemic fibrosis [8]. In addition, gadolinium retention in the brain after injection of GBCAs has been reported [9]. Thus, contrast-free alternatives are highly desired.

Quantitative myocardial tissue characterization has emerged with a wide spectrum of applications in various cardiomyopathies [313]. Native T_1 mapping has been explored for the assessment of myocardial infarction (MI) without the need for contrast agents [314–316]. However, mixed results have been reported on its sensitivity to focal scar and the approach remains the subject of ongoing research [317–319].

$T_{1\rho}$ mapping has been proposed as a promising non-contrast alternative for scar assessment, due to its increased sensitivity to slow molecular motion in the kilohertz range [320, 321]. First, Muthupillai et al. reported stronger post-contrast enhancement in acute MI cases for $T_{1\rho}$-weighted imaging compared with conventional T_1-weighted LGE imaging [322, 323]. More recently, quantitative $T_{1\rho}$ maps have demonstrated improved differentiation between infarcted and remote myocardium in swine models, compared with native T_1 and T_2 maps, yielding comparable contrast-to-noise ratio (CNR) to LGE images [87, 318, 324]. Similar results have been reported in mice [325–327] and monkeys [328]. In vivo $T_{1\rho}$ mapping has been successfully applied in patients with ischemic and non-ischemic cardiomyopathies at 1.5T [131, 329–333]. Implementing $T_{1\rho}$ mapping at 3T could further improve the diagnostic value of this approach, due to an increase in signal-to-noise ratio (SNR) and CNR, and the applicability in a growing number of 3T cardiac examinations. However, at 3T, only a few studies have been reported [334–336], highlighting limitations related to system imperfections and the specific absorption rate (SAR) at high field strengths.

Conventional $T_{1\rho}$ maps are obtained using spin-lock (SL) preparation pulses with various durations, which are most commonly based on continuous-wave RF irradiation. These preparations are inherently susceptible to B_0 and B_1^+ field inhomogeneities [337, 338]. To compensate for these inhomogeneities, continuous-wave SL pulses, in combination with refocusing pulses and phase cycling of SL modules, have been proposed [71, 337, 339].

An alternative strategy to achieve resilience against system imperfections is the use of adiabatic pulses [340]. The robustness of adiabatic pulses against field inhomogeneities has been studied in other 3T

cardiac MRI methods, such as inversion-recovery T_1 mapping [82] or refocusing in T_2 preparations [341]. Recently, similar adiabatic pulses have also been employed for refocusing in conventional SL preparations for cardiac $T_{1\rho}$ mapping [131] at 1.5T. Alternatively, SL preparations consisting of trains of adiabatic full passage (AFP) pulses have been proposed to generate $T_{1\rho}$ contrast in other anatomies [72, 73]. During the AFP frequency sweep, the magnetization is locked along the effective field. This induces $T_{1\rho,\,\mathrm{adiab}}$ as the dominant relaxation mechanism during the pulse application [342, 343]. $T_{1\rho,\,\mathrm{adiab}}$ will be used throughout the manuscript to indicate the rotating frame of reference relaxation constant measured by adiabatic preparations.

In this work, we sought to investigate the use of fully adiabatic SL (aSL) preparations for $T_{1\rho,\,\mathrm{adiab}}$ mapping of the myocardium at 3T. Bloch simulations were performed to optimize aSL pulse shapes for resilience against system imperfections. Phantom and in vivo imaging of the calf muscle were then carried out to compare aSL preparations against fully compensated conventional SL preparations. In vivo performance was shown with cardiac mapping in healthy subjects. Finally, clinical feasibility was evaluated in a small proof-of-principle cohort of patients.

4.2. Methods

4.2.1. Adiabatic spin-lock preparation design

In this work, adiabatic SL (aSL) preparations were based on a train of AFP pulses with an identical duration (Figure 4.1B). An even number of pulses was used to ensure that, at the end of the preparation ($t = \tau_{\mathrm{SL}}$), the magnetization $M(\tau_{SL})$ was stored along the $+z$ direction. Hyperbolic secant (HS) pulse shapes were employed, as commonly used in other imaging applications [73, 82, 341, 344, 345]. These are characterized by the following amplitude and frequency modulation functions:

$$B_1(t) = B_1^{\max} \cdot sech\left(\beta\left(\frac{2t}{\tau_{HS}} - 1\right)\right), \tag{4.1}$$

$$\Delta\omega_1(t) = \omega_1(t) - \omega_0 = 2f_{max} \cdot \tanh\left(\beta\left(\frac{2t}{\tau_{HS}} - 1\right)\right). \tag{4.2}$$

Here $B_1(t)$ represents the pulse amplitude, B_1^{max} the peak amplitude, and β a constant that characterizes the width of the pulse bell. The single HS pulse duration is indicated by τ_{HS}. $\Delta\omega_1(t)$ is the frequency modulation with respect to the Larmor frequency ω_0, $2f_{\max}$ is the amplitude of the frequency sweep, and $\Delta\omega_1(t) = d\Phi_1(t)/dt$, where $\Phi_1(t)$ represents the pulse phase as a function of time. The polarity of the frequency sweep was alternated between consecutive HS pulses to compensate for residual pulse imperfections.

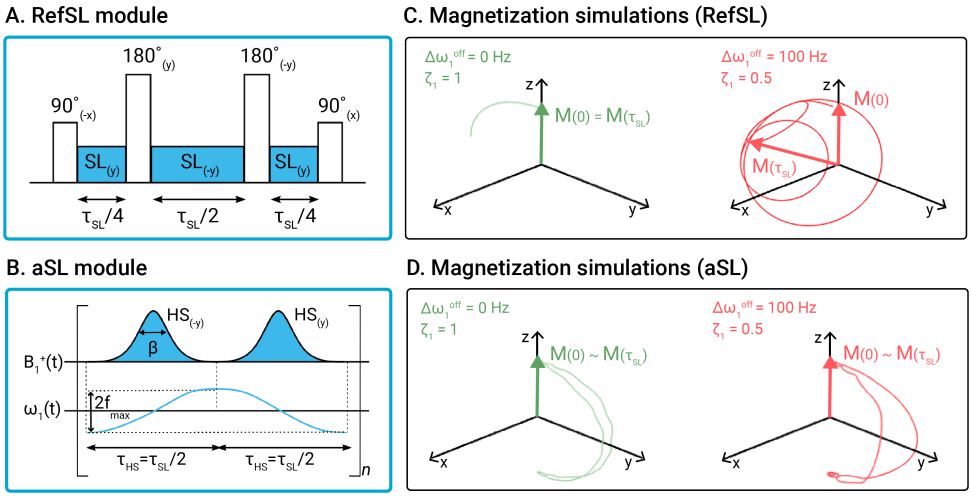

Figure 4.1 : (A) Conventional SL pulse (RefSL) and (B) adiabatic SL pulse (aSL), with corresponding amplitude and frequency modulation functions. Magnetization trajectories for the RefSL (C) and aSL (D) modules, simulated under ideal conditions (off-resonance $\Delta\omega_1^{off} = 0$ Hz, relative B_1^+ $\zeta_1 = 1$) and in presence of moderate B_0 and B_1^+ inhomogeneities ($\Delta\omega_1^{off} = 100$ Hz, $\zeta_1 = 0.5$). The parameters used for aSL were: τ_{HS} = 30 ms, β = 5.5, f_{max} = 350 Hz, $B_1^{max} = 13.5$ μT. Major deviations from the idealized case are observed for the RefSL preparation in the presence of inhomogeneities, while the aSL preparation produces similar results in both cases.

Preparations with variable SL durations were achieved by concatenating identical pulse modules multiple times. The total duration of a single aSL module (τ_{SL}) was fixed to 60 ms. This value was chosen as a trade-off between adequate sampling of the expected range of in vivo $T_{1\rho,\,adiab}$ times and restrictions imposed by the SAR limits (whole-body SAR < 2.0 W/kg) and the RF amplifier chain. To obtain constant preparation times, when changing the pulse duration (τ_{HS}), modules containing 2, 4 or 8 HS pulses (2HS-aSL, 4HS-aSL, 8HS-aSL) with relative pulse duration τ_{SL}, $\tau_{SL}/2$, and $\tau_{SL}/4$, were implemented. For SL modules with 4 and 8 HS pulses, phase cycling was adopted between pairs of HS pulses to achieve a full Malcolm-Levitt (MLEV) scheme compensation [65].

Bloch simulations

Bloch simulations were used to optimize β, f_{max} and τ_{HS} in the aSL preparations. All simulations were performed in MATLAB (MathWorks, Natick, USA).

The preparation efficiency was determined as $M_z(\tau_{SL})/M(0)$ and used as a metric to optimize the design of the aSL module. The aSL preparation modules were simulated using the maximum RF pulse

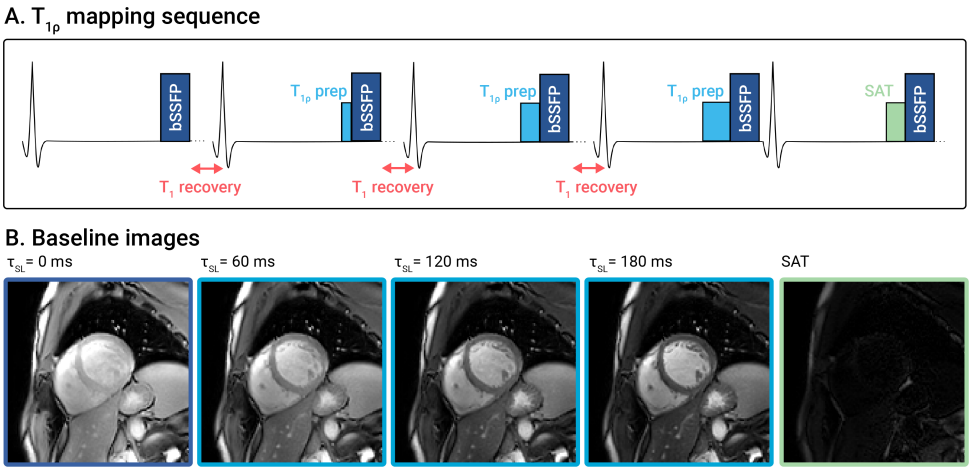

Figure 4.2 : (A) $T_{1\rho}$ mapping sequence diagram with (B) corresponding baseline images from a representative healthy subject. Five images are acquired, one without preparation, three with different $T_{1\rho,\,adiab}$ preparations (τ_{SL} = 60, 120, 180ms), and one with saturation preparation, to allow for accurate mapping of the induced $T_{1\rho}$ relaxation.

power, within the limits imposed by the peak B_1^+ (B_1^{max} = 13.5 μT) and SAR (whole-body SAR < 2.0 W/kg). The preparation efficiency was averaged over a design window covering the expected range of in vivo off-resonances ($\Delta\omega_1^{off} \in \{-150, -149, \ldots + 150\}$ Hz) and B_1^+ inhomogeneities ($\zeta_1 \in \{0.50, 0.49, \ldots 1.00\}$) [82, 346–348], where ζ_1 indicates the ratio between the effective and nominal B_1^+ power.

Two sets of optimizations were performed to identify the optimal pulse duration and amplitude/frequency modulation functions, respectively. First, the 2HS-aSL, 4HS-aSL, and 8HS-aSL modules were compared in terms of preparation efficiency. Then, the module that produced the highest preparation efficiency was selected to derive the optimal values of β and f_{max}. Bloch simulations covering the range of expected in vivo variability of B_0 and B_1^+ were performed to obtain optimized pulses for three design regions: 1) original balanced design region (Bal-aSL) ($\Delta\omega_1^{off} \in \{-150, -149, \ldots + 150\}$ Hz, $\zeta_1 \in \{0.50, 0.49, \ldots 1.00\}$); 2) B_0-skewed (B_0-aSL) ($\Delta\omega_1^{off} \in \{-200, -199, \ldots + 200\}$ Hz, $\zeta_1 \in \{0.75, 0.76, \ldots 1.00\}$); 3) B_1^+-skewed design regions (B_1-aSL) ($\Delta\omega_1^{off} \in \{-100, -99, \ldots + 100\}$ Hz, $\zeta_1 \in \{0.25, 0.26, \ldots 1.00\}$).

Pulse design validation

Phantom data were acquired to validate the simulation results. The preparation efficiency of three optimized SL modules B_0-aSL, Bal-aSL, and B_1-aSL was tested on the phantom by modifying the center

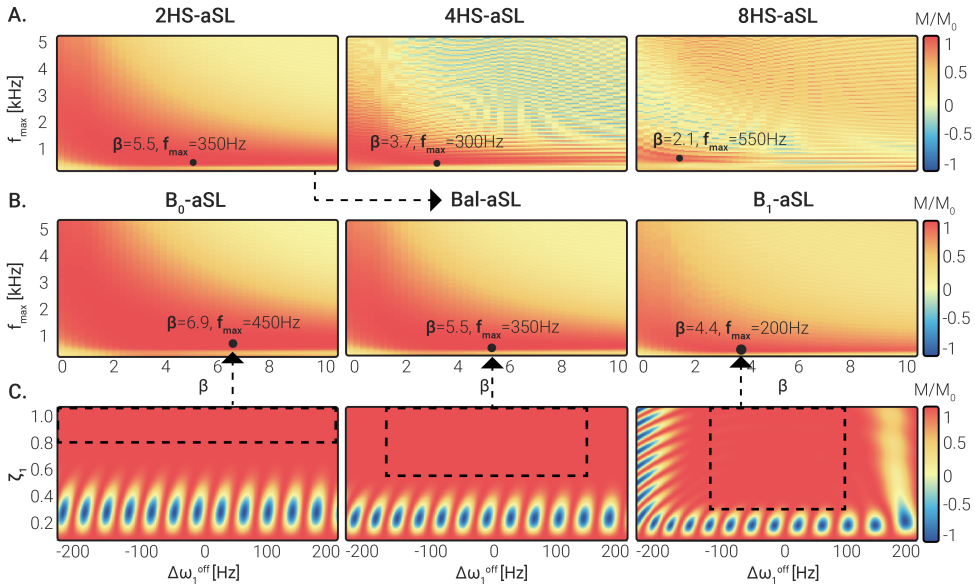

Figure 4.3 : (A) Simulated preparation efficiency for 2HS-aSL, 4HS-aSL and 8HS-aSL preparations, obtained by concatenating 2 ($\tau_{HS} = 30$ ms), 4 ($\tau_{HS} = 15$ ms), or 8 ($\tau_{HS} = 7.5$ ms) HS pulses, respectively. M_z/M_0 was averaged over a design window covering $\Delta\omega_1^{\text{off}} \in \{-150, -149, \ldots + 150\}$Hz and $\zeta_1 \in \{0.50, 0.49, \ldots 1.00\}$. Combinations of β and f_{max} yielding the highest efficiency are indicated for each module by a black dot. (B) Simulated preparation efficiency for 2HS-aSL, using three different design regions: B_0-aSL, Bal-aSL and B_1-aSL. Black dots mark the combination of β and f_{max} yielding the highest preparation efficiency. The highest efficiency was obtained for low f_{max} amplitudes and intermediate β. (C) Simulated preparation efficiency obtained for the optimal β and f_{max} combination identified in (B) for various $\Delta\omega_1^{\text{off}}$ and ζ_1. Dashed black boxes represent the design region considered for each pulse in (B).

frequency $\Delta\omega_1^{\text{off}} \in \{-200, -180, \ldots + 200\}$ Hz and scaling the pulse power by $\zeta_1 \in \{0.1, 0.2, \ldots 1.0\}$. A single bottle phantom (Spectrasyn 4 polyalphaolefin, ExxonMobil Chemical) was used for the experiments.

The same experiments were performed in vivo in the calf muscle of a healthy subject (21 y.o.) to validate simulations and phantom experiments for the three aSL preparations. Here, B_0 and B_1^+ inhomogeneities were varied in fewer steps ($\Delta\omega_1^{\text{off}} \in \{-200, -150, \ldots + 200\}$ Hz, $\zeta_1 \in \{0.2, 0.4, \ldots 1.0\}$).

For each SL module, $\Delta\omega_1^{\text{off}}$ and ζ_1, two snap-shot balanced steady-state free-precession (bSSFP) images were acquired: one preceded by the aSL preparation (τ_{SL} = 60ms) and one with no preparation. The two scans were interleaved by a 5s pause to allow longitudinal magnetization recovery. Low imaging resolution was used (10×10×10 mm^3), with TR = 1.9ms, TE = 0.72ms, flip angle = 90°and a SENSE factor of 2. The preparation efficiency $M_z(\tau_{SL})/M(0)$ was then calculated as the ratio

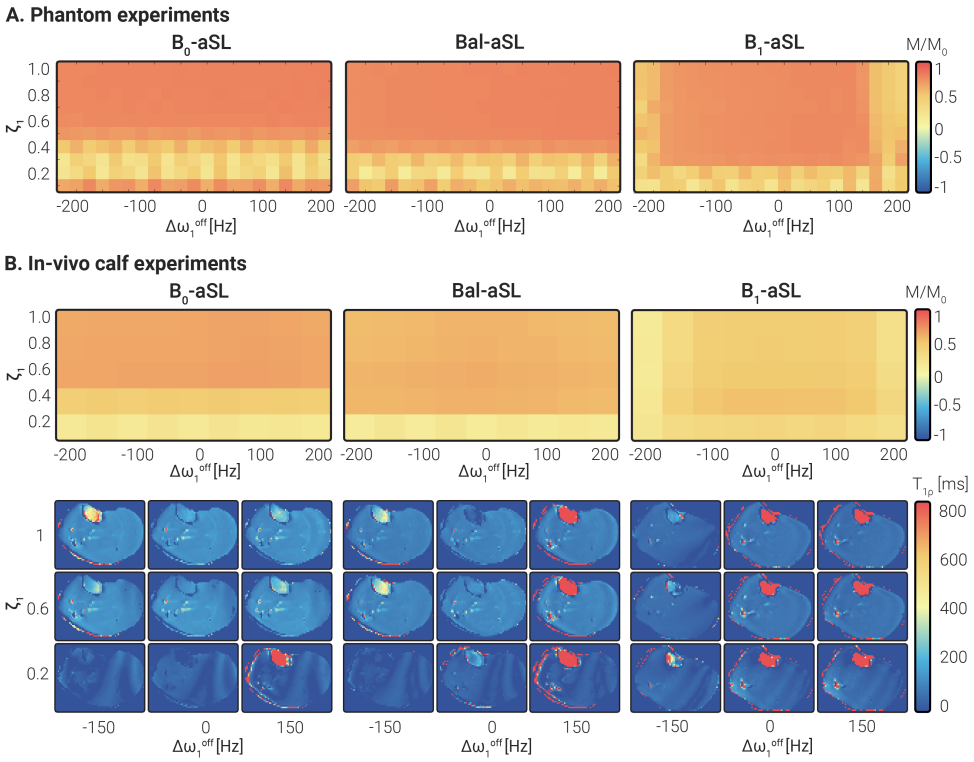

Figure 4.4 : (A) Experimental preparation efficiency measured in phantoms for a range of $\Delta\omega_1^{off}$ and ζ_1 with three aSL preparations. Experimental results were in agreement with simulations in Figure 4.3C, minus a scaling factor given by relaxation, which was ignored in simulations. (B) Adiabatic preparations efficiency was measured in vivo on a healthy subject's calf muscle for the same range of $\Delta\omega_1^{off}$ and ζ_1. Overall, the results were in good agreement with the phantom experiments (A) and the numerical simulations (Figure 4.3C). Representative calf $T_{1\rho,\,adiab}$ maps for different values of $\Delta\omega_1^{off}$ and ζ_1 illustrate the variation in image artifacts.

of the two magnitude images. Signal polarity was restored using the corresponding phase images prior to further processing. In phantoms, the entire phantom area was evaluated for each vial, while in the calf, manually drawn circular regions-of-interest (ROIs) were used.

4.2.2. $T_{1\rho}$ mapping

The proposed $T_{1\rho,\,adiab}$ mapping approaches were compared to each other and to a conventional, continuous-wave $T_{1\rho}$ mapping implementation in phantom and through in vivo experiments in the calf muscle and the myocardium in healthy subjects and patients. Phantoms and healthy subjects were scanned on a 3T Ingenia system (Philips, Best, The Netherlands). Patient data was acquired on a 3T Achieva system (Philips,

Best, The Netherlands). In vivo imaging was ethically approved by the competent review authorities (METC NL73381.078.20, UK National Research Ethics Service 15/NS/0030). Written informed consent has been obtained prior to all imaging sessions according to institutional guidelines.

The aSL preparations were compared to a fully balanced non-adiabatic SL pulse [71] (RefSL in Figure 4.1A). Three phase-cycled SL blocks with equal amplitude and durations of $\tau_{SL}/4$, $\tau_{SL}/2$, and $\tau_{SL}/4$, respectively, were played. The SL amplitude was chosen based on the RF amplifier constraints as $\gamma B_1^+ = 300$ Hz.

$T_{1\rho}$ and $T_{1\rho,\,\mathrm{adiab}}$ mapping was performed using a cardiac triggered breath-hold sequence (Figure 4.2). Five baseline single-shot bSSFP images were acquired: the first with no SL preparation, then three with increasing SL durations, and finally a saturation-prepared image used to approximate infinite SL length [349]. A composite "Water suppression Enhanced through T1-effects" (WET) pulse was used to achieve robust saturation in the presence of field inhomogeneities [350]. Total preparation durations were $\tau_{\mathrm{SL}} = 0, 60, 120, 180$ ms for aSL modules. Shorter preparations were employed for RefSL ($\tau_{\mathrm{SL}} = 0, 12, 24, 36$ ms) to account for higher SAR levels, heavier RF amplifier load, and significantly shorter non-adiabatic $T_{1\rho}$ times. Scans were acquired in the end-diastolic phase. All images, except the saturation-prepared image, were preceded by a pause to allow for longitudinal magnetization recovery. Other imaging parameters were: in-plane resolution = $2\times2\mathrm{mm}^2$, FOV = $220\times220\mathrm{mm}^2$, slice thickness = 8mm, TE/TR = 1.2/2.4 ms, flip angle = 70°, SENSE = 2.

$T_{1\rho}$ and $T_{1\rho,\,\mathrm{adiab}}$ maps were reconstructed in MATLAB using the following three-parameter model [349], to account for the effect of the imaging pulses:

$$S(t) = A \cdot e^{-\frac{t}{T_{1\rho(,\,adiab)}}} + B. \tag{4.3}$$

Phantom and in-vivo calf experiments

The T1MES phantom was used for phantom experiments to mimic blood and myocardium relaxation times at 3T [351]. Approximate T_1 and T_2 times of the phantom vials were estimated, using a MOLLI sequence for T_1 [81] and a Gradient Spin Echo (GraSE) sequence for T_2 [352]. To study repeatability, ten repetitions of $T_{1\rho}$ and $T_{1\rho,\,\mathrm{adiab}}$ mapping scans were acquired for each preparation (B_0-aSL, Bal-aSL, B_1-aSL and RefSL). Manually drawn circular ROIs were used to extract $T_{1\rho}$ and $T_{1\rho,\,\mathrm{adiab}}$ values for further processing. Repeatability was assessed using the coefficient of variability ($\overline{CV}$):

$$\overline{CV} = \sum_{i=1}^{N_v} \frac{\overline{wCV_i}}{N_v} \tag{4.4}$$

where N_v is the number of samples, corresponding to the number of vials in this case, and $\overline{wCV_i}$ is the coefficient of variability within the sample computed for every vial as:

$$\overline{wCV_i} = \frac{1}{R}\sum_{r=1}^{R}\frac{\sqrt{(\mu_{i,r}-\overline{\mu_i})^2}}{\overline{\mu_i}}. \tag{4.5}$$

Here, R = 10 represents the number of repetitions, $\mu_{i,r}$ is the average $T_{1\rho}$ or $T_{1\rho,\,\mathrm{adiab}}$ value for each vial i and repetition r and $\overline{\mu_i}$ is the average $T_{1\rho}$ or $T_{1\rho,\,\mathrm{adiab}}$ value for each vial across all repetitions.

In a second experiment, $T_{1\rho,\,\mathrm{adiab}}$ time was assessed as a function of the HS shape parameter β by acquiring phantom and calf $T_{1\rho,\,\mathrm{adiab}}$ maps for $\beta \in 1, 2, \ldots 10$. For each β, a constant sweep amplitude $f_{\max}$ value was acquired. The dependence between the parameter β and the measured $T_{1\rho,\,\mathrm{adiab}}$ values was tested using linear regression. R^2 coefficient, slope and intercept values were reported for a single exemplary vial and a manually drawn circular calf ROI.

Healthy subjects experiments

The proposed aSL preparations were tested in 6 healthy subjects (4 males, 2 females, 21.5±1.9 y.o.). For each subject, B_0-aSL, Bal-aSL, and B_1-aSL $T_{1\rho,\,\mathrm{adiab}}$ maps were acquired in three short-axis (SAX) slices (basal, mid, and apical) and a four-chamber (4ch) view. To assess reproducibility, the twelve maps were re-acquired following the repositioning of the subject [353]. In this cohort of healthy subjects, the magnetization recovery pause was 2.5s to limit the total scan time to 13s.

In a second cohort of 7 healthy subjects (5 males, 2 females, 24.7±2.5 y.o.), the best-performing aSL preparation was compared to RefSL. Similarly to the first cohort, three SAX slices and a 4ch view were acquired for each subject and preparation. Here, a magnetization recovery pause of 3.5s was employed to avoid relaxation time over-estimation (see Supporting Information Figure 4.S1). To assess robustness to B_0 and B_1^+ inhomogeneities, a second repetition of each map was acquired by moving the shimming volume only on the right ventricle, while keeping the position of the patient fixed.

The myocardium was automatically segmented using the nnU-Net framework [354] with uncertainty estimation [355]. Segmentation maps with predictive confidence below 75% were discarded and the segmentation was performed manually. The average values of $T_{1\rho}$ or $T_{1\rho,\,\mathrm{adiab}}$ and their corresponding standard deviation values (std) in the segmented myocardium were extracted according to the AHA 16 segment model. A group-wise ANOVA test followed by paired t-tests were used to assess statistical differences between the $T_{1\rho}$ and $T_{1\rho,\,\mathrm{adiab}}$ times with different preparations.

$T_{1\rho}$ and $T_{1\rho,\,\text{adiab}}$ quantification precision was assessed for each myocardial segment and SL module through the within-subject coefficient of variability (wCV):

$$wCV_{r,i} = \frac{\sqrt{\sigma_{r,i}^2}}{\mu_{r,i}} \tag{4.6}$$

computed for every repetition r and subject i, where μ and σ are the $T_{1\rho}$ or $T_{1\rho,\,\text{adiab}}$ mean and std, respectively. Then, the mean and std of $T_{1\rho}$ or $T_{1\rho,\,\text{adiab}}$ values across repetitions were computed as:

$$\bar{\mu}_i = \sum_{r=1}^{R} \frac{\mu_{r,i}}{R}, \quad \bar{\sigma}_i = \frac{1}{R}\sqrt{\sum_{r=1}^{R}(\mu_{r,i} - \bar{\mu}_i)^2} \tag{4.7}$$

and, therefore, the reproducibility as:

$$\overline{wCV}_i = \bar{\sigma}_i / \bar{\mu}_i, \tag{4.8}$$

where R=2 indicates the number of repetitions. Finally, the inter-subject variability was computed as a summary of the deviation of each subject's average $T_{1\rho}$ or $T_{1\rho,\,\text{adiab}}$ value from the overall mean:

$$\overline{CV} = \bar{\bar{\sigma}} / \bar{\bar{\mu}}, \tag{4.9}$$

where

$$\bar{\bar{\mu}} = \sum_{i=1}^{N} \frac{\bar{\mu}}{N_s}, \quad \bar{\bar{\sigma}} = \frac{1}{N_s}\sqrt{\sum_{i=1}^{N_s}(\bar{\mu}_i - \bar{\bar{\mu}})^2} \tag{4.10}$$

and N_s indicates the number of subjects. Statistical differences between the different SL preparations in terms of precision and reproducibility were investigated using a group-wise Kruskal-Wallis test and subsequently right-tailed pair-wise Mann-Whitney U-tests.

Patients experiments

Clinical feasibility was tested in a small proof-of-principle cohort of 6 patients (2 males, 4 females, 50.2±11.0 y.o.) referred to clinical CMR. All patients were imaged using standard clinical protocols, including MOLLI-based native T_1 mapping, LGE imaging and CINE scans. LGE imaging was performed 10-15 minutes after injection of 0.15 mmol/kg of Gadobutrol (Gadovist, Bayer Schering, Berlin, Germany). Extracellular volume (ECV) maps were estimated from native and post-contrast T_1 values. Synthetic haematocrit values were computed for each patient as Hct = $0.88 - (T_{1,blood}/3240)$ [356]. The proposed $T_{1\rho,\,\text{adiab}}$ mapping sequence and conventional $T_{1\rho}$ mapping of a single mid-ventricular SAX slice were included in the scan protocol prior to contrast administration.

Imaging parameters were chosen to closely match those used in the healthy subjects. PCA-based group-wise registration was used to mitigate residual cardiac and respiratory motion for baseline $T_{1\rho,\,\mathrm{adiab}}$ and $T_{1\rho}$ images [357]. T_1 and $T_{1\rho(,\,\mathrm{adiab})}$ baseline images were spatially co-registered to the corresponding LGE images applying a PCA-based group-wise method to the baseline images [357]. Finally, the resulting deformation matrices were transferred to the previously reconstructed maps. Manually drawn ROIs were defined on LGE images and then superimposed on the co-registered quantitative maps to extract scar and remote T_1, ECV, $T_{1\rho}$, and $T_{1\rho,\,\mathrm{adiab}}$ times.

4.3. Results

4.3.1. Bloch simulations results

The simulated preparation efficiency achieved with the 2HS-aSL, 4HS-aSL and 8HS-aSL preparations is shown in Figure 4.3A. For all three modules, the highest preparation efficiency was obtained for low to intermediate frequency sweep amplitudes and showed an inversely proportional relationship with the parameter β. However, very low values of β required a reduction of the pulse peak power to satisfy SAR limitations. In all three cases, the optimal region is well defined and separated from the non-adiabatic region at high sweep velocities (top-right corner). Overall, 2HS-aSL shows higher overall preparation efficiency than 4HS-aSL and 8HS-aSL. The 2HS-aSL module also presents a larger optimal region, indicating higher stability to the choice of parameters. Optimal values of $\{\beta, f_{\mathrm{max}}\}$ were chosen as $\{5.5, 350$ Hz $\}$ for 2HS-aSL, $\{3.7, 300$ Hz $\}$ for 4HS-aSL and $\{2.1, 550$ Hz $\}$ for 8HS-aSL, resulting in an average efficiency M_z/M_0 of 0.98 and 0.92 and 0.88 respectively. Hence, the 2HS-aSL configuration, consisting of 2 HS pulses of 30ms each, was selected for further investigation.

Simulation results for 2HS-aSL preparation with three different design regions are shown in Figure 4.3B. For B_0-aSL and B_1-aSL, similar patterns to the previously analyzed Bal-aSL case (Figure 4.3A) can be observed, with an inversely proportional relationship with the parameter β. The optimal region becomes narrower when using a more B_1^+ compensated preparation, with overall decreasing optimal values β and f_{max}. Optimal values of $\{\beta, f_{\mathrm{max}}\}$ were identified as $\{6.9, 450$ Hz $\}$ for B_0-aSL and $\{4.4, 200$ Hz $\}$ for B_1-aSL, yielding an average efficiency M_z/M_0 of 0.99 and 0.94 respectively. A summary of the parameters used for the optimized aSL preparations can be found in Table 4.1.

Figure 4.3C illustrates how the preparation efficiency $M_z(\tau_{SL})/M(0)$ varies over a range of off-resonant frequencies and B_1^+ inhomogeneities for the optimized B_0-aSL, Bal-aSL and B_1-aSL modules according to Bloch simulations. The corresponding design region used for the parameter optimization of each preparation is marked by the dashed rectangle.

Table 4.1 : Adiabatic spin-lock preparations design parameters

	Pulse shape			
Module	β	f_{max} [Hz]	τ_{HS} [ms]	B_1^{max} [μT]
8HS-aSL	2.1	550	7.5	13.5
4HS-aSL	3.7	300	15	13.5
B_0-aSL (2HS-aSL)	6.9	450	30	13.5
Bal-aSL (2HS-aSL)	5.5	350	30	13.5
B_1-aSL (2HS-aSL)	4.4	200	30	13.5

	Design region		*Performance*	
Module	ω_1^{off} [Hz]	ζ_1	**SAR [W/kg]**	**Efficiency**†
8HS-aSL	-150, ... +150	0.5, ... 1.0	<1.2	0.88
4HS-aSL	-150, ... +150	0.5, ... 1.0	<1.1	0.92
B_0-aSL	-200, ... +200	0.75, ... 1.0	<1.0	0.99
Bal-aSL	-150, ... +150	0.5, ... 1.0	<1.0	0.98
B_1-aSL	-100, ... +100	0.25, ... 1.0	<1.1	0.94

For all three aSL modules, the regions characterized by low preparation efficiency (in blue) are outside the design region.

4.3.2. Phantom and in vivo calf experiments

The experimental preparation efficiency measured in the phantom experiments with varying $\Delta\omega_1^{off}$ and ζ_1 conditions is depicted in Figure 4.4A. Good agreement between the simulated and experimental results can be observed. Broad areas of lower preparation efficiency are present for intermediate to low ζ_1 values with B_0-aSL, low to very-low ζ_1 values with Bal-aSL, and very low ζ_1 as well as high absolute $\Delta\omega_1^{off}$ values with B_1-aSL.

The results of preparation efficiency obtained in vivo in the calf muscle of a healthy subject are shown in Figure 4.4B. These results are in good agreement with both simulations and phantom data. In vivo preparation efficiency is compromised for $\zeta_1 < 0.6$ with the B_0-aSL module, while no substantial degradation was observed over the entire off-resonance range studied. On the opposite side, B_1-aSL yields robust preparation efficiency for ζ_1 values down to 0.2, but lower efficiency for $|\Delta\omega_1^{off}|$ >150Hz. The overall efficiency score measured in the phantom and calf experiments is lower than in simulations, as no relaxation contributions have been simulated.

Complete $T_{1\rho}$ and $T_{1\rho,\,adiab}$ mapping results for the T1MES phantom

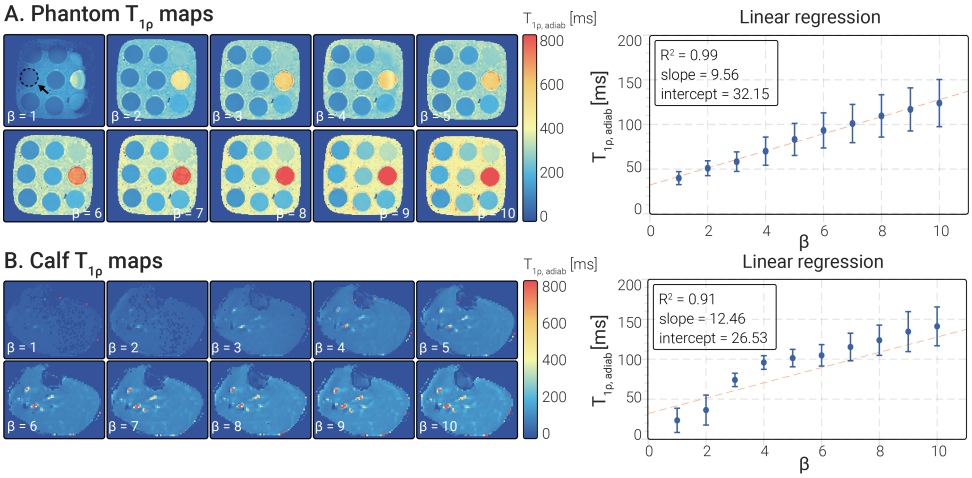

Figure 4.5 : (A) Phantom and (B) calf $T_{1\rho,\,\mathrm{adiab}}$ maps were obtained for various β and constant $f_{\max} = 350$ Hz. Linear regression analysis results showed that both phantoms and calf present a linear relationship between the pulse β and the measured $T_{1\rho,\,\mathrm{adiab}}$ values.

can be found in Supporting Information Figure 4.S2. Improved repeatability was observed ($p < 0.05$) in $T_{1\rho,\,\mathrm{adiab}}$ maps ($\overline{wCV_i} = 0.29 \pm 0.15$ for B_0-aSL, $p < 0.01$; $\overline{wCV_i} = 0.23 \pm 0.13$ for Bal-aSL, $p < 0.01$; $\overline{wCV_i} = 0.21 \pm 0.11$ for B_1-aSL, $p < 0.001$) with respect to conventional $T_{1\rho}$ maps ($\overline{wCV_i} = 1.30 \pm 1.34$ for RefSL).

In Figure 4.5, examples of phantom and calf $T_{1\rho,\,\mathrm{adiab}}$ maps acquired with different β values are displayed. $T_{1\rho,\,\mathrm{adiab}}$ values increase with an approximately linear trend for higher β in both cases ($R^2 = 0.99$, slope = 9.56, intercept = 32.15 for phantom, $R^2 = 0.91$, slope = 12.46, intercept = 26.53 for the calf). A higher deviation from linearity was observed in the calf values for $\beta \in 3, 4, 5$.

4.3.3. Healthy subjects experiments

Figure 4.6A shows mid-ventricular SAX and 4ch $T_{1\rho,\,\mathrm{adiab}}$ maps for one representative subject, displaying overall strong myocardium-to-blood contrast. No major off-resonance or B_1^+ artifacts are visually apparent on the $T_{1\rho,\,\mathrm{adiab}}$ maps. In agreement with phantom and calf results, myocardial $T_{1\rho,\,\mathrm{adiab}}$ values obtained with the B_0-aSL preparation (β=6.9) are higher than those obtained with the Bal-aSL preparation (β=5.5), which in turn are higher than those obtained with B_1-aSL preparations (β=4.4). Myocardial $T_{1\rho,\,\mathrm{adiab}}$ values averaged over slices, segments, and subjects were 194.22±24.54 ms, 155.59±18.09 ms, and 87.48±11.55 ms for B_0-aSL, Bal-aSL, and B_1-aSL, respectively.

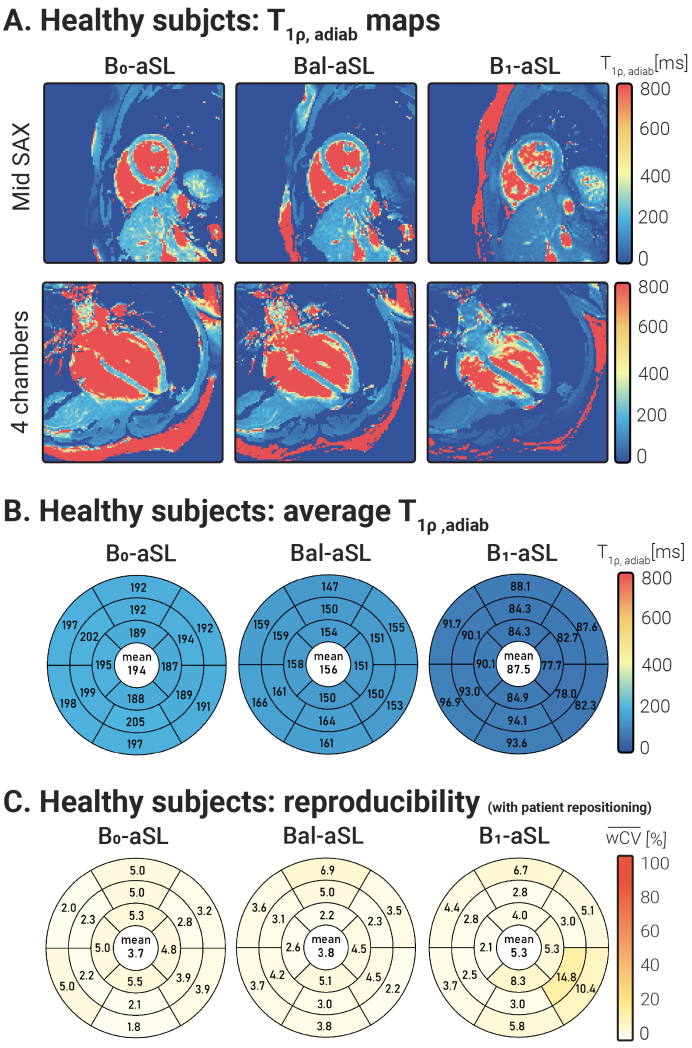

Figure 4.6 : (A) Mid SAX and 4ch $T_{1\rho,\,\text{adiab}}$ maps obtained with B_0-aSL, Bal-aSL, and B_1-aSL preparations in a representative healthy subject of the first cohort. $T_{1\rho,\,\text{adiab}}$ maps achieved good visual map quality, with a homogeneous myocardium and clear delineation against the blood pool across all acquired slices. (B) Bullseye plots showing the $T_{1\rho,\,\text{adiab}}$ values, averaged over all subjects and repetitions, for 16 AHA myocardial segments. $T_{1\rho,\,\text{adiab}}$ values are homogeneous across the 16 segments for all preparations. Average $T_{1\rho,\,\text{adiab}}$ increase with increasing beta β. (C) Bullseye plots report the average reproducibility ($\overline{wCV}$) coefficients, measured over 2 acquisitions interleaved by subject repositioning, for aSL-prepared maps in 16 AHA myocardial segments. Global average values are reported at the center of each bullseye plot. A mild improvement in reproducibility is observed for B_0-aSL and Bal-aSL preparations, compared to B_1-aSL, but the difference was not statistically significant ($p > 0.05$).

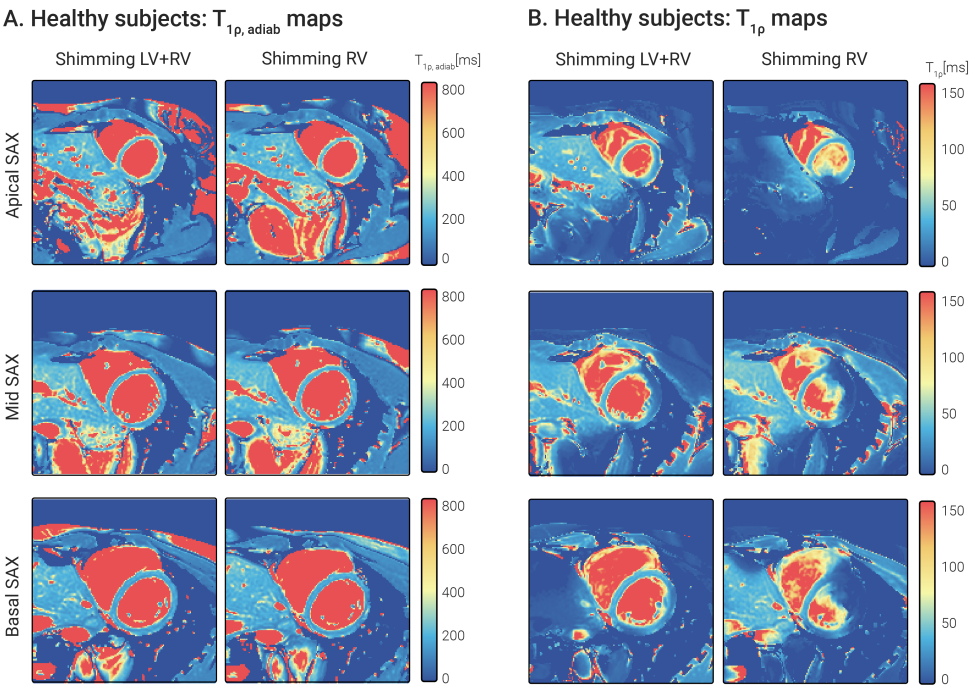

Figure 4.7 : Apical, mid, and basal SAX (A) B_0-aSL-prepared $T_{1\rho, adiab}$ maps and (B) RefSL-prepared $T_{1\rho}$ maps in a representative healthy subject. Two repetitions of each slice and preparation were acquired with different shim volumes: one covering the entire heart, the other covering only the right ventricle. $T_{1\rho, adiab}$ maps retain comparable map quality across repetitions with a nearly identical visual appearance of the maps. RefSL maps depict significant artifacts degrading the map quality in the myocardium, particularly in the second repetition.

The bullseye plots in Figure 4.6B show that the inter-subject average $T_{1\rho, adiab}$ values for all three aSL preparations are homogeneous across all segments. Bal-aSL and B_1-aSL bullseye plots depict lower $T_{1\rho, adiab}$ values in the apical slice (apical vs. basal slice: -2.64%, $p < 0.001$ for Bal-aSL, -6.62%, $p < 0.001$ for B_1-aSL) but not for B_0-aSL (-0.97%, $p = 0.12$).

Figure 4.6C depicts good reproducibility across the 16 AHA segments for all aSL preparations. Trends of improved precision and reproducibility were observed for B_0-aSL compared with B_1-aSL, but the differences were not significant ($p > 0.08$). However, B_0-aSL yielded significantly lower inter-subject variability than B_1-aSL ($p < 0.05$).

B_0-aSL $T_{1\rho, adiab}$ and RefSL $T_{1\rho}$ maps obtained in two repetitions under different shimming conditions for a representative subject are shown in Figure 4.7. RefSL preparations yield lower $T_{1\rho}$ values than B_0-aSL (average $T_{1\rho}$ over subjects, slices and segments = 38.21±14.37 ms for RefSL, compared with 183.28±25.53 ms for B_0-aSL,

Figure 4.8A). RefSL-based $T_{1\rho}$ maps display pronounced artifacts over large portions of the myocardium and poor reproducibility across the shimming conditions. B_0-aSL preparations, on the other hand, present comparable image quality for both cases free of visually apparent artifacts. The adiabatic B_0-aSL preparation resulted in significantly better precision compared with RefSL (B_0-aSL: $wCV_{i,r} = 14.51 \pm 3.71\%$, RefSL: $wCV_{i,r} = 37.61 \pm 19.42\%$; $p < 0.01$, Figure 4.8C).

At least ten times higher reproducibility was obtained with the B_0-aSL preparation compared with the RefSL module (average $\overline{wCV_i} = 4.64 \pm 2.18\%$ for B_0-aSL against average $\overline{wCV_i} = 47.39 \pm 12.06\%$ for RefSL, $p < 0.0001$), as shown in Figure 4.8C.

Finally, inter-subject variability was lower for the B_0-aSL preparation ($\overline{CV} = 8.76 \pm 3.65\%$ for B_0-aSL), compared with the conventional SL ($\overline{CV} = 51.90 \pm 15.27\%$ for RefSL, $p < 0.0001$), as shown in Figure 4.8C. A complete overview of the in vivo myocardial $T_{1\rho,\,\mathrm{adiab}}$ and $T_{1\rho}$ values, as well as precision, reproducibility, and inter-subject variability for each healthy subject across the two cohorts, can be found in Supporting Information Tables 4.S1, 4.S2, 4.S3, and 4.S4.

4.3.4. Patients experiments

Four of the six patients presented LGE-positive in the CMR. For two of those four patients, the mid-SAX slice intersected with the area of focal scar identified on the LGE images. Figure 4.9 shows the clinical sequences as well as aSL-based $T_{1\rho,\,\mathrm{adiab}}$ maps and RefSL-based $T_{1\rho}$ maps for the two subjects with LGE-identified scars in the mid-ventricular SAX slice. $T_{1\rho,\,\mathrm{adiab}}$ maps show visually discernable alteration in the myocardium, that spatially coincides with the areas of hyperenhancement in the LGE images. Any potential alteration in the RefSL-based $T_{1\rho}$ maps is obfuscated by the presence of substantial artifacts. B_1-aSL yielded the best maps quality among adiabatic preparations, with no visible B_0 or B_1^+-related artifacts. B_0-aSL and Bal-aSL maps were characterized by overall lower quality and presented visible artifacts across the myocardium, as shown in Supporting Information Figure 4.S3.

Patient 1 shows near transmural enhancement in the LGE images. $T_{1\rho,\,\mathrm{adiab}}$ in this subject shows a +47.48% elevation in the LGE-positive area compared with the remote myocardium for B_1-aSL, while RefSL-based $T_{1\rho}$ maps show a -33.26% difference. In comparison, native T_1 and ECV values for the same patient showed, respectively, +17.12% and +80.53% in the LGE-positive area. Patient 2, who showed signs of lipomatous metaplasia in bSSFP CINE images (Figure 4.9), decreased relaxation times were measured for the LGE positive area, compared with remote healthy myocardium (-6.04% for B_1-aSL $T_{1\rho,\,\mathrm{adiab}}$, -67.19% for RefSL $T_{1\rho}$, -3.11% for native T_1, -41.19% for ECV), as expected in

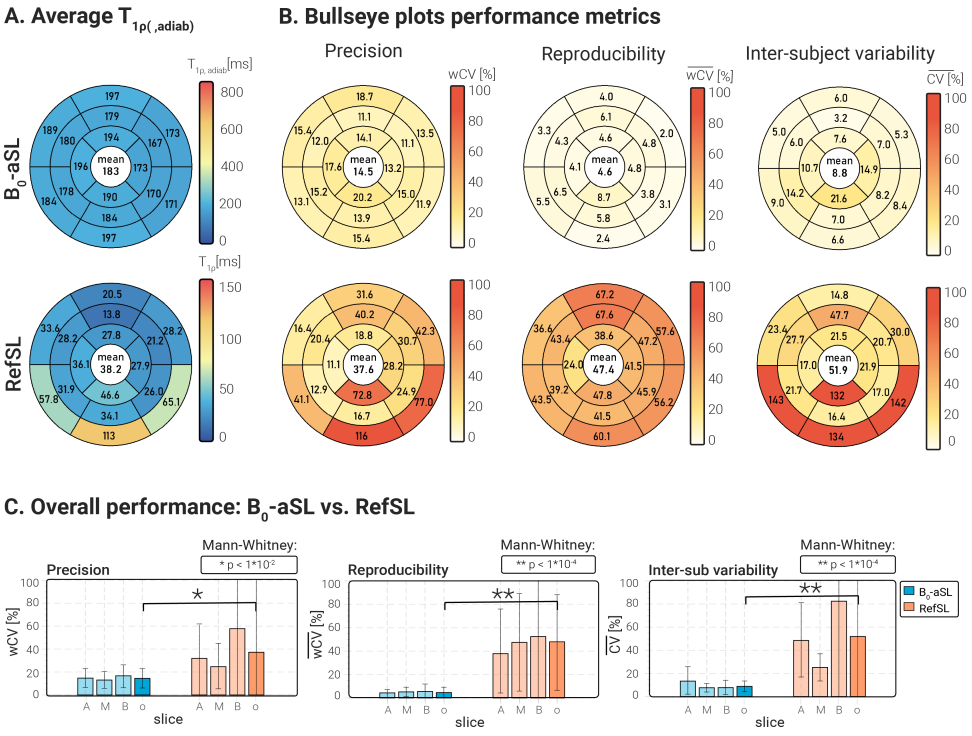

Figure 4.8 : (A) Bullseye plots showing the $T_{1\rho,\,\mathrm{adiab}}$ and $T_{1\rho}$ values, averaged over all cohort 2 subjects and repetitions, for 16 AHA myocardial segments. $T_{1\rho,\,\mathrm{adiab}}$ values are consistently higher, but more homogeneous across the 16 segments for all preparations, compared with RefSL-based $T_{1\rho}$ values. (B) Bullseye plots report the average precision (wCV), reproducibility ($\overline{wCV}$), and inter-subject variability ($\overline{CV}$) coefficients for B_0-aSL-based $T_{1\rho,\,\mathrm{adiab}}$ maps and RefSL $T_{1\rho}$ maps in 16 AHA myocardial segments. Global average values are reported at the center of each bullseye plot. Improved precision, reproducibility, and inter-subject variability are obtained with aSL preparations, compared to RefSL. (C) Bar plots comparing precision, reproducibility, and inter-subject variability for each preparation per slice and averaged across all slices (A=apical, M=mid-ventricular, B=basal, o=overall). Pair-wise statistical significance is marked by $*$ or $**$ and the corresponding p-values are shown on top of each plot. Significantly higher $wCV_{r,i}$, $\overline{wCV}$, and $\overline{CV}$ values are measured for conventional RefSL-based $T_{1\rho}$ mapping compared with $T_{1\rho,\,\mathrm{adiab}}$.

the presence of fatty infiltration. Major artifacts, however, impair the T_1 and ECV maps quality. For both patients, normal $T_{1\rho,\,\mathrm{adiab}}$ and $T_{1\rho}$ values were measured in the remote myocardium (202.18±17.79 ms, 169.42±13.06 ms, 97.98±11.35 ms, and 42.91±17.81 ms for B_0-aSL, Bal-aSL, B_1-aSL, and RefSL, respectively). Normal $T_{1\rho,\,\mathrm{adiab}}$ and $T_{1\rho}$ values were also measured in LGE-negative patients (191.32±13.53 ms, 148.46±12.95 ms, 92.35±7.29 ms, and 33.59±14.36 ms for B_0-aSL, Bal-aSL, B_1-aSL, and RefSL, respectively).

4.4. Discussion

In this study, we proposed a new cardiac $T_{1\rho,\,\mathrm{adiab}}$ mapping technique based on fully aSL preparation for myocardial tissue characterization at 3T. Numerical optimization yielded aSL preparations with tuneable resilience against B_0 and B_1^+ inhomogeneities. Phantom and in vivo measurements demonstrated that $T_{1\rho,\,\mathrm{adiab}}$ mapping achieved more robust results than conventional $T_{1\rho}$ mapping approaches. $T_{1\rho,\,\mathrm{adiab}}$ maps showed fewer artifacts, higher precision and reproducibility, and lower inter-subject variability. Initial data showed feasibility in patients and visual alignment of areas with altered $T_{1\rho,\,\mathrm{adiab}}$ and hyperenhancement in LGE images.

Conventional $T_{1\rho}$ values obtained with the RefSL preparation in this study were comparable to those reported in previous studies at 3T [334–336]. However, our results show slightly lower precision for the RefSL maps than in previous studies. This difference in variability may be because previous studies only evaluated a small ROI in the anteroseptal segment of the myocardium, while in this work, an automatic segmentation of the entire myocardium was used. Significant inhomogeneities are visible in conventional RefSL maps, both in our results and in other studies [334–336]. Han et al. found that at 1.5T B_0 variations over 10% of the SL field amplitude (typically $B_1/\gamma = 500$ Hz) cause $T_{1\rho}$ quantification errors and visible image artifacts [338]. At 3T, this limit is easily exceeded [82]. Furthermore, B_1^+ inhomogeneities have a much higher impact at high fields in cardiac imaging [358], thus necessitating more robust $T_{1\rho}$ mapping techniques.

Both adiabatic and conventional $T_{1\rho}$ maps showed lower $T_{1\rho,\,\mathrm{adiab}}$ or $T_{1\rho}$ values in the apical slice, compared to the mid and basal slices. This effect is less evident for the B_0-aSL preparations ($T_{1\rho,\,\mathrm{adiab}}$ values comparison apical vs. mid and basal slices: $p = 0.77$ for B_0-aSL, $p < 0.01$ for B_1-aSL and Bal-aSL, Figure 4.6). Hence, the lower $T_{1\rho,\,\mathrm{adiab}}$ and $T_{1\rho}$ values in the apical slice may be explained with the higher contribution of B_0 inhomogeneities at the apex.

Using fully aSL preparations has four major advantages. First, they yield more robust $T_{1\rho,\,\mathrm{adiab}}$ quantification in the presence of field inhomogeneities. Our results have shown that the $T_{1\rho,\,\mathrm{adiab}}$ maps have a lower level of noise and do not present significant B_0 or B_1^+-related artifacts, overcoming the limitations observed in the previous studies [334–336]. $T_{1\rho,\,\mathrm{adiab}}$ preparations also yielded higher precision, reproducibility and lower inter-subject variability. Resilience to artifacts is of particular importance for applications at high field strengths, like 3T, which have the potential advantage of increased SNR and CNR. Second, the use of amplitude-modulated HS pulses lowers the SAR demands compared to conventional continuous-wave preparations for the same duration. Wang et al. reported a SL pulse amplitude B_1/γ of 298 Hz [336], limited by SAR constraints and comparable with our findings.

Low SL pulse amplitudes result in lower measured $T_{1\rho}$ values and further compromise the CNR and robustness to system imperfections. The aSL pulses used in this study, on the other hand, allowed us to use maximum peak power and longer preparation times, while still satisfying SAR limitations. Third, $T_{1\rho,\,\mathrm{adiab}}$ preparations eliminate the need for the initial 90°tip of the magnetization, which introduces further imperfections in the presence of B_1^+ inhomogeneities [72, 349]. Finally, conventional SL preparations are orientation-dependent [359]. The high anisotropy of myocardial fibers yields orientation-dependent $T_{1\rho}$ times with conventional preparations [360]. Adiabatic $T_{1\rho}$ preparations, on the other hand, have been shown to be orientation-independent [359]. This may further contribute to more homogeneous and reproducible $T_{1\rho,\,\mathrm{adiab}}$ maps across the myocardium.

Besides the advantages in terms of robustness given by aSL preparations, the mechanism behind $T_{1\rho,\,\mathrm{adiab}}$ relaxation is intrinsically different from conventional $T_{1\rho}$. Each $T_{1\rho,\,\mathrm{adiab}}$ preparation probes a wider spectrum of SL frequencies through the adiabatic sweep, compared to mono-frequency conventional SL. Effective field strength and orientation vary during aSL preparations, as well as the angle between the effective field and the magnetization. On the one hand, these variations lead to relaxation rate changes throughout the preparation module, rather than sampling a uniform $T_{1\rho}$ [342, 343]. On the other hand, the variable transverse relaxation $T_{2\rho}$ contribution in the rotating frame of reference results in different $T_{1\rho}/T_{2\rho}$ ratios for any given time point. Furthermore, we observed higher $T_{1\rho,\,\mathrm{adiab}}$ times for preparations with higher β and, thus, a faster frequency sweep velocity. This indicates that the spectrum of relaxations rates probed during aSL varies depending on the pulse profiles. These factors may lead to a different sensitivity profile in pathological remodeling and its clinical value remains to be evaluated. An in-depth theoretical analysis of the mechanisms behind $T_{1\rho,\,\mathrm{adiab}}$ relaxation would be beneficial for the comprehension of its relationship with the underlying physiology.

In patients, the poor resilience of RefSL preparations to system imperfections significantly compromised the map quality. Artifacts in the area around the coronary sinus, as well as the lateral wall, appeared in all cases, preventing the unambiguous identification of focal alteration. Compared to healthy subjects, image artifacts were substantially more pronounced in the patient cohort. This likely stemmed from lower B_1^+ shim quality in the clinical setting. aSL-based preparations, in particular when tuned for B_1^+-resilience, yielded good map quality, comparable to the healthy subject cohort. This indicates fair resilience to system imperfections in clinical use.

Cardiac $T_{1\rho,\,\mathrm{adiab}}$ maps showed visible focal alteration that spatially coincided with areas of hyperenhancement in the LGE images. This is in line with previous studies indicating sensitivity to a range of

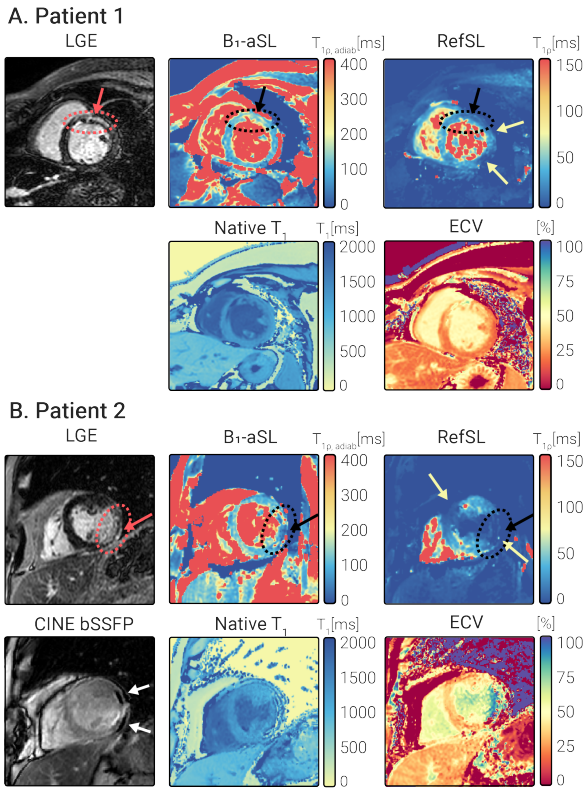

Figure 4.9 : (A) 53-year-old female patient suffering from ischemic cardiomyopathy. LGE images demonstrate myocardial infarction in the mid anteroseptal and anterior wall. A circular ghosting artifact is visible on the LGE image and partially overlaps with myocardial scar (red arrow). The B_1-aSL-based $T_{1\rho,\,\mathrm{adiab}}$ map shows elevation co-localized with LGE positive regions ($T_{1\rho,\,\mathrm{adiab}}$ = 146.24±25.34 ms scar -black arrow-, 99.40±11.58 ms remote). Native T_1 and ECV values are also focally elevated in the anterior and anteroseptal segments. Due to changes in the imaging slice position, however, the visible abnormalities in native T_1 maps are not precisely co-localized with the LGE positive area. Due to mapping inhomogeneity in the anterior and lateral regions (yellow arrows), no focal alteration is unambiguously identified in the conventional $T_{1\rho}$ maps. (B) 59-year-old male patient with a history of ischemic cardiomyopathy. LGE images demonstrate transmural myocardial enhancement in the mid-anterolateral segments (red arrow). Chemical shift artifacts in the bSSFP CINE images indicate lipomatous metaplasia. $T_{1\rho,\,\mathrm{adiab}}$ values decrease in the scar region ($T_{1\rho,\,\mathrm{adiab}}$ = 67.06±14.69 ms scar -black arrow-, 96.57±15.03 ms remote). Native T_1 and ECV values are also lower in correspondence of the scar region with respect to remote myocardium, although major artifacts impair the maps quality. In this patient, significant artifacts obfuscate any potential focal alteration in the RefSL-based $T_{1\rho}$ maps (yellow arrows).

diseases. Wang et al. found a +24% $T_{1\rho}$ elevation for hypertrophic cardiomyopathy patients with diffuse fibrosis [336]. At 1.5T, van Oorschot et al. measured +52% $T_{1\rho}$ elevation in infarcted myocardium of patients suffering from ischemic heart disease [361] and +46% in a

second ischemic cohort [331]. Furthermore, Bustin et al. have found a +40% elevation in infarcted myocardium of LGE-positive patients [131]. These trends are in agreement with the $T_{1\rho,\,\mathrm{adiab}}$ enhancement measured in patient 1. On the other hand, $T_{1\rho,\,\mathrm{adiab}}$ in the scar area of patient 2 was decreased. This is in good agreement with the CMR finding of lipomatous metaplasia [82, 98, 362], and expected in these cases due to the short $T_{1\rho,\,\mathrm{adiab}}$ component of the intramyocardial fat. Our preliminary results indicate that fully adiabatic $T_{1\rho}$ mapping can potentially yield more robust quantification than conventional continuous-wave SL in clinical use at high fields. However, clinical sensitivity of $T_{1\rho,\mathrm{adiab}}$ mapping may differ from conventional continuous wave $T_{1\rho}$ mapping due to the mechanistic differences and among different adiabatic preparations due to differences in the effective and fictitious fields. Consequently, larger dedicated cohorts of healthy controls and a targeted patient population are warranted to determine clinical sensitivity and potential cut-off values for the differentiation of healthy and infarcted myocardium.

Pulse design optimization was the key to achieving the desired resilience against B_0 and B_1^+ inhomogeneities. The HS pulse shape was chosen specifically for its enhanced resilience to B_0 inhomogeneities, superior to TANH/TAN pulses, as previously reported [82]. First, we observed that shorter aSL pulses (4HS-aSL and 8HS-aSL) performed worse than the longer one 2HS-aSL, despite allowing for complete MLEV compensation. Longer HS pulses are thus preferred for $T_{1\rho,\,\mathrm{adiab}}$ preparations. Second, we found that the optimal HS pulse shape varies significantly under different B_0 and B_1^+ conditions. Bloch simulations were in very good agreement with the experimental data acquired in both the phantoms and the calf muscle. Our in vivo results show that B_0-aSL preparations achieve better precision and inter-subject variability than Bal-aSL and B_1-aSL in healthy subjects. However, B_1-aSL has proven most robust in the clinical set-up where B_1-shim quality was reduced.

Increased $wCV_{r,i}$, $\overline{wCV_i}$, and $\overline{CV}$ values were observed in the basal and mid-inferolateral segment, as well as the apical lateral segment for B_1-aSL preparations (see Figure 4.8). These values were reflected in the B_1-aSL $T_{1\rho,\,\mathrm{adiab}}$ maps, which, for some subjects, presented residual B_0 artifacts in the same segments (Figure 4.7). These effects were not observed for B_0-aSL and Bal-aSL maps. Thus, depending on the application and the technical characteristics of the scanner either of the optimized preparations may be most suitable for robust $T_{1\rho,\,\mathrm{adiab}}$ quantification in the clinic. Adiabatic pulses that were previously used for other cardiac MRI applications were found to be closest to those used for B_1-aSL preparations ($\beta = 4.8$, $f_{\mathrm{max}} = 215$ Hz [341]). These pulses may be particularly warranted on systems where B_1 quality is the main concern, such as systems with a single transmit channel or a

lack of advanced shim modes. On other systems, B_0-aSL and Bal-aSL preparations may be preferred for the observed increase in precision and reproducibility.

In our study, patient scans showed pronounced cardiac and respiratory motion, despite cardiac triggering and breath-holding. Residual motion due to heart rate variability and poor breath-holding capacity in patients rendered retrospective image registration necessary to achieve satisfactory map quality in the final $T_{1\rho,\,\mathrm{adiab}}$ and $T_{1\rho}$ maps. Recently, specific attention has been dedicated on the development of accelerated, free-breathing, whole-heart $T_{1\rho}$ mapping sequences to facilitate its clinical implementation [332, 363, 364]. Furthermore, several motion correction approaches have been proposed to improve the quality of reconstructed $T_{1\rho}$ maps and mitigate the contribution of motion [131, 330]. These efforts are key to enabling the widespread use of quantitative parametric mapping sequences in clinical practice. Our aSL preparations are fully compatible with these sequence designs and reconstruction approaches and could, in the future, be integrated into accelerated and motion-corrected $T_{1\rho}$ mapping sequences. This may be particularly helpful to facilitate testing of the proposed $T_{1\rho,\,\mathrm{adiab}}$ mapping in large, relevant patient cohorts in order to demonstrate its clinical value.

4.5. Conclusions

In this work, $T_{1\rho,\,\mathrm{adiab}}$ mapping was proposed as an alternative to conventional $T_{1\rho}$ mapping to enable its application in the human myocardium at 3T. Our results show that adiabatic spin-lock preparations enable more robust mapping in the presence of B_0 and B_1^+ inhomogeneities while satisfying SAR limitations. Adiabatic preparation modules yielded quantification with high precision and reproducibility in healthy subjects. In patients, aSL-based $T_{1\rho,\mathrm{adiab}}$ maps depicted focal alterations in agreement with the reference LGE scans. Thus, $T_{1\rho}$ mapping can be a promising candidate for reproducible myocardial tissue characterization and bears potential as a contrast-free imaging biomarker for scar and fibrosis.

4.6. Supporting Information

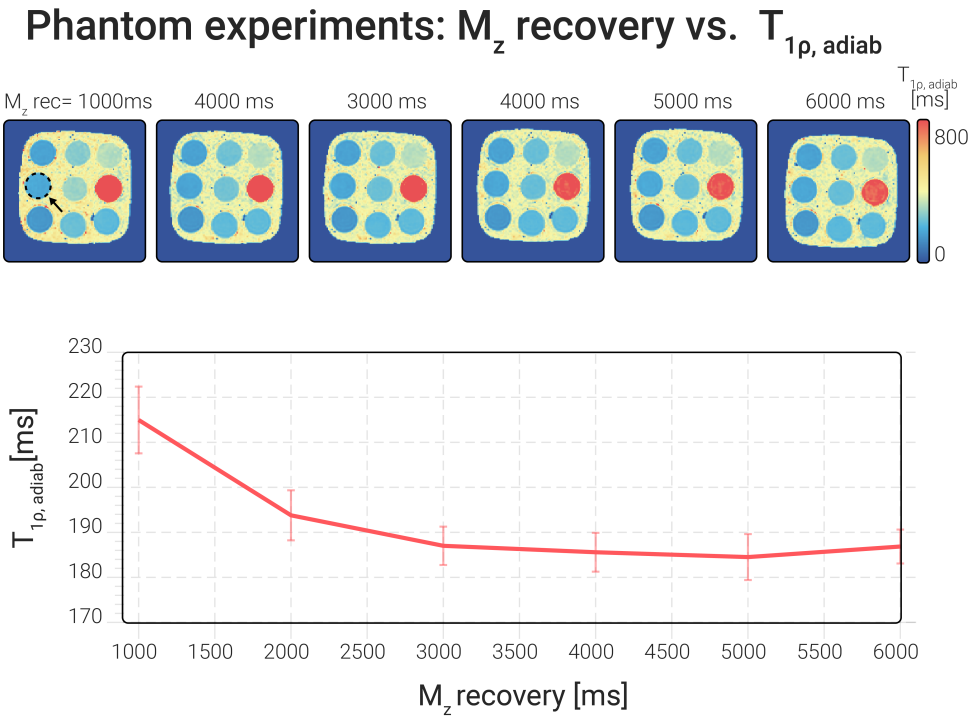

Figure 4.S1 : Phantom $T_{1\rho,\,\mathrm{adiab}}$ maps acquired with different rest periods for longitudinal magnetization recovery delays. $T_{1\rho,\,\mathrm{adiab}}$ values (± standard deviation) reported in the plot are measured from the normal myocardium-mimicking vial (left column, middle row). For longitudinal magnetization recovery delays ≥ 3000ms, the measured $T_{1\rho,\,\mathrm{adiab}}$ values deviate less than 5% from the asymptotic value.

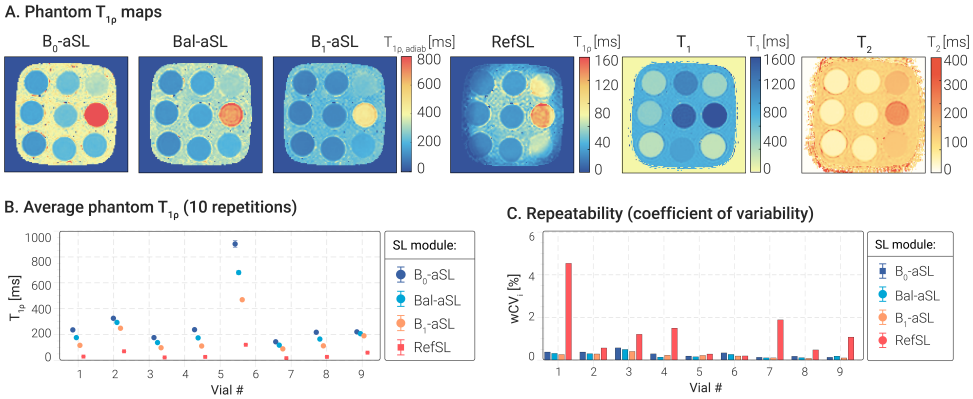

Figure 4.S2 : (A) Example of $T_{1\rho,\,\mathrm{adiab}}$ and $T_{1\rho}$ maps of the tissue-mimicking T1MES phantom. Good map quality was achieved with aSL preparations, whereas visible artifacts are apparent in most vials in the maps obtained with RefSL preparation. Approximate T_1 and T_2 maps are displayed for reference. (B) $T_{1\rho,\,\mathrm{adiab}}$ and $T_{1\rho}$ values with standard deviation bars for each vial, averaged over 10 repetitions. $T_{1\rho,\,\mathrm{adiab}}$ values are consistently higher than $T_{1\rho}$ values measured with RefSL preparations. $T_{1\rho,\,\mathrm{adiab}}$ dispersion is observed across B_0, Bal and B_1 optimized pulses, due to a progressively lower β value. (C) Repeatability measured as the coefficient of variability ($\overline{wCV_i}$) for each vial. Averaging across all the vials, aSL preparations yielded significantly improved repeatability ($\overline{wCV_i}$ = 0.29 ± 0.15 for B_0-aSL, $p < 0.01$; $\overline{wCV_i}$ = 0.23 ± 0.13 for Bal-aSL, $p < 0.01$; $\overline{wCV_i}$ = 0.21 ± 0.11 for B_1-aSL, $p < 0.001$ vs. $\overline{wCV_i}$ = 1.30 ± 1.34 for RefSL).

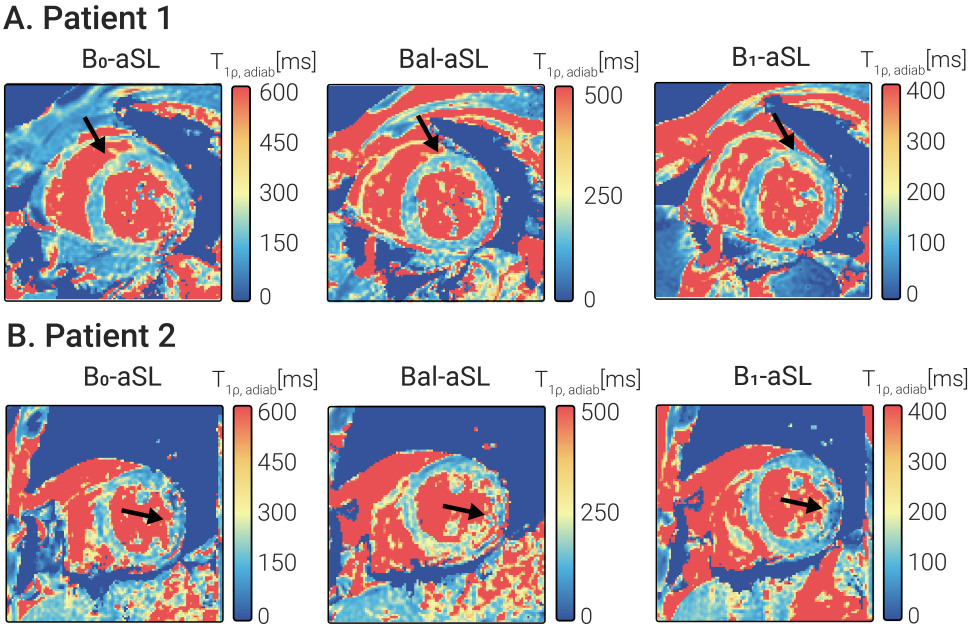

Figure 4.S3 : $T_{1\rho,\,\mathrm{adiab}}$ maps obtained with B_0-aSL, Bal-aSL and B_1-aSL preparations. Image quality is compromised due to artifacts visible in the maps for B_0-aSL in (A) and for Bal-aSL in (B). Furthermore Bal-aSL prepared baseline images were subject to substantial residual motion in both patients, lowering the image quality.

Table 4.S1 : In-vivo myocardial $T_{1\rho,\,\mathrm{adiab}}$ values [ms], averaged over all repetitions and segments for 6 healthy volunteers of cohort 1.

Subject #	B_0-aSL	Bal-aSL	B_1-aSL
1	196.41 ± 25.04	160.93 ± 15.50	93.76 ± 7.99
2	201.99 ± 25.30	162.66 ± 18.56	92.82 ± 11.00
3	197.61 ± 23.06	158.34 ± 17.04	92.70 ± 10.78
4	181.04 ± 24.73	139.07 ± 19.58	73.51 ± 14.42
5	190.37 ± 22.93	161.74 ± 15.86	92.83 ± 9.25
6	197.89 ± 26.17	150.82 ± 21.99	79.25 ± 15.89

Table 4.S2 : In-vivo myocardial $T_{1\rho,\,\mathrm{adiab}}$ precision, reproducibility and inter-subject variability (ISV), averaged over segments and repetitions for 6 healthy volunteers of cohort 1.

	B_0-aSL		Bal-aSL		B_1-aSL	
S.#	Prec. [%]	Repr. [%]	Prec.[%]	Repr. [%]	Prec. [%]	Repr. [%]
1	12.84±4.55	2.79±2.37	9.72±2.43	1.95±1.40	8.70±3.91	2.52±1.77
2	12.86±5.72	1.74±1.80	11.94±7.27	2.70±2.35	12.60±10.26	4.17±4.69
3	11.83±3.64	2.67±2.32	11.16±5.92	2.80±3.18	12.26±9.92	2.77±2.83
4	13.87±3.18	2.54±1.57	14.32±3.24	5.21±3.33	22.53±17.02	9.94±14.85
5	12.19±3.91	8.09±7.17	9.94±3.34	2.35±2.46	10.51±7.22	5.28±4.03
6	13.55±5.48	4.60±2.88	15.27±7.53	7.52±3.66	22.29±13.69	7.04±5.20
ISV	5.32±3.01 %		6.40±2.66 %		9.25±6.10 %	

Table 4.S3 : In-vivo myocardial $T_{1\rho,\,\mathrm{adiab}}$ and $T_{1\rho}$ values [ms], averaged over all repetitions and segments for 7 healthy volunteers of cohort 2.

Subject #	**B_0-aSL**	**RefSL**
1	196.41 ± 25.04	23.27 ± 25.05
2	201.99 ± 25.30	43.88 ± 46.04
3	197.61 ± 23.06	26.45 ± 13.50
4	181.04 ± 24.73	21.22 ± 29.12
5	190.37 ± 22.93	33.84 ± 23.42
6	197.89 ± 26.17	58.91 ± 32.78
7	181.25 ± 21.18	39.65 ± 29.42

Table 4.S4 : In-vivo myocardial $T_{1\rho,\,\mathrm{adiab}}$ and $T_{1\rho}$ precision, reproducibility and inter-subject variability (ISV), averaged over segments and repetitions for 7 healthy volunteers of cohort 2.

	B_0-aSL		**RefSL**	
S. #	Prec. [%]	Reprod. [%]	Prec.[%]	Reprod. [%]
1	12.84±4.55	2.79±2.37	38.72±25.56	29.15±23.26
2	18.86±5.72	1.74±1.80	69.46±38.78	59.35±24.41
3	11.83±3.64	2.67±2.32	54.81±28.70	28.31±24.14
4	15.87±3.18	2.54±1.57	26.13±39.69	57.65±25.94
5	12.19±3.91	8.09±7.17	34.92±20.38	27.85±16.20
6	13.55±5.48	4.60±2.88	28.40±26.49	40.20±23.70
7	11.19±3.28	2.96±3.05	43.81±19.70	24.76±24.14
ISV[%]	5.32±3.01		51.92±6.10	

5

Dark-blood adiabatic $T_{1\rho}$ mapping of the heart using combined non-selective and slice-selective RF pulses at 3T

Chiara Coletti, Joao Tourais, Anastasia Fotaki, Yidong Zhao, Yi Zhang, Christal van de Steeg-Henzen, Qian Tao, Claudia Prieto, Sebastian Weingärtner

Under review at the Journal of Cardiovascular Magnetic Resonance

Abstract

Background: $T_{1\rho}$ mapping is emerging as a potential, contrast-free alternative to late gadolinium enhancement (LGE) for assessment of myocardial viability. However, strong signal contributions from the blood pool can impede quantitative evaluation at the (sub)endocardium. In this work, we study the effectiveness of dark-blood (DB) contrast in adiabatic $T_{1\rho}$ ($T_{1\rho,\mathrm{adiab}}$) mapping at 3T, using slice-selective and non-selective adiabatic spin-lock pulses.

Methods: Adiabatic DB-$T_{1\rho,\mathrm{adiab}}$ preparations consisted of an odd number of slice-selective adiabatic full passage (AFP) pulses followed by a final non-selective AFP pulse. This preparation induces $T_{1\rho,\mathrm{adiab}}$ decay within the imaging slice while it inverts the magnetization outside. A delay (δ) between preparation and imaging allowed for relaxation and inflow of the inverted blood to achieve DB contrast. Bias and precision of DB and bright-blood (BB) $T_{1\rho,\mathrm{adiab}}$ were compared in phantom and in healthy subjects (n=10). Blood suppression efficacy and myocardial thickness in DB imaging were investigated in simulations, phantom, and in vivo. The clinical feasibility of DB-$T_{1\rho,\mathrm{adiab}}$ mapping was evaluated in a small cohort of patients (n=7) with suspected cardiovascular diseases.

Results: DB-$T_{1\rho,\mathrm{adiab}}$ values were in agreement with reference BB-$T_{1\rho,\mathrm{adiab}}$ values in phantom (myocardium-like vial BB: 219.27±4.80 ms, DB: 218.09±8.22 ms) and in healthy subjects (BB: 182.32±28.27 ms, DB: 183.49±45.54 ms). A moderate increase in intra- ($wCV_{i,r}$) and inter-scan variability ($\overline{wCV_i}$) was observed in the DB method, compared with conventional BB imaging, for phantom and healthy subjects (in vivo $wCV_{i,r}$ BB: 15.51±2.65%, DB: 24.82±4.18%; in vivo $\overline{wCV_i}$ BB: 3.38±0.86%, DB: 7.24±2.55%). Longer delay times improved blood suppression in vivo for DB-$T_{1\rho,\mathrm{adiab}}$, albeit at increased intra-scan variability in phantom and in vivo (DB $wCV_{i,r}$ for δ=0 ms: 4.90±0.83% in phantom, 16.67±2.91% in vivo, for δ=600 ms: 8.14±1.88% in phantom, 26.04±5.19% in vivo). Average myocardial thickness was slightly higher when using DB-$T_{1\rho,\mathrm{adiab}}$ compared with BB-$T_{1\rho,\mathrm{adiab}}$ (BB: 7.76±2.05 mm, DB: 8.63±2.46 mm). DB-$T_{1\rho,\mathrm{adiab}}$ maps yielded comparable image quality to BB-$T_{1\rho,\mathrm{adiab}}$ maps in patients.

Conclusion: DB-$T_{1\rho,\mathrm{adiab}}$ mapping represents an alternative to BB-$T_{1\rho,\mathrm{adiab}}$ for myocardial assessment with the potential for improved visualization of the (sub-)endocardium.

5.1. Introduction

$T_{1\rho}$ mapping is gaining attention as a promising method for contrast-free myocardial tissue characterization and a potential alternative to late gadolinium enhancement (LGE) imaging [12]. While LGE remains the clinical gold standard for the assessment of fibrosis in ischemic and non-ischemic cardiomyopathies, the use of gadolinium-based contrast agents (GBCA) warrants caution. Gadolinium deposition, particularly in the brain, was observed in subjects following repeated contrast agent administration [9]. Moreover, GBCA can put patients with severe renal impairment at risk of necrotic systemic fibrosis [8]. Thus, non-contrast alternatives to LGE, such as those using quantitative parametric mapping techniques, are long sought after.

$T_{1\rho}$ mapping has shown promise as a non-contrast alternative due to its sensitivity to slow molecular motion and other interactions in the low kHz range [11, 324]. $T_{1\rho}$ measures the longitudinal relaxation in the rotating frame of reference during irradiation with a radio-frequency (RF) pulse, the so-called spin-lock (SL) pulse. The SL field conventionally consists of moderate amplitude continuous-wave RF pulses, which lock the magnetization along the effective field and subject it to rotating-frame relaxation. Initial $T_{1\rho}$ mapping studies in animal models have reported improved contrast-to-noise ratio with respect to native T_1 and T_2 mapping for differentiating infarcted and remote myocardium [87, 318, 324, 325, 327, 328]. In vivo $T_{1\rho}$ mapping has been successfully applied for scar assessment in patients with ischemic cardiomyopathies in several studies at 1.5T [131, 329, 330, 332, 361, 365, 366]. Applications of conventional $T_{1\rho}$ mapping at 3T are limited [334–336]. At this field strength $T_{1\rho}$ is highly susceptible to B_0 and B_1^+ inhomogeneities and requires high specific absorption rate (SAR) [337, 338]. To overcome these limitations, adiabatic $T_{1\rho,\mathrm{adiab}}$ preparations [72, 73] have been explored in cardiac imaging and have achieved robust $T_{1\rho,\mathrm{adiab}}$ mapping at 3T [367]. In $T_{1\rho,\mathrm{adiab}}$ the magnetization is locked by the effective field of a series of amplitude and frequency-modulated adiabatic full passage pulses (AFP), yielding a time-varying rotating-frame orientation and $T_{1\rho,\mathrm{adiab}}$ constant. Adiabatic pulses have been shown to be more robust than continuous-wave SLs in the presence of B_0 and B_1^+ inhomogeneities and require less SAR burden [367].

As commonly observed in myocardial tissue characterization, the ability to discern signal alterations at the sub-endocardium is compromised in $T_{1\rho}$ and $T_{1\rho,\mathrm{adiab}}$ maps due to the strong blood-pool signal and the limited resolution. In LGE imaging, this issue can be circumvented, using blood signal suppression in so-called, black-blood or dark-blood contrast [368, 369]. Black-blood refers here to imaging techniques aimed at fully nulling the blood signal, while dark-blood techniques only attenuate the blood signal relative to the myocardium. In LGE imaging black- or dark-blood contrast has been previously achieved either

through flow-dependent techniques, such as double inversion-recovery (DIR) preparations [64]. Alternatively, differences in relaxation times or magnetization transfer properties between blood, healthy myocardium and scar can be exploited for black-blood contrast [243, 370–379]. Black-blood contrast has also been used in myocardial mapping. Black-blood T_1 mapping has previously been achieved with motion-sensitized driven-equilibrium (MSDE) preparations and demonstrated an increased thickness of the readily evaluable myocardium [346]. Black-blood T_2 and T_2^* using DIR preparations have shown comparable or improved reproducibility and fewer artifacts, in addition to improved scar-to-blood contrast, compared with conventional bright-blood maps in vivo [380–384]. DIR preparations have also been used for black-blood imaging in continuous-wave $T_{1\rho}$ mapping, demonstrating improved visualization of sub-endocardial scar [331].

In this work, we seek to investigate dark-blood contrast in adiabatic $T_{1\rho,\mathrm{adiab}}$ mapping. A combination of selective and non-selective adiabatic pulses is proposed to achieve flow-dependent signal suppression of the blood pool with no additional preparations. Bloch simulations and phantom imaging were performed to characterize the bias of dark-blood $T_{1\rho,\mathrm{adiab}}$ preparations compared with reference bright-blood preparations. Furthermore, the influence of preparation parameters on blood suppression and intra-scan variability was studied. Finally, in vivo dark-blood $T_{1\rho,\mathrm{adiab}}$ mapping was tested in healthy subjects and in a small cohort of patients with suspected cardiovascular disease and compared with the corresponding bright-blood reference.

5.2. Methods

5.2.1. $T_{1\rho,\mathrm{adiab}}$ preparations

The proposed adiabatic spin-lock preparation comprises a train of hyperbolic secant (HS) AFPs (Figure 5.1A) [72, 73, 367]. In the preparation train, pairs of AFP were concatenated, ensuring that the magnetization is aligned with the $+z$ direction at the end of the preparation. Each pair contained two HS pulses with alternating frequency sweep polarity to compensate for residual sensitivity to B_0 and B_1^+ inhomogeneities [367].

Dark-blood contrast was achieved by adding a slice-selection gradient for all HS pulses in the preparation train, except the last. This way, the labeling slab is exposed to an even number of AFPs, inducing $T_{1\rho,\mathrm{adiab}}$ decay (Figure 5.1B). Outside the labeling slab, only the last AFP is effective, leading to magnetization inversion (Figure 5.1B). A delay time δ between the preparation and the acquisition allows for the inverted blood to flow into the imaging slab. T_1 recovery of the inverted signal during the preparation delay enables the attenuation of the blood signal.

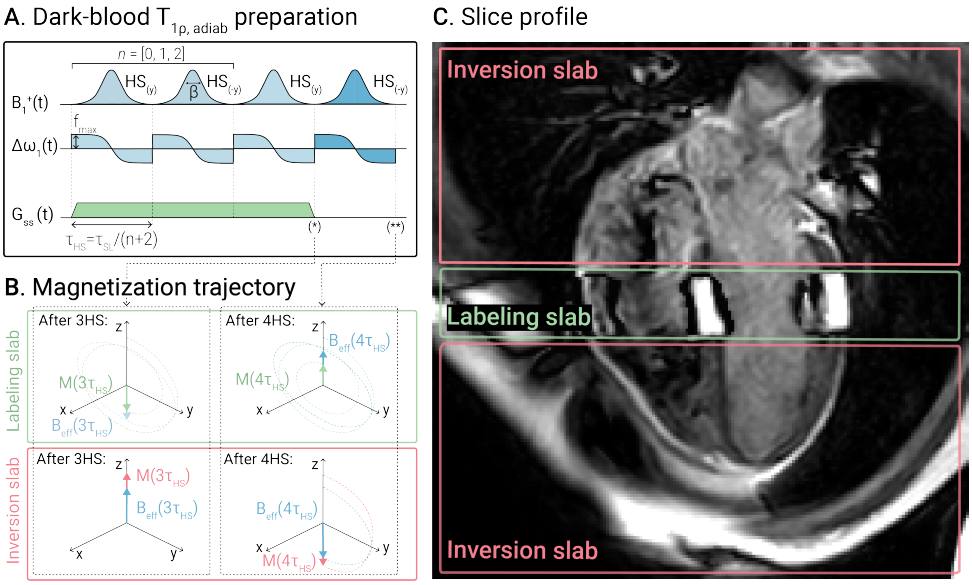

Figure 5.1 : A) $T_{1\rho,\text{adiab}}$ preparation module, consisting of a train of hyperbolic secant (HS) pulses, with corresponding amplitude and frequency modulation functions. A slice-selective gradient (G_{ss}) is used on all but the last HS to achieve dark-blood (DB) contrast. B) Magnetization (M) trajectories for spins in the labeling and inversion slabs during the slice-selective HS pulses (left) and at the end of the entire preparation module (right). Spins in the inversion slab only experience the last non-selective HS pulse and are effectively inverted at the end of the preparations, while spins in the labeling slab experience an even number of HS pulses, yielding a final $T_{1\rho,\text{adiab}}$-prepared positive longitudinal magnetization. C) Slice profile obtained with the DB-$T_{1\rho,\text{adiab}}$-preparations, with G_{ss} chosen orthogonal to the imaging slice orientation to visualize the labeling slab.

For bright-blood (BB) and dark-blood (DB) preparations, all HS AFP were played with a duration of τ_{HS} = 30 ms [367]. This value was chosen as a trade-off between adequate sampling of the expected range of in vivo $T_{1\rho,\text{adiab}}$ times and restrictions imposed by the SAR limits (whole-body SAR < 2.0 W/kg) and the RF amplifier chain. Width parameter β = 6.9 and frequency sweep amplitude $2 \times f_{max}$ = 900 Hz were chosen, based on robustness optimization for the off-resonance range $\Delta\omega_1^{\text{off}} \in \{-200, -199, \ldots + 200\}$ Hz and relative B_1^+ values $\zeta_1 \in \{0.75, 0.76, \ldots 1.00\}$ [367]. In dark blood preparations, the slab-selection gradient strength was set to 880 μT/m to achieve a labeling slab thickness of 24 mm, corresponding to three times the imaging slice thickness. The delay δ after the dark-blood preparation was adjusted according to the subject's heart rate to allow for maximum T_1 recovery of the inverted signal, within a single heartbeat. No delay was played after the BB preparations.

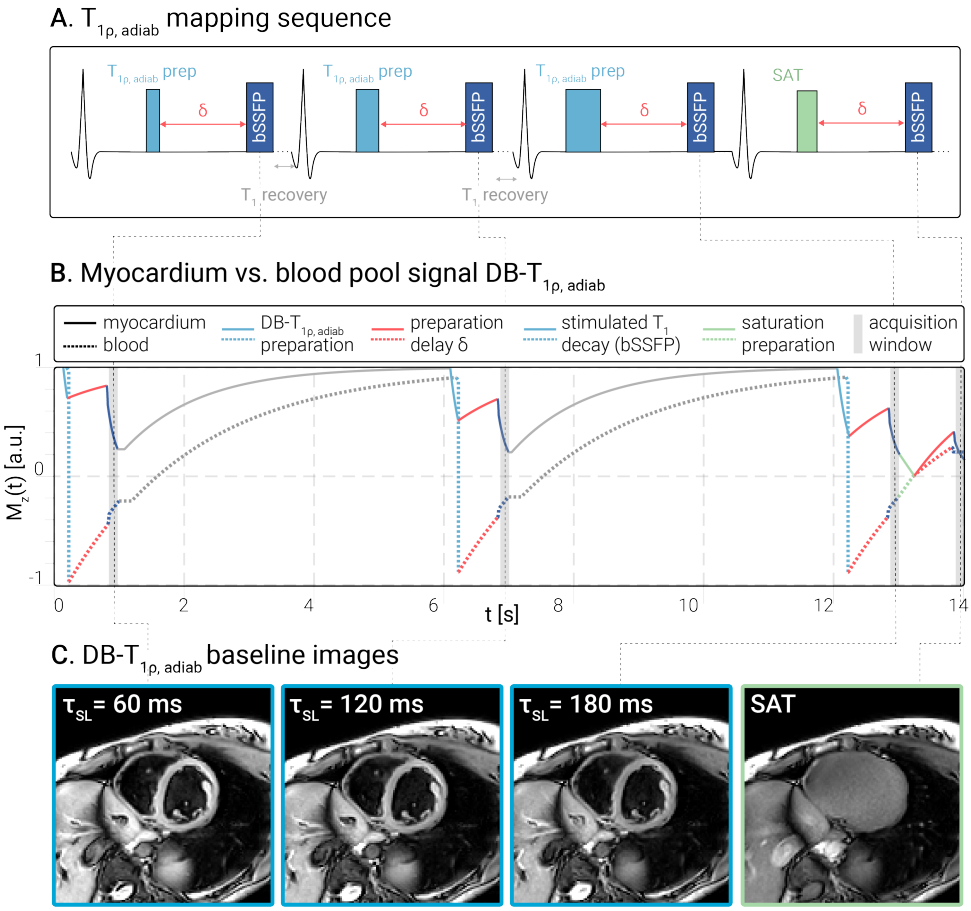

Figure 5.2 : A) Bright blood (BB)- and dark blood (DB)-$T_{1\rho}$ mapping sequence diagram. Four ECG-triggered end-diastolic bSSFP images were acquired in a single breath-hold. B) Corresponding longitudinal magnetization profile ($M_z(t)$) for simulated myocardium (solid line, $T_1/T_2/T_{1\rho,\text{adiab}}$ = 1165/45/183 ms) in the labeling slab and simulated blood (dashed line, $T_1/T_2/T_{1\rho,\text{adiab}}$ = 1932/275/934 ms) in the inversion slab. C) Corresponding DB-$T_{1\rho,adiab}$ baseline images from a representative healthy subject. The first three images are acquired with increasing $T_{1\rho,adiab}$ preparation duration (τ_{SL} = 60, 120, 180 ms), while the fourth is preceded by a saturation preparation, to allow for unbiased DB-$T_{1\rho,adiab}$ estimation.

5.2.2. $T_{1\rho,\text{adiab}}$ mapping sequence

Dark-blood preparations (DB-$T_{1\rho,\text{adiab}}$) were compared to reference bright-blood preparations (BB-$T_{1\rho,\text{adiab}}$) for adiabatic $T_{1\rho,\text{adiab}}$ mapping using a 2D balanced steady-state free-precession (bSSFP) sequence (Figure 5.2). Four end-diastolic cardiac-triggered bSSFP baseline images were acquired in a single 14 s breath-hold. The first three baseline images were preceded by BB or DB-$T_{1\rho,\text{adiab}}$ preparations of

increasing length (2, 4, and 6 HS pulses, yielding τ_{SL} = 60, 120, 180 ms). The last baseline image was preceded by a composite "Water suppression Enhanced through T_1-effects" (WET) saturation pulse [350], to compensate for the effects of magnetization recovery during the imaging readout in the fitting procedure [349]. For DB-$T_{1\rho,\text{adiab}}$ the saturation pulse was followed by the same preparation delay δ used in the $T_{1\rho,\text{adiab}}$-prepared dynamics, to also capture the effect of T_1 recovery during the delay period. All images, except the saturation-prepared image, were preceded by a 5s pause to allow for longitudinal magnetization recovery. Other imaging parameters were: in-plane resolution = 2×2 mm^2, FOV = 220×220 mm^2, slice thickness = 8 mm, TE/TR = 1.2/2.4 ms, flip angle = 70°, SENSE = 2, bandwidth = 1744 Hz/px.

BB and DB-$T_{1\rho,\text{adiab}}$ maps were generated in MATLAB using the following three-parameter model [349], to account for the effect of the imaging pulses and magnetization recovery during the preparation delay:

$$S(t) = A \cdot e^{-\frac{t}{T_{1\rho,\text{adiab}}}} + B. \tag{5.1}$$

Standard deviation maps were calculated alongside the parameter maps, based on the fit residuals, as described in Kellman et al. [385]. Thresholding was applied prior to the fitting procedure to focus the reconstruction on the region of interest. Voxels with a maximum intensity across all baseline images of less than 10% of the maximum signal intensity measured in the dynamic with the longest $T_{1\rho,\text{adiab}}$ preparation were thresholded.

5.2.3. Experimental evaluation

Phantoms and healthy subjects were scanned on a 3T Ingenia system (Philips, Best, The Netherlands). Patient data was acquired on a 3T Achieva system (Philips, Best, The Netherlands). In vivo imaging was ethically approved by the competent review authorities (volunteers: METC NL73381.078.20, patients: UK National Research Ethics Service 15/NS/0030). Written informed consent has been obtained prior to all imaging sessions according to institutional guidelines.

Phantom validation

Phantom experiments were carried out with the T1MES phantom to mimic blood and myocardium relaxation times at 3T [351]. A preparation delay δ = 500 ms was used in phantom. Ten repetitions of BB and DB-$T_{1\rho,\text{adiab}}$ mapping scans were acquired to assess intra-scan and inter-scan variability. Manually drawn circular ROIs were used to extract $T_{1\rho,\text{adiab}}$ values for subsequent statistical analysis. Intra-scan variability

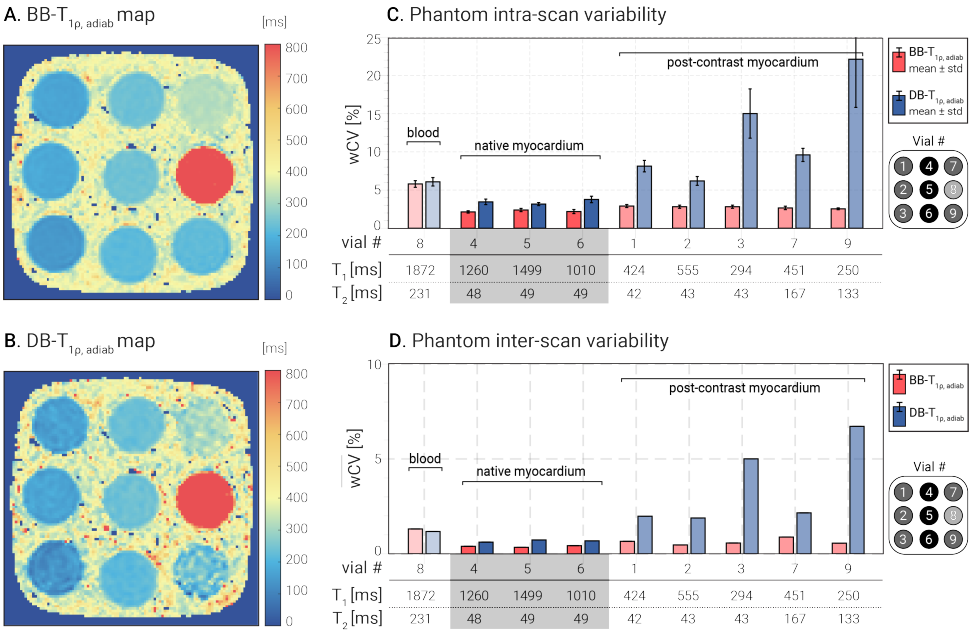

Figure 5.3 : Representative A) bright blood (BB)- and B) dark-blood (DB)-$T_{1\rho,adiab}$ maps of the tissue-mimicking T1MES phantom. Good map quality was achieved with both BB and DB preparations, but higher variability can be observed in DB-$T_{1\rho,adiab}$ maps, especially in vials #1-3, #7 and #9. C) Intra- and D) inter-scan variability measured for BB- and DB-$T_{1\rho,adiab}$ mapping over 10 repetitions, reported for each vial. In native myocardium-mimicking vials (#4-6) a moderate increase in both intra- and inter-scan variability was observed for DB compared with BB-$T_{1\rho,adiab}$ maps.

was assessed for each vial i and repetition r using the within-sample coefficient of variability $wCV_{i,r}$,

$$wCV_{i,r} = \frac{\sqrt{\sigma_{i,r}^2}}{\mu_{i,r}}. \tag{5.2}$$

Here $\mu_{i,r}$ is the average $T_{1\rho,adiab}$ within the ROI, while $\sigma_{i,r}$ is obtained by averaging the ROI values of the standard deviation maps. $wCV_{i,r}$ values were then averaged across repetitions to obtain the final intra-scan variability. Similarly, inter-scan variability was calculated for each vial i using the coefficient of variability $\overline{wCV_i}$ across different repetitions r:

$$\overline{wCV_i} = \frac{1}{R}\sum_{r=1}^{R}\frac{\sqrt{(\mu_{i,r}-\overline{\mu_i})^2}}{\overline{\mu_i}}, \tag{5.3}$$

where R = 10 represents the number of repetitions and $\overline{\mu_i}$ is the average over repetitions of mean $T_{1\rho,adiab}$ values for each vial ($\mu_{i,r}$).

For statistical analysis, phantom vials were divided into 3 groups (native myocardium, blood, and post-contrast tissues) based on their reference T_1 and T_2 values [351]. In each group, $wCV_{i,r}$ and $\overline{wCV_i}$ were averaged over all vials to obtain overall intra- and inter-scan variability. Paired Mann-Whitney U-tests were performed to test the statistical significance between BB- and DB-$T_{1\rho,\text{adiab}}$ maps. P-values of less than 0.05 were considered significant.

In vivo $T_{1\rho,\text{adiab}}$ mapping

Bright- and dark-blood $T_{1\rho,\text{adiab}}$ maps were acquired in 10 healthy subjects (5 male, 5 female, 24.10±6.08 y.o.) in 3 short-axis slices (apical, mid and basal). Three repetitions were acquired for each scan during a single session to study the reproducibility of BB- and DB-$T_{1\rho,\text{adiab}}$ mapping. In a subset of subjects, four-chamber and two-chamber views were also acquired for both $T_{1\rho,\text{adiab}}$ mapping techniques. The preparation delay δ was set to the maximum allowed value, ranging from 395 ms to 745 ms depending on each subject's heart rate.

Image registration was carried out in a pairwise manner using normalized mutual information [357]. The initial baseline image served as the reference template, and the remaining three baseline images were registered to this template. The myocardium was automatically segmented using the nnU-Net framework [354] with uncertainty estimation [355]. Segmentation maps with predictive confidence below 75% were discarded and the segmentation was performed manually. The average BB- or DB-$T_{1\rho,\text{adiab}}$ values and their standard deviation values (std) were extracted segment-by-segment in the myocardial ROI, following the 16-segments AHA model. A paired Mann-Whitney U-test was performed on average BB and DB-$T_{1\rho,\text{adiab}}$ values for each volunteer at a significance level of $p < 0.05$.

BB- and DB-$T_{1\rho,\text{adiab}}$ maps were compared in terms of intra- and inter-scan variability in a test-retest protocol. The within- ($wCV_{i,r}$) and across-repetitions coefficient of variability ($\overline{wCV_i}$) were computed segment-by-segment from the average $T_{1\rho,\text{adiab}}$ and the standard deviation maps for each slice, subject, and repetition , as described for the phantom scans. $wCV_{i,r}$ coefficients were then averaged over all repetitions and subjects to calculate the final intra-scan variability coefficient for each myocardial segment. Similarly, each segment $\overline{wCV_i}$ value was averaged over all subjects to obtain the total inter-scan coefficient of variability. Additionally, the inter-subject variability was computed as the root mean square error between each subject's segment-wise average $T_{1\rho,\text{adiab}}$ value and the overall segment average

across all subjects:

$$\overline{CV} = \frac{1}{N}\sum_{n=1}^{N}\frac{\sqrt{(\mu_i - \overline{\mu})^2}}{\overline{\mu}}. \quad (5.4)$$

Here N indicates the number of subjects.

Statistical differences between BB- and DB-$T_{1\rho,\text{adiab}}$ intra-scan, inter-scan, and inter-subject variability were assessed using segment-wise paired Mann-Whitney U-tests, with $p < 0.05$ considered as significant.

Blood suppression

Additional experiments were performed to assess the effect of the preparation delay δ on blood suppression, accuracy, and variability of the $T_{1\rho,\text{adiab}}$ quantification. Bloch simulations of the DB-$T_{1\rho,\text{adiab}}$ mapping sequence were performed for myocardium-like tissue (simulated $T_1/T_2/T_{1\rho,\text{adiab}}$ = 1165/45/183 ms [386]) with varying preparation delay δ = 0, 10, ..., 700 ms. Additive Gaussian noise was included to simulate SNR = 20. The same 3-parameter fit model described for phantom and in vivo mapping was used on simulated data. One hundred repetitions were computed for each preparation delay to estimate the DB-$T_{1\rho,\text{adiab}}$ mean and standard deviation.

Phantom imaging was also performed for varying preparation delay δ = 0, 50, ..., 700 ms. Mean and standard deviation were extracted from the DB-$T_{1\rho,\text{adiab}}$ maps and the standard deviation maps of fit residuals for the manually segmented myocardium-like vial (#4: T_1/T_2 = 1260/48 ms [351]), respectively. DB-$T_{1\rho,\text{adiab}}$ was then compared to the reference BB-$T_{1\rho,\text{adiab}}$ mean value of the same vial (δ = 0 ms).

Finally, DB-$T_{1\rho,\text{adiab}}$ maps for preparation delay δ = 0, 100, ..., 600 ms were acquired in the mid-short-axis slice of a healthy volunteer (male, 27 y.o.). DB-$T_{1\rho,\text{adiab}}$ mean and standard deviation were compared to reference values obtained for BB-$T_{1\rho,\text{adiab}}$ mapping (δ = 0 ms) in the automatically segmented myocardial ROI.

The effect of increasing preparation delay on DB-$T_{1\rho,\text{adiab}}$ mean and standard deviation was studied with linear regression analysis in simulations, phantom, and in vivo mapping. R^2 coefficient, slope, and intercept values were reported.

Myocardial thickness

The apparent myocardial thickness in the presence of partial-voluming for BB- or DB-$T_{1\rho,\text{adiab}}$ preparations was studied in simulations and in vivo. Bloch simulations were performed to estimate BB-$T_{1\rho,\text{adiab}}$ and DB-$T_{1\rho,\text{adiab}}$ values in a voxel with varying blood/myocardium compositions ([*blood*] = 100% - [*myocardium*], with [*myocardium*] = 0%, 1%, ..., 100%), assuming a fully inverted blood compartment. DB-$T_{1\rho,\text{adiab}}$ was simulated for preparation delays δ = 0, 200, 400, 600 ms. Gaussian

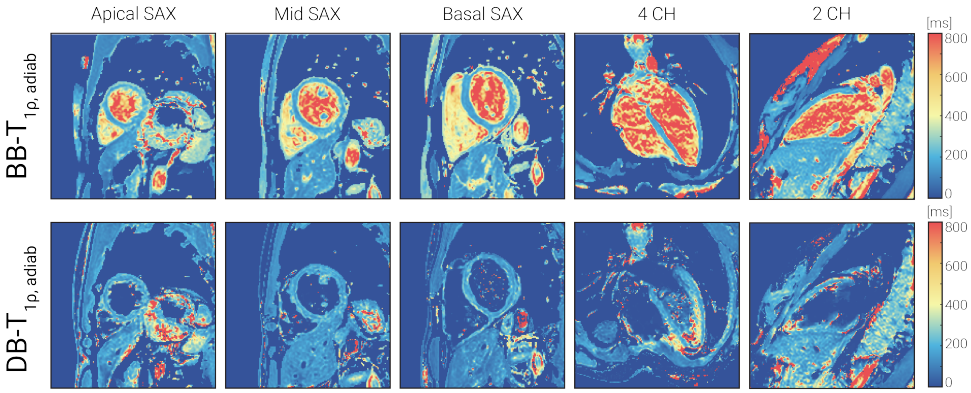

Figure 5.4 : Mid short-axis (SAX), four chambers (4CH) and two chambers (2CH) bright-blood (BB)- and dark-blood (DB)-$T_{1\rho,\mathrm{adiab}}$ maps in a representative healthy subject. Both BB- and DB-$T_{1\rho,\mathrm{adiab}}$ maps achieved good visual map quality, with homogeneous values across the myocardium and no visible artifacts. DB-$T_{1\rho,\mathrm{adiab}}$ maps display thorough suppression of the signal from the blood pool in SAX and 2CH view. Incomplete blood suppression is evident in the 4CH view, where the primary blood flow is directed within the labeling slab.

5

noise was added to the simulated baseline signal, corresponding to an imaging SNR of 20. The resulting BB- and DB-$T_{1\rho,\mathrm{adiab}}$ values were averaged over one hundred simulation runs.

The performance of BB- and DB-$T_{1\rho,\mathrm{adiab}}$ mapping in voxels with blood/myocardium partial-voluming was also investigated in the healthy subject cohort. Automatically segmented myocardial ROIs in all three repetitions of the three short-axis slices were eroded or dilated from the inner border with a circular element of up to 6 mm radii to progressively exclude or include voxels with potential partial-voluming. BB- and DB-$T_{1\rho,\mathrm{adiab}}$ values for each erosion/dilation case were averaged first over the myocardial ROI and then across all slices, repetitions, and subjects. The final mean BB- and DB-$T_{1\rho,\mathrm{adiab}}$ values for each erosion/dilation case were reported with the standard deviation of their mean ROI values across slices, repetitions, and subjects.

Finally, the apparent myocardial thickness was compared between BB- and DB-$T_{1\rho,\mathrm{adiab}}$ short-axis maps for all healthy subjects. The thickness was estimated by considering 5° circular sectors centered in the central point of the segmented myocardium ROI. In these sectors, the number of voxels with $T_{1\rho,\mathrm{adiab}}$ values that lie within the ± 15% interval around the mean myocardial $T_{1\rho,\mathrm{adiab}}$ value of each map was counted. The thickness was then averaged over all circular myocardial sectors to obtain the final myocardial thickness estimate. Left-tailed pair-wise Mann-Whitney U-tests were used to assess whether DB-$T_{1\rho,\mathrm{adiab}}$ maps yielded larger myocardial thickness than BB-$T_{1\rho,\mathrm{adiab}}$ maps. P-values smaller than 0.05 were considered significant.

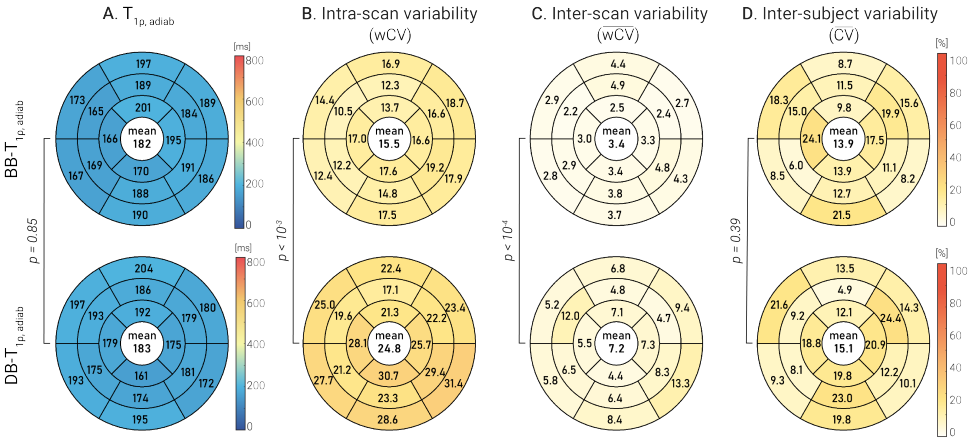

Figure 5.5 : A) Bullseye plots showing BB- and DB-$T_{1\rho,\text{adiab}}$ values, averaged over all subjects and repetitions, for 16 AHA myocardial segments. Both BB- and DB-$T_{1\rho,\text{adiab}}$ values are homogeneous across the 16 segments. No statistical difference was observed between BB- and DB-$T_{1\rho,\text{adiab}}$ values. Bullseye plots reporting B) the average intra-scan variability (wCV), C) the average inter-scan variability ($\overline{wCV}$) and D) the inter-subject variability ($\overline{CV}$) coefficients for BB- and DB-$T_{1\rho,\text{adiab}}$ maps in 16 AHA myocardial segments.

Patients $T_{1\rho,\text{adiab}}$ mapping

Clinical feasibility of BB and DB-$T_{1\rho,\text{adiab}}$ mapping sequences was tested in a cohort of seven patients (2 male, 5 female, 52.80±12.32 y.o.) referred to clinical CMR. Patients were imaged using clinical protocol sequences, including native MOLLI T_1 mapping (in-plane resolution = 1.1×1.1mm^2, FOV = 350×350mm^2, slice thickness = 10mm, TE/TR = 0.99/2.14 ms, SENSE = 2), native Gradient Spin Echo (GraSE) T_2 mapping (in-plane resolution = 1.4×1.4mm^2, FOV = 220×220mm^2, slice thickness = 8mm, TE/TR = 92/967 ms, SENSE = 2), and LGE imaging (inversion recovery spoiled Gradient Echo, PSIR, in-plane resolution = 0.7×0.7mm^2, FOV = 320×320mm^2, slice thickness = 8mm, TE/TR = 2.0/3.50 ms, SENSE = 2), performed 10-15 minutes after injection of 0.15 mmol/kg of Gadobutrol (Gadovist, Bayer Schering, Berlin, Germany). BB- and DB-$T_{1\rho,\text{adiab}}$ mapping were performed before contrast administration in a single mid-short-axis slice in all patients and a four-chamber view in four of the seven patients. The same image registration used for healthy subjects was applied to the $T_{1\rho,\text{adiab}}$ maps of patients. Manual segmentation was performed to extract myocardial $T_{1\rho,\text{adiab}}$, T_1 and T_2 in the septum.

5.3. Results

5.3.1. Phantom validation

In visual assessment, phantom $T_{1\rho,\text{adiab}}$ maps obtained with the BB and DB techniques appear free from artifacts and with homogeneous quantification within the vials. Quantitative analysis showed good agreement between DB-$T_{1\rho,\text{adiab}}$ and BB-$T_{1\rho,\text{adiab}}$ values (BB-$T_{1\rho,\text{adiab}}$ = 219.27 ± 4.80 ms, DB-$T_{1\rho,\text{adiab}}$ = 218.09 ± 8.22 ms for the myocardium-like vial #4, BB-$T_{1\rho,\text{adiab}}$ = 893.94 ± 51.81 ms, DB-$T_{1\rho,\text{adiab}}$ = 902.49 ± 55.93 ms in the blood-like vial #8).

In the native myocardium-like vials (vials #4: T_1 = 1260 ms, #5: T_1 = 1499 ms, #6: T_1 = 1010 ms in Figure 5.3 [351]), DB-$T_{1\rho,\text{adiab}}$ maps showed a moderate increase in intra-scan variability compared with BB-$T_{1\rho,\text{adiab}}$ maps as shown in Figure 5.3B (DB-$T_{1\rho,\text{adiab}}$ $wCV_{i,r}$ = 3.46 ± 0.41%, BB-$T_{1\rho,\text{adiab}}$ $wCV_{i,r}$ = 2.24 ± 0.23%, $p < 0.01$). For shorter T_1, larger differences in intra-scan variability were observed with the DB-$T_{1\rho,\text{adiab}}$ mapping technique (DB-$T_{1\rho,\text{adiab}}$ $wCV_{i,r}$ =12.21 ± 6.58%, BB-$T_{1\rho,\text{adiab}}$ $wCV_{i,r}$ = 2.75 ± 0.23%, $p < 10^{-4}$) in vials #1 (T_1 = 424 ms), #2 (T_1 = 555 ms), #3 (T_1 = 294 ms), #7 (T_1 = 451 ms) and #9 (T_1 = 250 ms). This indicated a smaller dynamic range in the DB-technique, following increased T_1 relaxation during the preparation delay. On the other hand, the blood-like vial (#8, T_1 = 1872 ms), characterized by very high T_1 yielded no significant difference in intra-scan variability between BB- and DB-$T_{1\rho,\text{adiab}}$ maps ((DB-$T_{1\rho,\text{adiab}}$ $wCV_{i,r}$ =6.08 ± 0.44%, BB-$T_{1\rho,\text{adiab}}$ $wCV_{i,r}$ = 5.80 ± 0.55%, $p = 0.06$).

The inter-scan variability followed similar but attenuated trends as the intra-scan variability for both BB- and DB-$T_{1\rho,\text{adiab}}$ values (myocardium like vials #4-6: DB-$T_{1\rho,\text{adiab}}$ $\overline{wCV_i}$ = 0.68 ± 0.06%, BB-$T_{1\rho,\text{adiab}}$ $\overline{wCV_i}$ = 0.39 ± 0.04%, p = 0.07; post-contrast tissue vials #1-3, #7 and #9: DB-$T_{1\rho,\text{adiab}}$ $\overline{wCV_i}$ = 3.55 ± 2.20%, BB-$T_{1\rho,\text{adiab}}$ $\overline{wCV_i}$ = 0.63 ± 0.16%, p = 0.04; blood-like vial #8: DB-$T_{1\rho,\text{adiab}}$ $\overline{wCV_i}$ = 1.17%, BB-$T_{1\rho,\text{adiab}}$ $\overline{wCV_i}$ = 1.31%).

5.3.2. In vivo $T_{1\rho,\text{adiab}}$ mapping

Figure 5.4 displays BB- and DB-$T_{1\rho,\text{adiab}}$ maps of a healthy volunteer in multiple orientations. Both DB and BB techniques show homogeneous $T_{1\rho,\text{adiab}}$ values across the myocardium, with no visually apparent artifacts. The subject's heart rate was on average 62 bpm, allowing a preparation delay δ = 610 ms and near-complete blood suppression in DB-$T_{1\rho,\text{adiab}}$ maps. Only areas of stagnant flow present residual blood signal intensity, as evident in the apical region of the four-chamber and two-chamber views. Moreover, blood suppression appears less effective in the four-chamber view left ventricle, where the flow is primarily directed parallel to the slice encoding direction.

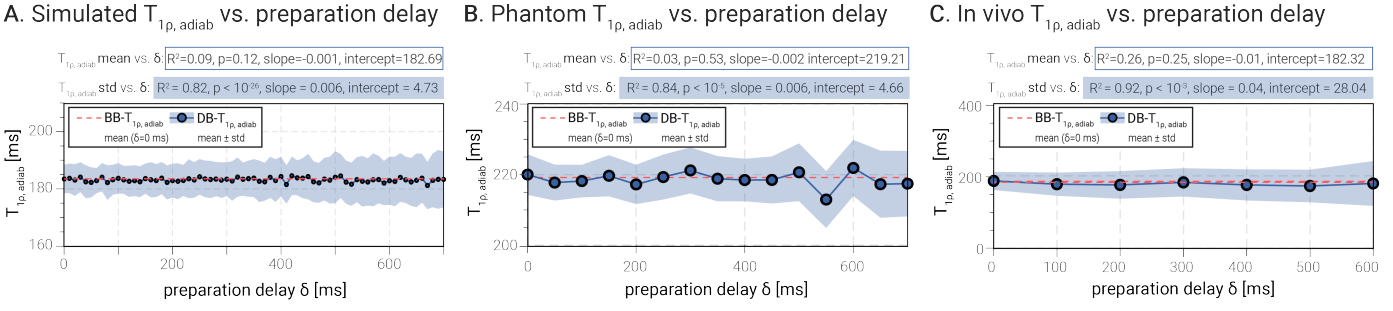

D. In vivo DB-$T_{1\rho, adiab}$ baselines and maps vs. preparation delay

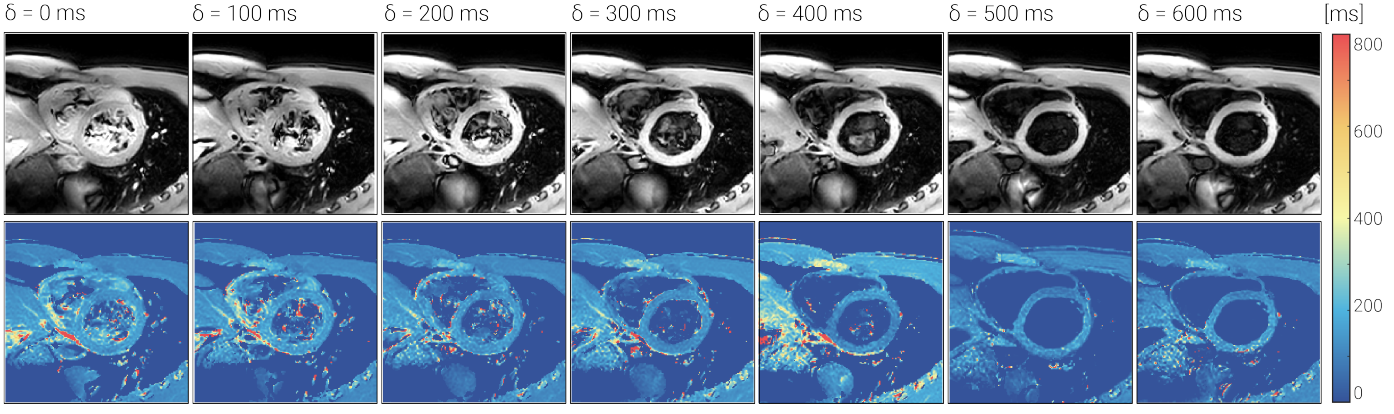

Figure 5.6 : Measured dark-blood (DB)-$T_{1\rho,\text{adiab}}$ values (blue dots) for varying preparation delay δ compared with reference bright-blood (BB)-$T_{1\rho,\text{adiab}}$ technique (dashed red line) in A) Bloch simulations ($T_1/T_2/T_{1\rho,\text{adiab}}$ = 1165/45/183 ms), B) phantom imaging (vial #4: T_1/T_2 = 1260/48 ms) and C) in-vivo imaging in the mid-short-axis of a healthy volunteer (male, 27 y.o.). Mean DB-$T_{1\rho,\text{adiab}}$ values remained approximately constant for increasing preparation delays. DB-$T_{1\rho,\text{adiab}}$ standard deviation increased linearly with the preparation delay. D) Example DB-$T_{1\rho,\text{adiab}}$ baseline image (for τ_{SL}=60 ms) and corresponding maps obtained in a single healthy volunteer for increasing preparation delays δ. At short delays clearly marked residual signal was obtained from the blood pool, while blood suppression visually improved for longer preparation delays.

No significant difference was found between BB- and DB-$T_{1\rho,\text{adiab}}$ myocardial values across the healthy volunteers ($p = 0.85$). Average BB-$T_{1\rho,\text{adiab}}$ across all volunteers and all three short-axis slices was 182.32 ± 28.27 ms, compared with 183.49 ± 45.54 for DB-$T_{1\rho,\text{adiab}}$. Both BB- and DB-$T_{1\rho,\text{adiab}}$ values were homogeneous across all myocardial segments, as shown in Figure 5.5. DB-$T_{1\rho,\text{adiab}}$ maps showed visually improved myocardium-blood pool delineation. Additionally, blood signal suppression in the DB technique also allowed better visualization of the thin RV myocardial wall (Figure 5.4).

DB-$T_{1\rho,\text{adiab}}$ maps showed a moderate increase in intra-scan variability compared with BB-$T_{1\rho,\text{adiab}}$ in vivo: $wCV_{i,r}$ = 15.51 ± 2.65 % for BB-$T_{1\rho,\text{adiab}}$, $wCV_{i,r}$ = 24.82 ± 4.18 % for DB-$T_{1\rho,\text{adiab}}$, $p < 10^{-3}$. Similarly, inter-scan variability was higher for DB-$T_{1\rho,\text{adiab}}$ maps ($\overline{wCV_i}$ = 3.38 ± 0.86 % for BB-$T_{1\rho,\text{adiab}}$, $\overline{wCV_i}$ = 7.24 ± 2.55 % for DB-$T_{1\rho,\text{adiab}}$, $p < 10^{-4}$). Finally, a trend of increased inter-subject variability with DB-$T_{1\rho,\text{adiab}}$ mapping was observed, but no statistical significance was observed ($\overline{CV}$ = 13.89 ± 5.27 % for BB-$T_{1\rho,\text{adiab}}$, $\overline{CV}$ = 15.13 ± 6.05 % for DB-$T_{1\rho,\text{adiab}}$, $p = 0.39$).

Blood suppression

In simulations, the estimated DB-$T_{1\rho,\text{adiab}}$ value remained constant across various preparation delays δ, as the T_1 recovery experienced during the preparation delay is captured by the remaining two fit parameters A and B (see Supporting Information Figure 5.S1). Accordingly, Bloch simulation and phantom results show no trend in DB-$T_{1\rho,\text{adiab}}$ for increasing preparation delays (simulations R^2 = 0.089, $p = 0.12$, slope = -0.0011, intercept = 182.69; phantom R^2 = 0.03, $p = 0.53$, slope = -0.0017, intercept = 219.21). Good agreement with the reference BB-$T_{1\rho,\text{adiab}}$ sequence was achieved for all preparation delays, with deviations of less than 3 ms for all preparation delays, except for δ = 550 ms in phantom (Figure 5.6A-B). At the same time, the dynamic range is noticeably decreased for increasing preparation delays (Figure 5.S1). Accordingly, increased standard deviation of the

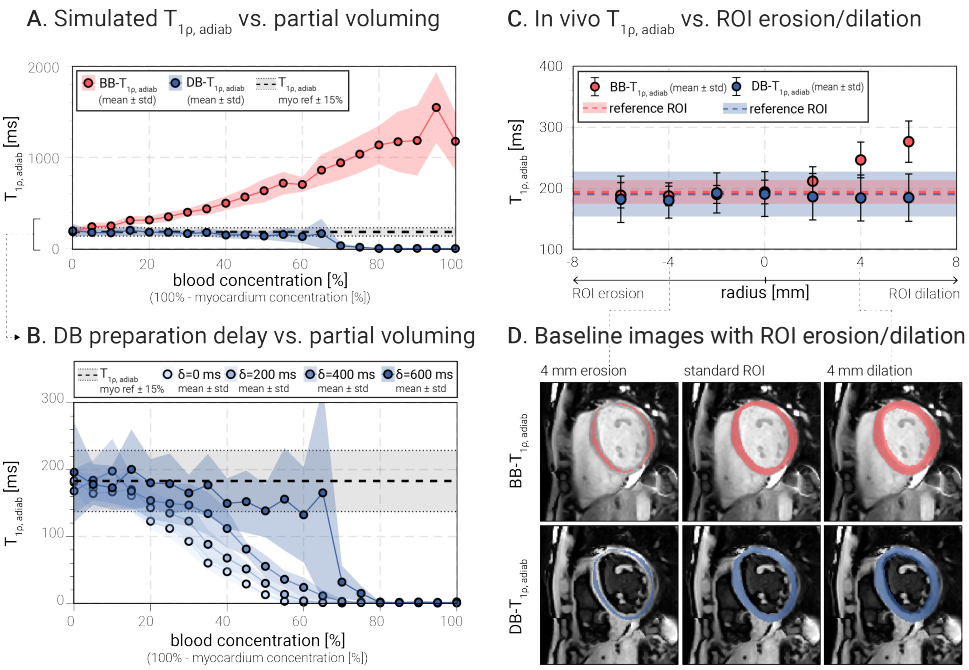

Figure 5.7 : A) Simulated bright-blood (BB)- (red) and dark-blood (DB)-$T_{1\rho,\text{adiab}}$ (blue) values for varying voxel compositions (mean ± standard deviation) compared with the reference ±15% deviation interval (gray shading) from the value obtained for 100% blood composition (black dashed line). BB-$T_{1\rho,\text{adiab}}$ values showed a strong non-linear increase for increasing blood concentration in voxels with partial-voluming. DB-$T_{1\rho,\text{adiab}}$ mapping showed reduced dependence on blood concentration. B) Zoomed-in plot showing DB-$T_{1\rho,\text{adiab}}$ values in the presence of partial-voluming for preparation delay δ = 0, 200, 400, 600 ms. Shorter preparation delays led to a progressively stronger dependence of DB-$T_{1\rho,\text{adiab}}$ values on the blood concentration. C) BB- and DB-$T_{1\rho,\text{adiab}}$ values obtained in vivo by using D) eroded and dilated myocardial ROIs. DB-$T_{1\rho,\text{adiab}}$ values remained within the reference interval for each case of dilation and erosion, while increasing BB-$T_{1\rho,\text{adiab}}$ values were measured with ROI dilation.

DB-$T_{1\rho,\text{adiab}}$ values was observed for increasing preparation delay δ (simulations $R^2 = 0.82$, $p < 10^{-26}$, slope = 0.0061, intercept = 4.73; phantom $R^2 = 0.84$, $p < 10^{-5}$, slope = 0.0060, intercept = 4.66).

The same trends were observed in the myocardial DB-$T_{1\rho,\text{adiab}}$ values obtained in a single healthy subject with different preparation delays (Figure 5.6C). The mean value showed no significant trend as a function of the delay time ($R^2 = 0.26$, $p = 0.25$, slope = -0.011, intercept = 182.32) and good agreement with the BB-$T_{1\rho,\text{adiab}}$ reference value (deviation < 16 ms for all preparation delays, Figure 5.6C). Intra-scan variability increased from 13.44% for 0 ms delay time to 26.25% at 600 ms delay time ($R^2 = 0.92$, $p < 10^{-3}$, slope = 0.035, intercept = 28.04). The blood signal suppression was visually improved at longer

delay times (Figure 5.6D). At short delays, substantial residual signal from the blood was obtained, particularly in areas of slow or stagnant flow, such as the right ventricular trabeculation or around the papillary muscles. At longer delay times, where more longitudinal magnetization recovery brings the signal of the inverted blood close to the zero crossing, complete blood suppression was observed. This was visible in both baseline images and maps (Figure 5.6D).

Myocardial thickness

Bloch simulations showed a strong non-linear increase of the BB-$T_{1\rho,\mathrm{adiab}}$ values with increasing blood concentration in voxels with partial-voluming (simulated BB-$T_{1\rho,\mathrm{adiab}}$ = 184 ms for 0% blood, 1386 ms for 100% blood, Figure 5.7A). Partial-voluming with more than 5% blood in a voxel, caused more than 15% deviation from the simulated $T_{1\rho,\mathrm{adiab}}$ time in the BB technique. On the other hand, DB-$T_{1\rho,\mathrm{adiab}}$ mapping showed reduced sensitivity to blood concentration. For a preparation delay of δ = 600 ms, deviations of less than 15% were observed in the presence of up to 65% blood concentration. Shorter preparation delays led to a progressively stronger dependence of DB-$T_{1\rho,\mathrm{adiab}}$ values on the blood concentration. With a blood concentration of 50% in the voxel, the DB-$T_{1\rho,\mathrm{adiab}}$ deviation from the 0% blood case was 88% for δ = 0 ms, 59% for δ = 200 ms, 31% for δ = 400 ms, and 6% for δ = 600 ms.

Figure 5.7C shows the BB- and DB-$T_{1\rho,\mathrm{adiab}}$ trends for eroded and dilated myocardial ROI in the healthy subjects cohort. Both BB- and DB-$T_{1\rho,\mathrm{adiab}}$ values vary less than 1 std from the value obtained for the automatic segmentation for all erosion cases. DB-$T_{1\rho,\mathrm{adiab}}$ values also remained within the reference interval defined by ±1 std for each case of dilation (DB-$T_{1\rho,\mathrm{adiab}}$ deviation from reference for 6 mm dilation: -7.15±3.04%). Altered BB-$T_{1\rho,\mathrm{adiab}}$ values were observed for ROI dilation, with an increase of +16.48±4.91% for a dilation radius of 2 mm and up to +47.8±15.85% for a dilation radius of 6 mm.

Figure 5.8A-B depicts the BB- and DB-$T_{1\rho,\mathrm{adiab}}$ profile, plotted along a row of pixels cutting horizontally through the center of the left ventricle in a representative healthy subject's mid-short-axis slice. BB-$T_{1\rho,\mathrm{adiab}}$ maps show a gradual transition of the myocardium to the blood pool. Contrarily, a sharp delineation at the myocardium interface is observed for DB-$T_{1\rho,\mathrm{adiab}}$. The average myocardial thickness in DB-$T_{1\rho,\mathrm{adiab}}$ maps across all subjects and slices, measured as the width of the plateau in the profile plot, shows a +9.86±2.27% increase compared with BB-$T_{1\rho,\mathrm{adiab}}$ maps ($p = 0.02$, Figure 5.8C). Specifically, DB-$T_{1\rho,\mathrm{adiab}}$ myocardial thickness was significantly higher than the corresponding BB-$T_{1\rho,\mathrm{adiab}}$ case for mid (BB: 7.08±1.74 mm, DB: 7.95±1.53 mm) and apical (BB: 6.19±1.82 mm, DB: 7.23±1.90 mm) short-axis slices. BB and DB myocardial thickness values were not significantly different in

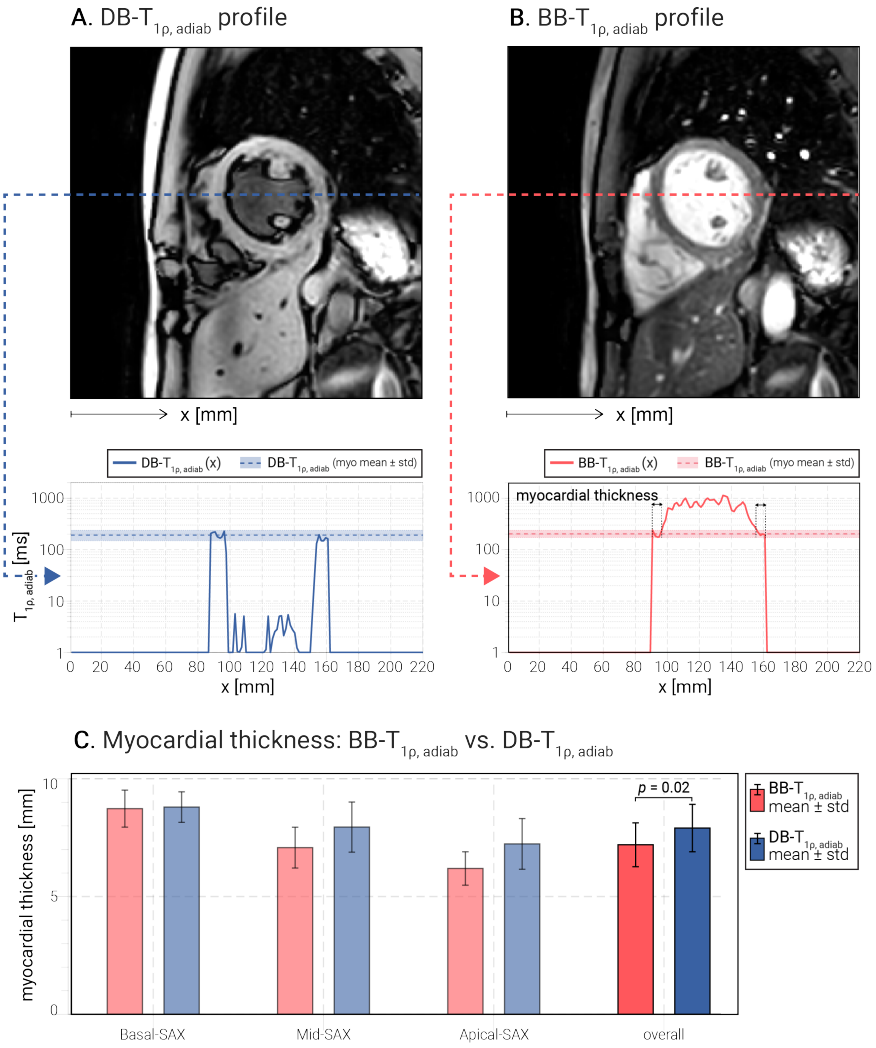

Figure 5.8 : A) Bright-blood (BB)- and dark-blood (DB)-$T_{1\rho,\text{adiab}}$ profile, illustrated along a horizontal line cutting through the center of the left ventricle, as shown on the corresponding baseline images. A sharp delineation at the myocardium interface is observed for DB-$T_{1\rho,\text{adiab}}$, while the BB-$T_{1\rho,\text{adiab}}$ profile presents a gradual transition between the myocardium and blood pool, with reduced thickness of the apparent myocardium. C) Average myocardial thickness in BB- and DB-$T_{1\rho,\text{adiab}}$ maps, measured as the width of the $T_{1\rho,\text{adiab}}$ profile plateau for 5° circular sectors and averaged over the 72 sectors around the entire myocardium. Overall, DB-$T_{1\rho,\text{adiab}}$ maps yielded a +9.86±2.27% increase in myocardial thickness compared with BB-$T_{1\rho,\text{adiab}}$ ($p = 0.02$).

the basal short-axis slice (BB: 8.73±2.16 mm, DB: 8.80±2.31 mm).

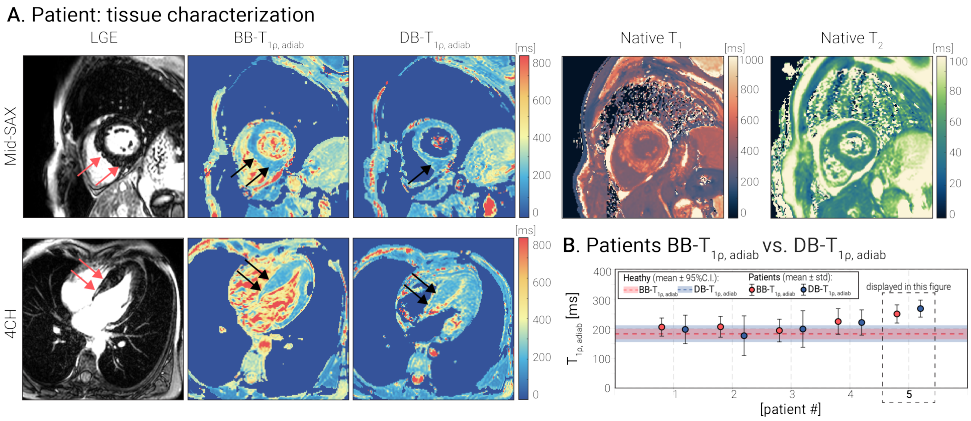

Figure 5.9 : A) Late gadolinium enhancement (LGE), bright-blood (BB)-, dark-blood (DB)-$T_{1\rho,\text{adiab}}$, T_1 and T_2 images of a 47-years-old female patient (#5) suffering from hypertrophic cardiomyopathy. LGE images show diffuse mid-wall myocardial enhancement in the mid-to-apical areas of myocardial septal hypertrophy (red arrows). BB-$T_{1\rho,\text{adiab}}$ and DB-$T_{1\rho,\text{adiab}}$ maps show $T_{1\rho,\text{adiab}}$ elevation corresponding to LGE positive regions. Residual off-resonance artifacts are visible in the infero-lateral segment of the BB- and DB-$T_{1\rho,\text{adiab}}$ short-axis maps and in the apical lateral BB-$T_{1\rho,\text{adiab}}$ 4CH segment. The native T_1 map also show diffuse and speckled enhancement, partially co-localized with LGE-positive areas, whereas the native T_2 map did not show visually discernable areas of enhancement. B) Mean BB-$T_{1\rho,\text{adiab}}$ (red) and DB-$T_{1\rho,\text{adiab}}$ (blue) mid-SAX myocardial values ± their standard deviation for all 5 patients compared with the mean ±95% confidence interval (dashed line) reference range obtained in healthy volunteers. Patient #5 (shown in A) displays increased BB-$T_{1\rho,\text{adiab}}$ and DB-$T_{1\rho,\text{adiab}}$ values above the reference 95% C.I. of healthy subjects, in agreement with the diagnosed diffuse LGE mid-wall enhancement caused by hypertrophic cardiomyopathy.

Patients $T_{1\rho,\text{adiab}}$ mapping

Two of the seven scanned patients were excluded because of severely compromised image quality in all parametric maps caused by excessive respiratory and cardiac motion. Of the remaining 5 patients, one subject was LGE-positive, with signs of fibrosis in the LV myocardium (see Supporting Information Table 1). Figure 5.9A shows the BB- and DB-$T_{1\rho,\text{adiab}}$ maps acquired in the LGE-positive patient (female, 47 y.o.), who suffered from asymmetrical hypertrophic cardiomyopathy (HCM). The patient presented diffuse mid-wall myocardial enhancement in the areas of hypertrophy (Figure 5.9A). Native T_1 maps show diffuse and speckled enhancement, partially co-localized with LGE-positive areas. Native T_2 maps did not show visually discernable areas of enhancement in the myocardium. Overall decreased visual BB- and DB-$T_{1\rho,\text{adiab}}$ map quality was observed compared with the healthy subjects due to different scanner hardware characteristics, such as the single transmit channel and the lack of advanced shim modes. Moreover, higher heart rates and heart rate variability, as well as reduced compliance to breath holding protocols could have negatively impacted image quality

in patients with respect to healthy subjects. An off-resonance artifact is visible in the infero-lateral segment of the BB- and DB-$T_{1\rho,\text{adiab}}$ short-axis maps and in the apical lateral DB-$T_{1\rho,\text{adiab}}$ 4CH segment, due to incomplete shimming. Yet, comparable image quality was observed between BB- and DB-$T_{1\rho,\text{adiab}}$ maps. Elevated $T_{1\rho,\text{adiab}}$ values were measured, spatially coinciding with the LGE positive areas. Global mean BB- and DB-$T_{1\rho,\text{adiab}}$ values in this patient were elevated compared with the rest of the patient cohort and fell above the 95% confidence interval of the reference BB- and DB-$T_{1\rho,\text{adiab}}$ values obtained in the healthy subjects (patient #5: BB-$T_{1\rho,\text{adiab}}$ = 249.98± 61.34 ms, DB-$T_{1\rho,\text{adiab}}$ = 268.01±57.44 ms; Figure 5.9B). Residual blood pool signal is observed in the mid-LV blood pool, as the high heart rate of the patient, limited the maximum allowed preparation delay to δ=480 ms.

5.4. Discussion

In this study, we proposed an adiabatic $T_{1\rho,\text{adiab}}$ mapping technique with intrinsic dark-blood contrast for myocardial tissue characterization at 3T. Dark-blood contrast was achieved through a combination of selective and non-selective AFPs, achieving $T_{1\rho,\text{adiab}}$ weighting within the labeling slab and signal inversion outside. The proposed DB-$T_{1\rho,\text{adiab}}$ mapping sequence led to an unbiased estimation of myocardial $T_{1\rho,\text{adiab}}$ values in phantoms and in vivo. Imaging in healthy volunteers and a small clinical, proof-of-principle cohort showed comparable mapping quality to BB contrast, with improved delineation of the myocardium/blood pool interface.

DB-$T_{1\rho,\text{adiab}}$ values were in line with BB-$T_{1\rho,\text{adiab}}$ values reported in this and previous studies [367], both in phantoms and in vivo. The additional T_1 recovery during the preparation delay was compensated for using an adapted saturation-prepared baseline image. The same delay used in $T_{1\rho,\text{adiab}}$-prepared images was played between the saturation preparation and the imaging block. This allowed capturing the effects of magnetization evolution during both the acquisition and the preparation delay. This additional relaxation component was then absorbed by parameters A and B of the 3-parameter model, while DB-$T_{1\rho,\text{adiab}}$ estimation remained unbiased in the presence of arbitrary preparation delay δ. Moreover, the dark-blood effect in the proposed technique relies on cross-slice inflow. Thus, unlike relaxation time-based blood suppression, it is not expected to affect intra-myocardial blood. Accordingly, good overall agreement of DB and BB $T_{1\rho,\text{adiab}}$ times was obtained in vivo. These results indicate that DB and BB protocols may allow for complimentary, and potentially cross-comparable assessment between and within patients.

Simulation results displayed a differential behavior of the DB-$T_{1\rho,\text{adiab}}$ mapping in voxels with partial-voluming for different preparation

delays. This trend appeared because the saturation baseline image was not acquired with dark-blood contrast. A combination of DIR and slice-selective saturation pulses could potentially be used to acquire the saturation-prepared image with dark-blood contrast. This warrants further investigation to eliminate residual dependence on the preparation delay and further increase the robustness of the DB-$T_{1\rho,\mathrm{adiab}}$ mapping technique in the presence of partial-voluming.

Increased preparation delays δ in the DB technique led on the one hand to compromised precision, because of the reduced dynamic range, and on the other hand to improved blood signal attenuation, due to the longer T_1 recovery after inversion. Hence, the choice of the preparation delay δ implicates a trade-off between variability and blood suppression. However, our results indicated that complete blood signal nulling is not necessary to achieve resilience against blood contributions in the voxel. Considering T_1 = 1932 ms [387] and $T_{1\rho,\mathrm{adiab}}$ = 934 ms for blood, a preparation delay $\delta \approx$ 1300 ms is required for complete blood nulling, which exceeds the typical RR duration. Nonetheless, good blood suppression was observed in vivo DB-$T_{1\rho,\mathrm{adiab}}$ maps already at intermediate preparation delays ($\delta >$ 500 ms). As the blood pool only experiences a single AFP pulse across the three DB-$T_{1\rho,\mathrm{adiab}}$-prepared dynamics its signal intensity remains largely constant. The constant blood signal is then captured in the B term of the three-parameter fit model, without biasing the estimation of the blood DB-$T_{1\rho,\mathrm{adiab}}$ (Supporting Information Figure 5.S1). Too low preparation delays, however, can compromise the precision of the DB technique in voxels with partial-voluming. Here, strong residual blood pool intensity can render the fitting susceptible to random fluctuations caused by beat-to-beat differences in flow patterns. Thus, careful consideration of the preparation delay is required to optimize the interplay between blood signal suppression and quantification precision. The results of this study suggest that moderately high δ in the range of 500-700 ms represent a good trade-off, achieving satisfactory DB contrast without significant drops in precision hindering the final mapping quality.

DB-$T_{1\rho,\mathrm{adiab}}$ mapping yielded slightly increased myocardial thickness compared to BB-$T_{1\rho,\mathrm{adiab}}$. Furthermore, due to the reduced effects of partial-voluming, increased resilience towards ROI size was observed. This trend is in agreement with previous DIR-based DB-T_2 mapping studies, reporting both visually and numerically larger (+1.43 mm) myocardial thickness in DB maps compared with BB maps [275, 388]. Increased thickness may aid in the reliable quantification in the presence of thin myocardiums, such as in the RV of patients with dilated cardiomyopathy (DCM). It can also reduce the intra-reader variability caused by variations in the placement of the myocardial ROI. Importantly, the improved visualization of the blood myocardium interface may enable reliable evaluation of the sub-endocardium. This

can be critical for the visualization and assessment of characteristic sub-endocardial scars [331]. Thus, the proposed DB technique may help distinguish scar-related myocardial $T_{1\rho,\mathrm{adiab}}$ hyperenhancement from $T_{1\rho,\mathrm{adiab}}$ enhancement caused by blood signal contributions. Further evaluation of the proposed technique in subjects with subendocardial scars in comparison to DB LGE techniques is warranted to assess its clinical use in this patient population.

5.4.1. Limitations

This study has several limitations. The initial proof-of-principle cohort demonstrated map quality that is comparable to BB-$T_{1\rho,\mathrm{adiab}}$. However, only a single patient was found to be LGE+, and no subjects with subendocardial scars were included. Furthermore, while robust image quality was obtained in the healthy volunteer cohort, overall lower image quality and residual artifacts, including off-resonance artifacts were observed in some patients, due to differences in the scanner hardware. Future studies should focus on investigating the clinical robustness, and the intra- and inter-scan variability of DB-$T_{1\rho,\mathrm{adiab}}$ and BB-$T_{1\rho,\mathrm{adiab}}$ mapping across various scanner platforms, to delineate its clinical value. Moreover, the intrinsic clinical sensitivity of adiabatic BB- and DB-$T_{1\rho,\mathrm{adiab}}$ relaxation towards scar and fibrosis needs to be studied in relevant patient cohorts. Specifically, it warrants characterization in cohorts of patients with pronounced myocardial scars, such as chronic myocardial infraction patients. This is a crucial step to evaluate the clinical value of BB and DB adiabatic $T_{1\rho,\mathrm{adiab}}$ mapping and determine its potential use for non-contrast assessment of scar.

5.5. Conclusions

In this work, a novel adiabatic DB-$T_{1\rho,\mathrm{adiab}}$ preparation was proposed as an alternative to conventional BB-$T_{1\rho,\mathrm{adiab}}$ mapping for improved visualization of the myocardium. A combination of selective and non-selective AFP pulses, effectively suppressing the blood signal and maintaining adiabatic $T_{1\rho,\mathrm{adiab}}$ contrast in the myocardium was used to generate dark-blood contrast. Phantom and in vivo mapping results showed that DB-$T_{1\rho,\mathrm{adiab}}$ preparation allowed unbiased estimation of myocardial $T_{1\rho,\mathrm{adiab}}$ values for the trade-off against moderately decreased precision. Thus, DB-$T_{1\rho,\mathrm{adiab}}$ mapping potentially represents an alternative to conventional BB-$T_{1\rho,\mathrm{adiab}}$ mapping to avoid high blood $T_{1\rho,\mathrm{adiab}}$ values overshadowing possible scar-related $T_{1\rho,\mathrm{adiab}}$ enhancement at the blood-to-myocardium interface.

5.6. Supporting Information

Table 5.S1 : Characteristics of the patients population

Patients characteristics	
Gender [F/M]	5/0
Age [years]	46.80±10.32
BMI [kg/m^2]	28.07±7.33
HR [beats/min]	67.40±11.10
CMR findings	
LGE positive	1
CMR diagnosis	
Hypertrophic cardiomyopathy	1
Non-dilated hypokinetic cardiomyopathy	1
Negative CMR	3

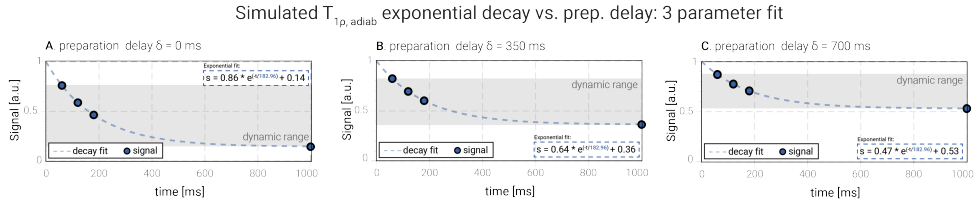

Figure 5.S1 : Simulated myocardial dark-blood (DB)-$T_{1\rho,\text{adiab}}$ signal sampled at the different baseline points ($\tau_S L$ = 60, 120, 180 ms and signal saturation) obtained for varying preparation delay A) δ = 0, B) δ = 350 and C) δ = 700 ms. The corresponding exponential fit results obtained from are displayed by the dashed blue line. For increasing preparation delay, the DB-$T_{1\rho,\text{adiab}}$ estimation remained unbiased, but the measurement dynamic range (gray area) was reduced.

6

Adiabatic spin-lock preparations for myocardial $T_{2\rho}$ mapping at 3T

Chiara Coletti, Joao Tourais, Christal van de Steeg-Henzen, Sebastian Weingärtner

Proceedings of the International Society of Magnetic Resonance in Medicine 32 (2024)

Abstract

Motivation: $T_{2\rho,adiab}$ may provide complementary information between $T_{1\rho,adiab}$ and T_2, but high sensitivity to field inhomogeneities has prevented its application in cardiac MRI.

Goal: We evaluated adiabatic $T_{2\rho,adiab}$ preparations for human myocardium mapping at 3T.

Approach: To obtain $T_{2\rho,adiab}$ preparations, adiabatic half-passage pulses were added before and after pairs of hyperbolic secant pulses. $T_{2\rho,adiab}$ mapping was tested and compared with adiabatic $T_{1\rho,adiab}$ and T_2 maps in phantoms and 5 healthy subjects.

Results: $T_{2\rho,adiab}$ maps yielded similar values to T_2, with improved repeatability and resilience to B_0 and B_1^+ field inhomogeneities in phantom, and better precision and reproducibility in vivo, complementing $T_{1\rho,adiab}$.

Impact

Adiabatic $T_{2\rho,adiab}$ preparations enable robust in vivo myocardial $T_{2\rho,adiab}$ mapping at 3T, potentially enabling the use of an alternative rotating-frame relaxation contrast mechanism for cardiac tissue characterization at high field strengths.

6.1. Introduction

Rotating frame relaxometry is gaining interest for contrast-free myocardial tissue characterization due to its sensitivity to slow and ultra-slow molecular motion [343]. Specifically, $T_{1\rho}$ mapping has shown promise in a range of ischemic and non-ischemic cardiomyopathies [12]. $T_{2\rho}$ may provide complementary information between $T_{1\rho}$ and T_2 regimes and has demonstrated improved sensitivity to iron deposition in neuroimaging compared with conventional T_2 mapping [389, 390]. However, cardiac $T_{2\rho}$ mapping studies are currently limited to animal models [391]. Furthermore, the high SAR levels required by spin-lock preparations and their sensitivity to B_0 and B_1^+ field inhomogeneities remain hindering factors for its in vivo application at high field strengths ($\geq$ 3T). In this study, we sought to evaluate adiabatic $T_{2\rho}$ preparations for myocardial $T_{2\rho,adiab}$ mapping at 3T, in comparison with adiabatic $T_{1\rho,adiab}$ and conventional T_2 mapping.

6.2. Methods

Adiabatic $T_{2\rho}$ preparations were implemented by adding adiabatic half passage (AHP) pulses before (flip-down) and after (flip-up) a $T_{1\rho}$ preparation module, consisting of pairs of hyperbolic secant (HS) adiabatic full passage (AFP) pulses, as previously proposed for cardiac $T_{1\rho}$ mapping (Figure 6.1) [367]. The pulse duration was chosen as τ_{AFP}=2 × τ_{AHP} = 20ms, to achieve good adiabaticity while allowing sufficiently dense sampling of the $T_{1\rho}/T_{2\rho}$ decay in vivo. Bloch simulations of the preparation efficiency (M_z/M_0) were used to determine the optimal HS width β and frequency sweep amplitude f_{max} over a design region with off-resonance $\in$ [-200, 200] Hz and relative $B_1^+ \in$ [0.5,1]. Adiabatically-refocused T_2 preparations were used for reference T_2 maps [341].

Imaging was performed at 3T (Ingenia, Philips). An ECG-triggered single-shot bSSFP sequence (resolution = 2x2x8 mm^3, TE/TR=1.2/2.4 ms) was used for mapping during a single 14 s breath-hold. The sequence consisted of one baseline image with no preparation, two $T_{1\rho}$, $T_{2\rho}$, or T_2-prepared baseline images (τ_{SL} = 40, 80 ms for $T_{1\rho}$, τ_{SL} = 60, 100 ms for $T_{2\rho}$, TE = 35, 55 ms for T_2), interleaved with 5 s rest period, and one saturation-prepared image (Figure 6.2). Relaxation time maps were generated using a 3-parameter model [367].

$T_{1\rho}$, $T_{2\rho}$, and T_2 mapping were performed in the T1MES phantom for artificially-induced off-resonance = -150, -75, ..., 150 Hz and relative B_1^+ = 0.25, 0.5, ..., 1 to investigate resilience against field inhomogeneities (CV_i) and repeatability (CV_r) over 10 repetitions. In vivo $T_{1\rho}$, $T_{2\rho}$, and T_2 maps were obtained for 3 short-axis (SAX) slices in 5 healthy subjects (2f, 34.2±11.6 yrs). Precision (CV_p) and reproducibility across subjects (CV_s) were measured for the 16-AHA segments. Pair-wise Mann-Whitney

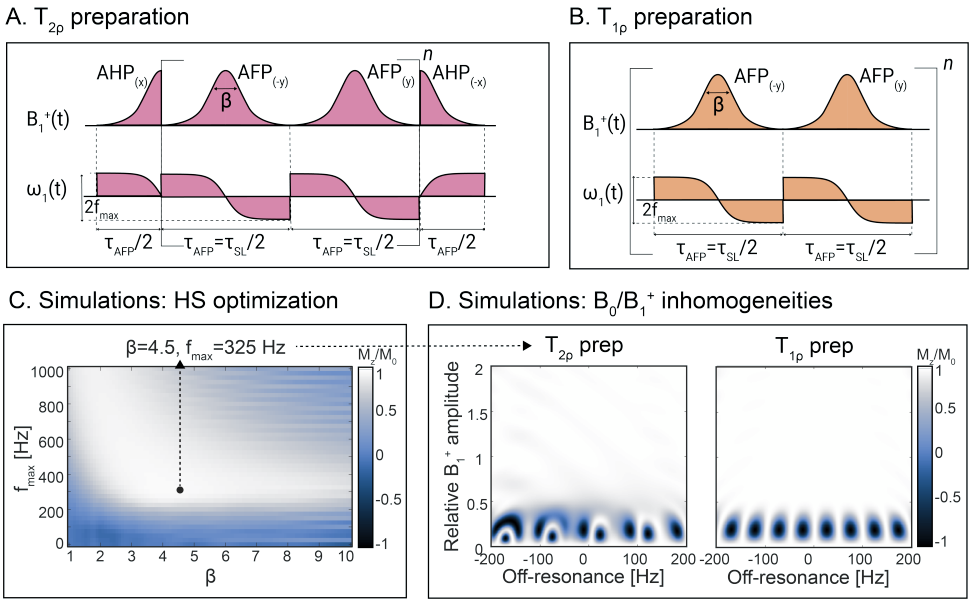

Figure 6.1 : A) $T_{2\rho,adiab}$ preparations consist of an AHP pulse (τ_{AHP}=10 ms) as flip-down, n pairs of HS AFP pulses (τ_{AFP}=20 ms), and a time-reversed flip-up AHP pulse. Phase cycling is used to compensate for B_0/B_1^+ inhomogeneities. B) $T_{1\rho,adiab}$ prep consists of n identical AFP trains. C) Bloch simulations of the preparation efficiency (M_z/M_0) over a design region of off-resonances $\in$[-200, 200] Hz and relative $B_1^+\in$[0.5, 1]. D) M_z/M_0 for the optimal parameters (β=4.5 and f_{max}=325 Hz) is shown for a range of off-resonances $\in$[-200, 200] Hz and relative $B_1^+\in$[0.5, 1]. Faint diagonal patterns of suboptimal efficiency are visible for $T_{2\rho,adiab}$ preparations.

U-tests were used to assess the statistical significance of differences between $T_{1\rho}$, $T_{2\rho}$, and T_2 mapping metrics.

6.3. Results

β=4.5 and f_{max}=325Hz were chosen as the optimal parameters for AHP and AFP pulses in $T_{1\rho}$ and $T_{2\rho}$ preparations, yielding average preparation efficiency over the design region of 0.99 and 0.95, respectively (Figure 6.1C-D). Average values in the myocardium-like phantom vial were: $T_{1\rho}$ = 115.2±5.4 ms, $T_{2\rho}$ = 58.1±1.6 ms, T_2 = 55.3±3.1 ms (Figure 6.3). In phantom $T_{2\rho}$ maps yielded better precision than T_2 (CV_p = 2.7 vs 5.6%), comparable repeatability (CV_r = 0.5 vs 0.8%), and higher resilience against B_0 and B_1^+ inhomogeneities (CV_i = 18.9 vs 67.2%). In vivo $T_{1\rho}$, $T_{2\rho}$, and T_2 maps showed good quality and homogeneous myocardial values (Figure 6.4). However, T_2 maps presented residual off-resonance artifacts in some volunteers. Average myocardial values were: $T_{1\rho}$ = 108.0±15.9 ms, $T_{2\rho}$ = 43.2±6.8 ms,T_2 = 40.8±15.5 ms (Figure 6.5). Overall, $T_{2\rho}$ maps yielded worse precision

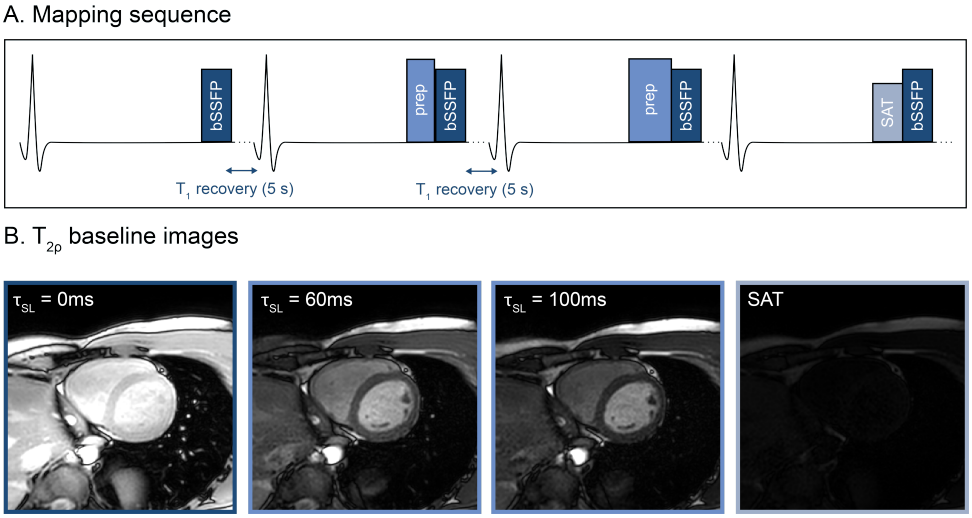

Figure 6.2 : A) $T_{1\rho,adiab}$, $T_{2\rho,adiab}$ or T_2 mapping sequence, consisting of 4 end-diastolic ECG-triggered bSSFP acquisitions (one with no preparation, two preceded by $T_{1\rho,adiab}$, $T_{2\rho,adiab}$ or T_2 preparations and a saturation-prepared image) with B) the corresponding baseline images for a representative $T_{2\rho,adiab}$ map. All but the saturation-prepared image are interleaved by 5 s pause to allow magnetization recovery. The entire acquisition is performed during a 14 s breath-hold. Other sequence parameters were: flip Angle=70°, resolution=2x2x8 mm^3, FOV=220x220 mm^2, TE/TR=1.2/2.4 ms, SENSE factor=2.

(CV_p = 16.4% vs 14.8%, p = 0.04) and reproducibility (CV_s = 14.4% vs 6.1%, p <0.01) than $T_{1\rho}$, but significantly better than T_2 (CV_p = 32.1%, p <10^{-3}; CV_s = 17.6%, p = 0.02).

6.4. Discussion

In this work, we investigated the use of adiabatic $T_{2\rho}$ preparations for rotating frame relaxometry of the myocardium at 3T.

Similarly to adiabatic $T_{1\rho}$, adiabatic $T_{2\rho}$ preparations apply a temporally-varying effective field. Consequently, adiabatic $T_{2\rho}$ relaxation is sensitive to interactions across a spectrum of frequencies, contrary to conventional spin-locks or pure T_2 mapping. Thus, its sensitivity to pathological alterations warrants further investigation in clinical studies.

T_2 mapping is commonly measured using T_2 preparations with lengthy adiabatic refocusing pulses to ensure B_0 and B_1^+ resilience. During those pulses, the magnetization is subject to $T_{2\rho}$ decay, yielding a mixed contrast. To assess the T_2 decay exclusively during free relaxation, long preparations are required, limiting the dynamic range of the measurement. Adiabatic $T_{2\rho}$ mapping, on the other hand, allows for prolonged adiabatic pulses, while staying true to the definition of its

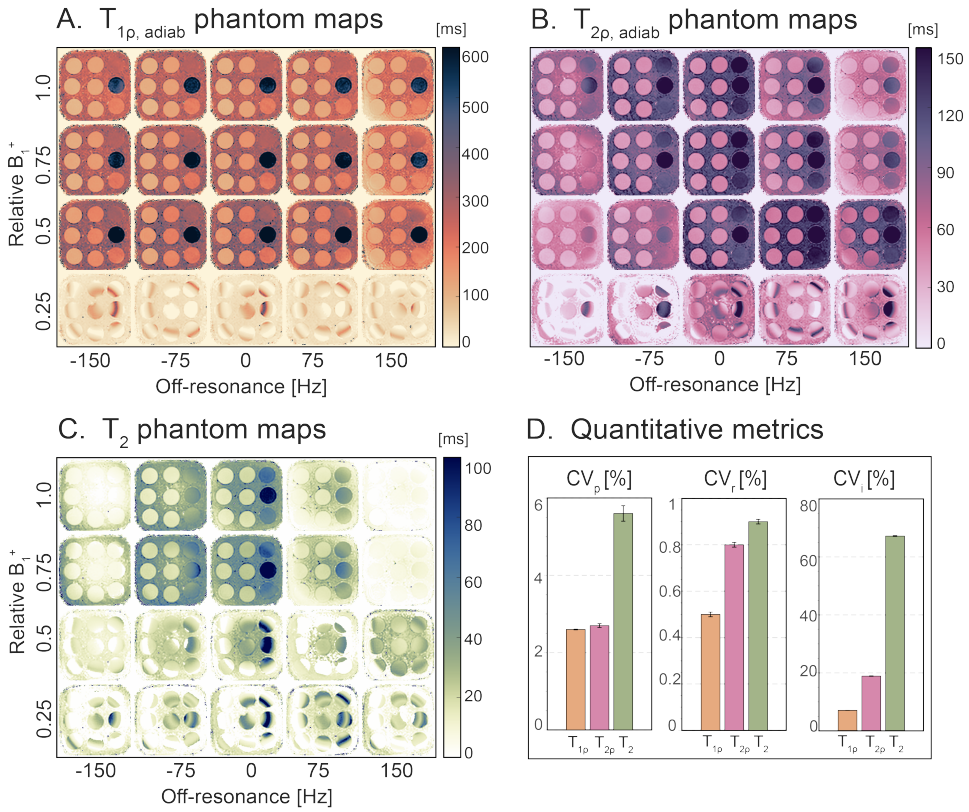

Figure 6.3 : A) $T_{1\rho,adiab}$, B) $T_{2\rho,adiab}$ and C) T_2 maps obtained in the T1MES phantom for off-res.=-150,-75,...,150 Hz and rel.B_1^+=0.25,0.5,...,1 values. $T_{1\rho,adiab}$ and $T_{2\rho,adiab}$ maps show resilience against B_1^+ variations up to 0.5, but $T_{1\rho,adiab}$ shows better resilience against B_0 inhomogeneities than $T_{2\rho,adiab}$. T_2 maps are compromised in all off-resonance cases and rel.B_1^+<0.75. D) Precision, repeatability, and resilience against B_0 and B_1^+ inhomogeneities averaged over all 9 vials. Repeatability is comparable for $T_{1\rho,adiab}$, $T_{2\rho,adiab}$ and T_2 maps, while $T_{1\rho,adiab}$ and $T_{2\rho,adiab}$ yield better precision and resilience against inhomogeneities than T_2.

measurand. Therefore, $T_{2\rho}$ mapping may present a promising alternative to T_2 mapping, with increased resilience against field inhomogeneities and the promise of improved reproducibility.

6.5. Conclusions

The proposed adiabatic $T_{2\rho}$ sequence enabled myocardial parameter mapping with high resilience against B_0 and B_1^+ inhomogeneities and could represent a complementary relaxation parameter to $T_{1\rho}$, suitable for mapping at high field strengths.

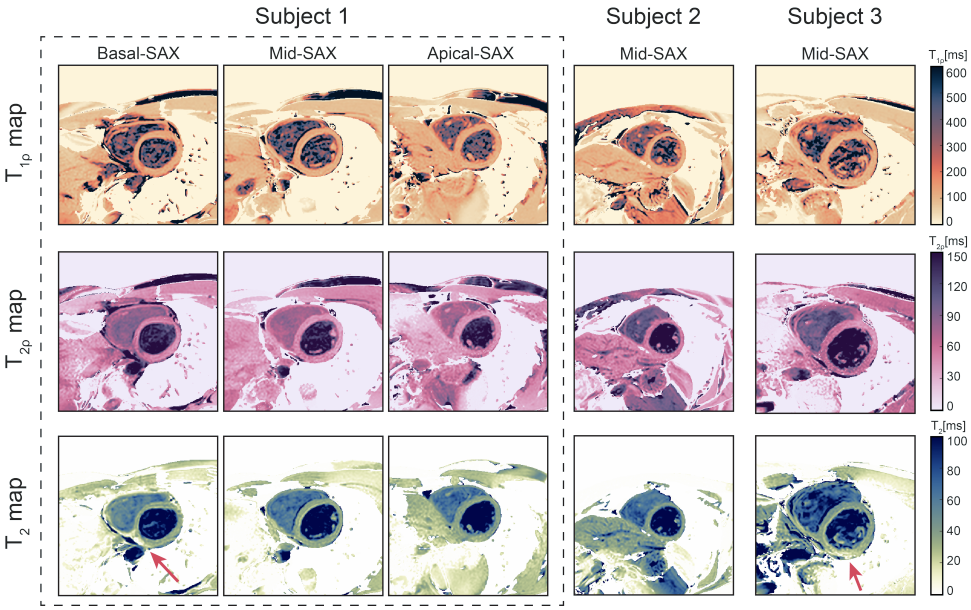

Figure 6.4 : A) In vivo cardiac short-axis (SAX) $T_{1\rho,adiab}$, $T_{2\rho,adiab}$ and T_2 maps for three representative healthy subjects (three SAX slices are displayed for subject 1). Good image quality is observed for all maps. Homogeneous $T_{1\rho,adiab}$, $T_{2\rho,adiab}$ and T_2 values are observed across the myocardium, except for off-resonance-related artifacts appearing in the T_2 basal inferior segment of subject 1 and mid-inferior segment of subject 3 (red arrow).

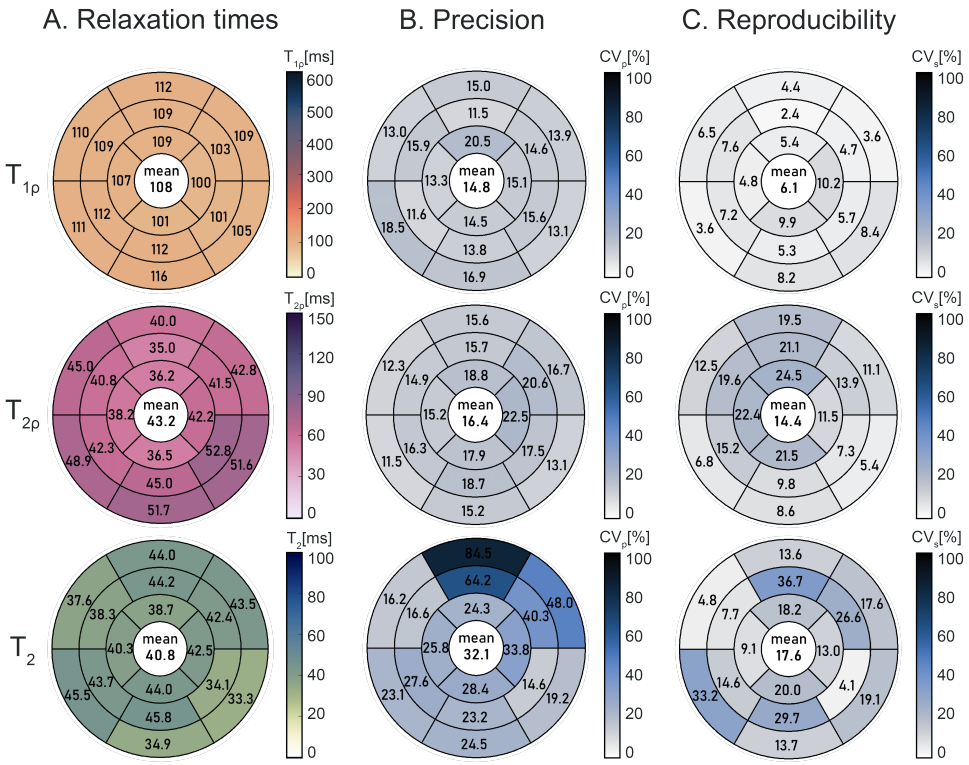

Figure 6.5 : Bullseye plot depicting A) measured $T_{1\rho,adiab}$, $T_{2\rho,adiab}$ and T_2 relaxation times, B) precision and C) inter-subject variability across all 5 subjects in the 16 AHA myocardial segments. Overall, $T_{2\rho,adiab}$ values are closer to T_2 than $T_{1\rho,adiab}$. On average, $T_{2\rho,adiab}$ maps yielded slightly worse precision ($p = 0.04$) and worse reproducibility ($p<10^{-2}$) than $T_{1\rho,adiab}$. However, $T_{2\rho,adiab}$ performed significantly better than T_2 terms of precision ($p<10^{-3}$) and reproducibility ($p = 0.02$).

7

Generalized inhomogeneity-resilient relaxation along a fictitious field (girRAFF) for improved robustness in rotating frame relaxometry at 3T

Chiara Coletti[†], Roeland Naaktgeboren[†], Joao Tourais, Christal van de Steeg-Henzen, Sebastian Weingärtner

Magnetic Resonance in Medicine, (2024): pp. 1-19,
doi: https://doi.org/10.1002/mrm.30219

[†]These authors contributed equally

Abstract

Purpose To optimize Relaxation along a Fictitious Field (RAFF) pulses for rotating frame relaxometry with improved robustness in the presence of B_0 and B_1^+ field inhomogeneities.

Methods The resilience of RAFF pulses against B_0 and B_1^+ inhomogeneities was studied using Bloch simulations. A parameterized extension of the RAFF formulation was introduced and used to derive a generalized inhomogeneity-resilient RAFF (girRAFF) pulse. RAFF and girRAFF preparation efficiency, defined as the ratio of the longitudinal magnetization before and after the preparation ($M_z(T_p)/M_0$), were simulated and validated in phantom experiments. T_{RAFF} and $T_{girRAFF}$ parameter maps were acquired at 3T in phantom, the calf muscle, and the knee cartilage of healthy subjects. The relaxation time maps were analyzed for resilience against artificially induced field inhomogeneities and assessed in terms of in vivo reproducibility.

Results Optimized girRAFF preparations yielded improved preparation efficiency (0.95/0.91 simulations/phantom) with respect to RAFF (0.36/0.67 simulations/phantom). $T_{girRAFF}$ preparations showed in phantom/calf 6.0/4.8 times higher resilience to B_0 inhomogeneities than RAFF, and a 4.7/5.3 improved resilience to B_1^+ inhomogeneities. In the knee cartilage, $T_{girRAFF}$ (53±14 ms) was higher than T_{RAFF} (42±11 ms). Moreover, girRAFF preparations yielded 7.6/4.9 times improved reproducibility across B_0/B_1^+ inhomogeneity conditions, 1.9 times better reproducibility across subjects and 1.2 times across slices compared with RAFF. Dixon-based fat suppression led to a further 15-fold improvement in the robustness of girRAFF to inhomogeneities.

Conclusions RAFF pulses display residual sensitivity to off-resonance and pronounced sensitivity to B_1^+ inhomogeneities. Optimized girRAFF pulses provide increased robustness and may be an appealing alternative for applications where resilience against field inhomogeneities is required.

7.1. Introduction

Quantitative Magnetic Resonance Imaging (MRI) is a rapidly growing research area as it enables intra-subject comparable tissue characterization [1, 353, 392, 393]. Conventional MRI relaxation times, T_1 and T_2, are most commonly used [394]. Rotating frame relaxation times, such as $T_{1\rho}$, offer complementary contrast information to T_1 and T_2, with increased sensitivity to slow molecular motion and chemical exchange [321, 395–399].

$T_{1\rho}$ describes the longitudinal relaxation in a rotating frame of reference (RFR), commonly measured during radiofrequency (RF) irradiation through continuous-wave spin-lock (SL) pulses. However, these SL pulses require a high specific absorption rate (SAR) burden and are highly susceptible to field inhomogeneities [337, 400]. This hinders their applicability in clinical practice, especially at high field strengths (≥3T). Improved resilience against field inhomogeneities can be achieved with adiabatic $T_{1\rho}$ [72, 73, 340, 367]. However, the pulses in adiabatic $T_{1\rho}$ commonly exhibit a non-constant effective and fictitious field, leading to differences in sensitivity compared with conventional SL pulses [342, 343].

To surmount the SAR constraints of continuous-wave SL while still exhibiting favorable sensitivity to slow molecular motion, Relaxation Along a Fictitious Field (RAFF) was proposed [401]. RAFF pulses are amplitude- and frequency-modulated (AM and FM) pulses that operate in a sub-adiabatic regime [401]. During the RAFF pulse, the behavior of the magnetic field can be described in a double-RFR, where the effective field in the second RFR acts as a spin-locking field [340]. Thus, RAFF generalizes spin-locking for higher-order rotating frames, while $T_{1\rho}$ operates in the first RFR. This allows for larger spin-locking field amplitude by increasing only the fictitious field component while maintaining the effective field amplitude within SAR limits [402]. T_{RAFF} times have shown promise for tissue characterization in a number of preclinical and clinical studies across various field strengths [119, 403–409]. While conventional RAFF pulses have shown moderate resilience against B_0 inhomogeneities, they exhibit high sensitivity to B_1^+ variations [401, 410]. Resilience against off-resonances can be improved by using RAFF in higher-order rotating frames (RAFFn) [410], but sensitivity to B_1^+ inhomogeneity remains a barrier to widespread clinical use.

In this study, we characterize the performances of RAFF pulses in the presence of B_0 and B_1^+ variations at 3T. Next, we introduce a parametric formulation of the conventional RAFF pulse to enable tailored off-resonance and B_1^+ resilience. Based on this we propose a Generalized inhomogeneity-resilient RAFF (girRAFF) pulse to improve both B_0 and B_1^+ resilience. Data acquired in phantom and in the calf muscle of healthy subjects are used to compare the performances of

conventional RAFF and optimized girRAFF preparations in the presence of field inhomogeneities. Quantitative mapping quality and robustness to system imperfections are compared for RAFF and girRAFF pulses in the knee cartilage. Finally, the reproducibility of quantitative mapping using RAFF and girRAFF is assessed in the calf and the articular cartilage of healthy subjects.

7.2. Methods

7.2.1. girRAFF Pulse Design

RAFF pulses are amplitude and frequency-modulated RF pulses designed to achieve constant and equal effective ($B_{eff}(t)$) and fictitious field ($F(t)$) in the second RFR [401]:

$$F(t) \triangleq \gamma^{-1}\frac{d\alpha(t)}{dt} = B_{eff}(t). \tag{7.1}$$

Here, γ is the gyromagnetic ratio and $\alpha(t)$ indicates the tilt angle of the effective field $B_{eff}(t)$ relative to the z'-axis in the first RFR. The first RFR is defined by convention as rotating with the time-variant SL pulse frequency $\omega_1(t)$ around the z-axis of the laboratory frame of reference ($z = z'$). The second RFR, instead, is defined as rotating around y' with $B_{eff}(t)$, such that $y' = y''$ and $B_{eff}(t)$ is locked on z''. The fictitious field $F(t)$ in the second RFR originates from the rotation of $B_{eff}(t)$ around the y'-axis. During RAFF pulses the magnetization is effectively locked along the effective field in the second RFR:

$$E(t) = \sqrt{B_{eff}^2(t) + (\gamma^{-1}d\alpha(t)/dt)^2}. \tag{7.2}$$

The RAFF AM and FM functions are given by:

$$\omega_1(t) = \omega_{max}\sin(\omega_{max}t); \tag{7.3}$$

$$\Delta\omega_1(t) = \omega_{max}\cos(\omega_{max}t), \tag{7.4}$$

with ω_{max} as the maximum pulse frequency. The pulse duration is set to $T_{p,RAFF} = \frac{4\pi}{\sqrt{2}\omega_{max}}$ to effectively achieve 90° of rotation in both the first and second RFR.

The conditions in Equation (7.1) can be relaxed to allow for constant but non-equal effective and fictitious field strength, similar to the approach used by Liimatainen et al. for RAFF dispersion measurements [402]. To this end, we propose to generalize Equations (7.3) and (7.4) with 3 degrees of freedom, θ, ν, ρ. The proposed Generalized Inhomogeneities Resilient RAFF (girRAFF) amplitude and frequency modulation functions

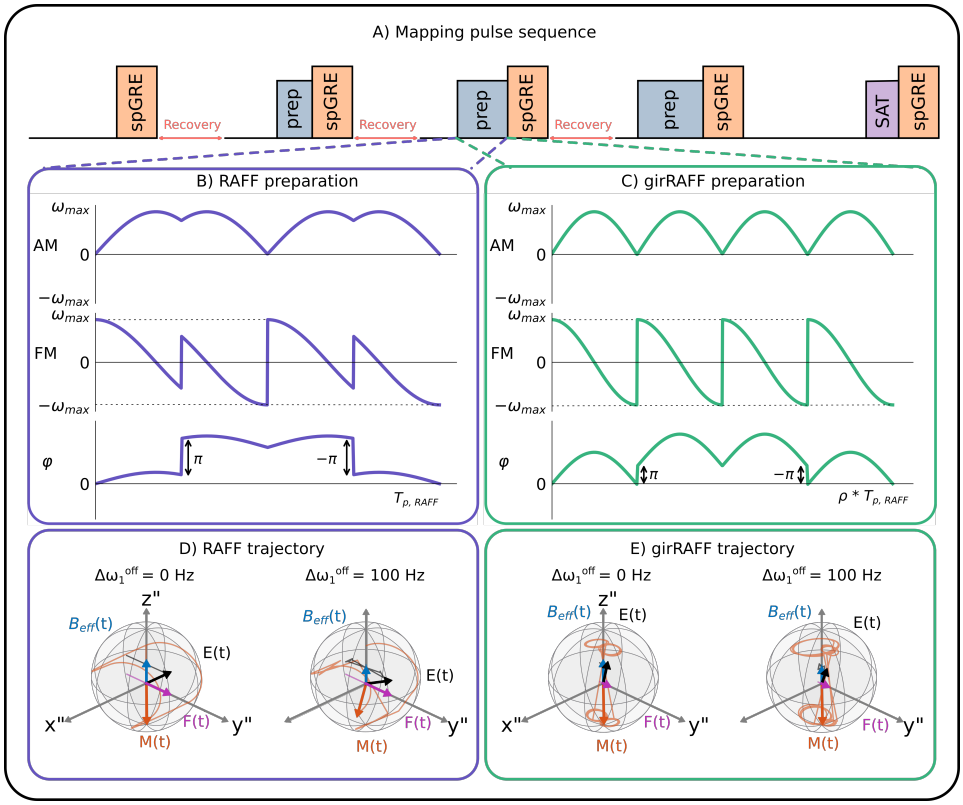

Figure 7.1 : (A) Schematic representation of the $T_{(gir)RAFF}$ mapping sequence comprising a baseline image with no preparation, three $T_{(gir)RAFF}$-prepared images with increasing durations and one saturation-prepared image, interleaved by magnetization recovery delays. (B, C) Radiofrequency (RF) pulse shapes: amplitude modulation (AM), frequency modulation (FM), and phase for both B) RAFF ($\theta = 0°$, $\nu = 1$ and $\rho = 1$) and C) girRAFF ($\theta = 0°$, $\nu = 5.53$ and $\rho = 7.82$), respectively. (D, E) M (orange) trajectory during RAFF and girRAFF pulses in the second RFR, displayed over a Bloch sphere. The first RFR effective field $B_{eff}(t)$, the fictitious field $F(t)$, and the second RFR effective field $E(t)$ are also illustrated. Plots are included for the ideal on-resonance case ($\Delta\omega_1^{off} = 0$ Hz) and for a simulated off-resonance value $\Delta\omega_1^{off} = 100$ Hz. Increased off-resonance resilience for girRAFF is indicated with better alignment of M with the z''-axis for larger off-resonances.

can then be written as:

$$\omega_1(t) = \omega_{max} \sin\left(\frac{\omega_{max}}{\nu} t - \theta\right), \tag{7.5}$$

$$\Delta\omega_1(t) = \omega_{max} \cos\left(\frac{\omega_{max}}{\nu} t - \theta\right), \tag{7.6}$$

with $T_{p,girRAFF} = \rho T_{p,RAFF}$.

Here ν determines the ratio of the fictitious and effective field strength, with $\nu = 1$ in conventional RAFF (Equation (7.1)), while large

ν values satisfy the adiabatic condition. θ denotes the starting angle of $B_{eff}(t)$ with respect to the z'-axis (for RAFF: $\theta = 0$). Finally, ρ is the scaling coefficient determining the girRAFF pulse duration relative to conventional RAFF, where $\rho = 1$ yields the original RAFF pulse duration.

Supporting Information Figures 7.S1-7.S3 illustrate the effects of the design parameters θ, ν and ρ on the pulse amplitude and frequency modulation functions. Examples of effective field $B_{eff}(t)$ and magnetization M trajectories for representative values of θ, ν and ρ are also depicted in the first RFR in Supporting Information Figures 7.S1-7.S3.

As proposed for RAFF, the complete preparation modules are formed by concatenating 4 (gir)RAFF segments using Malcolm Levitt (MLEV) phase cycling [65, 401] (Figure 7.1B-C), where the second and fourth segments are time inverted and the third and fourth are π phase-shifted with respect to the first and second.

7.2.2. Simulations

Bloch simulations were implemented in Python 3.6 [411] to study the performance of RAFF and girRAFF pulses in the presence of B_0 and B_1^+ inhomogeneities, neglecting relaxation effects. The preparation efficiency of a pulse module was defined as the ratio between the longitudinal magnetization before and after the module ($M_z(T_p)/M_0$). Here, a preparation efficiency value of +1, indicating fully balanced (gir)RAFF preparation schemes, with no B_0/B_1^+ inhomogeneity-related distortions, was considered optimal. Additionally, the magnetization trajectory length throughout (gir)RAFF irradiation was measured as a metric to ensure sufficient excursion of the magnetization and, consequently, spin-locking efficacy. The trajectory length was computed as the cumulative sum of the discretised angular distances covered by the magnetization vector on the Bloch sphere during simulations. All simulations were limited by the peak B_1^+ power ($B_1^{max} = 13.5$ µT) and a whole body SAR < 2.0 W/kg. For all pulses the peak amplitude, ω_{max}, was fixed to 500 Hz, in line with commonly used spin-locking amplitudes at 3T [398]. This yields a RAFF pulse reference duration of $T_{p,RAFF} = 2.83$ ms.

Next, the pulse performance of girRAFF was studied in the presence of field inhomogeneities. To find the girRAFF parameter combination with optimal resilience against field inhomogeneities the average preparation efficiency (Φ) was calculated over a design region of $\Delta\omega_1^{off} \in [-400; 400]$ Hz off-resonance and $\eta_1 \in [0.5, 1]$ B_1^+ scaling for different θ, ν and ρ in the three-dimensional girRAFF parameter space ($(\theta, \nu, \rho) \in [0°, 5°, \ldots, 180°] \times [0, 0.01, \ldots, 10] \times [0, 0.01, \ldots, 10]$). Low magnetization trajectory length ($< 3.2\pi$ rad) cases were discarded to avoid idle parameter configurations yielding low power pulses with

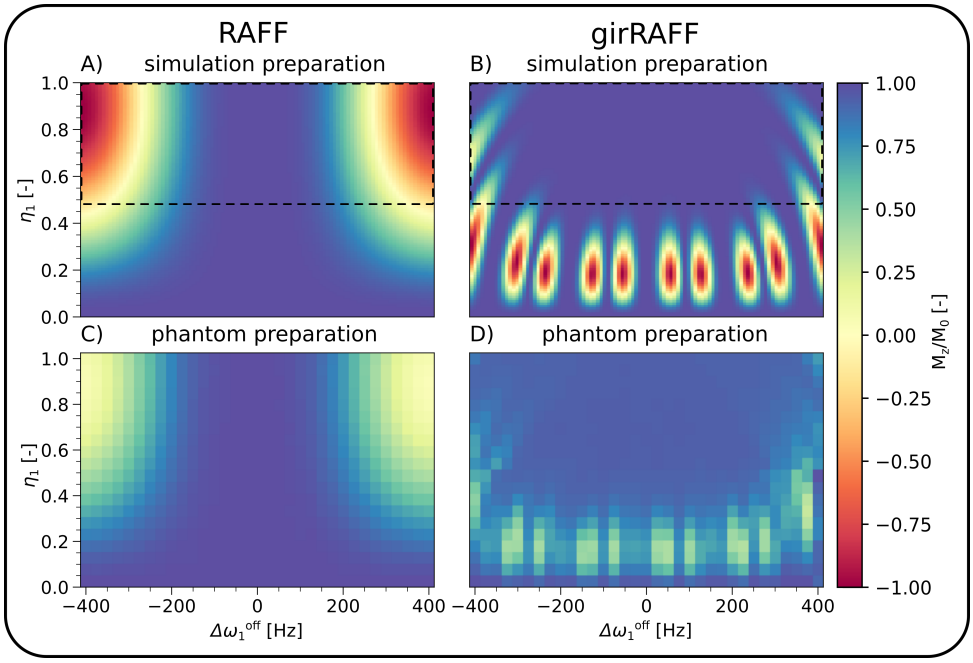

Figure 7.2 : Preparation efficiency (M_z/M_0) obtained with RAFF (A, C) and girRAFF (B, D) pulses for $(\eta_1, \Delta\omega_1^{off}) \in [0,1] \times [-400, 400]$ Hz in simulations (top) and in phantom experiments (bottom). Here $\Delta\omega_1^{off}$ indicates the off-resonance value and η_1 is the ratio between the effective and nominal B_1^+ power. The dashed rectangle indicates the design region used for pulse optimization. In simulations, an average of 0.36 and 0.95 was measured for RAFF, and girRAFF, respectively. In the phantom, a single RAFF preparation of 2.83 ms resulted in an averaged M_z of 0.67 and a single girRAFF preparation (7.82 $T_{p,RAFF}$) resulted in an average of 0.91 for the upper half-plane. Improved resilience against field inhomogeneities is obtained for girRAFF compared to RAFF, shown in the enlarged off-resonance bandwidth for the homogeneous performance plane close to 1.

high preparation efficiency but no spin-lock relaxation. The parameter combination (θ, ν, ρ) resulting in the best pulse performance was selected as the optimal girRAFF design for further investigation. Similarly to RAFF, the performance of the optimal girRAFF design was analyzed across a visualization region with off-resonances $\Delta\omega_1^{off} \in [-400; 400]$ Hz and relative B_1^+ scaling factors $\eta_1 \in [0, 1]$.

7.2.3. Imaging

Imaging was performed on a 3T scanner (Ingenia, Philips, Best, The Netherlands). All subjects provided written, informed consent prior to participation in this research.

Pulse Performance in Phantom

Simulation results of B_0 and B_1^+ performances for both RAFF and the optimized girRAFF were validated with phantom experiments using a bottle phantom (Spectrasyn 4 polyalphaolefin, ExxonMobil Chemical). The preparation efficiencies were tested by modifying the offset frequency $\Delta\omega_1^{off} \in [-400, -375, \ldots, 400]$ Hz and scaling the pulse amplitude by $\eta_1 \in [0.05, 0.1, \ldots, 1.0]$ for each $\Delta\omega_1^{off}$ value. The pulse preparation efficiency, $M_z(T_p)/M_0$, was estimated as the ratio of two balanced steady-state free-precession (bSSFP) images, one with and one without preparation. The low-resolution bSSFP images were obtained with the following imaging parameters: resolution = 2x2 mm^2, slice thickness = 8 mm, FOV = 204x204 mm^2, flip-angle = 70°, TE/TR = 1.37/2.7 ms and a SENSE factor of 2. A 4 s gap between the two bSSFP images was applied to allow for longitudinal magnetization recovery (phantom $T_1 \approx 242$ ms). Phase images were used to extract the signal polarity.

T_{RAFF} and $T_{girRAFF}$ Mapping

In phantom, in vivo calf muscle and knee cartilage T_{RAFF} and $T_{girRAFF}$ relaxation time mapping were performed by acquiring 5 spoiled gradient echo (spGRE) baseline images: one with no preparation, three preceded by a (gir)RAFF preparation and the final one preceded by a saturation preparation. The saturation-prepared image was used to capture the effect of the imaging readout [349] (Figure 7.1A). 10, 20, and 30 RAFF pulses or 1, 2, and 4 girRAFF pulses were concatenated to obtain preparation modules with varying durations. The pulse repetitions were interspersed with 3 ms spoiler gradients to suppress stimulated echos and aggravating excitation by off-resonance effects. After each readout, a 3 s gap was applied to allow for longitudinal magnetization recovery. All scans shared the following imaging parameters: resolution = 0.8x0.8 mm^2, slice-thickness = 3 mm, FOV = 181x181 mm^2, flip-angle = 15°, number of shots = 6, and a SENSE factor of 2. The TE/TR was 2.5/7.9 ms, 2.4/7.8 ms, and 1.94/6.7 ms for phantoms, calf, and knee cartilage imaging, respectively.

T_{RAFF} and $T_{girRAFF}$ relaxation time maps were obtained in MATLAB (MathWorks, Natick, USA) by fitting the following three-parameter model [349], to account for the readout effect of the imaging pulses:

$$S(t) = A \cdot e^{-\frac{t}{T_{(gir)RAFF}}} + B. \tag{7.7}$$

T_{RAFF} and $T_{girRAFF}$ Relaxation Times

RAFF and girRAFF relaxation times obtained in the T_1 Mapping and ECV Standardization in cardiovascular magnetic resonance (TIMES) phantom

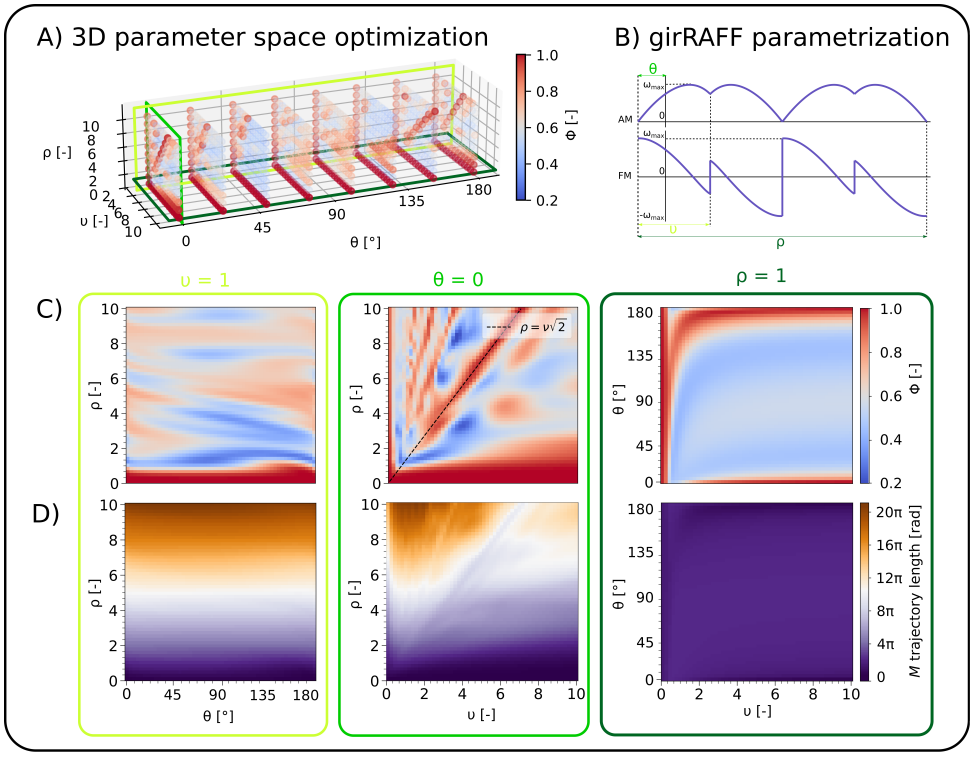

Figure 7.3 : (A) Visualization of the pulse efficiency for the girRAFF 3D parameter space within the bounds: $(\theta, \nu, \rho) \in [0°, 180°] \times [0, 10] \times [0, 10]$. The pulse peak power ($\omega_{max}$) was fixed to 500 Hz. For each parameter combination, the preparation efficiency M_z/M_0 was averaged over the region $(\eta_1, \Delta\omega_1^{off}) \in [0.5, 1] \times [-400, 400]$ Hz. The optimal shape parameters, identified by an exhaustive search of the parameter grid for the maximum Φ, while maintaining a magnetization trajectory length above 10, were $\theta = 0°$, $\nu = 5.53$ and $\rho = 7.82$. (B) Schematic representation of θ, ν and ρ parameters effect on the girRAFF pulse shape. (C) 2D preparation efficiency and (D) trajectory length maps, obtained by fixing one parameter at a time ($\theta = 0$ in the center, $\nu = 1$ on the left, and $\rho = 1$ on the right). All 2D plots indicated an increased averaged M_z for small values of ρ and ν, which was accompanied by a dramatic drop in trajectory length.

were compared to conventional T_1 and T_2 times. The optimal girRAFF configuration was used for $T_{(gir)RAFF}$ mapping. T_{RAFF} and $T_{girRAFF}$ values were extracted for each vial of the T1MES phantom using manually-drawn circular ROIs. Their mean and standard deviation values were computed for 10 repetitions. The mean T_{RAFF} and $T_{girRAFF}$ values were compared with reference T_1 and T_2 values reported in Captur et al. [351] via linear regression analysis. p-values < 0.05 were considered to be statistically significant.

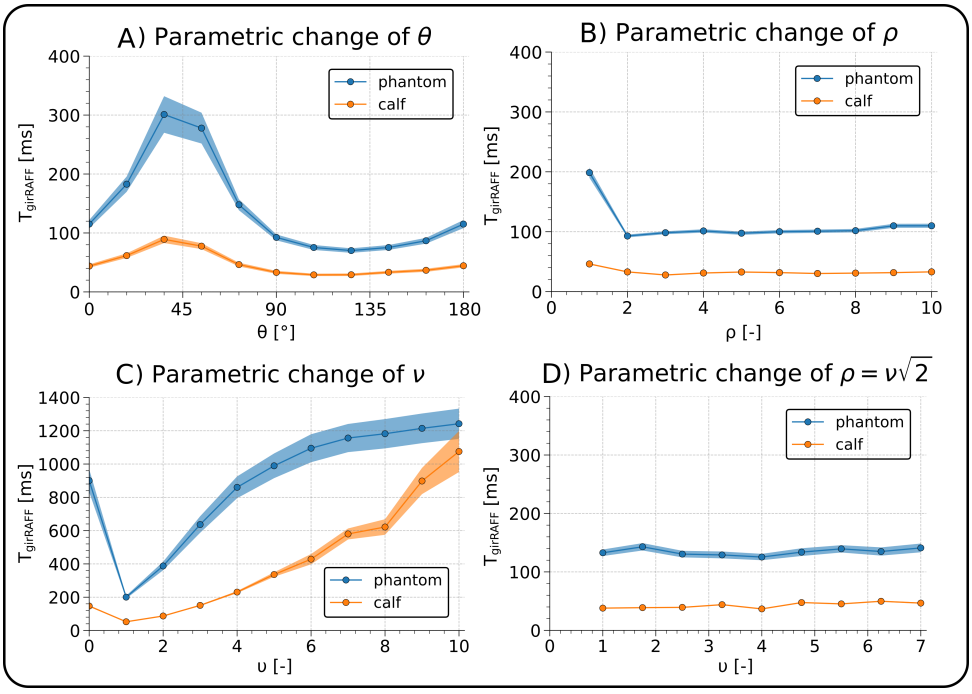

Figure 7.4 : Quantitative assessment of $T_{girRAFF}$ for A) $\theta \in \{0, 18°, \ldots, 180°\}$, B) $\rho \in \{0, 1, 2, \ldots, 10\}$ and C) $\nu \in \{0, 1, 2, \ldots, 10\}$ in the T1MES [351] phantom (blue) and in the calf muscle (orange). $T_{girRAFF}$ dependency on the pulse parameters is also investigated for $\rho = \nu\sqrt{2}$ with $\nu \in \{1, 1.75, 2.5, \ldots, 7\}$, along which the optimal combination of girRAFF parameters is found. Phantom and calf results show good agreement for the investigated parameters.

7

Parameter Space Evaluation

The effect of design parameter changes in (gir)RAFF was studied in phantom (T1MES [351]) and the calf muscle of four healthy subjects (3 male and 1 female, 26.5 ± 2.1 y.o.). $T_{girRAFF}$ maps were acquired by independently varying each parameter while keeping the other two parameters fixed at the original RAFF value ($\theta = 0°$, $\nu = 1$, and $\rho = 1$).θ, ν and ρ were varied across the following ranges: $\theta = [0°, 18°, \ldots, 180°]$, $\nu = [0, 1, 2, 3, \ldots, 10]$ and $\rho = [0, 1, 2, \ldots, 10]$, respectively. Moreover, maps were acquired for (ρ, ν), with $\rho = \nu\sqrt{2}$ and $\nu = [1, 1.75, 2.5, \ldots, 7]$, corresponding to the 1-degree of freedom space where the optimal girRAFF solution was found, as illustrated in Supporting Information Figure 7.S4. In the T1MES phantom experiments, relaxation times were evaluated using a circular ROI manually drawn in the vial that most closely resembles the RAFF/girRAFF relaxation times of the muscle tissue. In vivo, ROIs were manually drawn in the central part of the calf muscle.

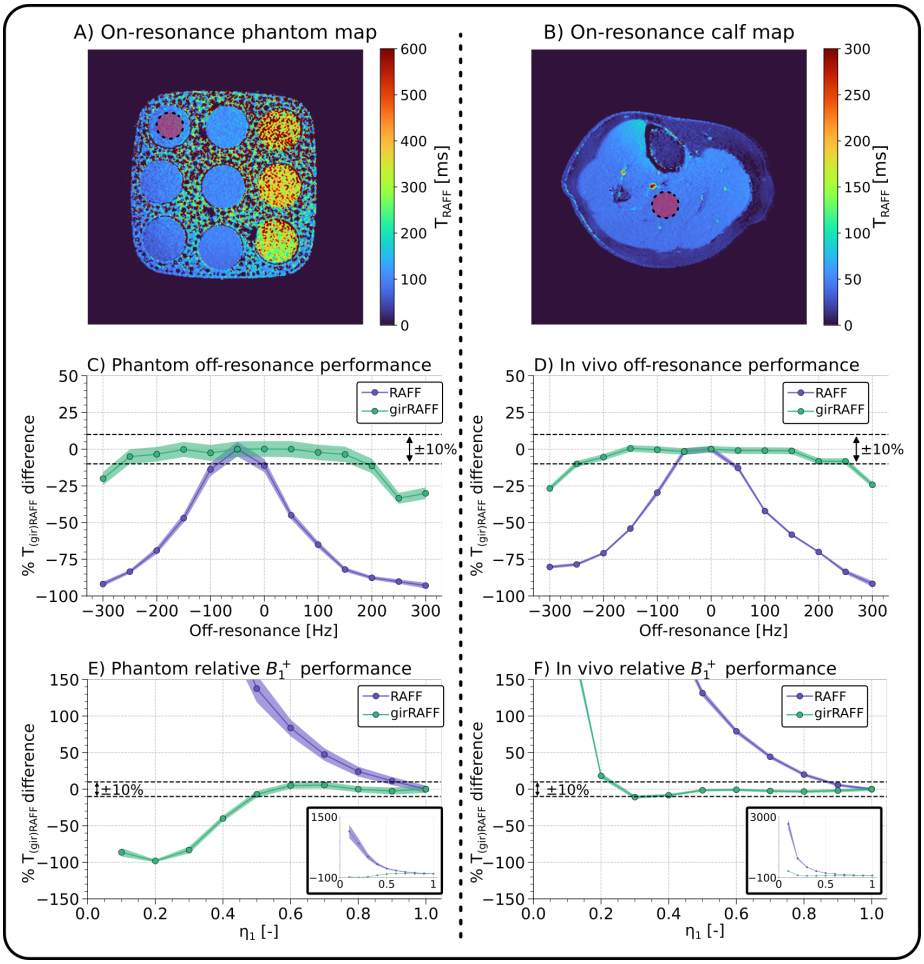

Figure 7.5 : (A-B) Phantom and in vivo calf RAFF maps, respectively. For RAFF and girRAFF, a circular region of interest (ROI) containing a vial or muscle tissue was selected to assess relaxation time for different off-resonance ($\Delta\omega_1^{off}$) and relative B_1^+ (η_1) values. Off-resonance performance of RAFF (blue) and girRAFF (green) C) in the phantom vial and D) in the calf muscle for $\Delta\omega_1^{off} \in \{-300, -250, ..., 300\}$ Hz obtained for $B_{1,max}^+ = 13.5$ μT. Relative B_1^+ performance of RAFF and girRAFF E) in the phantom and F) the calf muscle for $\eta_1 \in \{0.1, 0.2, ..., 1\}$ obtained for $\Delta\omega_1^{off} = 0$ Hz. Increased off-resonance and relative B_1^+ resilience is obtained for girRAFF compared with RAFF in the phantom and in the calf. $T_{girRAFF}$ oscillations remain lower than 10% for a 447 ± 31 Hz wide frequency range compared with 74 ± 23 Hz for RAFF in the phantom. In vivo, a 496 ± 14 Hz wide frequency range is obtained for girRAFF compared with 104 ± 8 Hz for RAFF. For relative B_1^+ performance, $T_{girRAFF}$ the ranges are: $0.48 \leq \eta_1 \leq 1$ and $0.42 \leq \eta_1 \leq 1$ in the phantom and calf, respectively. T_{RAFF} exceeds the tolerance for $\eta_1 < 0.89$ for both phantom and calf.

B_0 and B_1^+ Resilience

The effects of off-resonance and B_1^+ inhomogeneity on the mapping performance were investigated in isolation. To this end, acquisitions were performed in the T1MES phantom (3 repetitions) and in the calf muscle of three healthy subjects (2 males and 1 female, 24.8 ± 3.0 y.o.). For each pulse, maps were acquired at 13 off-resonance frequencies $\Delta\omega_1^{off} = [-300, -250, \ldots, 300]$ Hz in a first experiment and for 10 relative B_1^+ inhomogeneities $\eta_1 = [0.1, 0.2, \ldots, 1]$ in a second experiment. The B_0/B_1^+ resilience of both pulses was quantified as the range of B_0/B_1^+ inhomogeneities for which less than 10% deviation in the relaxation time from the on-resonant case is observed.

Next, mapping performance was measured for a combination of B_0 and B_1^+ field inhomogeneities, covering the range of inhomogeneities reported for knee cartilage imaging at 3T [412]: $\Delta\omega_1^{off} \in \{-150, 0, 150\}$ Hz for each $\eta_1 \in \{0.5, 0.75, 1.0\}$. Two sets of experiments were performed. In the first set, RAFF and girRAFF were compared with comparable preparation duration ($T_{prep,RAFF}$ = 28.3, 56.6, 84.9 ms, $T_{prep,girRAFF}$ = 22.2, 44.3, 88.6 ms). In the second set, RAFF was performed with shorter preparations ($T_{prep,RAFF}$ = 16.5, 34.0, 67.9 ms), to account for the shorter in vivo T_{RAFF} relaxation times. For each pulse, 9 maps were obtained in the T1MES phantom, in the calf muscle of one healthy subject (first set: male, 28 y.o., second set: female, 24 y.o.) and the knee cartilage of another healthy subject (first set only: male, 27 y.o.). Imaging parameters were the same as described in Section 2.3.2, except for the second set of phantom and calf maps, where a half-scan factor of 0.6 was used to speed up the acquisition. For phantom and calf maps ROIs were manually drawn. For the knee cartilage, relaxation times were assessed in manually drawn ROIs containing the central articular cartilage. The resilience against field inhomogeneities of $T_{(gir)RAFF}$ mapping was assessed with 3 cases: the ideal case (I_0: $\eta_1 = 1$, $\Delta\omega_1^{off} = 0$ Hz), an off-resonance case (I_{B_0}: $\eta_1 = 1$, $\Delta\omega_1^{off} = 150$ Hz), and an imperfect B_1^+ case (I_{B_1}: $\eta_1 = 0.5$, $\Delta\omega_1^{off} = 0$ Hz). The variability of the phantom, calf muscle and knee cartilage relaxation times was assessed using the following metrics: 1) relative difference between the on-resonance case $\Delta\omega_1^{off} = 0$ Hz and $\Delta\omega_1^{off} = 150$ Hz $\left(\Delta I|_{\Delta B_0} = \left|\frac{2(I_0 - I_{B_0})}{I_0 + I_{B_0}}\right|\right)$ and 2) relative difference across B_1^+ conditions $\left(\Delta I|_{\Delta B_1} = \left|\frac{2(I_0 - I_{B_1})}{I_0 + I_{B_1}}\right|\right)$. Each metric was computed based on average T_{RAFF} and $T_{girRAFF}$ intensities I extracted from the corresponding ROIs.

In a second cohort of 5 healthy subjects (4 males, 1 female, 27.4±3.1 y.o.), girRAFF and RAFF mapping was performed in the knee cartilage using Dixon fat-water separation to exclude the effect of adipose tissue on B_0 and B_1^+ resilience. Dixon imaging was performed with a multi-echo

acquisition (3 echoes, ΔTE = 2.5 ms), and the following imaging parameters: resolution = 0.9x0.9 mm^2, slice-thickness = 3 mm, FOV = 181x181 mm^2, flip-angle = 15°, number of shots = 3, SENSE factor = 2, TE/ΔTE/TR = 1.93/1.5/6.9 ms. Imaging was performed for a single slice in the lateral section of the knee articulation of each subject (3 left knee, 2 right knee). Artificial off-resonance of $\Delta\omega_1^{off} = [-150, -75, ...150]$ Hz was additionally induced. Fat-suppressed T_{RAFF} and $T_{girRAFF}$ relaxation maps were generated from the water-only images obtained with a 3-point Dixon reconstruction. Robustness against B_0 inhomogeneities was compared for the fat-suppressed maps and maps without fat-suppression obtained from the first echo of the Dixon scan. To this end, the relative difference between the on-resonance $\Delta\omega_1^{off} = 0$ Hz and off-resonance cases $\Delta\omega_1^{off} = [-150, -75, 75, 150]$ Hz was used $\left(\Delta I|_{\Delta B_0} = \frac{1}{4}\sum_{B_0=[-150,-75,75,150]}\left|\frac{2(I_0-I_{B_0})}{I_0+I_{B_0}}\right|\right)$. Mann-Whitney *U*-tests were used to assess the statistical significance of differences between RAFF/girRAFF performance metrics with and without fat suppression.

In Vivo Reproducibility

Inter-slice reproducibility was investigated by acquiring 5 on-resonance sagittal slices (slice gap = 3 mm) of the knee cartilage for each subject. All scans were acquired in a cohort of 5 healthy volunteers (3 males and 2 females, 25.2 ± 2.7 y.o.). The same imaging parameters as for the above-listed in-vivo acquisitions were used for this cohort, except for a longer recovery time between each shot (4 s) to improve quantification accuracy.

The reproducibility of the knee cartilage relaxation times was assessed using the inter-subject variability ($CoV_{subject}$) and the inter-slice (CoV_{slice}) coefficients of variation. Mann-Whitney *U*-tests were used to assess the statistical significance of differences between RAFF and girRAFF performance metrics, $p < 0.05$ was considered statistically significant.

7.3. Results

7.3.1. Bloch Simulations

Figure 7.2A shows the RAFF performance plots for $(\eta_1, \Delta\omega_1^{off}) \in [0, 1] \times [-400, 400]$ Hz in simulations. Here, RAFF preparations present moderate resilience against B_0 inhomogeneities, with a bandwidth of 318 Hz for a 10% tolerance threshold. Figure 7.2B shows the pulse performance for girRAFF with parameters $\theta = 0°$, $\nu = 5.53$, $\rho = 7.82$. With these parameters, girRAFF has an increased off-resonance bandwidth (536 Hz) yielding a larger homogeneous pulse performance compared with RAFF. The average preparation efficiency Φ

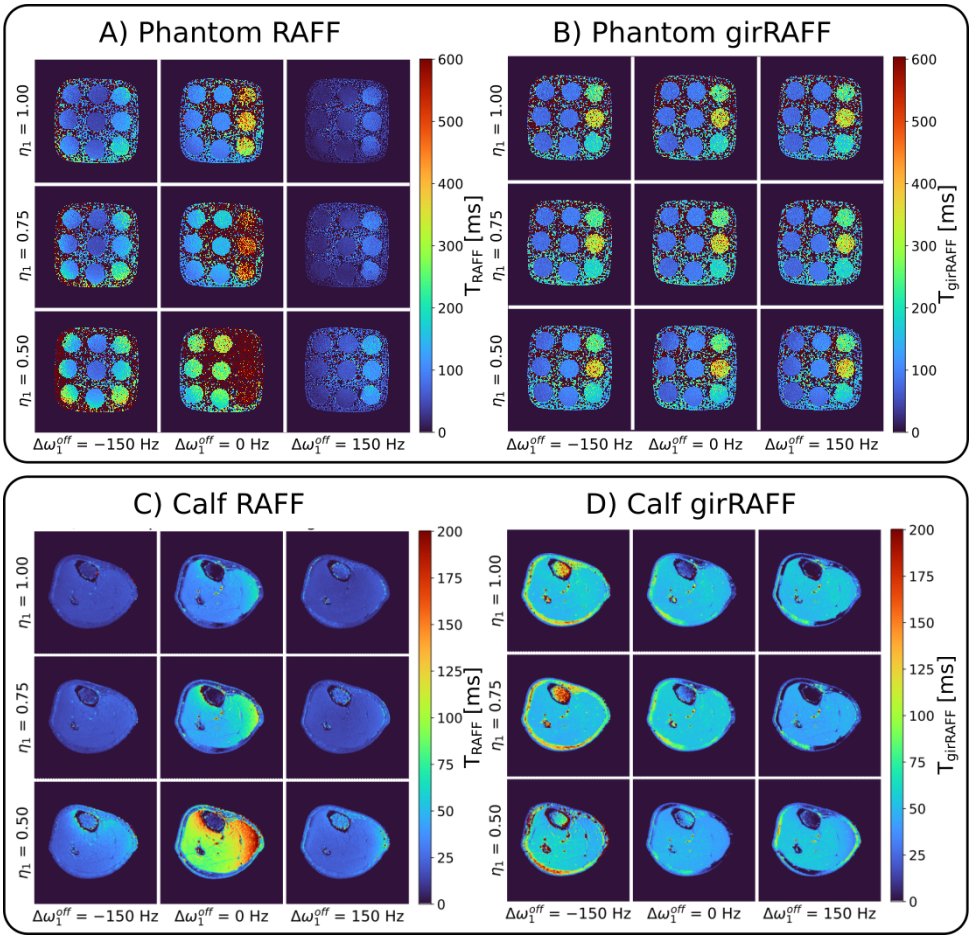

Figure 7.6 : (A-B) Phantom and (C-D) in-vivo calf RAFF and girRAFF maps obtained for each combination of $(\Delta\omega_1^{off}, \eta_1) \in \{-150, 0, 150\}$ Hz $\times \{0.5, 0.75, 1.0\}$. Both phantom and calf maps show high variability for RAFF preparations across inhomogeneity combinations. $T_{girRAFF}$ maps, on the other hand, show good resilience to system imperfections.

over the design window (dashed black rectangle in Figure 7.2A-B) was considerably higher for girRAFF (Φ = 0.95) preparations than for RAFF (Φ = 0.36).

Figure 7.3A depicts the average pulse performance across the inhomogeneity design region for various girRAFF pulses in the three-dimensional parameter space. Preparation efficiency and magnetization trajectory length are depicted in Figure 7.3C-D for the 2D planes in the parameter space intersecting with the original RAFF pulse parameters ($\theta = 0°$, $\nu = 1$ and $\rho = 1$). All cross-sectional plots indicate an

increased Φ for small preparation duration factors ρ and small values of ν. Simultaneously, however, the magnetization trajectory length drops substantially for small ρ and ν (Figure 7.3C-D, left and middle), indicating no effective spin-locking behavior caused by reduced effective field amplitudes. A pattern of high preparation efficiency and trajectory length is observed for $\rho = \nu\sqrt{2}$ (Figure 7.3C-D, middle). Improved performance is also shown for higher harmonics ($\rho = n\sqrt{2}\nu, n = 2, 3, \ldots$). The optimal combination of parameters for girRAFF is found for $\theta = 0°$, $\nu = 5.53$ and $\rho = 7.82$ with $\rho \approx \sqrt{2}\nu$.

7.3.2. Pulse Performance in Phantom

Figure 7.2C-D depict the experimental validation of the simulated pulse performances for the same B_0 and B_1^+ range. The averaged preparation efficiencies over the design region are $\Phi = 0.67$ for RAFF and $\Phi = 0.91$ for girRAFF, confirming the improvement in robustness for girRAFF over RAFF observed in simulations. In visual inspection, the simulated RAFF pulse performance closely matches the hyperbolic shape observed in the phantom experiments, also exhibiting a comparable bandwidth. Similarly, good agreement between simulations and phantom experiments is visually apparent for girRAFF. The location of the low-resolution speckle structure for low η_1 values agrees well between simulation and phantom performance.

T_{RAFF} and $T_{girRAFF}$ Relaxation Times

Supporting Information Figure 7.S6 shows the T_{RAFF} and $T_{girRAFF}$ trends as a function of T_1 (Figure 7.S6A) and T_2 (Figure 7.S6B) in the T1MES phantom vials. $T_{girRAFF}$ values are consistently higher than T_{RAFF}. The relaxation times in the central phantom vial are measured as $T_{RAFF} = 62 \pm 14$ ms and $T_{girRAFF} = 71 \pm 16$ ms, respectively. Linear regression analysis yields that neither T_{RAFF} nor $T_{girRAFF}$ are linearly dependent on T_1 (T_{RAFF} vs. T_1: $R^2 = 0.001$, $p = 0.94$, $T_{girRAFF}$ vs. T_1: $R^2 = 0.09$, $p = 0.44$). While a linear dependence is observed for both RAFF and girRAFF as a function of T_2 (T_{RAFF} vs. T_2: $R^2 = 0.87$, $p < 10^{-3}$, $T_{girRAFF}$ vs. T_2: $R^2 = 0.99$, $p < 10^{-8}$), differential behavior is still observed, particularly for short T_2 times.

7.3.3. Parameters Space Evaluation

Figure 7.4 shows the $T_{girRAFF}$ relaxation times across various parameter changes in the phantom and in the calf muscle. The parametric change of θ (Figure 7.4A) demonstrates a cyclic behavior with a maximum around $\theta \approx \pi/4$ and a minimum around $\theta \approx 3\pi/4$ both in phantom and in vivo. Changes in ρ lead to only minor alteration in $T_{girRAFF}$, except

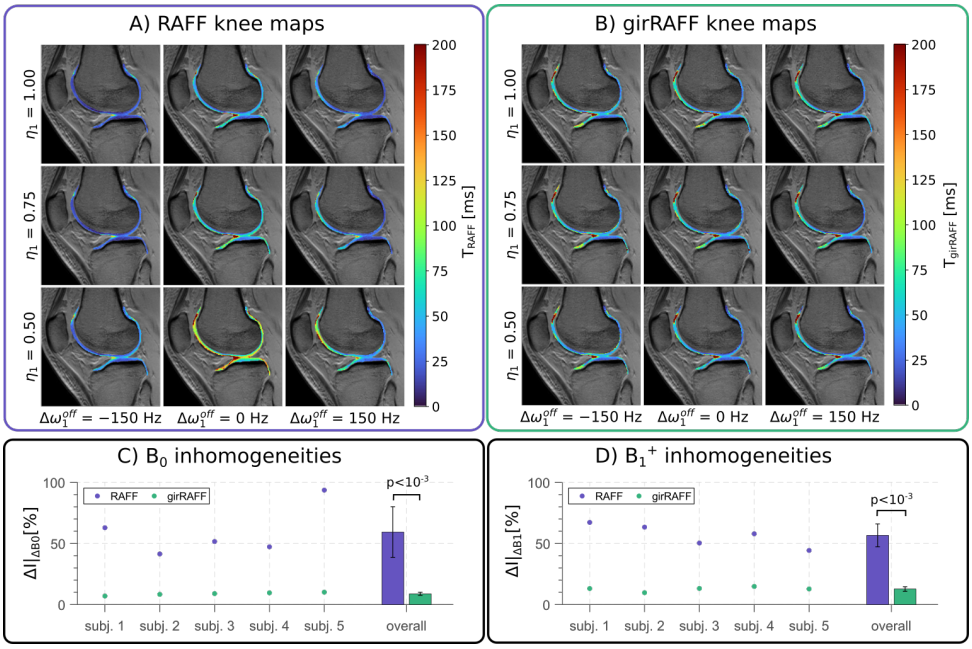

Figure 7.7 : (A-B) In vivo maps, for both RAFF and girRAFF, obtained for each combination of $\Delta\omega_1^{off} \in \{-150, 0, 150\}$ Hz and $\eta_1 \in \{0.5, 0.75, 1.0\}$. Manually segmented cartilage T_{RAFF} and $T_{girRAFF}$ values are displayed over a baseline image acquired with no preparation. Improved consistency is shown for girRAFF in the knee cartilage, as shown in the plots (C) and (D) illustrating the $\Delta I|_{\Delta B_0}$ and $\Delta I|_{\Delta B_1}$, respectively, for each subject and then averaged over all subjects.

for $\rho = 1$ (Figure 7.4B). For the parametric change of ν, increasing relaxation times are obtained for increased $B_{eff}(t)$ strength relative to $F(t)$, both in the phantom and calf, except for $\nu = 0$ (Figure 7.4C). Finally, the parametric change for $\rho = \nu\sqrt{2}$, in Figure 7.4D, shows only minor changes in $T_{girRAFF}$ for increasing ρ and ν.

B_0 and B_1^+ Resilience

Figure 7.5, shows the field inhomogeneities performances of RAFF and girRAFF, studied individually with dense η_1 and $\Delta\omega_1^{off}$ sampling. For phantom and in vivo calf mapping, on-resonance maps with the manually drawn ROIs containing a vial or muscle tissue are shown in Figure 7.5A & B, respectively. For both, the calf and phantom, $T_{girRAFF}$ shows less than ±10% deviation over a large range of off-resonances (bandwidth = 447 ± 31 Hz in phantom, 496 ± 14 Hz in the calf), while T_{RAFF} times are marked with large deviations in the presence of smaller off-resonances (bandwidth = 74 ± 23 Hz in phantom, 104 ± 8 Hz in the calf). For both pulses, a B_0 shift of approximately 50 Hz off the center

frequency is visible, likely due to imperfect shimming. For relative B_1^+ performance, RAFF exhibits increased relaxation times at decreased effective B_1^+ and exceeds the ±10% bound for $\eta_1 < 0.89$ (standard deviation = 0.04) for both phantom and calf. girRAFF remains within the tolerance for a larger range, $0.48 \leq \eta_1 \leq 1$ (standard deviation = 0.01) and $0.42 \leq \eta_1 \leq 1$ (standard deviation = 0.03), in the phantom and calf, respectively. Thus, girRAFF yielded 6.04× (phantom) or 4.77× (calf muscle) larger B_0 bandwidth than RAFF, as well as 4.73× (phantom) or 5.27× (calf muscle) better resilience to B_1^+ inhomogeneities.

In Figure 7.6A & B, the first set of phantom girRAFF and RAFF maps, acquired with comparable RAFF and girRAFF preparation durations, for nine different B_0 and B_1^+ inhomogeneity combinations are shown. For the on-resonant case ($\eta_1 = 1, \Delta\omega_1^{off} = 0$ Hz), the relaxation times in the muscle-like vial are measured as $T_{RAFF} = 74 \pm 2$ ms and $T_{girRAFF} = 98 \pm 3$ ms, respectively. Visually consistent mapping quality is obtained for girRAFF across the studied range of B_0 and B_1^+ inhomogeneities, with only minor differences between the off-resonance and η_1 values. RAFF mapping yields larger fluctuations in the measured relaxation time for all studied field inhomogeneities. Similar results are shown in the $T_{(gir)RAFF}$ maps of the calf muscle acquired in the presence of artificially induced field inhomogeneities (Figure 7.6C-D). The average relaxation time in the selected ROI is $T_{RAFF} = 34 \pm 1$ ms and $T_{girRAFF} = 50 \pm 1$ ms at on-resonance. Across B_0 field inhomogeneities, RAFF has a $\Delta I|_{\Delta B_0}$ of 48.2% and 56.3% in the phantom and calf, respectively. girRAFF shows increased consistency with $\Delta I|_{\Delta B_0}$ of 6.3% in the phantom and 7.9% in the calf. Resilience to B_1^+ inhomogeneities is also higher for girRAFF ($\Delta I|_{\Delta B_1}$ = 9.4% in phantom, 12.2% in the calf) than for RAFF ($\Delta I|_{\Delta B_1}$ = 45.7% in phantom, 49.1% in the calf). Phantom and calf girRAFF and RAFF maps obtained in the second set of experiments are shown in the Supporting Information Figure 7.S7. Here adapted RAFF preparation durations are used to achieve comparable exponential decay fractions between RAFF and girRAFF. Mildly improved resilience to B_0 and B_1^+ inhomogeneities is observed using adapted RAFF preparations ($\Delta I|_{\Delta B_0}$ = 40.6% in phantom, 45.8% in the calf, $\Delta I|_{\Delta B_1}$ = 42.3% in phantom, 41.8% in the calf) compared to the T_{RAFF} maps obtained in the first set. However, even with adapted preparation delays the resilience of RAFF against off-resonances is still ≈4.8 times lower than for girRAFF in phantom and ≈4.3 times in the calf. Similarly, the resilience to B_1^+ inhomogeneities is ≈5.0 lower in the phantom and ≈4.7 times in the calf.

T_{RAFF} and $T_{girRAFF}$ relaxation maps, acquired for different combinations of B_0 and B_1^+ inhomogeneities in the knee cartilage are depicted in Figure 7.7A-B. $T_{RAFF} = 42 \pm 11$ ms $T_{girRAFF} = 53 \pm 14$ ms are found in the knee cartilage for the on-resonance condition. Higher variability can

be observed for T_{RAFF} maps across inhomogeneity conditions compared with $T_{girRAFF}$. The $\Delta I|_{\Delta B_0}$ scores, averaged across the 5 subjects, are significantly higher for RAFF ($\Delta I|_{\Delta B_0}$ = 61%) than girRAFF ($\Delta I|_{\Delta B_0}$ = 8%, $p < 10^{-3}$), as shown in Figure 7.7C-D. Similarly, the RAFF pulse is significantly less resilient against B_1^+ inhomogeneities ($\Delta I|_{\Delta B_1}$ = 54% for RAFF, 11% for girRAFF, $p < 10^{-3}$), as shown in Figure 7.7A-B.

The comparison of T_{RAFF} and $T_{girRAFF}$ knee cartilage maps obtained with and without Dixon fat-suppression for five different values of B_0 inhomogeneities ($\Delta\omega_1^{off}$) is shown in Figure 7.9. T_{RAFF} maps acquired both with and without fat suppression display high variability in the presence of B_0 inhomogeneities ($\Delta I|_{\Delta B_0}$ = 40% without fat suppression, $\Delta I|_{\Delta B_0}$ = 47% with Dixon fat suppression, $p < 10^{-2}$). Specifically, T_{RAFF} values show a trend of substantial reduction for increasing $|\Delta\omega_1^{off}|$. The influence of adipose tissue in the proximity of the knee cartilage creates areas of enhanced T_{RAFF} which partially balance the trend of decreasing T_{RAFF} for increasing $|\Delta\omega_1^{off}|$, leading to a reduced $\Delta I|_{\Delta B_0}$ coefficient. On the other hand, girRAFF maps show overall more homogeneous values across different $\Delta\omega_1^{off}$ conditions. However, localized hyperenhancement is visible in the proximity of adipose tissue in the knee joint, especially for $\Delta\omega_1^{off} > 0Hz$ (red arrows in Figure 7.9B). These regions of hyperenhancement are visibly suppressed with the use of Dixon fat-water separation. As a result, fat suppression significantly improves the robustness of $T_{girRAFF}$ maps to B_0 inhomogeneities ($\Delta I|_{\Delta B_0}$ = 6% without fat suppression, $\Delta I|_{\Delta B_0}$ = 0.4% with Dixon fat suppression, $p < 10^{-8}$).

In Vivo Reproducibility

Figure 7.8 displays one of the sagittal slices acquired for all 5 healthy subjects and an example of the 5 sagittal T_{RAFF} and $T_{girRAFF}$ slices for a representative subject. The inter-subject analysis across all field inhomogeneities and slices yields $CoV_{subjects}$ = 27% for RAFF, while girRAFF shows improved reproducibility with $CoV_{subjects}$ = 14% ($p < 10^{-2}$). Moreover, $T_{girRAFF}$ maps yield homogeneous relaxation times across all slices (CoV_{slice} = 10%), whereas T_{RAFF} are characterized by higher variability across the 5 slices (CoV_{slice} = 16%, $p < 0.01$), with decreased values in lateral and medial extremities. Moderate relaxation time variations across slices, however, could also be caused by the intrinsic $T_{(gir)RAFF}$ anisotropy, as shown in previous studies [359, 413], as well as differences in partial voluming of the thin ROIs.

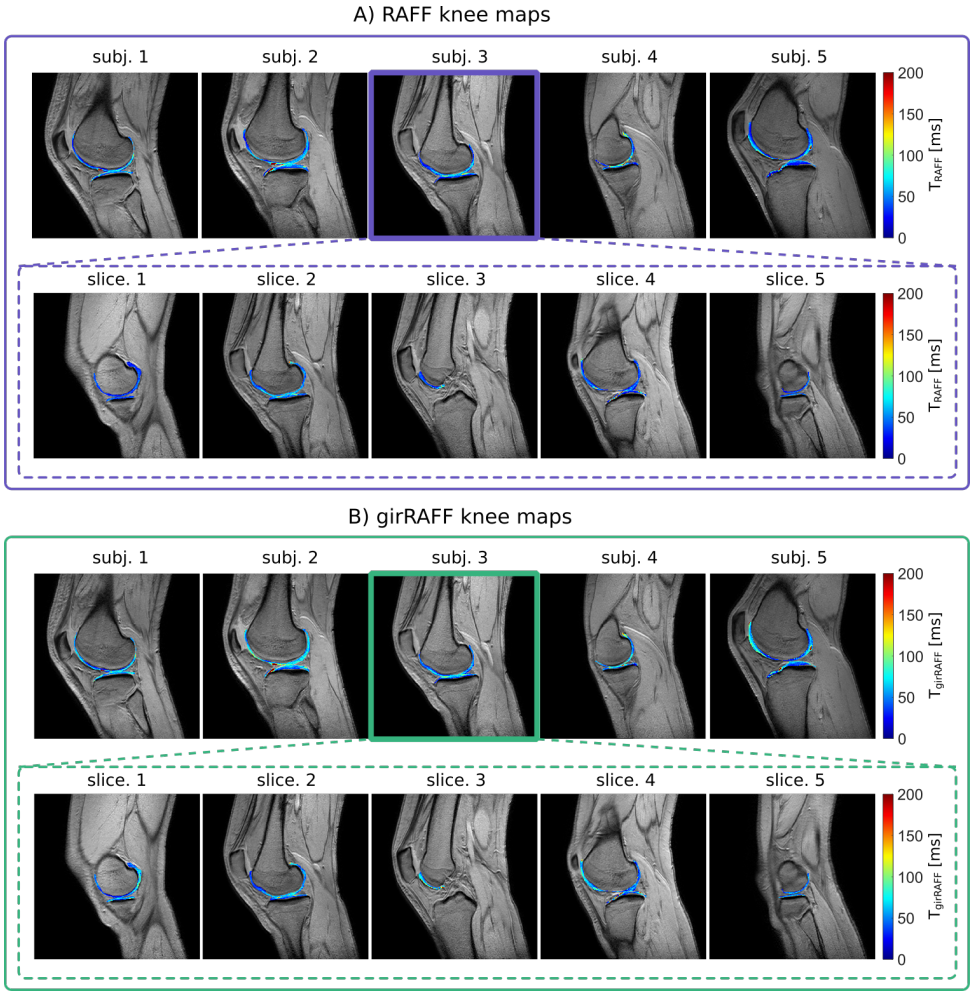

Figure 7.8 : Example of in-vivo (A) RAFF and (B) girRAFF maps obtained in the knee cartilage of 5 healthy subjects. For a representative subject, examples of 5 different sagittal maps are shown below. Cartilage $T_{girRAFF}$ values appear more homogeneous than T_{RAFF} across the 5 subjects ($CoV_{subjects}$ = 27% for RAFF, 14% for girRAFF, $p < 0.01$) and 5 slices (CoV_{slices} = 16% for RAFF, 10% for girRAFF, $p < 0.01$).

7.4. Discussion

In this work, the resilience of RAFF pulses against field inhomogeneities was investigated. Both simulations and phantom experiments showed strong susceptibility to changes in the B_1^+ field and moderate resilience against off-resonances for RAFF. A parametric formulation of RAFF was introduced to explore pulse shapes that yield constant but non-equal effective and fictitious fields. The resilience of these pulses to B_0 and B_1^+ inhomogeneities was investigated to find the optimal candidate for

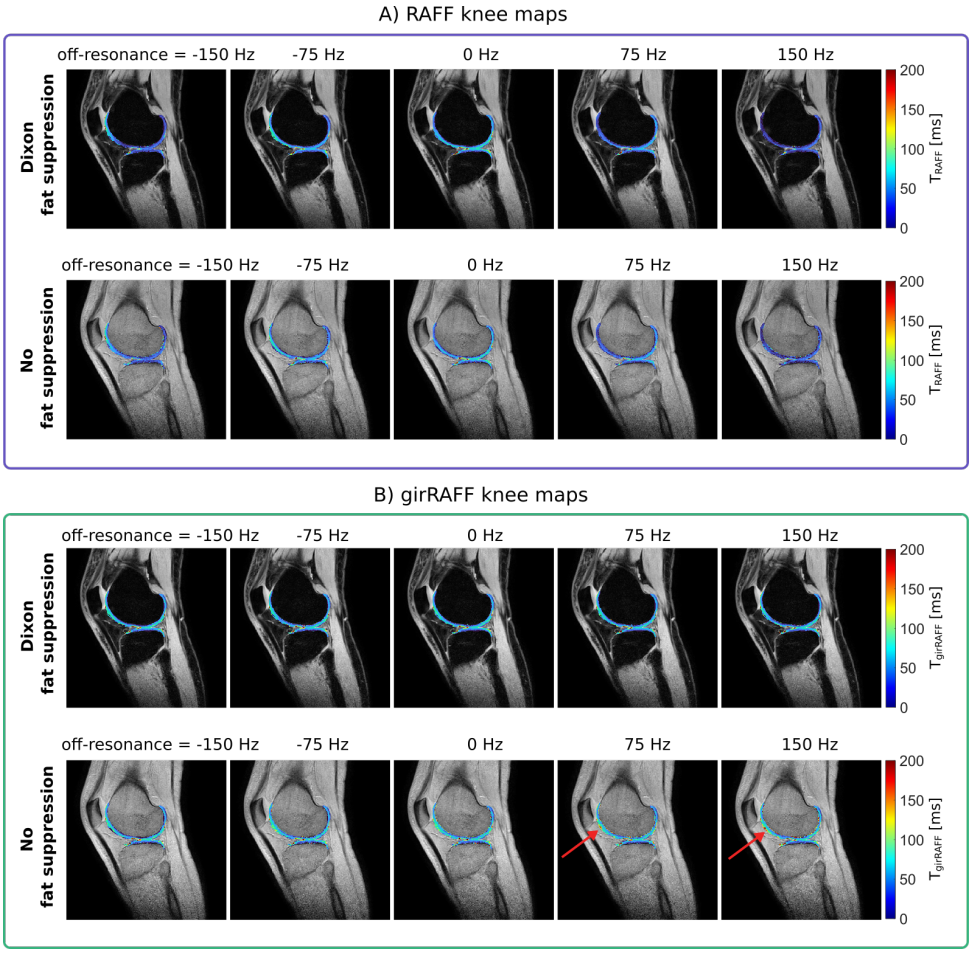

Figure 7.9 : Example T_{RAFF} (A) and $T_{girRAFF}$ (B) relaxation maps of the articular cartilage, acquired in a healthy subject with Dixon fat-water separation (top) and without fat suppression (bottom), for various artificially induced off-resonance values. T_{RAFF} maps show strong variability across the off-resonance conditions with and without fat-suppression. The variability is visually reduced in the $T_{girRAFF}$ maps. Residual artifacts are observed in the $T_{girRAFF}$ maps in areas close to adipose tissue (red arrow). Dixon fat-water separation successfully alleviates these artifacts leading to visually homogeneous maps across the off-resonance conditions.

robust rotating frame relaxation mapping. For the optimal parameters, girRAFF showed 4.77 and 5.27 times increased resilience against B_0 and B_1^+ inhomogeneities in the human calf, respectively, while maintaining good tissue contrast and mapping quality in phantom, calf, and knee cartilage imaging.

RAFF represents an emerging biomarker for tissue characterization and has already proven sensitivity to proteoglycan concentration in

articular cartilage, making it a promising candidate for osteoarthritis detection [414]. Previous RAFF mapping studies focused on ex-vivo samples or animal models of the knee cartilage and were performed at pre-clinical systems with ultrahigh field strengths (9.4T) [359, 399, 403, 413–415]. In healthy subjects at 3T, Tourais et al. recently reported an average of T_{RAFF}=45.2 ± 11.3 ms [408], which is in close agreement with the values obtained in this study. Optimized girRAFF preparations yield longer relaxation times compared with RAFF, a trend consistent with findings by Liimatainen et al. [402]. Specifically, they found a significant dependence of RAFF relaxation times on the ratio between the effective and fictitious field components (equivalent to ν in our study). The lowest T_{RAFF} values were measured when the effective field strength was almost equal to the fictitious field strength (corresponding to values of ν just below 1), whereas higher T_{RAFF} when the effective field was much stronger or much weaker than the fictitious field. This dependence is confirmed by the phantom and in-vivo results in Figure 7.4C. The variability in the measured $T_{girRAFF}$ times for different ν hints at differential sensitivity to underlying physical processes such as dipole-dipole interactions or chemical exchange when moving from the sub-adiabatic condition towards an adiabatic regime. Evaluation in patients is warranted to fully characterize the sensitivity of RAFF and girRAFF pulses to underlying tissue composition and their pathological state alterations.

RAFF pulses were originally proposed as an alternative to conventional continuous-wave $T_{1\rho}$ preparations for robust rotating frame relaxation quantification with limited SAR burden. As Liimatainen at al. have shown in their original study, T_{RAFF} relaxation displays a pattern of sensitivity to molecular motion that is similar to $T_{1\rho,adiab}$ and $T_{2\rho,adiab}$ [401], and related to continuous-wave $T_{1\rho}$ and $T_{2\rho}$ relaxation times. Thus, RAFF pulses were proposed as an alternative to conventional continuous-wave rotating frame relaxation techniques with the promise of comparable clinical sensitivity. Initial studies showed a moderate increase in off-resonance bandwidth up to ∼ 100 Hz [401, 410]. However, this came at the expense of a loss of resilience against B_1^+ field inhomogeneities, with simulated T_{RAFF} times significantly impaired for $\eta_1 < 0.8$ [401]. These results are well in line with the results obtained in this study, where a bandwidth of 74 ± 23 Hz and 10% tolerance to B_1^+ inhomogeneities were measured in phantom for RAFF. In this study, we proposed a RAFF optimization, girRAFF, based on the combined study of both B_0 and B_1^+ inhomogeneities. By relaxing the RAFF condition (Equation (7.1)), introducing three degrees of freedom, constant yet not necessarily equal effective and fictitious field components are achieved. In agreement with previous findings [410], our results show that the average preparation efficiency improved for higher fictitious field ratios ($\nu < 1$). However, even better performances were achieved for $\nu > 1$,

with the optimal value found for $\nu = 5.53$. Increasing ν values yield an increasingly strong effective field component with respect to the fictitious field, gradually moving from a sub-adiabatic to an adiabatic regime. Accordingly, the analysis of contrast sensitivity in the presence of dipole-dipole interactions showed that girRAFF falls between the sensitivity profiles or RAFF and $T_{1\rho,adiab}$. Notably, optimal girRAFF performances were observed for configurations where $\rho = n\sqrt{2}\nu$. This parameter combination corresponds to cases where the argument of girRAFF amplitude and frequency modulation functions ranges from 0 to 180° within a single P-packet. Thus, the effective field completes a full 180° inversion, leading to increased robustness against field inhomogeneities in the optimization.

Higher rank RAFF pulses (RAFFn, with $n > 2$) were previously proposed as a solution to improve the pulse resilience to B_0 field inhomogeneities [410]. RAFFn pulses generalize the RAFF conditions of equal and time-invariant effective and fictitious field components to higher-order RFRs. Observed in the second RFR, these pulses are characterized by a higher fictitious field component with respect to the effective field. A joint optimization of B_0 and B_1^+ inhomogeneity resilience, as proposed in the current study, can also be applied to RAFFn pulses. The expected degree of B_0 and B_1^+ inhomogeneities greatly depends on the target application. For body imaging at 3T, commonly observed off-resonances and B_1^+ inhomogeneities are in the range of ±300 Hz, and ±60%, respectively [82, 416–418]. In the knee cartilage, only a limited number of studies have investigated B_0 and B_1^+ inhomogeneities. However, a reduced impact for both B_0 (< 150 Hz) and B_1^+ (> 75%) inhomogeneities has been reported [412]. These applications may be sufficiently covered by the design regions chosen for the girRAFF pulses. However, for imaging at ultra-high fields, a similar optimization of higher-order RAFF pulses may provide a promising way to further improve off-resonance tolerances. Thus, the comparison of girRAFF with higher-order RAFF pulses and their combination with a parametrization approach remain interesting subjects for future work.

The bandwidth of a single pulse module was studied in the simulation and phantom experiments (Figure 7.2). Phantom experiments closely reproduced the results from simulations, with the exception of a lower resolution and the contribution of relaxation effects during (gir)RAFF preparations. Relaxation effects caused a minor reduction in preparation efficiency values in the optimal plateau region for phantom experiments. This effect is more visible for girRAFF, which has longer preparation time, than with RAFF. In both cases, however, the difference in preparation efficiency between simulations and phantom experiments was < 4% in the plateau region thanks to the use of only a single (gir)RAFF module and a phantom with long relaxation times (Spectrasyn $T_{1\rho,adiab}/T_{2\rho,adiab}$ = 176.16 ms/98.53 ms [367, 419]). Thus, the

preparation efficiency variations due to relaxation effects in phantom did not overshadow those caused by field inhomogeneities targeted by the study. However, to obtain reliable quantification, multiple repetitions of the pulse module are required to enable sufficient sampling of the relaxation curve. The girRAFF module is 7.82 times longer than RAFF (Figure 7.1C), thus, requiring fewer repetitions to achieve the same preparation duration. Taking the in-vivo relaxation time ($T_{RAFF} = 34 \pm 1$ ms versus $T_{girRAFF} = 50 \pm 1$ ms), effectively 5.32 times fewer repetitions are needed for comparable relaxation curve sampling. As a result, the differences in bandwidth between girRAFF and RAFF are further exacerbated in phantom and in vivo mapping results, leading to an overall +504.1% bandwidth increase in girRAFF vs. RAFF for phantom mapping experiments, compared with 66.67% in single module phantom experiments.

This study has several limitations. The proposed pulse optimization was only applied to RAFF in the second RFR, as this pulse was available for reference comparison. Nevertheless, the approach could be applied to a wide variety of pulses for rotating frame relaxometry, such as continuous-wave and adiabatic $T_{1\rho}$ and $T_{2\rho}$ preparations, higher order RAFFn pulses, and more, as resilience to field inhomogeneities remains a common limiting factor at high field strengths. Furthermore, only a small number of healthy subjects were included in the evaluation of the pulses. Ultimately, thoroughly characterizing the sensitivity of novel relaxation parameters to pathological alterations in tissue composition is necessary to validate their diagnostic value. The theoretical sensitivity to molecular motion at different correlation times derived in this and previous studies [401] for giRAFF and RAFF pulses does not capture the true complexity of relaxation processes in vivo. The model used was limited to dipole-dipole interactions and neglected contributions from other relaxation mechanisms, such as chemical exchange and diffusion, which are important drivers of in vivo rotating-frame relaxation. Thus, ultimately only in vivo clinical validation can fully determine the parameter sensitivity and diagnostic values of the proposed $T_{girRAFF}$ relaxation.

Finally, the proposed technique was only tested in vivo on the calf muscle and the knee cartilage, where both B_0 and B_1^+ inhomogeneities are limited in normal conditions. Other anatomies, like the heart or the liver, might present stronger field inhomogeneities and, thus, benefit more from the use of an optimized girRAFF preparation for rotating frame relaxation mapping. The scope of this study was kept on anatomies characterized by rather homogeneous B_0 and B_1^+ fields to avoid introducing additional confounders in the quantitative analysis of the pulse performance.

7.5. Conclusions

Our results show that spin-lock relaxation measurements using RAFF exhibit moderate resilience against off-resonances but strong susceptibility to B_1^+ inhomogeneities. A parameterized RAFF (girRAFF) formulation allowed for the derivation of preparation pulses with improved resilience against field inhomogeneities in phantom. Quantitative mapping obtained with girRAFF showed only minor variations across field inhomogeneities in vivo. Thus, girRAFF may provide a promising tool for clinical applications in body imaging at 3T where larger off-resonance resilience is needed. Further investigation of its sensitivity toward pathological remodeling is warranted.

Appendix

Relaxation rates were derived for both RAFF and girRAFF methods using second-order perturbation theory of dipole-dipole interactions [401, 420]. The relaxation rates during amplitude- and frequency-modulated RF irradiation were previously described for a system of nuclei with spin I and gyromagnetic ratio γ by Michaeli et al. in Equation 7 and 8 of [343], as:

$$R_{1\rho,adiab}(t) = \frac{1}{10k_{dd}}\left[\frac{3sin^2\alpha(t)cos^2\alpha(t)}{1+\omega_{eff}^2(t)\tau_c^2} + \frac{3sin^4\alpha(t)}{1+4\omega_{eff}^2(t)\tau_c^2} \right. \\ \left. \frac{2+3sin^2\alpha(t)}{1+\omega_0^2\tau_c^2} + \frac{8-6sin^2\alpha(t)}{1+4\omega_0^2\tau_c^2}\right]. \tag{7.8}$$

and

$$R_{2\rho,adiab}(t) = \frac{1}{40k_{dd}}\left[3(3cos^2\alpha(t)-1)^2 \right. \\ + \frac{30sin^2\alpha(t)cos^2\alpha(t)}{1+\omega_{eff}^2(t)\tau_c^2} + \frac{3sin^4\alpha(t)}{1+4\omega_{eff}^2(t)\tau_c^2} \\ \left. + \frac{20-6sin^2\alpha(t)}{1+\omega_0^2\tau_c^2} + \frac{8+12sin^2\alpha(t)}{1+4\omega_0^2\tau_c^2}\right], \tag{7.9}$$

where:

$$1/k_{dd} = 2I(I+1)\hbar^2\gamma^2 r^{-6}\tau_c. \tag{7.10}$$

Here, $\hbar$ is the reduced Planck constant ($\hbar = 1.0546 \times 10^{-34}$ Js), r is the internuclear distance (r = 1.58 Å, τ_c is the correlation time and $\alpha(t) = tan^{-1}\left(\frac{\omega_1(t)}{\Delta\omega(t)}\right)$).

To compute RAFF and girRAFF relaxation rates for different correlation times τ_c, RAFF and girRAFF amplitude and frequency-modulation functions can be used to extract the (gir)RAFF pulse amplitude $\omega_1(t)$, its off-resonance $\Delta\omega(t)$ and the effective field amplitude $\omega_{eff}(t)$. The effective field evolution throughout the preparation pulse was obtained from Bloch simulations and used to derive the resulting $R_{1\rho,adiab}$ and $R_{2\rho,adiab}$ at each time point. Using a quasi-static approximation, the final relaxation during RAFF or girRAFF irradiation can then be expressed as:

$$R_{(gir)RAFF} = \frac{1}{2T_p}\int_0^{T_p}\left(AR_{1\rho,adiab}(t) + BR_{2\rho,adiab}(t)\right)dt, \tag{7.11}$$

where A = $cos^2(\delta(t))$ and B = $sin^2(\delta(t))$, with $\delta(t)$ as the angle between the magnetization and the effective field.

R_{RAFF} and $R_{girRAFF}$ relaxation rates were compared with $R_{1\rho}$, $R_{2\rho}$, $R_{1\rho,adiab}$ and $R_{2\rho,adiab}$ for different correlation times. Conventional $T_{1\rho}$ and $T_{2\rho}$ relaxation was obtained for a constant-amplitude on-resonance RF irradiation, with ω_1 = 500 Hz and T_p = 30 ms. Adiabatic spin-lock preparations were obtained using hyperbolic secant pulses, with ω_1^{max} = 500 Hz, T_p = 30 ms, β = 6.9, f_{max} = 450 Hz, as previously used for in vivo imaging at 3T [367, 419].

Supporting Information Figure 7.S5 shows the relaxation rates and relaxation times as a function of the correlation time τ_c. Relaxation rates of RAFF and girRAFF fall between $R_{1\rho,adiab}$ and $R_{2\rho,adiab}$ and show similar trends across the range of correlation times. The relaxation time trend of RAFF and girRAFF show less similarity to conventional continuous wave $R_{1\rho}$ and $R_{2\rho}$ at a single frequency. Compared with R_{RAFF}, $R_{girRAFF}$ falls closer to $R_{1\rho,adiab}$. Together with the relaxation rates observed in phantom and in vivo, these results suggest that $R_{girRAFF}$ exhibits intermediate contrast weighting between R_{RAFF} and $R_{1\rho,adiab}$. Thus, girRAFF may be a promising candidate for the depiction of pathologies, that have been studied with $T_{1\rho,adiab}$ and T_{RAFF}, including myocardial and in the liver fibrosis [329, 331, 361, 365, 421–423], cartilage degeneration and concentration of proteoglycans [424–427], Alzheimer's and Parkinson's diseases [428, 429], breast tissue lesions [430] and tumors [431–433].

7.6. Supporting Information

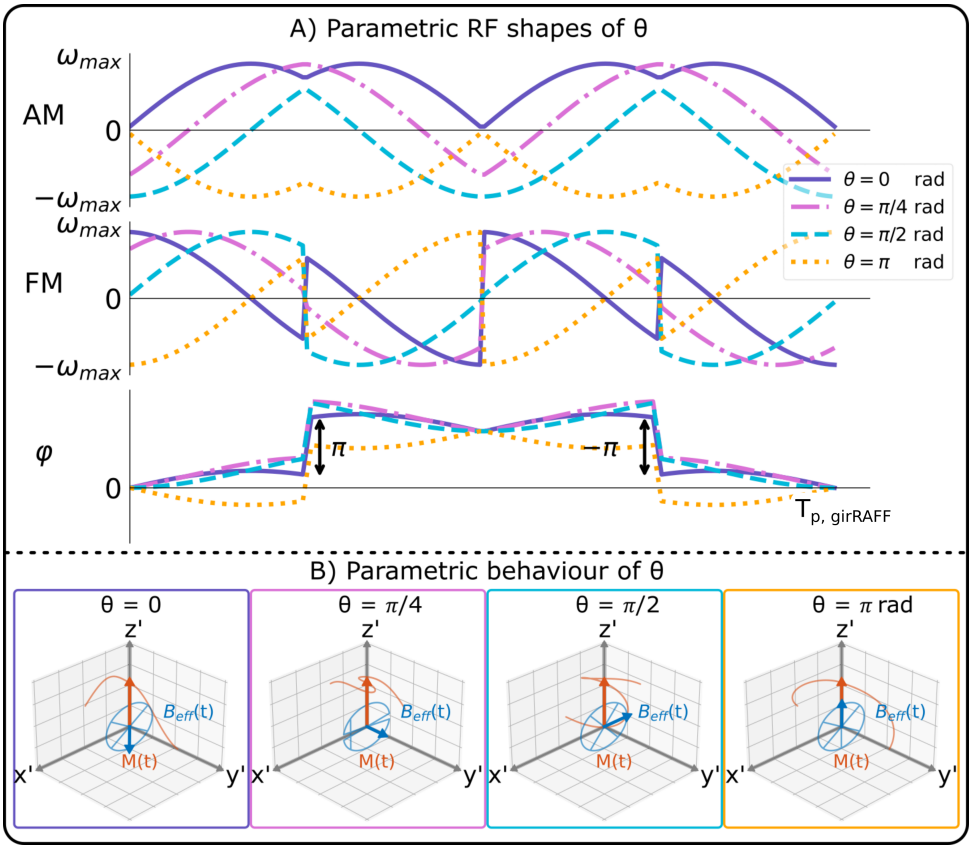

Figure 7.S1 : A) Radiofrequency shapes: amplitude modulation, frequency modulation, and phase for the changing parametric behavior of θ with respect to RAFF ($\theta = 0°$, $\nu = 1$ and $\rho = 1$) as default. B) Corresponding magnetization behavior for all RF shapes in the first rotating frame. Indicating the magnetization vector ($M(t)$, orange) with its trajectory and the effective field ($B_{eff}(t)$, blue).

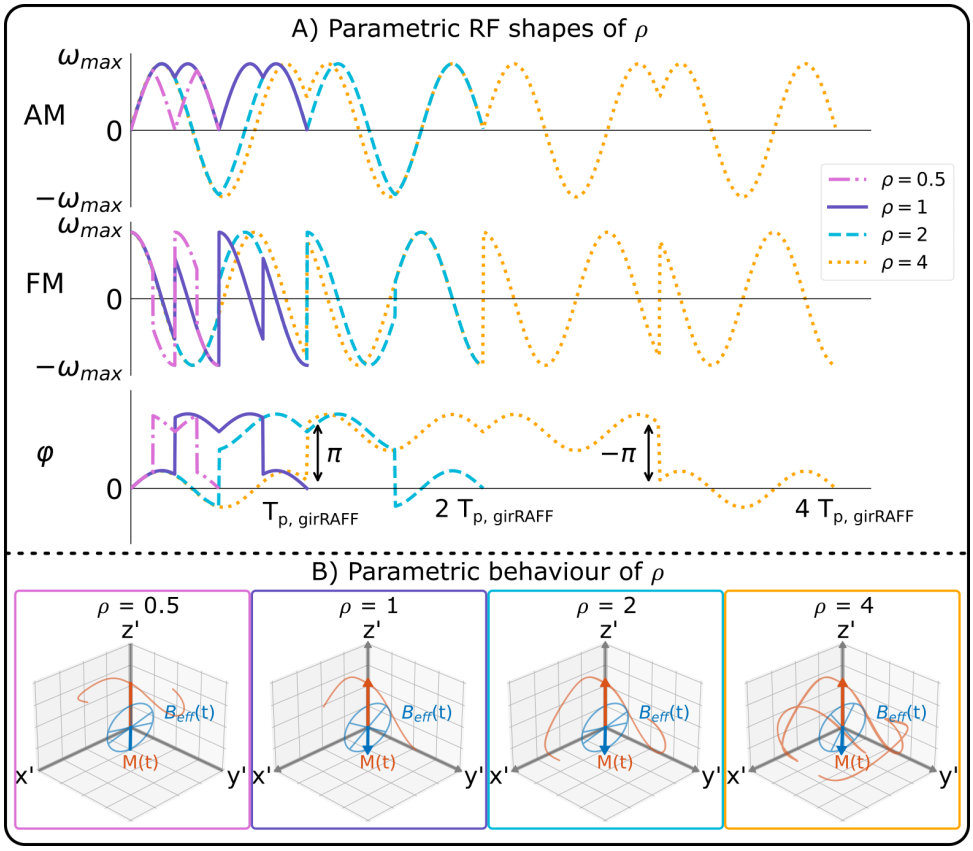

Figure 7.S2 : A) Radiofrequency shapes: amplitude modulation, frequency modulation, and phase for the changing parametric behavior of ρ with respect to RAFF ($\theta = 0°$, $\nu = 1$ and $\rho = 1$) as default. B) Corresponding magnetization behavior for all RF shapes in the first rotating frame. Indicating the magnetization vector ($M(t)$, orange) with its trajectory and the effective field ($B_{eff}(t)$, blue).

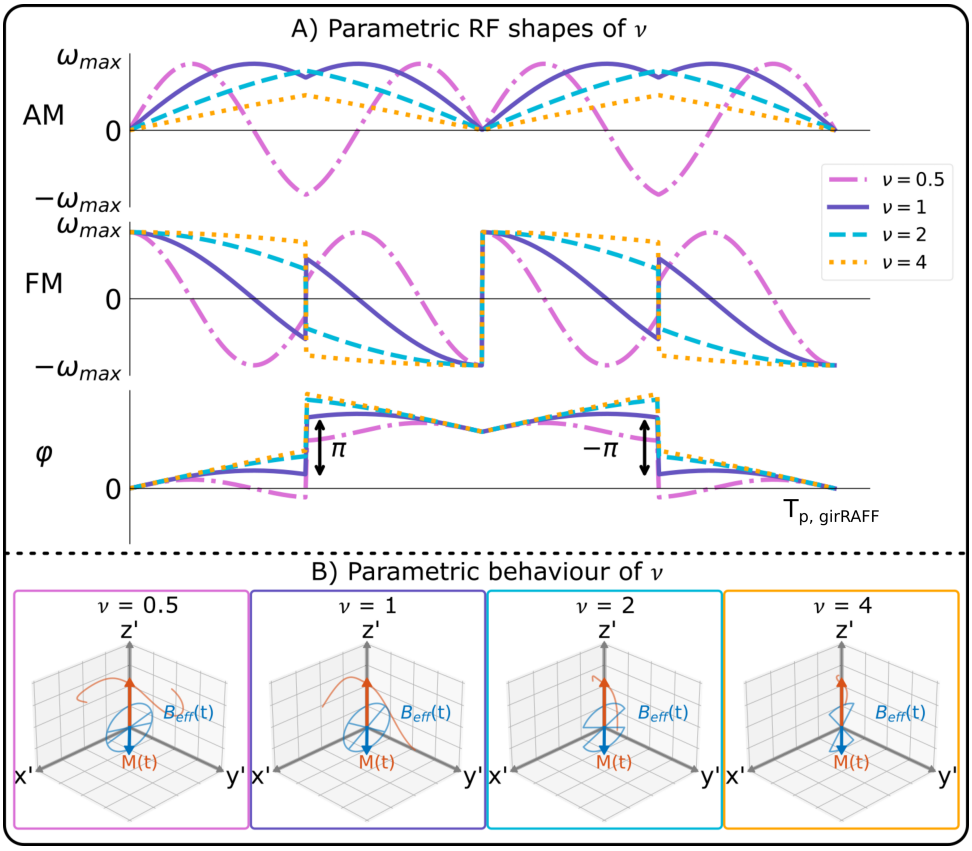

Figure 7.S3 : A) Radiofrequency shapes: amplitude modulation, frequency modulation, and phase for the changing parametric behavior of ν with respect to RAFF ($\theta = 0°$, $\nu = 1$ and $\rho = 1$) as default. B) Corresponding magnetization behavior for all RF shapes in the first rotating frame. Indicating the magnetization vector ($M(t)$, orange) with its trajectory and the effective field ($B_{eff}(t)$, blue).

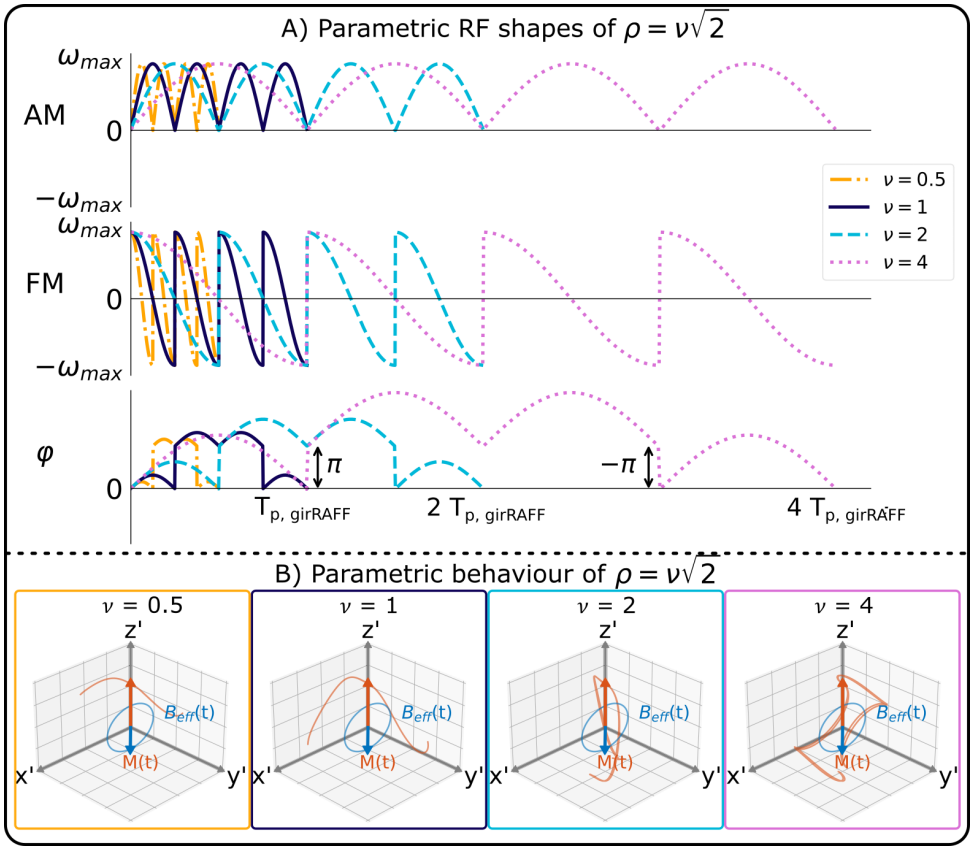

Figure 7.S4 : A) Radiofrequency shapes: amplitude modulation, frequency modulation, and phase for the changing parametric behavior of the line $\rho = \nu\sqrt{2}$ with respect to RAFF ($\theta = 0°$, $\nu = 1$ and $\rho = 1$) as default. B) Corresponding magnetization behavior for all RF shapes in the first rotating frame. Indicating the magnetization vector ($M(t)$, orange) with its trajectory and the effective field ($B_{eff}(t)$, blue).

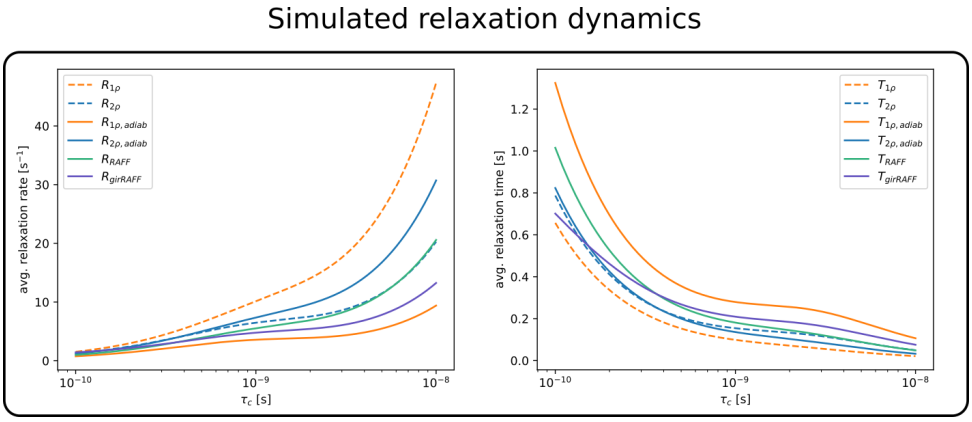

Figure 7.S5 : Rotating frame relaxation rates and relaxation times, for conventional continuous wave $T_{1\rho}$ and $T_{2\rho}$ at 500 Hz, adiabatic $T_{1\rho,adiab}$ and $T_{2\rho,adiab}$, and RAFF and girRAFF, for various correlation times. The relaxation rates were derived from second-order perturbation theory for the case of dipole-dipole interaction of like spins. RAFF and girRAFF show similar relation trends as $T_{1\rho,adiab}$ and $T_{2\rho,adiab}$, where RAFF falls between $T_{1\rho,adiab}$ and $T_{2\rho,adiab}$ and girRAFF falls between $T_{1\rho,adiab}$ times and RAFF. Continuous wave $T_{1\rho}$ and $T_{1\rho}$ trends show less similarity with RAFF and girRAFF.

7

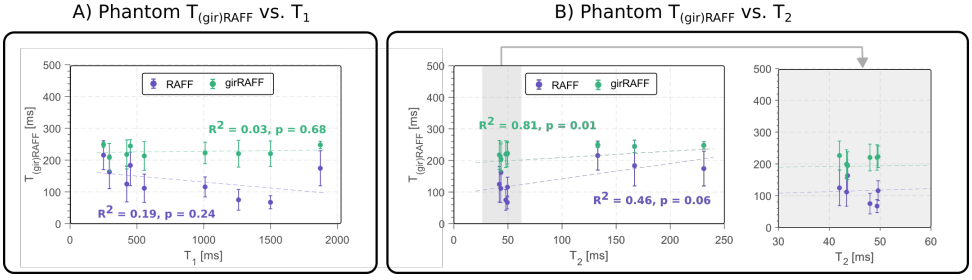

Figure 7.S6 : T_{RAFF} and $T_{girRAFF}$ relaxation times obtained in various vials of the T1MES phantom as a function of the T_1 (a) and T_2 time (b). Linear regression analysis shows no correlation with T_1 times for either T_{RAFF} and $T_{girRAFF}$. A linear dependence on T_2 times is observed for both RAFF and girRAFF. However, differential behavior remains visible, especially for short T_2 times (b, right plot).

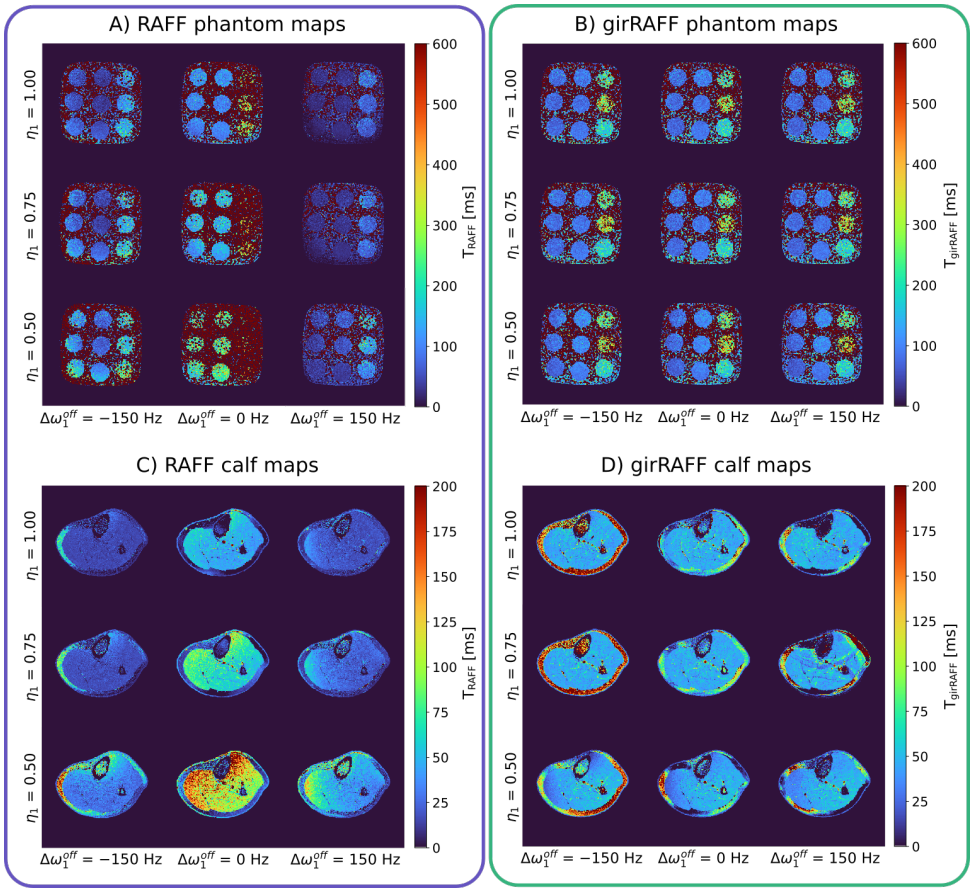

Figure 7.S7 : Second set of (A-B) phantom and (C-D) in-vivo calf RAFF and girRAFF maps obtained for each combination of $(\Delta\omega_1^{off}, \eta_1) \in \{-150, 0, 150\}$ Hz $\times \{0.5, 0.75, 1.0\}$. This set of maps was acquired with shorter RAFF preparation durations ($T_{prep,RAFF}$ = 16.5, 34.0, 67.9 ms), to account for the shorter in vivo T_{RAFF} relaxation times and achieve comparable relaxation decay sampling between RAFF and girRAFF. Trends are comparable to those observed in the first set of phantom and calf maps, displayed in Figure 5. Both phantom and calf T_{RAFF} maps show high variability across inhomogeneity combinations. $T_{girRAFF}$ maps, on the other hand, depict improved resilience to system imperfections.

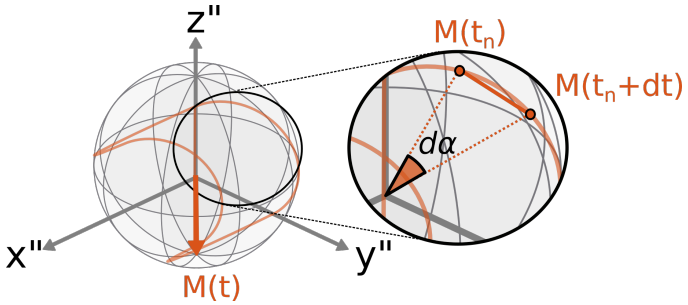

Figure 7.S8 : Magnetization trajectory length, computed as the cumulative sum of the discretised angular distances covered by the magnetization vector on the Bloch sphere during simulations. The trajectory length is measured in radians and low trajectory length ($< 3.2\pi$ rad) cases were discarded to avoid idle parameter configurations yielding low power pulses with high preparation efficiency but no spin-lock relaxation.

8

Optimizing dipole-dipole relaxation resilience to off-resonance fields during adiabatic $T_{1\rho}$

Chiara Coletti[†], Mark Vermeulen[†], Sebastian Weingärtner

Proceedings of the 46th Annual International Conference of the IEEE Engineering in Medicine and Biology Society, (2024)

[†]These authors contributed equally

Abstract

Quantitative MRI measurements with adiabatic $T_{1\rho}$ can provide sensitive markers to pathological alterations in the presence of system imperfections, especially at high field strengths. However, the mechanisms behind $T_{1\rho,adiab}$ relaxation during adiabatic RF pulses are complex and present strong dependence on the pulse design. The aim of this study is to investigate the resilience of $T_{1\rho,adiab}$ times measured during adiabatic RF irradiation to B_0 inhomogeneities, considering both $T_{1\rho}$ dispersion and inversion efficiency. Redfield relaxation theory is used to study the effect of off-resonance on the efficiency of the underlying relaxation processes and Bloch simulations are used to investigate the pulse efficiency. Joint optimization of hyperbolic secant adiabatic pulses yields optimal off-resonance resilience for β=5.9 and moderate FM amplitude≈1500 Hz. For this combination the off-resonance-induced dispersion is seven-fold reduced when compared to pulses obtained with conventional Bloch simulations only. The proposed optimization provides promising candidates for robust $T_{1\rho,adiab}$ preparation pulses for in vivo applications at 3T.

8.1. Introduction

Quantitative Magnetic Resonance Imaging (MRI) is increasingly gaining attention due to its ability to provide inter- and intra-patient comparable non-invasive tissue characterization. The quantification of relaxation times, such as T_1, T_2, or T_2^*, emerged as a promising tool to differentiate healthy and diseased states across several anatomies [434]. While T_1 and T_2 relaxation times display sensitivity to molecular interactions near the Larmor frequency and at 0 Hz, respectively, alternative relaxation mechanisms can tap into a wider range of molecular sensitivities [343]. Rotating frame relaxation techniques, such as $T_{1\rho}$ mapping, have been explored for their intrinsic sensitivity to interactions at intermediate frequencies, in the Hz-kHz range. Clinical application of these techniques has shown promise in a range of pathologies, including assessment of cartilage degeneration [435], ischemic and non-ischemic heart diseases [330, 361, 365], neuro-pathologies [429, 436, 437] and liver fibrosis [421, 438, 439].

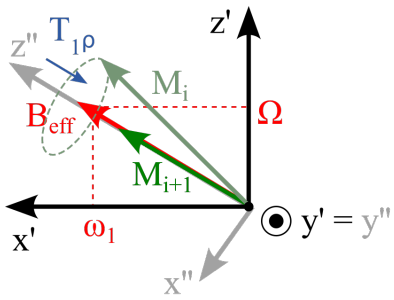

Figure 8.1 : The effective field B_{eff} and the magnetization vector M in the first rotating frame. In the second rotating frame, B_{eff} is aligned with the z-axis. In this figure, the magnetization vector evolves from M_i to M_{i+1}, following the effective field. It also shortens due to $T_{1\rho}$ relaxation.

$T_{1\rho}$ is the time constant that characterizes the longitudinal magnetization relaxation in the rotating frame of reference, during radio-frequency (RF) irradiation. Conventionally, $T_{1\rho}$ relaxation is induced by the continuous application of an RF pulse, the so-called spin-lock (SL) pulse [320]. However, continuous-wave SL pulses are highly susceptible to B_0 and B_1^+ inhomogeneities. This hinders robust quantification, particularly at high field strengths. Adiabatic $T_{1\rho}$ preparations have been proposed to overcome such limitations and enable robust $T_{1\rho,adiab}$ mapping at 3T [72, 73, 367, 440]. Due to the use of frequency-modulated pulses, $T_{1\rho,adiab}$, however, exhibits a different spectrum of sensitivities compared with conventional $T_{1\rho}$. Previously, it has been proposed to use Redfield relaxation theory to characterize the relaxation properties of $T_{1\rho,adiab}$ as a function of the adiabatic pulse parameters [343]. Alternatively, Bloch simulations have been used to optimize adiabatic

pulse shapes for improved performances in the presence of field inhomogeneities [82, 367].

In this study, we propose a comprehensive optimization of adiabatic pulse design for $T_{1\rho,adiab}$ mapping at 3T. Redfield-based relaxation theory was used to minimize $T_{1\rho,adiab}$ dispersion in the presence of B_0 inhomogeneities and combined with Bloch simulations to optimize inversion efficacy of adiabatic pulses for a range of off-resonances. Optimal pulse shape parameters were identified in a joint optimization and compared to pulse optimization based on Bloch simulations only.

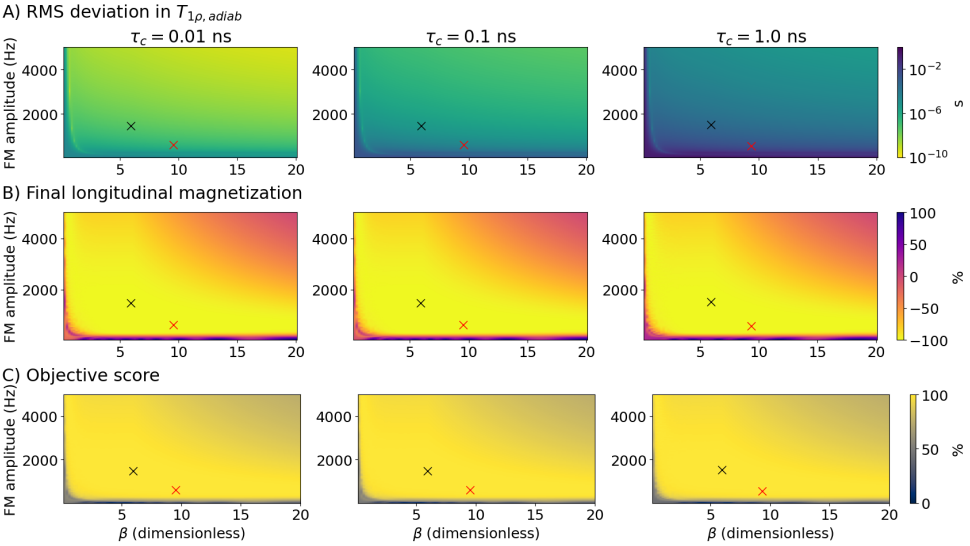

Figure 8.2 : A) RMS deviation of the $T_{1\rho,adiab}$ in the presence of off-resonance, B) inversion efficiency, C) combined objective, as a function of different pulse parameters β and the FM amplitude for three correlation times, with the optimal parameters obtained from the joint optimization (black) and Bloch-optimization only (red).

8.2. Methods

8.2.1. Redfield theory

The effect of off-resonance on the relaxation during the frequency-modulated pulses was studied using Redfield theory. Step-wise estimation of the rotating frame relaxation in the presence of a field with variable amplitude- (AM) and frequency-modulation (FM) functions was performed. Using this instantaneous $T_{1\rho,adiab}(t_i)$, the effective $T_{1\rho,adiab}$ over the entire pulse was obtained as: $\frac{1}{T_{1\rho,adiab}} = \frac{1}{T_p}\sum_i \frac{\Delta t}{T_{1\rho,adiab}(t_i)}$, with pulse duration T_p, and time discretization Δt.

Relaxation was modeled for the interactions between the spins and

random, isotropic field fluctuations, as commonly assumed for dipole-dipole interactions. The power spectrum of the fluctuation was assumed to be Lorentzian with correlation time τ_c. A transformation to the second rotating frame, where the effective field ω_{eff}/γ is aligned with the z-axis, allows the calculation of the instantaneous relaxation time as:

$$\begin{aligned}\frac{1}{T_{1\rho,adiab}}(t) = \frac{\gamma^2\omega_1^2}{\omega_{\text{eff}}^2}\left\langle B^2\right\rangle J(\omega_{\text{eff}}) \\ + \frac{\gamma^2}{2\omega_{\text{eff}}^2}\left\langle B^2\right\rangle(\Omega+\omega_{\text{eff}})^2 J(\omega_{\text{rf}}+\omega_{\text{eff}}) \\ + \frac{\gamma^2}{2\omega_{\text{eff}}^2}\left\langle B^2\right\rangle(\Omega-\omega_{\text{eff}})^2 J(\omega_{\text{rf}}-\omega_{\text{eff}}) \quad (8.1)\end{aligned}$$

Here $\Omega = \omega_0 - \omega_{\text{rf}}$ is the off-resonance, $\omega_{\text{eff}} = \sqrt{\omega_1^2+\Omega^2}$ is the frequency corresponding to the effective field strength, and $J(x)$ represents the spectral density function of the fluctuations.

8.2.2. Bloch simulations

Bloch simulations were used to assess the pulse performance in terms of inversion efficiency. For each time discretization step the effective field was calculated and used iteratively to derive the magnetization evolution throughout the pulse, starting from the initial magnetization along the z-axis.

8.2.3. Optimization

In this study, hyperbolic secant (HS) adiabatic pulses were used for optimization, with AM and FM given as:

$$\omega_1(t) = \omega_1^{\max} sec\left(\beta\left(\frac{2t}{T_p}-1\right)\right) \quad (8.2)$$

$$-\Omega(t) = A\,\text{tanh}\left(\beta\left(\frac{2t}{T_p}-1\right)\right). \quad (8.3)$$

The degrees of freedom in the pulse shape optimization are the B_1^+ peak amplitude $\omega_1^{\max}$, the pulse duration T_p, the peak width of the RF pulse β, and the FM amplitude. For optimal performance $\omega_1^{\max}$ and T_p were chosen as dependent parameters in the optimization, leaving β and the FM amplitude as optimization parameters. The optimization was performed using grid search, with $\beta \in \{0.1, 0.3, \ldots, 20\}$ and the FM amplitude $\in \{0, 50.4, \ldots, 5000\}$ Hz. For each grid point, the optimization

was performed iteratively. The pulse was initialized with a pulse duration of $T_p = 30$ ms and $T_{1\rho,adiab}$ was calculated. Based on this value, the pulse duration was rescaled to achieve a total $T_{1\rho,adiab}$ decay fraction of 0.970 ± 0.001. The pulse amplitude was then maximized within the constraints $B^+_{1,max} \leq 13.43$ μT and $B^+_{1,rms} \leq 5.48$ μT. The relaxation was then recalculated. The optimization was truncated after 1.5 iterations, as heuristically minimal changes in the $T_{1\rho,adiab}$ are observed during the rescaling.

Based on the adapted pulse, the $T_{1\rho,adiab}$ value was calculated for $0, 50, \ldots, 200$ Hz off-resonance. The relative root-mean-square (RMS) deviation between the on- and off-resonance values in percent was used as a measure of the off-resonance resilience. Next, Bloch simulations were carried out for the same pulse module. The relative deviation of the average final longitudinal magnetization from perfect inversion in percent was used as a measure of the inversion efficiency. The product of the relative off-resonance deviation and the inversion efficiency was used as the combined objective score. The optimization was repeated for three different correlation times ($\tau_c = 0.01, 0.1$ and 1 ns, representing liquids with molecular masses of 20, 200 and 2000 Da), each with the magnitude of the field fluctuations normalized to yield $T_1 = 1.5$ s.

8.3. Results

Figure 8.2A shows the simulated $T_{1\rho,adiab}$ deviation measured for different combinations of β and FM amplitude in the presence of B_0 inhomogeneities up to 200 Hz. The different correlation times display similar patterns of minimal $T_{1\rho,adiab}$ dispersion for very high β and FM amplitude values (light green/yellow regions). Significantly larger $T_{1\rho,adiab}$ dispersion was observed for pulses with $\beta < 1$ or FM amplitude < 200 Hz. Overall, $T_{1\rho,adiab}$ deviation in the presence of B_0 inhomogeneities increased with longer correlation times τ_c for each combination of β and FM amplitude.

Average pulse inversion efficiency over a range of off-resonances shows only small differences between different correlation times. The differences are caused by the rescaling of the adiabatic pulse duration. For all correlation times, the best preparation efficiency was obtained for intermediate frequency sweep amplitudes and showed an inversely proportional relationship with β. The final objective score shows relatively robust performance over a large parameter space for all three correlation times. The optimal pulse parameter combination yielding the highest score was $\beta = 5.9$ for all correlation times, FM amplitude = 1472 Hz for $\tau_c = 0.1$ and 0.01 ns, and 1522 Hz for $\tau_c = 1$ ns. The optimal pulse duration was = 44.4 ms for $\tau_c = 0.01$ and 0.1 ns, and 43.2 ms for $\tau_c = 1$ ns. The optimal max $B^+_1 = 13.35$ μT for all correlation times.

The pulses obtained across the parameter space are illustrated in

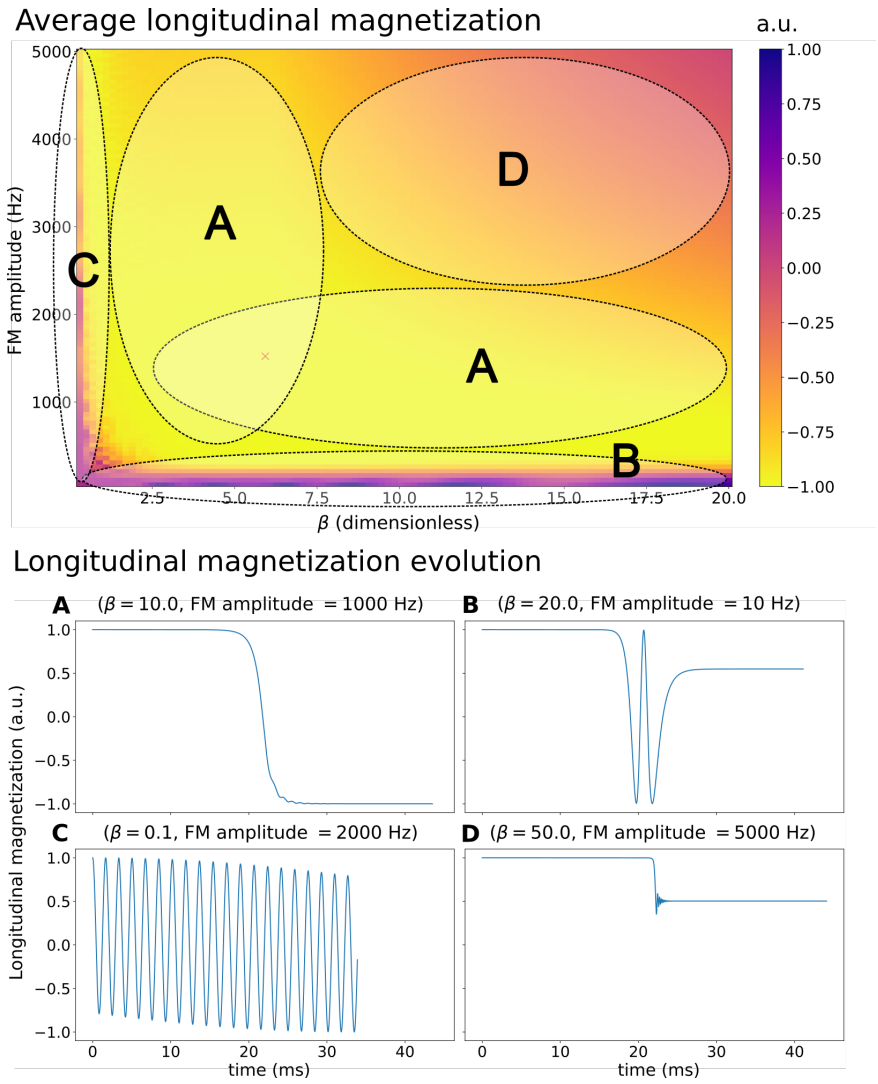

Figure 8.3 : Different pulse regimes in the parameter space of the hyperbolic secant pulses (left panel) overlaid on the inversion efficiency at $\tau_c = 1$ ns. Regime A) corresponds to the adiabatic region, B) corresponds to block-like pulses, C) chirp-like pulses and regime, and D) non-adiabatic region. (A-D) Corresponding evolution of the magnetization over time for representative pulse shape within each of the regimes.

Figure 8.3A. In the regime of intermediate frequency sweep amplitudes and inversely proportional βs, where optimal pulse performance was achieved, the pulses operate in an adiabatic regime (Figure 8.3B). HS pulses with low FM amplitudes approximate chirp pulse shapes and result in low effective field strengths and fast frequency sweep, yielding

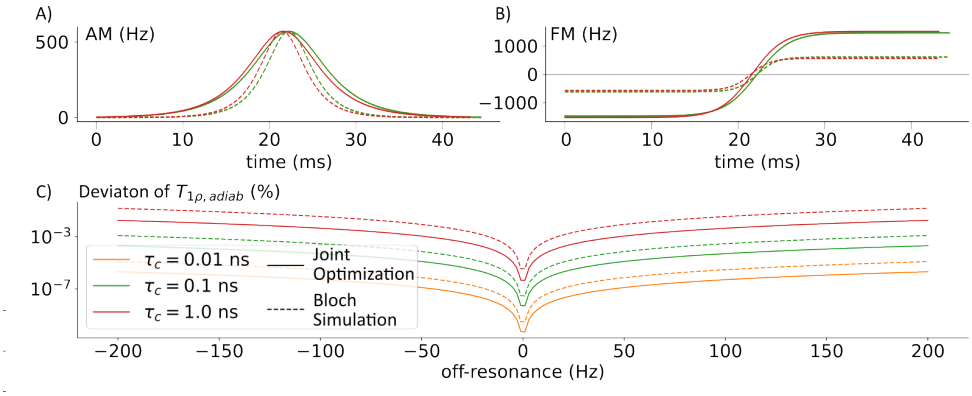

Figure 8.4 : A) Amplitude and B) Frequency modulation functions of the pulses optimized with the joint optimization (solid) and Bloch simulations only (dashed) for the three correlation times. $\tau_c = 0.1$ and 0.01 ns are nearly identical results and, thus, visually barely discernable. C) Logarithmic $T_{1\rho,adiab}$ deviation as a function of the off-resonance for the optimized pulses.

imperfect inversion (Figure 8.3C). Low β values produce block-like AM functions, which prevent spin-locking throughout HS pulse irradiation and result in non-robust inversion mechanisms (Figure 8.3D). Finally, the combination of high β and very high FM amplitudes leads to pulses operating in the sub-adiabatic regime, with fast amplitude and frequency sweep speed preventing robust adiabatic inversion (Figure 8.3E).

The optimal pulses are shown alongside the off-resonance susceptibility of the $T_{1\rho,adiab}$ time in Figure 8.4. In agreement with results in Figure 8.2A, longer correlation times lead to larger absolute $T_{1\rho,adiab}$ deviations in the presence of B_0 inhomogeneities. When compared to adiabatic pulses chosen based on Bloch simulations only, the optimized pulse yields 83%, 83%, and 88% improved resilience in relaxation time in the presence of off-resonance at $\tau_c = 0.01, 0.1$, and 1 ns respectively.

8.4. Discussion

In this study, we proposed a framework to optimize adiabatic HS pulse design for robust $T_{1\rho,adiab}$ mapping at 3T. By jointly minimizing $T_{1\rho,adiab}$ dispersion in the presence of B_0 inhomogeneities and maximizing inversion efficiency of single HS pulses, optimal performances were found for intermediate β and FM amplitudes ($\beta = 5.9$, FM amplitude = 1472 and 1522 Hz).

Conventional pulse design optimization schemes proposed in previous studies [82, 367] focused on the effectiveness of the adiabatic inversion process. However, $T_{1\rho,adiab}$ relaxation follows complex dynamics throughout the pulse. Optimization based exclusively on Bloch

simulations led to intermediate-to-low β and FM amplitude choices. These pulses, while providing great image quality and robustness to both B_0 and B_1^+ inhomogeneities, can induce significant $T_{1\rho,adiab}$ dispersion in the presence of off-resonances. The proposed optimization includes the effects of off-resonance on the $T_{1\rho,adiab}$ relaxation. This allows to maintain high pulse efficiency while ensuring the effectiveness of the underlying relaxation processes remains high.

The employed Redfield-based relaxation model has been shown to be a good approximation for liquids with primarily dipole-dipole interactions [441]. However, for biological tissue other relaxation mechanisms are contributing, including chemical exchange, chemical shift anisotropy, or diffusion. Future work will focus on extending the pulse optimization to include more extensive relaxation models to better approximate certain in vivo applications.

The pulse optimization considering relaxation during the adiabatic pulses is specifically targeted for quantitative $T_{1\rho,adiab}$ measurements. However, for other uses of adiabatic pulses, like robust inversion or refocusing, the relaxation throughout the pulse may be less relevant, warranting a different objective function. Furthermore, the pulses were optimized for minimal dispersion of the relaxation mechanism. However, this may not necessarily yield the largest clinical effect size to a given pathological alteration. Thus, further studies in animal models or well-controlled pathologies are warranted to investigate clinical sensitivity and robustness of the proposed pulse modules for in vivo mapping.

8.5. Conclusions

Using a combination of relaxation theory and Bloch simulations, optimal parameters for $T_{1\rho,adiab}$ mappings were found to be in the intermediate range ($\beta = 5.9$, FM amplitude = 1472 and 1522 Hz). These pulses can provide a promising starting point for use in adiabatic $T_{1\rho,adiab}$ measurements with high confounder resilience and minimal off-resonance dispersion.

9

Functional MRI of neuro-electro-magnetic oscillations: Statistical processing in the presence of system imperfections

Chiara Coletti, Sebastian Domsch, Frans M. Vos, Sebastian Weingärtner

2020 IEEE-EMBS Conference on Biomedical Engineering and Sciences (IECBES). IEEE, 2021, pp. 172-177, doi:10.1109/IECBES48179.2021.9398751

Abstract

Direct detection of magnetic fields elicited by neuronal activity using Magnetic Resonance Imaging (MRI) has been a long-standing research goal, due to its potential to overcome limitations that are inherent to BOLD fMRI. The MRI signal can be sensitized to oscillating magnetic fields using spin-lock preparations. However, the susceptibility of spin-lock sequences to system imperfections has so far hindered their translational potential for in vivo experiments. Moreover, the sensitivity of the neuro-current MRI signal to the phase of neuro-electric oscillations generates high variance time courses that are not suited for analysis with traditional fMRI data processing techniques.

In this work, we study the impact of various MRI system imperfections on neuro-current MRI in simulations. Furthermore, we propose Statistical Variance Mapping (SVarM) as a new data processing technique for generating activity maps from neuro-current MRI signal variance. Bloch simulations demonstrated substantial variations of the signal intensity for a 400 Hz range of off-resonances and a 360° range of neuro-current oscillating phases. SVarM was tested on synthetic neuro-current data simulated with various degrees of system imperfections. The proposed technique was compared to the previously developed NEMO processing, which is based on the mean analysis of time courses. Simulation results show improved resilience against B_0 inhomogeneities with SVarM compared with NEMO processing (Dice coefficient of activation maps: 64.07% SVarM, 57.76% NEMO, $p<0.02$). Comparable or slightly improved robustness against B_1^+ inhomogeneities was observed as well as higher sensitivity in the absence of B_1^+ inhomogeneities (Dice score of activation maps: 58.34% SVarM, 49.70% NEMO, $p<0.01$). Finally, SVarM achieved better specificity for low SNR, resulting in activation maps with fewer false positive voxels (FP rate: 0.53% SVarM, 19.28% NEMO, $p<0.01$). These results underscore the importance of dedicated data processing methods and robust pulse sequences to facilitate the widespread use of direct neuro-current MRI in the presence of system imperfections.

9.1. Introduction

Functional Magnetic Resonance Imaging (fMRI) is one of the leading tools for the study of brain activation in vivo, due to its ability to obtain non-invasive functional imaging with high spatial resolution and whole brain coverage. fMRI is conventionally based on the Blood-Oxygen-Level-Dependent (BOLD) contrast, which is caused by local field inhomogeneities related to the neurovasculature and the local concentration of oxygenated and deoxygenated-hemoglobin [442]. Thus, BOLD fMRI provides only an indirect marker of neuronal activity, via the hemodynamic response of the brain [443]. Specifically, the signal is limited by the temporal delay of the hemodynamic response function.

The direct detection of magnetic fields elicited by neuronal activity has been a long-standing goal in MRI, due to the potential of overcoming the mentioned limitations intrinsic to BOLD-fMRI. Direct neuro-current MRI could enable the investigation of brain activity with high temporal resolution and specificity. Early attempts focused on imaging the neuronal current distribution originating from neuronal action potentials ex vivo. Multiple methods sought to pick up magnitude or phase changes in the MRI signal as a direct result of neuronal activation [444–446]. However, these approaches were never successfully applied in vivo because of the temporal and spatial cancellation effects inside single voxels [447–449]. Over the last decade, studies have demonstrated the feasibility of sensitizing MRI signals to concerted voltage fluctuations, so-called Local Field Potentials (LFP) [450], using spin-lock preparations [451–453]. These techniques, based on the rotary saturation effect induced by a resonant spin-lock field, overcame the issue of cancellation in phase and magnitude contrast imaging [451]. Moreover, the spin-lock field can be tuned to a specific frequency band of oscillating neuroelectric currents (Figure 9.1). Halpern-Manners et al. have shown that the frequency selectivity of the contrast mechanism allows to compensate for experimental non-idealities with specific band-selective variants of the spin-lock sequence, as demonstrated in a phantom study [452]. Most recently, promising results were reported, demonstrating the viability of spin-lock techniques for in vivo experiments in the human brain [453]. However, direct current imaging requires very high sensitivities to detect magnetic fields in the order of magnitude of a few nT [454]. Consequently, system imperfections compromising the sensitivity in in vivo experiments have so far prevented this technique from more widespread use in the study of brain activation.

In this work, the effects of system imperfections on the state-of-the-art spin-lock sequence for direct current imaging are investigated in simulations. The studied variables include B_0 and B_1^+ field inhomogeneities, phase differences between the spin-lock and neuro-current-induced fields, and background noise. Furthermore, to improve

the robustness of this technique, a new data processing technique, specifically designed for neuro-current MRI is proposed. This technique is compared to the existing post-processing pipeline. The resilience against system imperfections of the two processing techniques is further evaluated in synthetic neuro-current data.

9.2. Methods

Figure 9.1 depicts the spin-lock-based method for neuronal current imaging [453], as used in this study. In the spin-lock preparation, prior to imaging, the magnetization is flipped to the transverse plane. The application of a spin-lock field B_{SL} achieves, in addition to regular $T_{1\rho}$ relaxation, sensitization to oscillating currents, such as

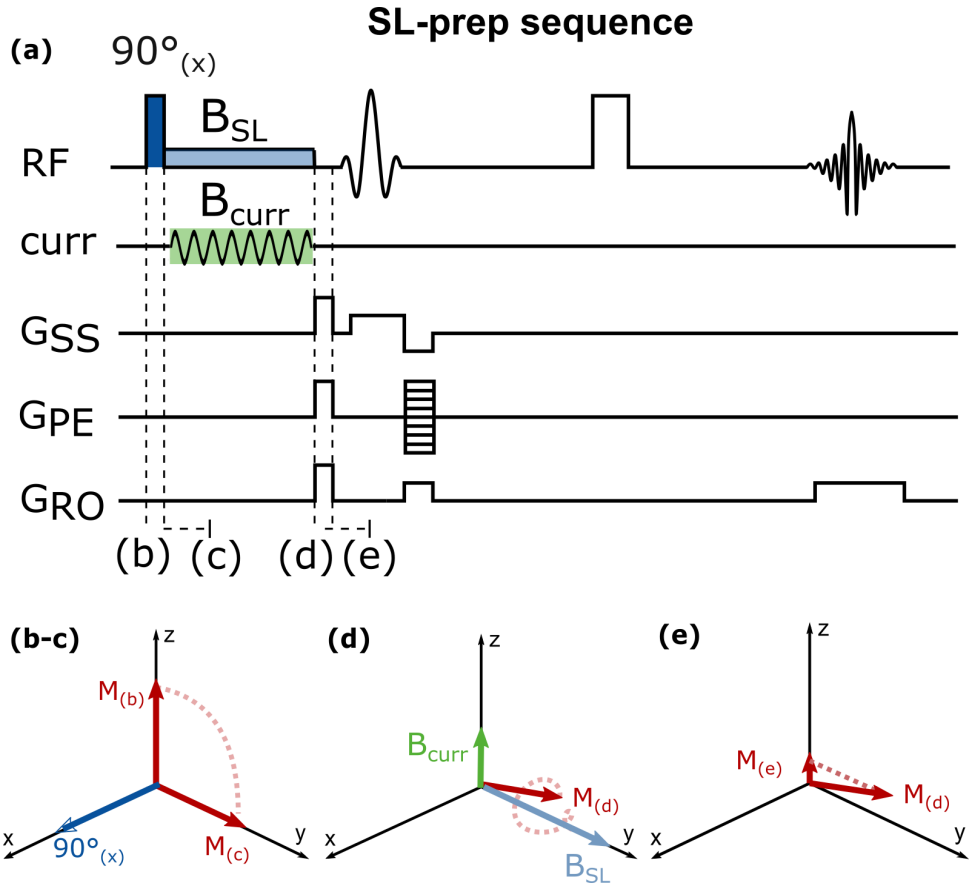

Figure 9.1 : Spin-lock sequence diagram (a). Evolution of the net magnetization during spin-lock preparation with concomitant neuro-current field action (b-e).

generated by LFPs. Subsequently, the transverse magnetization is depleted with spoiler gradients. Hence, the effect of neuro-currents near the resonance frequency is encoded in the residual longitudinal magnetization. The amplitude of the spin-lock field is tuned to the frequency ω_{CURR} of the resonant oscillating neuro-magnetic fields B_{CURR}, with $B_{SL} = \omega_{CURR}/\gamma$. Here γ is the gyromagnetic ratio. Following the magnetization preparation, the signal is then read out with spin-echo Echo-Planar Imaging (EPI).

9.2.1. Bloch simulations

Bloch simulations were performed to assess the sensitivity of spin-lock-prepared imaging to oscillating neuro-currents in the presence of system imperfections. Signals were simulated for various B_0 inhomogeneities and varying phase differences between the neuro-current oscillations and the spin-lock field.

The evolution of the magnetization during the application of a spin-lock field along the y-axis can be described in a doubly rotating frame of reference, rotating about the z-axis with $\omega_0 = \gamma B_0$ and about the y-axis with $\omega_{SL} = \gamma B_{SL}$. Neglecting T_2^* decay yields the following signal description:

$$\frac{dM}{dt} = \gamma M \times [B_{SL}(1 - \frac{\omega_{curr}}{\gamma |B_{SL}|}) + B_{CURR} + \frac{\Delta\omega}{\gamma}] - R \times (M - M_\rho). \tag{9.1}$$

Here B_{CURR} is the amplitude of the neuro-current oscillating field, ω_{CURR} is the frequency of these oscillations, $\Delta\omega = \omega_0 - \omega$, with ω_0 being the B_0 field frequency and ω being the B_{SL} field frequency. M_ρ is the equilibrium value of the magnetization under the spin-lock condition. The relaxation matrix R is defined as:

$$R = \begin{pmatrix} 1 & 0 & 0 \\ 0 & \frac{1}{T_{1\rho}} & 0 \\ 0 & 0 & 1 \end{pmatrix}. \tag{9.2}$$

According to Equation 9.1, when the oscillating currents are in resonance with the spin-lock field, the magnetization rotates in the transverse plane of the doubly rotating frame of reference. The relative phase between the spin-lock field and neuro-current oscillations determines the final phase of the magnetization in the rotation about the spin-lock axis. However, in the presence of B_0 inhomogeneities, the spin-lock field is tipped away from the transverse plane, inducing spurious longitudinal magnetization even in the absence of neuro-currents.

Bloch simulations were performed for off-resonance $\Delta\omega$ values between -200 Hz and 200 Hz, covering the realistic range of off-resonance values for brain scans at 3T, and for phases of the neuro-currents varying

between 0° and 360°. Signals with or without concomitant neuro-magnetic fields caused by neuro-currents were compared. The remaining simulation parameters were B_0 = 3.0 T, neuro-current field strength B_{CURR} = 200 nT oscillating at 100 Hz, spin-lock duration = 100 ms and $T_{1\rho}$ = 78 ms [436].

9.2.2. Synthetic neuro-current MRI data

Based on the results of Bloch simulations, neuro-current MRI time series were simulated for an entire brain volume (1 x 1 x 3 mm^3 resolution). A common experimental design was reproduced from a previous BOLD fMRI study [455]: A simple block design paradigm was adopted, consisting of interleaving 10 bilateral fingertapping and 10 rest periods. Each block had a duration of 13.5 s (total duration = 4 min 30 s).

Synthetic neuro-current MRI datasets were generated using BOLD response as a rough proxy for LFPs activation [450]. BOLD fMRI data obtained in a previous study with the same experimental design as the simulated time series were used [455]. Six healthy subjects (24±3 years old) performed a bilateral finger-tapping task with the paradigm described above. BOLD fMRI data were processed through Statistical Parametric Mapping (SPM) [456], with a standard fMRI first-level analysis, using a General Linear Model (GLM) to model BOLD signal on a voxel-by-voxel basis. The SPM design matrix X was composed of one regressor modeling the BOLD response (a boxcar function convolved with the hemodynamic response), six regressors modeling low-frequency confounds due to motion, and a final regressor for a constant baseline shift. Active areas identified with BOLD imaging were used as ground truth for the generation of neuro-current data.

Neuro-current time courses were modulated to account for off-resonances and phase differences between the spin-lock field and the neuro-current field, as well as B_1^+ inhomogeneities, using Bloch simulations as described above. f_{SL} values were derived by normalizing a representative B_1^+ map with the nominal 100 Hz resonant frequency. The B_1^+ map was rescaled to simulate different levels of inhomogeneities. Similarly, the off-resonances were derived from a characteristic B_0 map [456], rescaled to account for different off-resonances intensities, up to 200 Hz. Each voxel was assumed to have a constant value of off-resonance and B_1^+ over the duration of the experiment. The relative phase values at each repetition time were modeled to account both for random and deterministic components. At the beginning of each active period, the phase difference between the spin-lock and the neuro-current fields was sampled from a uniform distribution, given the impossibility of exactly synchronizing the spin-lock pulse onset with the task eventually performed by human subjects. The relative phase values

for the following TRs are instead determined from the repetition time $TR = 2.7s$ and the neuro-current frequency f_{CURR}. Finally, additive white Gaussian noise was added with SNR ranging from 0.1 to 2.

Representative simulated time series are shown in Figure 9.2 for two areas of the brain either with or without brain activation and corresponding simultaneous neuro-current (off-resonance = 100 Hz, f_{SL} map scaling factor = 1, SNR = 0). Traditional BOLD response for the proposed experimental design follows a cyclic pattern oscillating at the task frequency (f_{task} = 1/27 s ≈ 0.037 Hz), with active and rest phases presenting different mean values. Neuro-current MRI time courses, instead, depict a constant mean over the entire duration of the experiment but with increased variance in the presence of neuronal activation. The variability is induced by varying phase differences between the spin-lock and neuro-current fields.

Finally, full synthetic neuro-current datasets Y_{NC} were computed, using the β parameters estimated with the SPM analysis, as:

$$Y_{NC} = X_{NC}\beta + \epsilon, \tag{9.3}$$

where ϵ is additive white Gaussian noise and X_{NC} is a modified design matrix that has the simulated neuro-current time series (Figure 9.2) in place of the boxcar BOLD regressor.

9.2.3. Post-processing

As neuronal activity is encoded in signal variability in the spin-lock method, standard fMRI processing is not suitable. Instead, the use of a new data processing pipeline specifically designed for neuro-current MRI is investigated. This post-processing is compared to the method used by Truong et al., termed Neuro-Electric Magnetic Oscillations (NEMO) processing [453].

NEMO processing is based on frequency component analysis of the time series, to separate BOLD contributions from neuro-current-induced signal variability. First, region-based normalization was performed using the Destrieux atlas [457], by subtracting the region-average time course from each voxel. Destrieux regions were obtained by cortical parcellation of the anatomical images in FreeSurfer [457], and then merged across hemispheres. This step reduces residual physiological and hemodynamic confounds. Second, the signal was high-pass filtered with a cut-off frequency above the task frequency but below TR (0.1 Hz for the proposed paradigm), to eliminate mean fluctuations between on and off blocks as created by BOLD contributions (Figure 9.3B). Finally, a rectification step was applied, converting the high-variance/low-variance oscillations to differences in the mean signal between on and off blocks (Figure 9.3C). These signal components were observed at the task frequency f_{task}. Consequently, activation maps were generated from spectral components of the signal at the task frequency (Figure 9.3D).

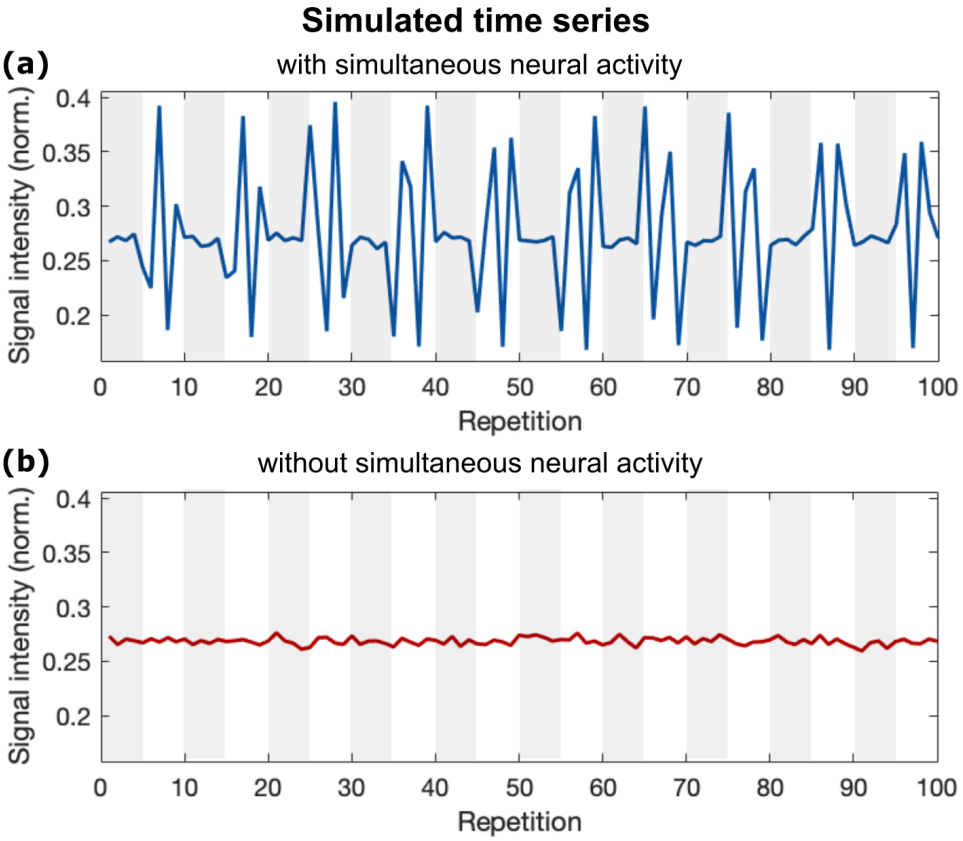

Figure 9.2 : Representative simulated neuro-current MRI time courses, with (a) or without (b) concomitant neuronal activation.

To specifically exploit the pattern of differences in the signal variance, in a statistically rigorous way, a new processing pipeline is proposed, akin to SPM (Figure 9.3E-H). In Statistical Variance Mapping (SVarM), first, a GLM was used to remove physiological motion confounds and other low-frequency artifacts from the neuro-current signal. For this purpose, the GLM design matrix was built using the same regressors described in Section 9.2.2, except for the regressor modeling the BOLD response. This yields time course signals as shown in Figure 9.3F. Next, the data in the time series was pooled into two groups, corresponding to signals acquired during active (Figure 9.3G) and rest blocks (Figure 9.3H), respectively. Non-paired statistical variance testing was performed across the two groups to detect significant differences in variability between on and off periods. Levene's test with the null hypothesis of equal variability was used for statistical testing. Levene's test was chosen to account for non-Gaussian signal distribution caused

by the homogeneously distributed phase variations. Activation maps were generated, akin to SPM, by displaying the statistical significance on a voxel-by-voxel basis.

The performance of both processing methods was quantified using two

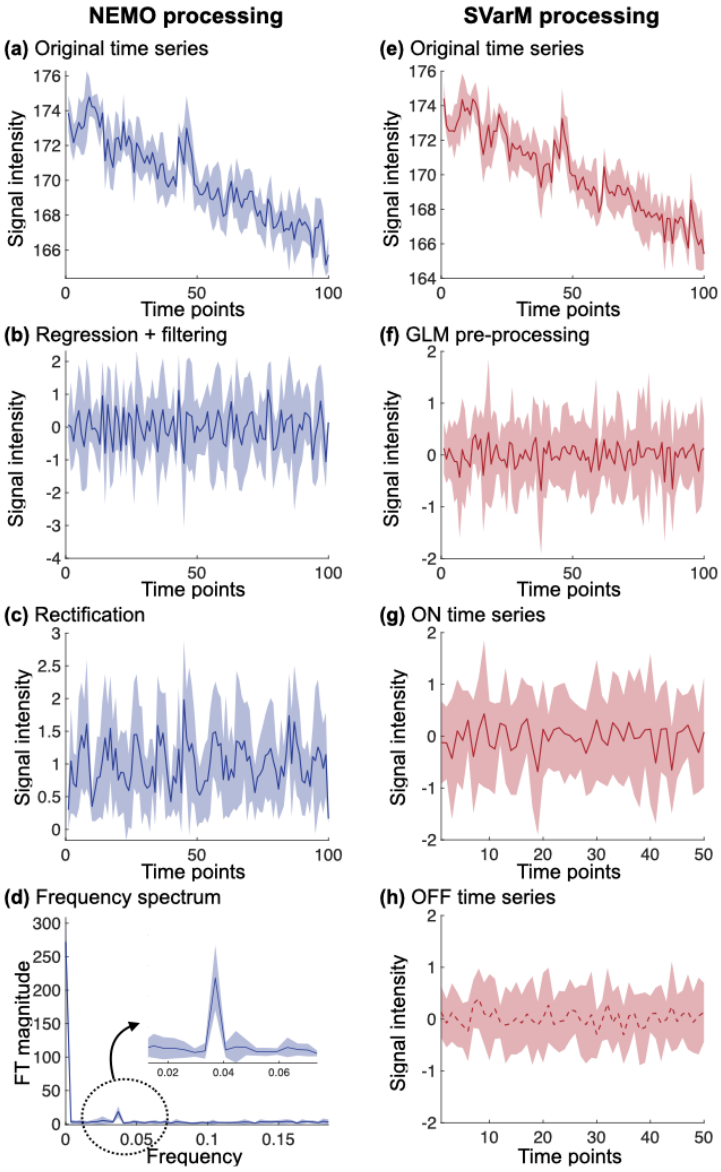

Figure 9.3 : Representative time courses and power spectra after each step of the NEMO processing (a-d) and SVarM processing (e-h). Darker lines represent the mean, shaded areas the standard deviation.

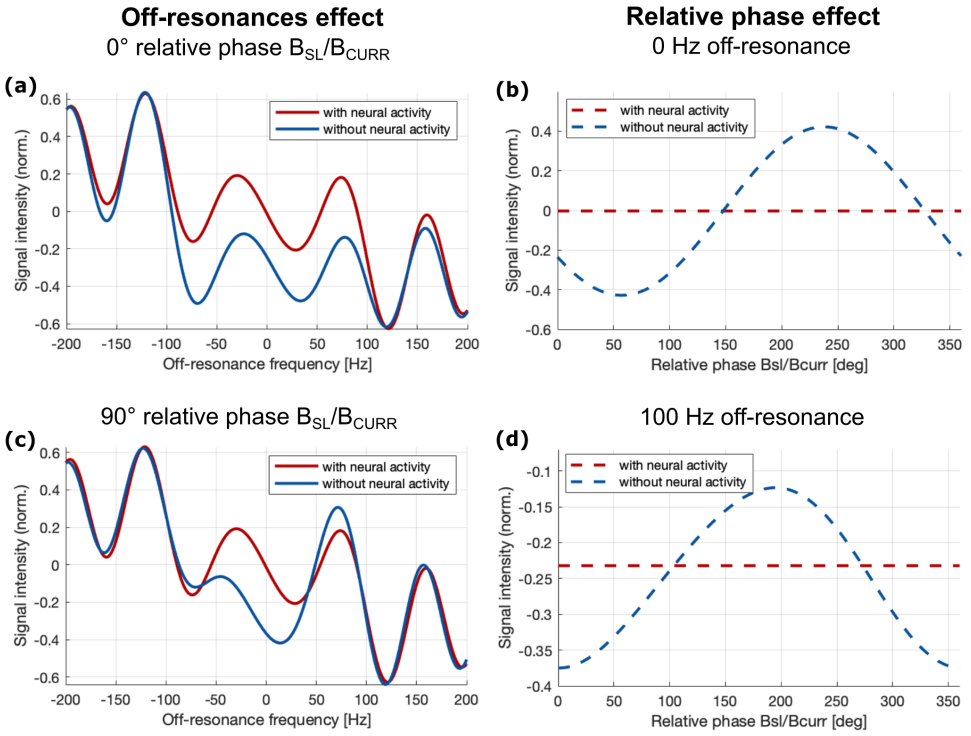

Figure 9.4 : Bloch simulation results for a 400 Hz range of off-resonances (a,c) and a 360° range of relative phases between B_{SL} and B_{CURR} (b,d).

different measures to compare the activation maps with the reference: 1) Dice coefficient of the activation area with respect to the ground truth activation ($Dice = 2TP/(2TP + FP + FN)$; 2) surviving pixels coefficient, normalized to the number of the active pixels in the reference activation ($SP = TP + FP$). The two coefficients were computed by averaging the results of 10 runs for each experimental condition. The statistical significance of the results was tested with a two-way ANOVA analysis.

9.3. Results

The Bloch simulation results in Figure 9.4 depict the dependence of neuro-current MRI signals on different values of off-resonances and B_{SL}/B_{CURR} relative phase, compared with the reference signal with no concomitant neuronal activation. Figure 9.4A-C shows substantial variation of the sensitivity for a range of 400 Hz of off-resonances, ranging between ±60% of the original signal intensity. The contrast between active and inactive areas diminishes substantially for absolute values of off-resonances higher than 100 Hz. Figure 9.4B-D shows that

the signal dependence on the relative phase between the neuro-current and spin-lock fields is sinusoidal in active areas, whereas the signal from inactive areas does not depend on the relative phase at all, as it is not perturbed by B_{CURR}.

The two post-processing methods, NEMO processing, and SVarM, were compared using the outcome of synthetic neuro-current fMRI experiments. Activation maps, shown in Figures 9.5, 9.6 and 9.7, were obtained by analyzing synthetic neuro-current datasets through NEMO analysis and the proposed SVarM technique. Thresholded maps are shown for a representative horizontal slice of a single subject and compared to the ground truth T-maps obtained by running SPM first-level analysis on the original BOLD fMRI dataset.

Figure 9.5 shows the performance of the two post-processing techniques as a function of off-resonance. The different values of off-resonances were modeled by scaling the B_0 maps from the ideal zero off-resonance case up to a maximum off-resonance value of 200 Hz. Sensitivity shows an approximately linear decrease for increasing off-resonance values. Mean Dice score values are 64.07% ± 2.35% for SVarM and 57.76% ± 3.24% for NEMO processing ($p < 0.02$). The surviving pixel ratio reached 66.53% ± 4.70% in SVarM and 49.88% ± 4.30% in NEMO processing ($p < 0.01$).

Figure 9.6 shows the dependence on B_1^+ inhomogeneities. The trends in the Dice and surviving pixel coefficients plots indicate that both methods obtained better results when the level of B_{SL} inhomogeneity increased. In particular, substantial signal degradation appears on activation maps when the scaling factor for ω_{SL} maps decreases below 0.5. With SVarM, Dice coefficients drop from values of 63.57% ± 3.38% to a minimum of 40.05% ± 13.95% and the surviving pixel ratio from values around 66.59% ± 6.79%to a minimum of 33.17% ± 17.75%. The sensitivity loss is more severe for NEMO processing (Dice: from 59.41% ± 3.74% to 15.71% ± 24.48%, surviving pixel ratio: from 51.91% ± 5.94% to 12.25% ± 18.63%).

Finally, Figure 9.7 depicts the effect of different noise levels on both the post-processing techniques. High noise levels (SNR<1) incur significant sensitivity loss, with less than 10% of the Dice score for both methods. NEMO activation maps at this noise level depict false positive voxels scattered randomly. For SVarM at high noise levels, almost no voxels reach statistical significance, resulting in lower false positive ratios. This trend is confirmed by the surviving pixel ratio plot for NEMO: for SNR = 0.1 the surviving pixel ratio reaches 3261.70% ± 5.48%, corresponding to a false positives rate of 98.59% ± 0.17%.

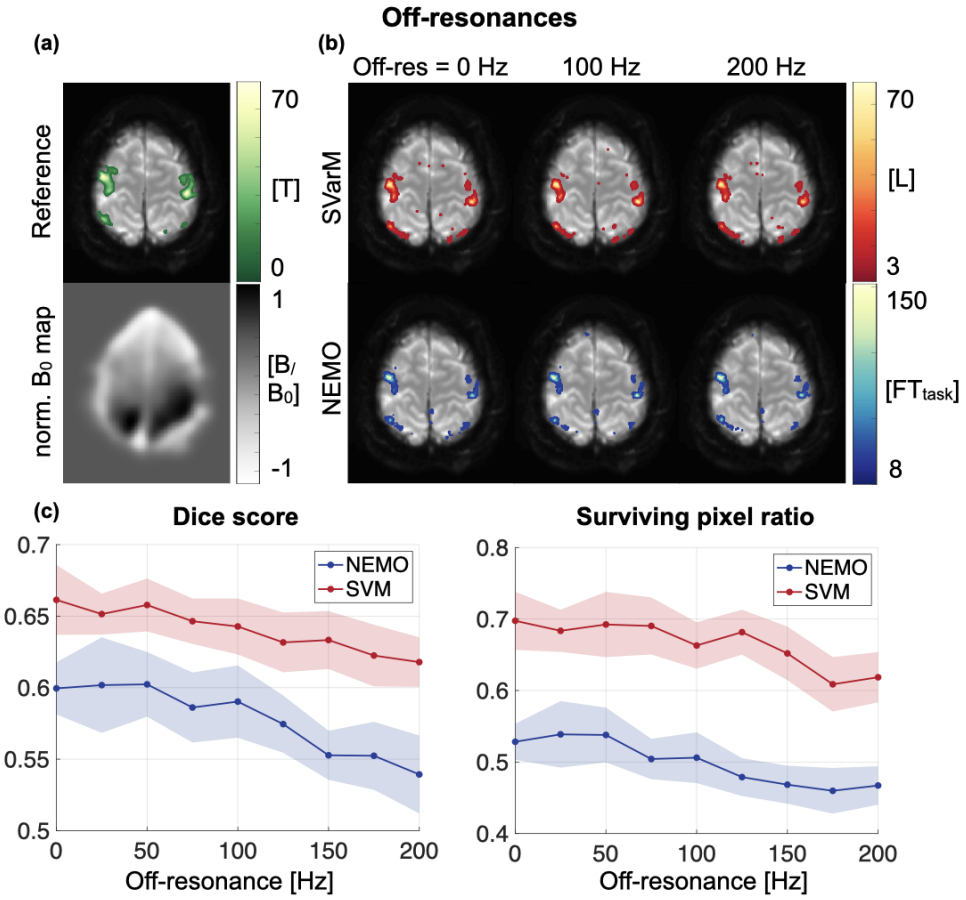

Figure 9.5 : a) Ground truth activation and normalized B_0 map. b) Representative activation maps for the two processing methods, with different levels of B_0 inhomogeneities. c) Plots of corresponding Dice coefficients and surviving pixels ratio (mean ± std. dev.).

9

9.4. Discussion

In this work, a study of direct neuro-current MRI signals in the presence of system imperfections was presented. Sensitivity to neuro-currents was found to be highly susceptible to B_1^+ inhomogeneities and SNR. Variance-based processing, termed SVarM, was found to successfully alleviate these effects and provide an overall increase in sensitivity.

In the studied neuro-current MRI sequence, brain activity was encoded as signal variability, rather than variation of the mean signal, as in BOLD MRI. Thus, corresponding time courses have a constant mean, but a significant difference in variance between active and rest periods. As a result, conventional fMRI data processing techniques, such as

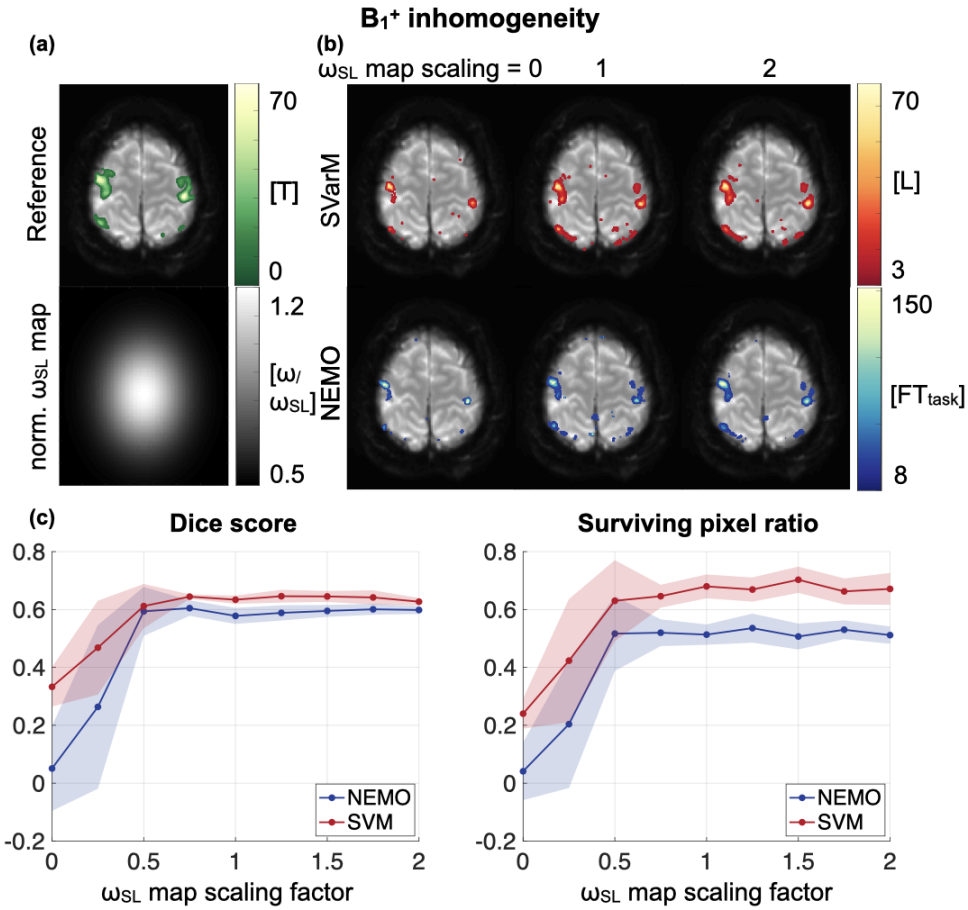

Figure 9.6 : a) Ground truth activation and normalized ω_{SL} map. b) Representative activation maps for the two processing methods, with different levels of B_1^+ inhomogeneities. c) Plots of corresponding Dice coefficients and surviving pixels ratio (mean ± std. dev.).

SPM, based on the assumption of a mean difference, lose validity when analyzing neuro-current MRI data. In order to enable statistically rigorous processing SVarM was processed. A pipeline comparable to SPM was incorporated to normalize and pre-process the data. However, the final analysis step performed variance testing pooled over the block design of the experiment. Levene's test on variance for non-Gaussian distributions was found to be effective in this step. This way neuronal activity can be represented by the level of statistical significance similar to SPM. At present, this approach is limited to on/off designs, as pooling of the data is required prior to processing. Extension to more complex study designs will be investigated in future work.

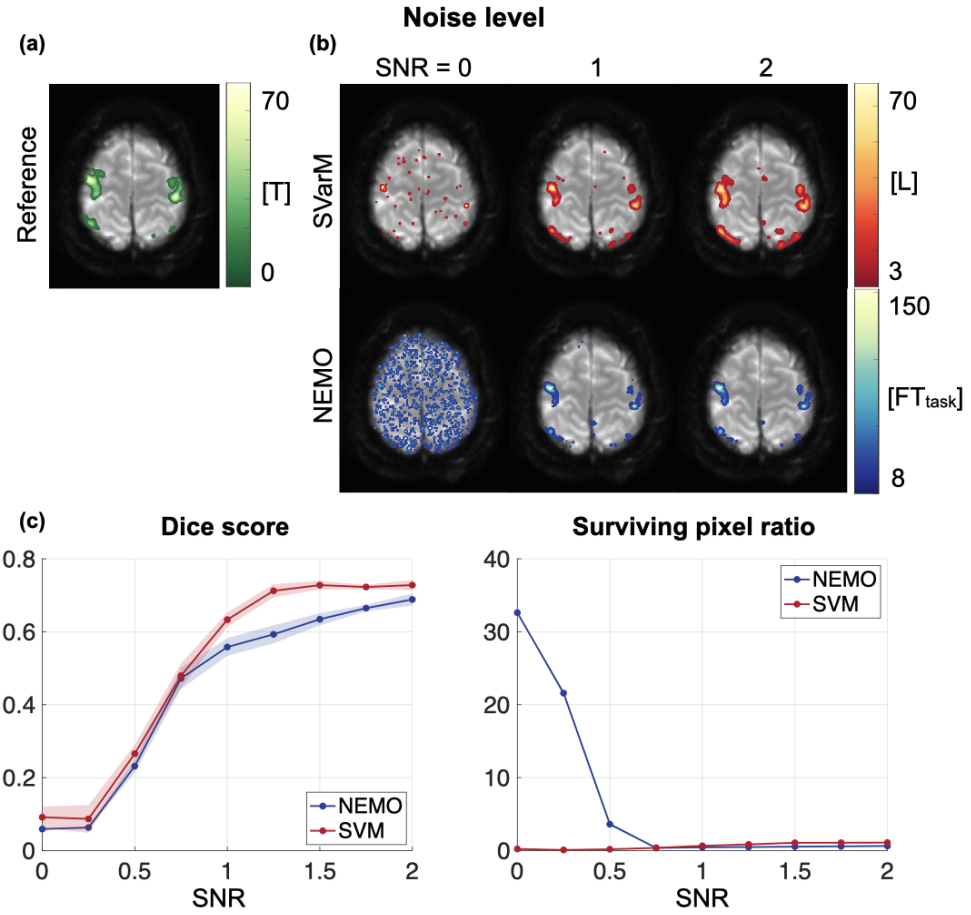

Figure 9.7 : a) Ground truth activation. b) Representative activation maps for the two processing methods, with different values of signal-to-noise ratio. c) Plots of corresponding Dice coefficients and surviving pixels ratio (mean ± std. dev.).

9

SVarM was compared to an existing data analysis approach, namely NEMO processing. Overall, the proposed SVarM analysis performs comparably or better than the NEMO processing for all levels of off-resonances, B_1^+ scaling and noise. Using SVarM instead of NEMO increases detection sensitivity without loss of specificity in the presence of system imperfections. However, the neuro-current MRI remains limited by intrinsically lower sensitivity to neuronal activation, compared with BOLD MRI. Advanced neuro-current MRI pulse sequence design is warranted to achieve further improved sensitivity and robustness of this contrast mechanism.

NEMO processing relied on the use of FreeSurfer to perform brain parcellation. This has the drawback of long execution times (>20 hours

for every patient). Parcellation was used to reduce the contribution of slow cyclic physiological or hemodynamic confounds since these signals have periodic patterns while preserving the non-periodic neuro-current signal. Relying on a GLM approach to perform the removal of physiological confounds, as proposed in SVarM, is both faster and more flexible. The modular structure of the GLM regressor matrix, in fact, allows to easily tailor the pre-processing step to the adopted experimental design. For example, BOLD-like artifacts were neglected for the purpose of this work, focusing on simulated data. Future studies on neuro-current MRI data acquired in vivo, however, could benefit from the integration of BOLD confounds removal in the pre-processing configuration. This approach might even allow for joint assessment of BOLD and neuro-current-induced functional activation and will be the subject of future research.

NEMO analysis was less sensitive when the time series were more homogeneous across the brain volume, because of the effect of the region-based regression step. This is particularly relevant for the special case of perfectly homogeneous B_1^+. In this case, when the spin-lock pulse and neuro-current oscillations are perfectly in phase, the phase-dependent variability can be neglected. As a result, time courses have constant values during active phases, as well as rest periods. The resulting time series follows a BOLD-like pattern, with each active phase assuming different constant values. However, step-shaped signals were completely suppressed with the first two operations of the pre-processing procedure in the NEMO analysis, regression, and high-pass filtering, resulting in almost empty activation maps. SVarM processing, instead, preserves signals from singular TR cases. However, this special case is relevant only if neural activation occurs solely at a single frequency component. Thus, this difference is expected to be of minor relevance in in vivo experiments.

9.5. Conclusion

Our results indicate that the efficient application of neuro-current MRI is strongly dependent on the level of system imperfections. Reaching higher sensitivity in neuro-current MRI is crucial for the detection of weak magnetic oscillations induced by neural activity. Improved post-processing based on statistical analysis of signal variability has demonstrated the potential to improve the robustness of neuro-current MRI. However, besides the design of tailored data-processing approaches, more robust neuro-current MRI pulse sequences are necessary to facilitate the widespread use of neuro-current MRI for the detection of brain activity.

10 Discussion

10.1. Summary of Key Findings

With this dissertation, we introduced novel techniques to achieve robust spin-lock preparations for quantitative MRI. Specifically, the proposed adiabatic spin-lock techniques showed improved resilience against field inhomogeneities and lower SAR burden than conventional continuous-wave techniques, leading to great image quality in vivo. This can pave the way for widespread use of rotating-frame relaxation techniques in clinical settings.

In Chapter 4 we proposed a novel $T_{1\rho,adiab}$ mapping sequence for myocardial tissue characterization, based on fully adiabatic spin-lock preparations to improve the robustness against B_0 and B_1^+ field inhomogeneities. With the proposed method, we obtained excellent image quality in healthy volunteers. Contrary to the reference non-adiabatic $T_{1\rho}$ mapping technique, no artifacts were visible across the myocardium. Moreover, $T_{1\rho,adiab}$ maps yielded a significant improvement in precision, reproducibility, and inter-subject variability compared with conventional non-adiabatic $T_{1\rho}$ maps.

In Chapter 5 we built on the proposed $T_{1\rho,adiab}$ preparations introduced in Chapter 4, using a combination of slice-selective and non-selective adiabatic pulses. This way we obtained an adiabatic spin-lock module with intrinsic dark-blood contrast. DB-$T_{1\rho,adiab}$ mapping yielded an unbiased estimation of myocardial $T_{1\rho,adiab}$ values, compared with the reference bright-blood $T_{1\rho,adiab}$ technique. At the same time, DB-$T_{1\rho,adiab}$ maps presented good suppression of the signal from the blood pool, improving the visual contrast at the myocardium-to-blood interface.

To further explore the gains in mapping quality and robustness achieved with the proposed $T_{1\rho,adiab}$ preparations, we set out to explore additional relaxation mechanisms, potentially providing complementary informa-

tion to $T_{1\rho,adiab}$, through adiabatic spin-locks. In Chapter 6 we introduced a technique for in vivo myocardial $T_{2\rho,adiab}$ mapping at 3T. Conventional $T_{2\rho}$ preparations are highly sensitive to field inhomogeneities. Thus, cardiac $T_{2\rho}$ mapping applications had been so far been limited to animal models, and $T_{2\rho}$ contrast remained mostly unexplored. With the proposed $T_{2\rho,adiab}$ technique we achieved good image quality and T_2-like contrast with improved precision and resilience against inhomogeneities over conventional maps obtained from adiabatically-refocused T_2 preparations.

While the applications proposed in Chapters 4-6 were based on hyperbolic-secant adiabatic pulse shapes, we also sought to investigate rotating-frame relaxation preparations robustness for different pulse shapes and non-adiabatic regimes. In Chapter 7 we explored sub-adiabatic rotating-frame relaxation along a fictitious field through RAFF preparations. We observed that conventional RAFF preparations showed moderate resilience against off-resonances, but strong susceptibility to B_1^+ inhomogeneities. Thus, we proposed a parametric formulation of RAFF pulses, generalized inhomogeneity resilient RAFF (girRAFF), and optimized its resilience to both B_0 and B_1^+ inhomogeneities. Our results showed that optimized girRAFF pulses, approaching the adiabatic regime, yielded robust relaxation values in both calf skeletal muscle and knee cartilage, even in the presence of strong field inhomogeneities. Hence, girRAFF mapping may provide a promising tool for clinical applications in body imaging at high field strengths, where large off-resonance resilience is needed.

The techniques introduced in Chapters 4-7 rely on rotating-frame relaxation measured during adiabatic RF irradiation. As a result, $T_{1\rho,adiab}$, $T_{2\rho,adiab}$ and $T_{girRAFF}$ present sensitivity to a wide range of frequencies, unlike conventional $T_{1\rho}$ and $T_{2\rho}$ measured through constant-wave spin-locks. Thus, in Chapter 8 we investigated the relaxation mechanism induced by adiabatic spin-lock pulses. Redfield relaxation theory was used to minimize $T_{1\rho,adiab}$ dispersion in the presence of B_0 inhomogeneities and combined with Bloch simulations to optimize inversion efficacy of adiabatic pulses for a range of off-resonances. The optimized hyperbolic-secant pulses could provide a promising starting point for use in adiabatic $T_{1\rho,adiab}$ measurements with high confounder resilience and minimal off-resonance dispersion.

Finally, an alternative application of spin-lock preparations, where robustness to field inhomogeneities was also crucial, was considered in Chapter 9. There, we investigated the use of continuous-wave spin-lock preparation to sensitize the MRI signal to weak oscillating neuronal currents induced by local field potentials and obtain direct functional brain MRI imaging. We found a strong dependence of the neuro-current MRI signal on system imperfections, indicating that more robust spin-lock preparations are necessary to facilitate its widespread use. In addition, we proposed a novel post-processing method, based on the statistical

analysis of the signal variability, which improved the overall robustness of the final neuro-current activation maps.

10.2. Rotating-frame relaxation mapping: current challenges and future directions

As MRI researchers, our commitment extends beyond technical advancement, to creating tangible clinical value. In this perspective, quantitative MRI techniques, with their ability to provide objective and reproducible measurements, have emerged as indispensable tools in the field of MRI. The increasing popularity of quantitative MRI can be attributed to its potential to enhance diagnostic precision and therapeutic monitoring by quantifying physiological and pathological tissue properties. Specifically, rotating-frame relaxation techniques, such as $T_{1\rho}$ mapping, are gaining attention for their ability to offer quantitative insights into tissue characteristics without the need for external contrast agents. Rotating frame relaxation can potentially capture subtle alterations in the micro-environment of tissues, thanks to their intrinsic sensitivity to slow molecular motional processes [11]. These techniques, when compared to traditional contrast-agent-based qualitative methods, present advantages such as reduced risk of contrast agent retention, cost-effectiveness, and the possibility of repeated assessments over time. Based on those advantages an increasing number of technical and clinical studies has been published on rotating frame relaxometry in recent years.

However, unlike conventional parametric mapping techniques, such as T_1, T_2 and T_2^*, rotating-frame relaxation techniques are still in the early development stage and are not part of standard clinical diagnostic protocols yet. In my view, there are two main issues to address in order to achieve diagnostic value with rotating-frame relaxation techniques. On the one hand, efforts must be directed at ensuring that rotating-frame relaxation techniques yield robust results across different system conditions, field strengths, and levels of patient compliance. On the other hand, in-depth theoretical and clinical studies are necessary to characterize the sensitivity profile of emerging relaxation parameters and derive reference normal and pathological values. Recent developments and future opportunities in both directions will be discussed in the next sections.

10.2.1. Enhancing robustness across experimental conditions

Rotating-frame relaxation methods critically depend on signal preparation modules. These pose challenges due to their high SAR demands and strong sensitivity to both B_0 and B_1^+ inhomogeneities [337, 338]. This concern becomes particularly pronounced in cardiac MRI due to strong inhomogeneities at the lung air interface. Both field inhomogeneities and

SAR exacerbate with increasing field strength. Low field systems, such as 0.5 T scanners, present a potentially viable alternative for their improved RF field homogeneity [458]. However, in addition to the inherently lower SNR, rotating-frame relaxation at low fields is often challenged by the limited capabilities of RF amplifiers present on lower field scanners [459, 460].

Consequently, most successful cardiac applications of conventional continuous-wave rotating-frame relaxation mapping have been limited to intermediate field strength (1.5 T) [87, 131, 330, 331, 333, 361, 365]. At higher field strengths, conventional continuous-wave spin-lock preparations have so far been limited by hardware and SAR constraints to around 300-400 Hz amplitude for total durations of 35 to 45 ms, depending on the specific system [334–336]. This is in agreement with our experience on a 3T Philips Ingenia scanner, where the maximum amplitude and duration combination that we could use was w_{SL} = 350 Hz and τ_{SL} = 35 ms. Reduced spin-lock amplitudes cause a decrease in $T_{1\rho}$ times, and, thus, reduced dynamic range. It also leads to less resilience against B_0 field inhomogeneities [338]. While moderate amplitude spin-lock pulses may still yield satisfactory image quality in animal models or human anatomies where B_0 and B_1^+ field inhomogeneities are less significant [461], the $T_{1\rho}$ mapping quality in the human myocardium is severely compromised [334–336]. Recent non-cardiac $T_{1\rho}$ mapping studies performed on clinical 3T scanners have reported the use of more SAR-intensive continuous-wave spin-lock preparations, with amplitudes up to 575 Hz and durations up to 60 ms [422, 423, 462]. This was possible thanks to the choice of very long TRs. However, such TRs are often incompatible with the temporal constraints of ECG-triggered and breath-held cardiac sequences. A method to reduce SAR in conventional $T_{1\rho}$ was proposed by Wheaton et al., based on a partial k-space acquisition approach in which the full power spin-lock is applied to only the central lines of the k-space [389]. This method, however, introduces errors in $T_{1\rho}$ quantification and has found limited adoption in subsequent studies. Alternatively, off-resonance spin-lock pulses have been proposed to increase the strength of the locking effective field (ω_{eff}) without an increase in SAR [463, 464]. Nonetheless, high SAR of spin-lock preparations still constitutes a limiting factor for in vivo application of rotating-frame relaxation techniques, especially at high field strengths.

In addition to SAR limitations, rotating-frame relaxation mapping at high field strengths is also compromised by the strong susceptibility to system inhomogeneities. A common approach to mitigate artifacts induced by B_0 and B_1^+ inhomogeneities is the use of composite RF pulses with alternating phase and/or the use of interleaved refocusing pulses [71, 327, 337, 391, 465]. More recently, adiabatic pulses have been used to replace 90° and 180° pulses in spin-lock preparations and improve resilience against B_0 and B_1^+ inhomogeneities [131, 293, 466,

467]. However, despite the use of compensated preparation schemes or adiabatic excitation and refocusing, the cardiac maps achieved with continuous-wave preparations at 3T still display visible artifacts due to off-resonances and B_1^+ inhomogeneities [334–336]. Moreover, the use of hybrid continuous-wave/adiabatic preparations includes contributions from $T_{1\rho,adiab}$ relaxation, which follows a distinct mechanism from conventional $T_{1\rho}$ relaxation and may introduce sensitivity to different relaxation pathways. $T_{1\rho,adiab}$ contributions are usually neglected in hybrid spin-lock studies, but careful consideration may be warranted in light of the long duration of adiabatic excitation and refocusing pulses, necessary to operate in the adiabatic regime [468].

A noteworthy approach to overcome both these challenges lies in the design of spin-lock preparations consisting exclusively of subadiabatic or adiabatic pulses. This can mitigate the SAR requirements and significantly reduce the sensitivity to inhomogeneities. Studies proposing trains of adiabatic amplitude- and frequency-modulated RF pulses as spin-lock preparations have been emerging in the last years [72, 73, 345, 413, 440, 469, 470]. A few studies also suggested using RF pulses operating in the sub-adiabatic regime for increased SAR gains [401, 408, 409, 413, 469]. However, no application has been proposed yet for myocardial rotating-frame relaxation mapping. In our group, we worked on designing and optimizing amplitude- and frequency-modulated RF pulses for cardiac MRI, operating both in the sub-adiabatic [119, 471] and in the adiabatic regime (as described in Chapters 4-6 of this dissertation). We found that optimized adiabatic spin-lock preparations consisting of hyperbolic-secant pulses yield significantly more robust $T_{1\rho,adiab}$ and $T_{2\rho,adiab}$ quantification, with improved precision and reproducibility with respect to conventional continuous-wave RF pulses, and with the possibility to achieve intrinsic dark-blood contrast without additional preparation modules. With the work presented in Chapter 7, we also investigated amplitude- and frequency-modulated RF pulse in the sub-adiabatic to adiabatic regime transition and compared their performances. We concluded that the additional gain in SAR achieved through sub-adiabatic RAFF pulses comes at the expense of resilience to system inhomogeneities.

When presenting our proposed adiabatic rotating-frame relaxation mapping methods, several recurrent observations emerge that warrant discussion. Firstly, a common misconception often arises regarding possibly increased SAR levels with adiabatic pulses, since many continuous-wave $T_{1\rho}$ studies mention increased SAR as a limitation to their use as excitation or refocusing pulses in hybrid spin-lock preparations [12]. It is important to clarify that adiabatic pulses do entail higher SAR when used to replace very short 90° or 180° block pulses ($\leq$ 1 ms duration) as they typically require longer duration to achieve adiabaticity (5-10 ms duration). However, when adiabatic pulses, such as hyperbolic secants, are

used to completely replace continuous-wave spin-lock pulses, the SAR is significantly reduced because of the amplitude-modulation function. For equal preparation duration, the integral under the curve of a constant-amplitude spin-lock at 500 Hz is much higher than a train of hyperbolic secant-modulated pulses which only reach 500 Hz as a peak amplitude. Secondly, discrepancies in $T_{1\rho,adiab}$ or $T_{2\rho,adiab}$ relaxation values compared to conventional $T_{1\rho}$ or $T_{2\rho}$ may raise questions. $T_{1\rho,adiab}$ values of the healthy myocardium can be up to 3 or 4 times larger than reference $T_{1\rho}$ values and show dependence on the pulse amplitude- and frequency-modulation function shape. The differences stem from the fact that adiabatic spin-locks methods induce a distinctly different relaxation mechanism, as described in Chapter 8. This may lead, on the one hand, to increased variability and the need for thorough characterization of adiabatic rotating-frame relaxation methods, but on the other end, to potentially increased contrast-to-noise ratio. Another potential confusion pertains to the characteristic spin-lock (SL) frequency. Contrary to conventional constant-amplitude spin-lock pulses, which can be characterized by a single frequency ω_1, adiabatic preparations involve an amplitude and frequency sweep, introducing sensitivity to a wider range of frequencies. In amplitude- and frequency-modulated pulses, the locking field is the effective field. Hence, the spin-lock strength is $\omega_{eff}(t)$, which is given by the vectorial sum of the amplitude (ω_1(t)) and frequency components. This characteristic can be viewed as advantageous, as it allows to reach higher spectral density frequencies through larger frequency sweeps without an associated increase in SAR.

Despite the additional pulse design efforts required to implement adiabatic spin-lock preparations to quantify rotating-frame relaxation, the significant improvements in resilience to field inhomogeneities and SAR reduction make them prime candidates for in vivo applications at high field strengths. The method for myocardial adiabatic $T_{1\rho,adiab}$ mapping proposed in Chapter 4 has already been adopted in several other works [472–474]. Specifically, Chow et al. have integrated our proposed adiabatic $T_{1\rho,adiab}$ preparations in a multi-parametric saturation-recovery single-shot acquisition (mSASHA) for contrast-free simultaneous T_1, T_2, and adiabatic $T_{1\rho,adiab}$ mapping in a single breath-hold [472]. Pearce et al. have proposed a clinical evaluation of this novel T_1, T_2, and adiabatic $T_{1\rho,adiab}$ mSASHA sequence on patients with a broad range of cardiomyopathies at 3T [473]. They found that myocardial lesions had larger changes compared to remote myocardium for $T_{1\rho,adiab}$ than T_2 and T_1 (35 ± 44%, 24 ± 29% and 10 ± 10% respectively) and that septal foci were more visible on $T_{1\rho,adiab}$ maps and T_2 maps than T_1 maps. Finally, Tyler et al. proposed an accelerated version of our myocardial $T_{1\rho,adiab}$ mapping sequence by rendering all the $T_{1\rho,adiab}$ preparations slice selective to reduce the necessary T_1 recovery time between multiple acquisitions [474].

10.2.2. Standardization and reference values

Once robust preparations inducing rotating-frame relaxation are available, in-depth investigation into the relaxation mechanisms contributing to the measured $T_{1\rho}$, $T_{2\rho}$, $T_{1\rho,adiab}$, $T_{2\rho,adiab}$ or $T_{(gir)RAFF}$ is warranted. MRI physics most commonly adopts a macroscopic interpretation of the relaxation phenomenon and assumes reference T_1 and T_2 values, for example, as axiomatic tissue properties. This approach can be sufficient for most applications of MRI physics pertaining to clinical imaging. However, its limitations start to emerge when investigating the mechanism behind biological tissue relaxation. Several comprehensive theories have been elaborated to describe both conventional and rotating-frame relaxation in simple environments, such as water or homogeneous solids [11, 21, 223, 475, 476]. These can provide useful insight into the relaxation trends to expect in vivo, as we have shown in Chapter 8. However, biological tissues are composed of complex compartments of non-homogeneous mixtures of substrates, such as water or macro-molecules. As of present, there is no rigorous and comprehensive theory linking specific tissues to their corresponding normal relaxation values. This holds true for both conventional T_1 or T_2 relaxation and for rotating-frame relaxation values. In the case of $T_{1\rho}$, for instance, we know that the constituent mechanisms are manifold. In liquids, $T_{1\rho}$ relaxation is caused primarily by dipole-dipole interactions. However, this phenomenon only explains part of the $T_{1\rho}$ relaxation mechanisms in vivo. $T_{1\rho}$ relaxation due to dipole-dipole interactions, in fact, cannot account for relaxation dispersion at varying spin-lock amplitudes, as shown by Michaeli et al. [73]. In vivo, on the other hand, $T_{1\rho}$ dispersion is evident in a number of studies [119, 397, 477, 478]. $T_{1\rho}$ dispersion could be explained by considering the contributions of chemical exchange and diffusion factors to $T_{1\rho}$ relaxation [478]. Specifically, recent studies have shown that chemical exchange may dominate in vivo relaxation at high field strengths, especially for moderately high spin-lock strengths [479, 480]. On the other hand, diffusing spins exposed to relatively large variations of magnetic fields may be an important contributor to $T_{1\rho}$ dispersion at lower spin-lock amplitudes (<200 Hz) [478, 481].

In addition, adiabatic and sub-adiabatic rotating-frame relaxation preparations introduce an extra layer of complexity, as relaxation times gain additional time dependence. Thus, we currently have no tools to determine universal reference rotating-frame relaxation values in vivo and their sensitivity to normal or pathological tissue compositions.

In parallel with the continued work on theoretical relaxation modelling, further clinical studies are necessary to characterize rotating -frame relaxation sensitivity to different pathologies. There is strong evidence that rotating-relaxation is sensitive to fibrosis both in the myocardium and in the liver [329, 331, 361, 365, 421–423], to edema [365], to cartilage degeneration and concentration of proteoglycans [424–427], to

Alzheimer's and Parkinson's diseases [428, 429], to breast tissue lesions [430], to several kinds of tumors [431–433] and tumor degeneration in response to radiation therapy [482]. However, these studies are still limited in number and size, and additional variability is introduced by the lack of standardized spin-locking methods. Further research on larger cohorts of patients is required in order to include rotating-frame relaxation techniques in the clinical point-of-care standards [3].

In this context, developing MRI sequences that yield a reduction of total scan time and enable multi-slice or 3D acquisition is essential to enable larger clinical studies. In cardiac and abdominal MRI, motion correction or compensation techniques warrant additional care. This also includes alternatives to breath-holding and ECG triggering to facilitate patient compliance. Examples of these approaches have recently started to emerge and will hopefully continue to expand in the near future. MR fingerprinting has been proposed to achieve simultaneous T_1, T_2, T_2^*, $T_{1\rho}$ and fat fraction quantification at various field strengths in the liver [364] and in the heart [366, 459, 483, 484]. Other frameworks, such as MR multitasking [251] or the free-running 5D whole-heart CMR [485], could also be adapted to include rotating-frame relaxation as an additional parameter.

10.3. Towards direct detection of neuronal currents through MRI

Spin-lock preparations have also been proposed as a tool to directly sensitize the MRI signal to weak oscillating magnetic fields induced by synchronized neural activity. This has been a long-standing research goal in MRI as it may provide direct insight into functional brain mechanisms at fast time scales. Currently, the gold standard for functional brain MRI is the BOLD contrast, which offers only indirect measurement of neuronal activity, mediated by the hemodynamic response. This greatly limits the effective temporal-resolution of BOLD-fMRI [442, 443]. Very recently, a novel method for direct imaging of mice neuronal activity with millisecond precision at 9.4T garnered much interest within the scientific community [486]. However, concerns around its reproducibility were rapidly raised as other scientists were unable to replicate the findings [487].

The problem of optimizing spin-lock preparations for the direct detection of neuronal activity has a lot of similarities to the topic of optimizing rotating-frame relaxation preparation for tissue characterization discussed in Chapters 4-8. In both cases, improving resilience to field inhomogeneities is a priority to ensure artifact-free quantification of the underlying phenomenon and a critical factor to enable in vivo applicability. The difference lies in the fact that in direct neuro-current fMRI the contrast is not generated by $T_{1\rho}$ relaxation but comes from resonant in-

teractions between the spin-lock field and the neuronal current-induced field, which effectively excites the magnetization away from the spin-lock field axis during the preparation [451–453].

Research has been focused on developing signal preparations that enable the direct detection of neuro-current oscillations with good sensitivity and resilience to confounding artifacts, such as B_0 and B_1^+ inhomogeneities. After our work presented in Chapter 9 was published, other studies have emerged aiming to characterize in simulations and in phantom experiments the sensitivity of proposed spin-lock preparation for direct neuro-currents detection and the robustness in the presence of B_0 and B_1^+ inhomogeneities [488–491]. In the studies by Capiglioni et al., Gram et al. and Albertova et al., our method for the statistical analysis of neuro-currents MRI time-series, based on the analysis of the signal variance, was adopted for signal processing. Moreover, Gram et al. proposed a method to validate neuro-currents fMRI measurements in vivo by controlled induction of oscillating magnetic fields in the human brain through weak oscillating gradient fields [490]. This approach, however, does not capture the true complexity of in vivo neuro-currents detection through spin-lock-prepared MRI. The induced oscillating magnetic fields are in fact homogeneous in the imaging slice, and only oriented along the z axis. Finally, the fluctuations are perfectly sinusoidal and do not reflect the spatial and spectral complexity of the weak oscillations induced by local field potentials.

Major limitations still need to be addressed to allow the robust in vivo quantification of neuronal activity directly with spin-lock-prepared MRI. First, the sensitivity of proposed techniques needs to be characterized through simulation and phantom experiments. Efforts should be directed at designing spin-lock preparations with improved sensitivity to neuronal activation, higher contrast between active and non-active regions, and better resilience against field inhomogeneities. In light of this, the use of adiabatic RF pulses for spin-lock preparations could potentially result in a gain in terms of robustness to B_0 and B_1^+ imperfections, similar to what has been observed for rotating-frame relaxation mapping. Whether adiabatic pulses also yield a change in sensitivity remains the subject of further investigations.

Another major challenge lies in untangling of the neuro-current fMRI signal from other confounds, especially from the BOLD effects. Sensitivity to residual physiological motion or BOLD effects has been addressed so far by combining novel contrast mechanisms, based on spin-lock preparations retaining the longitudinal component of the magnetization, and post-processing strategies, targeted at removing low-frequency variations from the measured neuro-currents fMRI signal [453]. This approach appears to successfully suppress BOLD signals from in vivo neuro-currents maps, but further validation in controlled phantom environments is warranted.

Ultimately, adequate sensitivity for the detection of very weak neuro-currents oscillation in the order of a few nT requires further research. The development of acquisition and post-processing strategies to isolate the neuro-currents effect from signal confounds is much needed to enable the robust use of neuro-current fMRI for neuroscience research. When these objectives are met, however, the ability to directly detect neural activity through fMRI may allow insights into the functional brain mechanisms in humans with whole brain coverage at an unprecedented time scale.

10.4. Conclusion

In this dissertation, we have proposed alternative RF pulse design approaches to optimize spin-lock preparations for applications in quantitative MRI. Specifically, we aimed at improving the resilience of RF preparations in the presence of system inhomogeneities with the ultimate goal of pushing the boundaries of their in vivo applicability at high field strengths. Our results showed that careful RF pulse design can have a significant impact on the robustness of quantitative MRI methods. The developments are particularly important where B_0 and B_1^+ field inhomogeneities constitute limiting factors. Here the proposed techniques can yield greatly improved precision and reproducibility. These improvements could facilitate clinical translation of rotating-frame relaxation techniques and provide MRI scientists and clinicians with powerful tools for non-invasive assessment of a variety of pathologies.

Bibliography

[1] D. Binks, R. Hodgson, M. Ries, R. Foster, S. Smye, D. McGonagle, and A. Radjenovic. “Quantitative parametric MRI of articular cartilage: a review of progress and open challenges”. In: *The British journal of radiology* 86.1023 (2013), p. 20120163.

[2] M. Cercignani, N. G. Dowell, and P. S. Tofts. *Quantitative MRI of the brain: principles of physical measurement*. Boca Raton, Florida, 2018.

[3] D. R. Messroghli, J. C. Moon, V. M. Ferreira, L. Grosse-Wortmann, T. He, P. Kellman, J. Mascherbauer, R. Nezafat, M. Salerno, E. B. Schelbert, *et al.* “Clinical recommendations for cardiovascular magnetic resonance mapping of T1, T2, T2* and extracellular volume: a consensus statement by the Society for Cardiovascular Magnetic Resonance (SCMR) endorsed by the European Association for Cardiovascular Imaging (EACVI)”. In: *Journal of Cardiovascular Magnetic Resonance* 19.1 (2016), p. 75.

[4] I. A. Dekkers, A. de Boer, K. Sharma, E. F. Cox, H. J. Lamb, D. L. Buckley, O. Bane, D. M. Morris, P. V. Prasad, S. I. Semple, *et al.* “Consensus-based technical recommendations for clinical translation of renal T1 and T2 mapping MRI”. In: *Magnetic Resonance Materials in Physics, Biology and Medicine* 33 (2020), pp. 163–176.

[5] D. H. Hoffman, A. Ayoola, D. Nickel, F. Han, H. Chandarana, and K. P. Shanbhogue. “T1 mapping, T2 mapping and MR elastography of the liver for detection and staging of liver fibrosis”. In: *Abdominal Radiology* 45 (2020), pp. 692–700.

[6] L. M. De León-Rodríguez, A. F. Martins, M. C. Pinho, N. M. Rofsky, and A. D. Sherry. “Basic MR relaxation mechanisms and contrast agent design”. In: *Journal of Magnetic Resonance Imaging* 42.3 (2015), pp. 545–565.

[7] P. Haaf, P. Garg, D. R. Messroghli, D. A. Broadbent, J. P. Greenwood, and S. Plein. “Cardiac T1 mapping and extracellular volume (ECV) in clinical practice: a comprehensive review”. In: *Journal of Cardiovascular Magnetic Resonance* 18.1 (2017), pp. 1–12.

[8] E. Ledneva, S. Karie, V. Launay-Vacher, N. Janus, and G. Deray. “Renal safety of gadolinium- Based contrast media in patients with chronic renal insufficiency”. In: *Radiology* 250 (3 2009), pp. 618–628.

[9] T. Kanda, K. Ishii, H. Kawaguchi, K. Kitajima, and D. Takenaka. “High signal intensity in the dentate nucleus and globus pallidus on unenhanced T1-weighted MR images: Relationship with increasing cumulative dose of a gadoliniumbased contrast material”. In: *Radiology* 270 (3 2014), pp. 834–841.

[10] A. Al-Muhanna. “Gadolinium retention after contrast-enhanced magnetic resonance imaging: A narrative review”. In: *Saudi Journal of Medicine and Medical Sciences* 10.1 (2022), p. 12.

[11] I. A. Gilani and R. Sepponen. “Quantitative rotating frame relaxometry methods in MRI”. In: *NMR in Biomedicine* 29.6 (2016), pp. 841–861.

[12] A. Bustin, W. R. Witschey, R. B. van Heeswijk, H. Cochet, and M. Stuber. “Magnetic resonance myocardial T1ρ mapping: Technical overview, challenges, emerging developments, and clinical applications”. In: *Journal of Cardiovascular Magnetic Resonance* 25.1 (2023), p. 34.

[13] P. C. Lauterbur. “Image Formation by Induced Local Interactions: Examples Employing Nuclear Magnetic Resonance”. In: *Nature* 242.5394 (1973), pp. 190–191.

[14] I. I. Rabi. “Space Quantization in a Gyrating Magnetic Field”. In: *Phys. Rev.* 51 (8 1937), pp. 652–654.

[15] I. I. Rabi, J. R. Zacharias, S. Millman, and P. Kusch. “A New Method of Measuring Nuclear Magnetic Moment”. In: *Phys. Rev.* 53 (4 1938), pp. 318–318.

[16] F. Bloch. “Nuclear induction”. In: *Physical review* 70.7-8 (1946), p. 460.

[17] E. M. Purcell, H. C. Torrey, and R. V. Pound. “Resonance Absorption by Nuclear Magnetic Moments in a Solid”. In: *Phys. Rev.* 69 (1-2 1946), pp. 37–38.

[18] H. Y. Carr. “Free Precession Techniques in Nuclear Magnetic Resonance.” In: *PhDT* (1953).

[19] P. Mansfield and P. K. Grannell. “NMR diffraction in solids”. In: *Journal of Physics C: solid state physics* 6.22 (1973), p. L422.

[20] L. G. Hanson. “Is quantum mechanics necessary for understanding magnetic resonance?” In: *Concepts in Magnetic Resonance Part A: An Educational Journal* 32.5 (2008), pp. 329–340.

[21] A. Abragam. *The principles of nuclear magnetism*. 32. Oxford university press, 1961.

[22] J. Larmor. “LXIII. On the theory of the magnetic influence on spectra; and on the radiation from moving ions”. In: *The London, Edinburgh, and Dublin Philosophical Magazine and Journal of Science* 44.271 (1897), pp. 503–512.

[23] I. I. Rabi, N. F. Ramsey, and J. Schwinger. “Use of rotating coordinates in magnetic resonance problems”. In: *Reviews of Modern Physics* 26.2 (1954), p. 167.

[24] E. L. Hahn. “Spin Echoes”. In: *Phys. Rev.* 80 (4 1950), pp. 580–594.

[25] F. Bloch, W. W. Hansen, and M. Packard. “Nuclear Induction”. In: *Phys. Rev.* 69 (3-4 1946), pp. 127–127.

[26] M. A. Bernstein, K. F. King, and X. J. Zhou. “Handbook of MRI pulse sequences”. In: *Elsevier* (2004).

[27] S. Ljunggren. “A simple graphical representation of fourier-based imaging methods”. In: *Journal of Magnetic Resonance (1969)* 54.2 (1983), pp. 338–343.

[28] D. B. Twieg. “The k-trajectory formulation of the NMR imaging process with applications in analysis and synthesis of imaging methods”. In: *Medical physics* 10.5 (1983), pp. 610–621.

[29] P. Mansfield. “Multi-planar image formation using NMR spin echoes”. In: 10.3 (1977), pp. L55–L58.

[30] G. H. Glover and J. M. Pauly. “Projection reconstruction techniques for reduction of motion effects in MRI”. In: *Magn Reson Med* 28.2 (1992), pp. 275–89.

[31] C. B. Ahn, J. H. Kim, and Z. H. Cho. “High-speed spiral-scan echo planar NMR imaging-I”. In: *IEEE Trans Med Imaging* 5.1 (1986), pp. 2–7.

[32] C. H. Meyer, B. S. Hu, D. G. Nishimura, and A. Macovski. “Fast spiral coronary artery imaging”. In: *Magn Reson Med* 28.2 (1992), pp. 202–13.

[33] B. A. Jung and M. Weigel. “Spin echo magnetic resonance imaging”. In: *Journal of Magnetic Resonance Imaging* 37.4 (2013), pp. 805–817.

[34] J. Hennig, A. Nauerth, and H. Friedburg. “RARE imaging: a fast imaging method for clinical MR”. In: *Magnetic resonance in medicine* 3.6 (1986), pp. 823–833.

[35] M. Markl and J. Leupold. “Gradient echo imaging”. In: *Journal of Magnetic Resonance Imaging* 35.6 (2012), pp. 1274–1289.

[36] A. D. Elster. “Gradient-echo MR imaging: techniques and acronyms.” In: *Radiology* 186.1 (1993), pp. 1–8.

[37] Y. Zur, M. Wood, and L. Neuringer. “Spoiling of transverse magnetization in steady-state sequences”. In: *Magnetic resonance in medicine* 21.2 (1991), pp. 251–263.

[38] H. Carr. “Steady-state free precession in nuclear magnetic resonance”. In: *Physical Review* 112.5 (1958), p. 1693.

[39] O. Bieri and K. Scheffler. “Fundamentals of balanced steady state free precession MRI”. In: *Journal of Magnetic Resonance Imaging* 38.1 (2013), pp. 2–11.

[40] G. B. Chavhan, P. S. Babyn, B. G. Jankharia, H.-L. M. Cheng, and M. M. Shroff. “Steady-state MR imaging sequences: physics, classification, and clinical applications”. In: *Radiographics* 28.4 (2008), pp. 1147–1160.

[41] T. C. Cosmus and M. Parizh. “Advances in whole-body MRI magnets”. In: *IEEE Trans on applied superconductivity* 21.3 (2010), pp. 2104–2109.

[42] B. Chapman. “Shielded gradients. And the general solution to the near field problem of electromagnet design”. In: *Magnetic Resonance Materials in Physics, Biology and Medicine* 9.3 (1999), 146 –151.

[43] B. Gruber, M. Froeling, T. Leiner, and D. W. Klomp. “RF coils: A practical guide for nonphysicists”. In: *Journal of magnetic resonance imaging* 48.3 (2018), pp. 590–604.

[44] R. Turner. “Gradient coil design: a review of methods”. In: *Magnetic resonance imaging* 11.7 (1993), pp. 903–920.

[45] S. Hidalgo-Tobon. “Theory of gradient coil design methods for magnetic resonance imaging”. In: *Concepts in Magnetic Resonance Part A* 36A.4 (2010), pp. 223–242.

[46] R. M. Henkelman. “Measurement of signal intensities in the presence of noise in MR images”. In: *Medical physics* 12.2 (1985), 232 –233.

[47] H. Gudbjartsson and S. Patz. “The Rician distribution of noisy MRI data”. In: *Magnetic resonance in medicine* 34.6 (1995), pp. 910–914.

[48] S. O. Rice. “Mathematical analysis of random noise”. In: *The Bell System Technical Journal* 23.3 (1944), pp. 282–332.

[49] G. M. Pohost. “The History of Cardiovascular Magnetic Resonance”. In: *JACC: Cardiovascular Imaging* 1.5 (2008), pp. 672–678.

[50] J. P. Ridgway. “Cardiovascular magnetic resonance physics for clinicians: part I”. In: *Journal of Cardiovascular Magnetic Resonance* 12.1 (2010).

[51] J. D. Biglands, A. Radjenovic, and J. P. Ridgway. “Cardiovascular magnetic resonance physics for clinicians: part II”. In: *Journal of Cardiovascular Magnetic Resonance* 14.1 (2012).

[52] T. Leiner, D. Rueckert, A. Suinesiaputra, B. Baeßler, R. Nezafat, I. Išgum, and A. A. Young. “Machine learning in cardiovascular magnetic resonance: basic concepts and applications”. In: *Journal of Cardiovascular Magnetic Resonance* 21.1 (2019).

[53] C. M. Kramer, J. Barkhausen, C. Bucciarelli-Ducci, S. D. Flamm, R. J. Kim, and E. Nagel. “Standardized cardiovascular magnetic resonance imaging (CMR) protocols: 2020 update”. In: *Journal of Cardiovascular Magnetic Resonance* 22.1 (2020).

[54] R.-M. Menchón-Lara, F. Simmross-Wattenberg, P. Casaseca-de-la-Higuera, M. Martín-Fernández, and C. Alberola-López. “Reconstruction techniques for cardiac cine MRI”. In: *Insights into Imaging* 10.1 (2019).

[55] J. Hamilton, D. Franson, and N. Seiberlich. “Recent advances in parallel imaging for MRI”. In: *Progress in Nuclear Magnetic Resonance Spectroscopy* 101 (2017), pp. 71–95.

[56] L. Feng, D. Ma, and F. Liu. “Rapid MR relaxometry using deep learning: An overview of current techniques and emerging trends”. In: *NMR in Biomedicine* 35.4 (2020).

[57] D. J. Larkman and R. G. Nunes. “Parallel magnetic resonance imaging”. In: *Physics in Medicine and Biology* 52.7 (2007), R15–R55.

[58] N. Kawel-Boehm, S. J. Hetzel, B. Ambale-Venkatesh, G. Captur, C. J. Francois, M. Jerosch-Herold, M. Salerno, S. D. Teague, E. Valsangiacomo-Buechel, R. J. van der Geest, and D. A. Bluemke. “Reference ranges (“normal values”) for cardiovascular magnetic resonance (CMR) in adults and children: 2020 update”. In: *Journal of Cardiovascular Magnetic Resonance* 22.1 (2020).

[59] M. Sermesant, H. Delingette, H. Cochet, P. Jaïs, and N. Ayache. “Applications of artificial intelligence in cardiovascular imaging”. In: *Nature Reviews Cardiology* 18.8 (2021), pp. 600–609.

[60] P. Mansfield and A. A. Maudsley. “Planar spin imaging by NMR”. In: *Journal of Physics C: Solid State Physics* 9.15 (1976), pp. L409–L412.

[61] K. Sekihara. “Steady-State Magnetizations in Rapid NMR Imaging Using Small Flip Angles and Short Repetition Intervals”. In: *IEEE Transactions on Medical Imaging* 6.2 (1987), pp. 157–164.

[62] K. Scheffler and S. Lehnhardt. “Principles and applications of balanced SSFP techniques”. In: *European Radiology* 13.11 (2003).

[63] G. M. Bydder and I. R. Young. “MR Imaging: Clinical Use of the Inversion Recovery Sequence”. In: *Journal of Computer Assisted Tomography* 9.4 (1985), pp. 659–675.

[64] R. R. Edelman, D. Chien, and D. Kim. “Fast selective black blood MR imaging.” In: *Radiology* 181.3 (1991), pp. 655–660.

[65] M. H. Levitt. “Composite pulses”. In: *Progress in Nuclear Magnetic Resonance Spectroscopy* 18.2 (1986), pp. 61–122.

[66] K. Uğurbil, M. Garwood, and M. Robin Bendall. “Amplitude- and frequency-modulated pulses to achieve 90° plane rotations with inhomogeneous B1 fields”. In: *Journal of Magnetic Resonance* 72.1 (1987), pp. 177–185.

[67] J. H. Brittain, B. S. Hu, G. A. Wright, C. H. Meyer, A. Macovski, and D. G. Nishimura. “Coronary Angiography with Magnetization-Prepared T2 Contrast”. In: *Magnetic Resonance in Medicine* 33.5 (1995), pp. 689–696.

[68] W. D. Foltz, O. Al-Kwifi, M. S. Sussman, J. A. Stainsby, and G. A. Wright. “Optimized spiral imaging for measurement of myocardial T2 relaxation”. In: *Magnetic Resonance in Medicine* 49.6 (2003), pp. 1089–1097.

[69] S. Giri, Y.-C. Chung, A. Merchant, G. Mihai, S. Rajagopalan, S. V. Raman, and O. P. Simonetti. “T2 quantification for improved detection of myocardial edema”. In: *Journal of Cardiovascular Magnetic Resonance* 11.1 (2009).

[70] T.-Y. Huang, Y.-J. Liu, A. Stemmer, and B. P. Poncelet. “T2 measurement of the human myocardium using a T2-prepared transient-state trueFISP sequence”. In: *Magnetic Resonance in Medicine* 57.5 (2007), pp. 960–966.

[71] M. Gram, M. Seethaler, D. Gensler, J. Oberberger, P. M. Jakob, and P. Nordbeck. “Balanced spin-lock preparation for B1-insensitive and B0-insensitive quantification of the rotating frame relaxation time T1ρ”. In: *Magnetic Resonance in Medicine* 85 (5 2021), pp. 2771–2780.

[72] S. Mangia, T. Liimatainen, M. Garwood, and S. Michaeli. “Rotating frame relaxation during adiabatic pulses vs. conventional spin lock: simulations and experimental results at 4 T”. In: *Magnetic Resonance Imaging* 27 (8 2009), pp. 1074–1087.

[73] S. Michaeli, D. J. Sorce, C. S. Springer, K. Ugurbil, and M. Garwood. “T1ρ MRI contrast in the human brain: Modulation of the longitudinal rotating frame relaxation shutter-speed during an adiabatic RF pulse”. In: *Journal of Magnetic Resonance* 181 (1 2006), pp. 135–147.

[74] J. C. Carr, O. Simonetti, J. Bundy, D. Li, S. Pereles, and J. P. Finn. “Cine MR Angiography of the Heart with Segmented True Fast Imaging with Steady-State Precession”. In: *Radiology* 219.3 (2001), pp. 828–834.

[75] Y. Amano, M. Takayama, and S. Kumita. “Contrast/enhanced myocardial T1/weighted scout (Look–Locker) imaging for the detection of myocardial damages in hypertrophic cardiomyopathy”. In: *Journal of Magnetic Resonance Imaging* 30.4 (2009), 778 –784.

[76] P. Kellman, A. E. Arai, E. R. McVeigh, and A. H. Aletras. “Phase-sensitive inversion recovery for detecting myocardial infarction using gadolinium-delayed hyperenhancement”. In: *Magnetic Resonance in Medicine* 47.2 (2002), pp. 372–383.

[77] A. Qayyum and J. Kastrup. “Measuring myocardial perfusion: the role of PET, MRI and CT”. In: *Clinical Radiology* 70.6 (2015), 576 –584.

[78] P. Kellman and A. E. Arai. “Imaging Sequences for First Pass Perfusion - A Review”. In: *Journal of Cardiovascular Magnetic Resonance* 9.3 (2007), pp. 525–537.

[79] P. Haaf, P. Garg, D. R. Messroghli, D. A. Broadbent, J. P. Greenwood, and S. Plein. “Cardiac T1 Mapping and Extracellular Volume (ECV) in clinical practice: a comprehensive review”. In: *Journal of Cardiovascular Magnetic Resonance* 18.1 (2016).

[80] D. C. Look and D. R. Locker. “Time Saving in Measurement of NMR and EPR Relaxation Times”. In: *Review of Scientific Instruments* 41.2 (1970), pp. 250–251.

[81] D. R. Messroghli, A. Radjenovic, S. Kozerke, D. M. Higgins, M. U. Sivananthan, and J. P. Ridgway. “Modified Look-Locker inversion recovery (MOLLI) for high-resolution T1 mapping of the heart”. In: *Magnetic Resonance in Medicine: An Official Journal of the International Society for Magnetic Resonance in Medicine* 52.1 (2004), pp. 141–146.

[82] P. Kellman and M. S. Hansen. “T1-mapping in the heart: Accuracy and precision”. In: *Journal of Cardiovascular Magnetic Resonance* 16 (1 2014), pp. 1–20.

[83] K. Chow, J. A. Flewitt, J. D. Green, J. J. Pagano, M. G. Friedrich, and R. B. Thompson. “Saturation recovery single-shot acquisition (SASHA) for myocardial T1 mapping”. In: *Magnetic Resonance in Medicine* 71.6 (2013), pp. 2082–2095.

[84] S. Weingärtner, M. Akçakaya, T. Basha, K. V. Kissinger, B. Goddu, S. Berg, W. J. Manning, and R. Nezafat. “Combined saturation-inversion recovery sequences for improved evaluation of scar and diffuse fibrosis in patients with arrhythmia or heart rate variability”. In: *Magnetic Resonance in Medicine* 71.3 (2013), pp. 1024–1034.

[85] H. Ding, L. Fernandez de Manuel, M. Schär, K. H. Schuleri, H. Halperin, L. He, M. M. Zviman, R. Beinart, and D. A. Herzka. “Three-dimensional whole-heart T2 mapping at 3T”. In: *Magnetic Resonance in Medicine* 74.3 (2014), pp. 803–816.

[86] L. Anderson. “Cardiovascular T2-star (T2*) magnetic resonance for the early diagnosis of myocardial iron overload”. In: *European Heart Journal* 22.23 (2001), pp. 2171–2179.

[87] W. R. Witschey, G. A. Zsido, K. Koomalsingh, N. Kondo, M. Minakawa, T. Shuto, J. R. McGarvey, M. M. Levack, F. Contijoch, J. J. Pilla, J. H. Gorman, and R. C. Gorman. “In vivo chronic myocardial infarction characterization by spin locked cardiovascular magnetic resonance”. In: *Journal of Cardiovascular Magnetic Resonance* 14 (1 2012), pp. 1–9.

[88] D. Ma, V. Gulani, N. Seiberlich, K. Liu, J. L. Sunshine, J. L. Duerk, and M. A. Griswold. “Magnetic resonance fingerprinting”. In: *Nature* 495.7440 (2013), pp. 187–192.

[89] Y. Liu, J. Hamilton, S. Rajagopalan, and N. Seiberlich. “Cardiac Magnetic Resonance Fingerprinting”. In: *JACC: Cardiovascular Imaging* 11.12 (2018), pp. 1837–1853.

[90] G. Cruz, O. Jaubert, R. M. Botnar, and C. Prieto. “Cardiac Magnetic Resonance Fingerprinting: Technical Developments and Initial Clinical Validation”. In: *Current Cardiology Reports* 21.9 (2019).

[91] J. I. Hamilton, Y. Jiang, Y. Chen, D. Ma, W.-C. Lo, M. Griswold, and N. Seiberlich. “MR fingerprinting for rapid quantification of myocardial T1, T2, and proton spin density: Cardiac MR Fingerprinting for T1, T2, and M0Mapping”. In: *Magnetic Resonance in Medicine* 77.4 (2016), pp. 1446–1458.

[92] G. Cruz, O. Jaubert, H. Qi, A. Bustin, G. Milotta, T. Schneider, P. Koken, M. Doneva, R. M. Botnar, and C. Prieto. “3D free/breathing cardiac magnetic resonance fingerprinting”. In: *NMR in Biomedicine* 33.10 (2020).

[93] D. J. Bryant, J. A. Payne, D. N. Firmin, and D. B. Longmore. “Measurement of Flow with NMR Imaging Using a Gradient Pulse and Phase Difference Technique”. In: *Journal of Computer Assisted Tomography* 8.4 (1984), pp. 588–593.

[94] L. Wigström, L. Sjöqvist, and B. Wranne. “Temporally resolved 3D phase-contrast imaging”. In: *Magnetic Resonance in Medicine* 36.5 (1996), pp. 800–803.

[95] F. Kober, T. Jao, T. Troalen, and K. S. Nayak. “Myocardial arterial spin labeling”. In: *Journal of Cardiovascular Magnetic Resonance* 18.1 (2016).

[96] Z. Zun, E. C. Wong, and K. S. Nayak. “Assessment of myocardial blood flow (MBF) in humans using arterial spin labeling (ASL): Feasibility and noise analysis”. In: *Magnetic Resonance in Medicine* 62.4 (2009), pp. 975–983.

[97] R. B. Buxton, L. R. Frank, E. C. Wong, B. Siewert, S. Warach, and R. R. Edelman. “A general kinetic model for quantitative perfusion imaging with arterial spin labeling”. In: *Magnetic Resonance in Medicine* 40.3 (1998), pp. 383–396.

[98] V. M. Ferreira, C. J. Holloway, S. K. Piechnik, T. D. Karamitsos, and S. Neubauer. “Is it really fat? Ask a T1-map”. In: *European Heart Journal – Cardiovascular Imaging* 14.11 (2013), pp. 1060–1060.

[99] M. Adamo, R. S. Gardner, T. A. McDonagh, and M. Metra. “The ‘Ten Commandments’ of the 2021 ESC Guidelines for the diagnosis and treatment of acute and chronic heart failure”. In: *European Heart Journal* 43.6 (2021), pp. 440–441.

[100] F. Beyersdorf, A. Vahanian, M. Milojevic, F. Praz, S. Baldus, J. Bauersachs, D. Capodanno, L. Conradi, M. De Bonis, R. De Paulis, V. Delgado, N. Freemantle, M. Gilard, K. H. Haugaa, A. Jeppsson, P. Jüni, L. Pierard, B. D. Prendergast, J. R. Sádaba, C. Tribouilloy, W. Wojakowski, F.-J. Neumann, P. Myers, M. Abdelhamid, S. Achenbach, R. Asteggiano, F. Barili, M. A. Borger, T. Carrel, J.-P. Collet, D. Foldager, G. Habib, C. Hassager, A. Irs, B. Iung, M. Jahangiri, H. A. Katus, K. C. Koskinas, S. Massberg, C. E. Mueller, J. C. Nielsen, P. Pibarot, A. Rakisheva, M. Roffi, A. Rubboli, E. Shlyakhto, M. Siepe, M. Sitges, L. Sondergaard, M. Sousa-Uva, G. Tarantini, J. L. Zamorano, F. Praz, M. Milojevic, S. Baldus, J. Bauersachs, D. Capodanno, L. Conradi, M. De Bonis, R. De Paulis, V. Delgado, N. Freemantle, M. Gilard, K. H. Haugaa, A. Jeppsson, P. Jüni, L. Pierard, B. D. Prendergast, J. R. Sádaba, C. Tribouilloy, and W. Wojakowski. “2021 ESC/EACTS Guidelines for the management of valvular heart disease”. In: *European Journal of Cardio-Thoracic Surgery* 60.4 (2021), pp. 727–800.

[101] D. J. Pennell. “Cardiovascular magnetic resonance: twenty-first century solutions in cardiology”. In: *Clinical Medicine* 3.3 (2003), pp. 273–278.

[102] J. Schulz-Menger, D. A. Bluemke, J. Bremerich, S. D. Flamm, M. A. Fogel, M. G. Friedrich, R. J. Kim, F. von Knobelsdorff-Brenkenhoff, C. M. Kramer, D. J. Pennell, S. Plein, and E. Nagel. “Standardized image interpretation and post-processing in cardiovascular magnetic resonance - 2020 update: Society for Cardiovascular Magnetic Resonance (SCMR): Board of Trustees Task Force on Standardized Post-Processing”. In: *Journal of Cardiovascular Magnetic Resonance* 22.1 (2020).

[103] R. Bing and M. R. Dweck. “Myocardial fibrosis: why image, how to image and clinical implications”. In: *Heart* 105.23 (2019), pp. 1832–1840.

[104] H. Mahrholdt, A. Wagner, R. M. Judd, U. Sechtem, and R. J. Kim. “Delayed enhancement cardiovascular magnetic resonance assessment of non-ischaemic cardiomyopathies”. In: *European Heart Journal* 26.15 (2005), pp. 1461–1474.

[105] M. Gulati, P. D. Levy, D. Mukherjee, E. Amsterdam, D. L. Bhatt, K. K. Birtcher, R. Blankstein, J. Boyd, R. P. Bullock-Palmer, T. Conejo, D. B. Diercks, F. Gentile, J. P. Greenwood, E. P. Hess, S. M. Hollenberg, W. A. Jaber, H. Jneid, J. A. Joglar, D. A. Morrow, R. E. O’Connor, M. A. Ross, and L. J. Shaw. “2021 AHA-ACC-ASE-CHEST-SAEM-SCCT-SCMR Guideline for the Evaluation and Diagnosis of Chest Pain: Executive Summary”. In: *Journal of the American College of Cardiology* 78.22 (2021), pp. 2218–2261.

[106] T. F. Ismail, S. K. Prasad, and D. J. Pennell. “Prognostic importance of late gadolinium enhancement cardiovascular magnetic resonance in cardiomyopathy”. In: *Heart* 98.6 (2011), pp. 438–442.

[107] B. P. Halliday, D. J. Pennell, and S. K. Prasad. “Response by Halliday et al to Letter Regarding Article, “Association Between Midwall Late Gadolinium Enhancement and Sudden Cardiac Death in Patients with Dilated Cardiomyopathy and Mild and Moderate Left Ventricular Systolic Dysfunction””. In: *Circulation* 137.1 (2018), pp. 101–102.

[108] A. Gulati, A. G. Japp, S. Raza, B. P. Halliday, D. A. Jones, S. Newsome, N. A. Ismail, K. Morarji, J. Khwaja, N. Spath, C. Shakespeare, P. R. Kalra, G. Lloyd, A. Mathur, J. G. Cleland, M. R. Cowie, R. G. Assomull, D. J. Pennell, T. F. Ismail, and S. K. Prasad. “Absence of Myocardial Fibrosis Predicts Favorable Long-Term Survival in New-Onset Heart Failure: A Cardiovascular Magnetic Resonance Study”. In: *Circulation: Cardiovascular Imaging* 11.9 (2018).

[109] A. Gulati, A. Jabbour, T. F. Ismail, K. Guha, J. Khwaja, S. Raza, K. Morarji, T. D. H. Brown, N. A. Ismail, M. R. Dweck, E. Di Pietro, M. Roughton, R. Wage, Y. Daryani, R. O’Hanlon, M. N. Sheppard, F. Alpendurada, A. R. Lyon, S. A. Cook, M. R. Cowie, R. G. Asso-

mull, D. J. Pennell, and S. K. Prasad. “Association of Fibrosis With Mortality and Sudden Cardiac Death in Patients With Nonischemic Dilated Cardiomyopathy”. In: *JAMA* 309.9 (2013), p. 896.

[110] G. Georgiopoulos, S. Figliozzi, F. Sanguineti, G. D. Aquaro, G. di Bella, K. Stamatelopoulos, A. Chiribiri, J. Garot, P. G. Masci, and T. F. Ismail. “Prognostic Impact of Late Gadolinium Enhancement by Cardiovascular Magnetic Resonance in Myocarditis: A Systematic Review and Meta-Analysis”. In: *Circulation: Cardiovascular Imaging* 14.1 (2021).

[111] R. J. Kim, E. L. Chen, J. A. Lima, and R. M. Judd. “Myocardial Gd-DTPA Kinetics Determine MRI Contrast Enhancement and Reflect the Extent and Severity of Myocardial Injury After Acute Reperfused Infarction”. In: *Circulation* 94 (12 1996), pp. 3318–3326.

[112] A. R. Patel, M. Salerno, R. Y. Kwong, A. Singh, B. Heydari, and C. M. Kramer. “Stress Cardiac Magnetic Resonance Myocardial Perfusion Imaging”. In: *Journal of the American College of Cardiology* 78.16 (2021), pp. 1655–1668.

[113] T. Leiner, J. Bogaert, M. G. Friedrich, R. Mohiaddin, V. Muthurangu, S. Myerson, A. J. Powell, S. V. Raman, and D. J. Pennell. “SCMR Position Paper (2020) on clinical indications for cardiovascular magnetic resonance”. In: *Journal of Cardiovascular Magnetic Resonance* 22.1 (2020).

[114] A. E. Arai and L.-Y. Hsu. “Global Developments in Stress Perfusion Cardiovascular Magnetic Resonance”. In: *Circulation* 141.16 (2020), pp. 1292–1294.

[115] A. Gulati, T. F. Ismail, A. Ali, L.-Y. Hsu, C. Gonçalves, N. A. Ismail, K. Krishnathasan, N. Davendralingam, P. Ferreira, B. P. Halliday, D. A. Jones, R. Wage, S. Newsome, P. Gatehouse, D. Firmin, A. Jabbour, R. G. Assomull, A. Mathur, D. J. Pennell, A. E. Arai, and S. K. Prasad. “Microvascular Dysfunction in Dilated Cardiomyopathy”. In: *JACC: Cardiovascular Imaging* 12.8 (2019), pp. 1699–1708.

[116] L.-Y. Hsu, M. Jacobs, M. Benovoy, A. D. Ta, H. M. Conn, S. Winkler, A. M. Greve, M. Y. Chen, S. M. Shanbhag, W. P. Bandettini, and A. E. Arai. “Diagnostic Performance of Fully Automated Pixel-Wise Quantitative Myocardial Perfusion Imaging by Cardiovascular Magnetic Resonance”. In: *JACC: Cardiovascular Imaging* 11.5 (2018), pp. 697–707.

[117] E. C. Sammut, A. D. Villa, G. Di Giovine, L. Dancy, F. Bosio, T. Gibbs, S. Jeyabraba, S. Schwenke, S. E. Williams, M. Marber, K. Alfakih, T. F. Ismail, R. Razavi, and A. Chiribiri. “Prognostic Value of Quantitative Stress Perfusion Cardiac Magnetic Resonance”. In: *JACC: Cardiovascular Imaging* 11.5 (2018), pp. 686–694.

[118] N. Zarinabad, A. Chiribiri, G. L. T. F. Hautvast, M. Ishida, A. Schuster, Z. Cvetkovic, P. G. Batchelor, and E. Nagel. “Voxel-wise quantification of myocardial perfusion by cardiac magnetic resonance. Feasibility and methods comparison”. In: *Magnetic Resonance in Medicine* 68.6 (2012), pp. 1994–2004.

[119] J. Tourais, O. B. Demirel, Q. Tao, I. Pierce, G. D. Thornton, T. A. Treibel, M. Akcakaya, and S. Weingärtner. “Myocardial Approximate Spin-lock Dispersion Mapping using a Simultaneous T_2 and T_{RAFF2} Mapping at 3T MRI”. In: *2022 44th Annual International Conference of the IEEE Engineering in Medicine & Biology Society (EMBC)*. IEEE. 2022, pp. 1694–1697.

[120] A. D. M. Villa, E. Sammut, N. Zarinabad, G. Carr-White, J. Lee, N. Bettencourt, R. Razavi, E. Nagel, and A. Chiribiri. “Microvascular ischemia in hypertrophic cardiomyopathy: new insights from high-resolution combined quantification of perfusion and late gadolinium enhancement”. In: *Journal of Cardiovascular Magnetic Resonance* 18.1 (2015).

[121] T. F. Ismail, L.-Y. Hsu, A. M. Greve, C. Gonçalves, A. Jabbour, A. Gulati, B. Hewins, N. Mistry, R. Wage, M. Roughton, P. F. Ferreira, P. Gatehouse, D. Firmin, R. O’Hanlon, D. J. Pennell, S. K. Prasad, and A. E. Arai. “Coronary microvascular ischemia in hypertrophic cardiomyopathy - a pixel-wise quantitative cardiovascular magnetic resonance perfusion study”. In: *Journal of Cardiovascular Magnetic Resonance* 16.1 (2014).

[122] L.-Y. Hsu, D. W. Groves, A. H. Aletras, P. Kellman, and A. E. Arai. “A Quantitative Pixel-Wise Measurement of Myocardial Blood Flow by Contrast-Enhanced First-Pass CMR Perfusion Imaging”. In: *JACC: Cardiovascular Imaging* 5.2 (2012), pp. 154–166.

[123] A. R. Patel, P. F. Antkowiak, K. R. Nandalur, A. M. West, M. Salerno, V. Arora, J. Christopher, F. H. Epstein, and C. M. Kramer. “Assessment of Advanced Coronary Artery Disease”. In: *Journal of the American College of Cardiology* 56.7 (2010), pp. 561–569.

[124] D. R. Messroghli, J. C. Moon, V. M. Ferreira, L. Grosse-Wortmann, T. He, P. Kellman, J. Mascherbauer, R. Nezafat, M. Salerno, E. B. Schelbert, A. J. Taylor, R. Thompson, M. Ugander, R. B. van Heeswijk, and M. G. Friedrich. “Clinical recommendations for cardiovascular magnetic resonance mapping of T1, T2, T2* and extracellular volume: A consensus statement by the Society for Cardiovascular Magnetic Resonance (SCMR) endorsed by the European Association for Cardiovascular Imaging (EACVI)”. In: *Journal of Cardiovascular Magnetic Resonance* 19.1 (2017).

[125] B. Modell, M. Khan, M. Darlison, M. A. Westwood, D. Ingram, and D. J. Pennell. “Improved survival of thalassaemia major in the UK and relation to T2* cardiovascular magnetic resonance”. In: *Journal of Cardiovascular Magnetic Resonance* 10.1 (2008).

[126] M. M. Kittleson, M. S. Maurer, A. V. Ambardekar, R. P. Bullock-Palmer, P. P. Chang, H. J. Eisen, A. P. Nair, J. Nativi-Nicolau, and F. L. Ruberg. “Cardiac Amyloidosis: Evolving Diagnosis and Management: A Scientific Statement From the American Heart Association”. In: *Circulation* 142.1 (2020).

[127] R. G. Assomull, C. Shakespeare, P. R. Kalra, G. Lloyd, A. Gulati, J. Strange, W. M. Bradlow, J. Lyne, J. Keegan, P. Poole-Wilson, M. R. Cowie, D. J. Pennell, and S. K. Prasad. “Role of Cardiovascular Magnetic Resonance as a Gatekeeper to Invasive Coronary Angiography in Patients Presenting With Heart Failure of Unknown Etiology”. In: *Circulation* 124.12 (2011), pp. 1351–1360.

[128] B. J. Maron and M. S. Maron. “The Remarkable 50 Years of Imaging in HCM and How it Has Changed Diagnosis and Management”. In: *JACC: Cardiovascular Imaging* 9.7 (2016), pp. 858–872.

[129] A. S. te Riele, H. Tandri, and D. A. Bluemke. “Arrhythmogenic right ventricular cardiomyopathy (ARVC): cardiovascular magnetic resonance update”. In: *Journal of Cardiovascular Magnetic Resonance* 16.1 (2014).

[130] I. Eitel and M. G. Friedrich. “T2-weighted cardiovascular magnetic resonance in acute cardiac disease”. In: *Journal of Cardiovascular Magnetic Resonance* 13.1 (2011).

[131] A. Bustin, S. Toupin, S. Sridi, J. Yerly, O. Bernus, L. Labrousse, B. Quesson, J. Rogier, M. Haïssaguerre, R. van Heeswijk, P. Jaïs, H. Cochet, and M. Stuber. “Endogenous assessment of myocardial injury with single-shot model-based non-rigid motion-corrected T1 rho mapping”. In: *Journal of Cardiovascular Magnetic Resonance* 23 (1 2021), pp. 1–14.

[132] V. M. Ferreira, J. Schulz-Menger, G. Holmvang, C. M. Kramer, I. Carbone, U. Sechtem, I. Kindermann, M. Gutberlet, L. T. Cooper, P. Liu, and M. G. Friedrich. “Cardiovascular Magnetic Resonance in Nonischemic Myocardial Inflammation”. In: *Journal of the American College of Cardiology* 72.24 (2018), pp. 3158–3176.

[133] A. Kolandaivelu, A. C. Lardo, and H. R. Halperin. “Cardiovascular magnetic resonance guided electrophysiology studies”. In: *Journal of Cardiovascular Magnetic Resonance* 11.1 (2009).

[134] G. F. Michaud and W. G. Stevenson. “Atrial Fibrillation”. In: *New England Journal of Medicine* 384.4 (2021). Ed. by C. G. Solomon, pp. 353–361.

[135] H. Chubb, R. Karim, R. Mukherjee, S. E. Williams, J. Whitaker, J. Harrison, S. A. Niederer, W. Staab, J. Gill, T. Schaeffter, M. Wright, M. O'Neill, and R. Razavi. "A comprehensive multi-index cardiac magnetic resonance-guided assessment of atrial fibrillation substrate prior to ablation: Prediction of long-term outcomes". In: *Journal of Cardiovascular Electrophysiology* 30.10 (2019), pp. 1894–1903.

[136] D. Soto-Iglesias, D. Penela, B. Jáuregui, J. Acosta, J. Fernández-Armenta, M. Linhart, G. Zucchelli, V. Syrovnev, F. Zaraket, C. Terés, R. J. Perea, S. Prat-González, A. Doltra, J. T. Ortiz-Pérez, X. Bosch, O. Camara, and A. Berruezo. "Cardiac Magnetic Resonance-Guided Ventricular Tachycardia Substrate Ablation". In: *JACC: Clinical Electrophysiology* 6.4 (2020), pp. 436–447.

[137] H. N. Ntsinjana, M. L. Hughes, and A. M. Taylor. "The Role of Cardiovascular Magnetic Resonance in Pediatric Congenital Heart Disease". In: *Journal of Cardiovascular Magnetic Resonance* 13.1 (2011).

[138] A. J. Marelli, A. S. Mackie, R. Ionescu-Ittu, E. Rahme, and L. Pilote. "Congenital Heart Disease in the General Population: Changing Prevalence and Age Distribution". In: *Circulation* 115.2 (2007), pp. 163–172.

[139] S. V. Babu-Narayan, G. Giannakoulas, A. M. Valente, W. Li, and M. A. Gatzoulis. "Imaging of congenital heart disease in adults". In: *European Heart Journal* 37.15 (2015), pp. 1182–1195.

[140] A. Gulati, T. F. Ismail, A. Jabbour, F. Alpendurada, K. Guha, N. A. Ismail, S. Raza, J. Khwaja, T. D. Brown, K. Morarji, E. Liodakis, M. Roughton, R. Wage, T. C. Pakrashi, R. Sharma, J.-P. Carpenter, S. A. Cook, M. R. Cowie, R. G. Assomull, D. J. Pennell, and S. K. Prasad. "The Prevalence and Prognostic Significance of Right Ventricular Systolic Dysfunction in Nonischemic Dilated Cardiomyopathy". In: *Circulation* 128.15 (2013), pp. 1623–1633.

[141] I. Rashid, A. Mahmood, T. F. Ismail, S. O'Meagher, S. Kutty, D. Celermajer, and R. Puranik. "Right ventricular systolic dysfunction but not dilatation correlates with prognostically significant reductions in exercise capacity in repaired Tetralogy of Fallot". In: *European Heart Journal - Cardiovascular Imaging* 21.8 (2019), pp. 906–913.

[142] H. Baumgartner and J. De Backer. "The ESC Clinical Practice Guidelines for the Management of Adult Congenital Heart Disease 2020". In: *European Heart Journal* 41.43 (2020), pp. 4153–4154.

[143] P. J. Cawley, J. H. Maki, and C. M. Otto. "Cardiovascular Magnetic Resonance Imaging for Valvular Heart Disease: Technique and Validation". In: *Circulation* 119.3 (2009), pp. 468–478.

[144] S. G. Myerson. “Heart valve disease: investigation by cardiovascular magnetic resonance”. In: *Journal of Cardiovascular Magnetic Resonance* 14.1 (2012).

[145] D. G. Lohan, M. Krishnam, A. Tomasian, R. Saleh, and J. P. Finn. “Time-Resolved MR Angiography of the Thorax”. In: *Magnetic Resonance Imaging Clinics of North America* 16.2 (2008), pp. 235–248.

[146] G. Ginami, R. Neji, I. Rashid, A. Chiribiri, T. F. Ismail, R. M. Botnar, and C. Prieto. “3D whole-heart phase sensitive inversion recovery CMR for simultaneous black-blood late gadolinium enhancement and bright-blood coronary CMR angiography”. In: *Journal of Cardiovascular Magnetic Resonance* 19.1 (2017).

[147] T. Correia, G. Ginami, I. Rashid, G. Nordio, R. Hajhosseiny, T. F. Ismail, R. Neji, R. M. Botnar, and C. Prieto. “Accelerated high-resolution free-breathing 3D whole-heart T2-prepared black-blood and bright-blood cardiovascular magnetic resonance”. In: *Journal of Cardiovascular Magnetic Resonance* 22.1 (2020).

[148] A. Bustin, G. Ginami, G. Cruz, T. Correia, T. F. Ismail, I. Rashid, R. Neji, R. M. Botnar, and C. Prieto. “Five-minute whole-heart coronary MRA with sub-millimeter isotropic resolution, 100% respiratory scan efficiency, and 3D-PROST reconstruction”. In: *Magnetic Resonance in Medicine* 81.1 (2018), pp. 102–115.

[149] M. N. Velasco Forte, S. Roujol, B. Ruijsink, I. Valverde, P. Duong, N. Byrne, S. Krueger, S. Weiss, Y. Arar, S. R. V. Reddy, T. Schaeffter, T. Hussain, R. Razavi, and K. Pushparajah. “MRI for Guided Right and Left Heart Cardiac Catheterization: A Prospective Study in Congenital Heart Disease”. In: *Journal of Magnetic Resonance Imaging* 53.5 (2020), pp. 1446–1457.

[150] D. S. Knight, T. Kotecha, A. Martinez-Naharro, J. T. Brown, M. Bertelli, M. Fontana, V. Muthurangu, and J. G. Coghlan. “Cardiovascular magnetic resonance-guided right heart catheterization in a conventional CMR environment – predictors of procedure success and duration in pulmonary artery hypertension”. In: *Journal of Cardiovascular Magnetic Resonance* 21.1 (2019).

[151] R. M. Botnar and W. Y. Kim. “Coronary MR Imaging”. In: *JACC: Cardiovascular Imaging* 8.10 (2015), pp. 1153–1155.

[152] K. Matsumoto, S. Ehara, T. Hasegawa, M. Sakaguchi, K. Otsuka, J. Yoshikawa, and K. Shimada. “Localization of Coronary High-Intensity Signals on T1-Weighted MR Imaging”. In: *JACC: Cardiovascular Imaging* 8.10 (2015), pp. 1143–1152.

[153] M. Motwani, A. Kidambi, B. A. Herzog, A. Uddin, J. P. Greenwood, and S. Plein. “MR Imaging of Cardiac Tumors and Masses: A Review of Methods and Clinical Applications”. In: *Radiology* 268.1 (2013), pp. 26–43.

[154] S. Tyebally, D. Chen, S. Bhattacharyya, A. Mughrabi, Z. Hussain, C. Manisty, M. Westwood, A. K. Ghosh, and A. Guha. “Cardiac Tumors”. In: *JACC: CardioOncology* 2.2 (2020), pp. 293–311.

[155] M. S. Nazir, T. F. Ismail, E. Reyes, A. Chiribiri, P. A. Kaufmann, and S. Plein. “Hybrid positron emission tomography–magnetic resonance of the heart: current state of the art and future applications”. In: *European Heart Journal - Cardiovascular Imaging* 19.9 (2018), pp. 962–974.

[156] K. T. Block, M. Uecker, and J. Frahm. “Undersampled radial MRI with multiple coils. Iterative image reconstruction using a total variation constraint”. In: *Magnetic Resonance in Medicine* 57.6 (2007), pp. 1086–1098.

[157] M. Lustig, D. Donoho, and J. M. Pauly. “Sparse MRI: The application of compressed sensing for rapid MR imaging”. In: *Magnetic Resonance in Medicine* 58.6 (2007), pp. 1182–1195.

[158] M. A. Griswold, P. M. Jakob, R. M. Heidemann, M. Nittka, V. Jellus, J. Wang, B. Kiefer, and A. Haase. “Generalized autocalibrating partially parallel acquisitions (GRAPPA)”. In: *Magnetic Resonance in Medicine* 47.6 (2002), pp. 1202–1210.

[159] K. P. Pruessmann, M. Weiger, M. B. Scheidegger, and P. Boesiger. “SENSE: Sensitivity encoding for fast MRI”. In: *Magnetic Resonance in Medicine* 42.5 (1999), pp. 952–962.

[160] R. Otazo, D. Kim, L. Axel, and D. K. Sodickson. “Highly-accelerated first-pass cardiac perfusion MRI using compressed sensing and parallel imaging”. In: *Journal of Cardiovascular Magnetic Resonance* 12.S1 (2010).

[161] R. L. Ehman and J. P. Felmlee. “Adaptive technique for high-definition MR imaging of moving structures.” In: *Radiology* 173.1 (1989), pp. 255–263.

[162] A. J. van der Kouwe, T. Benner, and A. M. Dale. “Real-time rigid body motion correction and shimming using cloverleaf navigators”. In: *Magnetic Resonance in Medicine* 56.5 (2006), pp. 1019–1032.

[163] M. Henningsson, P. Koken, C. Stehning, R. Razavi, C. Prieto, and R. M. Botnar. “Whole-heart coronary MR angiography with 2D self-navigated image reconstruction”. In: *Magnetic Resonance in Medicine* 67.2 (2011), pp. 437–445.

[164] K. Kawaji, P. Spincemaille, T. D. Nguyen, N. Thimmappa, M. A. Cooper, M. R. Prince, and Y. Wang. “Direct coronary motion extraction from a 2D fat image navigator for prospectively gated coronary MR angiography”. In: *Magnetic Resonance in Medicine* 71.2 (2013), pp. 599–607.

[165] T. D. Nguyen, P. Spincemaille, M. D. Cham, J. W. Weinsaft, M. R. Prince, and Y. Wang. “Free-breathing 3D steady-state free precession coronary magnetic resonance angiography: Comparison of diaphragm and cardiac fat navigators”. In: *Journal of Magnetic Resonance Imaging* 28.2 (2008), pp. 509–514.

[166] J. Maclaren, M. Herbst, O. Speck, and M. Zaitsev. “Prospective motion correction in brain imaging: A review”. In: *Magnetic Resonance in Medicine* 69.3 (2012), pp. 621–636.

[167] N. De Zanche, C. Barmet, J. A. Nordmeyer-Massner, and K. P. Pruessmann. “NMR probes for measuring magnetic fields and field dynamics in MR systems”. In: *Magnetic Resonance in Medicine* 60.1 (2008), pp. 176–186.

[168] T. Vahle, M. Bacher, D. Rigie, M. Fenchel, P. Speier, J. Bollenbeck, K. P. Schäfers, B. Kiefer, and F. E. Boada. “Respiratory Motion Detection and Correction for MR Using the Pilot Tone: Applications for MR and Simultaneous PET/MR Examinations”. In: *Investigative Radiology* 55.3 (2019), pp. 153–159.

[169] M. Zaitsev, J. Maclaren, and M. Herbst. “Motion artifacts in MRI: A complex problem with many partial solutions”. In: *Journal of Magnetic Resonance Imaging* 42.4 (2015), pp. 887–901.

[170] A. H. Aletras, S. Ding, R. S. Balaban, and H. Wen. “DENSE: Displacement Encoding with Stimulated Echoes in Cardiac Functional MRI”. In: *Journal of Magnetic Resonance* 137.1 (1999), pp. 247–252.

[171] Y. Wang, P. S. Christy, F. R. Korosec, M. T. Alley, T. M. Grist, J. A. Polzin, and C. A. Mistretta. “Coronary MRI with a Respiratory Feedback Monitor: The 2D Imaging Case”. In: *Magnetic Resonance in Medicine* 33.1 (1995), pp. 116–121.

[172] E. Nagel, A. Bornstedt, B. Schnackenburg, J. Hug, H. Oswald, and E. Fleck. “Optimization of realtime adaptive navigator correction for 3D magnetic resonance coronary angiography”. In: *Magnetic Resonance in Medicine* 42.2 (1999), pp. 408–411.

[173] D. J. Atkinson and R. R. Edelman. “Cineangiography of the heart in a single breath hold with a segmented turboFLASH sequence.” In: *Radiology* 178.2 (1991), pp. 357–360.

[174] M. E. Crowe, A. C. Larson, Q. Zhang, J. Carr, R. D. White, D. Li, and O. P. Simonetti. “Automated rectilinear self-gated cardiac cine imaging”. In: *Magnetic Resonance in Medicine* 52.4 (2004), pp. 782–788.

[175] A. C. Larson, R. D. White, G. Laub, E. R. McVeigh, D. Li, and O. P. Simonetti. “Self-gated cardiac cine MRI”. In: *Magnetic Resonance in Medicine* 51.1 (2003), pp. 93–102.

[176] D. A. Bluemke, J. L. Boxerman, E. Atalar, and E. R. McVeigh. “Segmented K-space cine breath-hold cardiovascular MR imaging: Part 1. Principles and technique.” In: *American Journal of Roentgenology* 169.2 (1997), pp. 395–400.

[177] B. Sievers, M. Addo, S. Kirchberg, A. Bakan, B. John-Puthenveettil, U. Franken, and H.-J. Trappe. “Impact of the ECG Gating Method on Ventricular Volumes and Ejection Fractions Assessed By Cardiovascular Magnetic Resonance Imaging”. In: *Journal of Cardiovascular Magnetic Resonance* 7.2 (2005), pp. 441–446.

[178] T. Leiner, G. Katsimaglis, E. N. Yeh, K. V. Kissinger, G. van Yperen, H. Eggers, W. J. Manning, and R. M. Botnar. “Correction for heart rate variability improves coronary magnetic resonance angiography”. In: *Journal of Magnetic Resonance Imaging* 22.4 (2005), pp. 577–582.

[179] F. Han, Z. Zhou, E. Han, Y. Gao, K.-L. Nguyen, J. P. Finn, and P. Hu. “Self-gated 4D multiphase, steady-state imaging with contrast enhancement (MUSIC) using rotating cartesian K-space (ROCK): Validation in children with congenital heart disease: Ferumoxytol-enhanced 4D ROCK-MUSIC”. In: *Magnetic Resonance in Medicine* 78.2 (2016), pp. 472–483.

[180] M. Weiger, P. Börnert, R. Proksa, T. Schäffter, and A. Haase. “Motion-adapted gating based on k-space weighting for reduction of respiratory motion artifacts”. In: *Magnetic Resonance in Medicine* 38.2 (1997), pp. 322–333.

[181] Y. Wang and R. L. Ehman. “Retrospective adaptive motion correction for navigator-gated 3D coronary MR angiography”. In: *Journal of Magnetic Resonance Imaging* 11.2 (2000), pp. 208–214.

[182] Y. Wang, R. Watts, I. R. Mitchell, T. D. Nguyen, J. W. Bezanson, G. W. Bergman, and M. R. Prince. “Coronary MR Angiography: Selection of Acquisition Window of Minimal Cardiac Motion with Electrocardiography-triggered Navigator Cardiac Motion Prescanning—Initial Results”. In: *Radiology* 218.2 (2001), pp. 580–585.

[183] J. Ludwig, P. Speier, F. Seifert, T. Schaeffter, and C. Kolbitsch. “Pilot tone–based motion correction for prospective respiratory compensated cardiac cine MRI”. In: *Magnetic Resonance in Medicine* 85.5 (2020), pp. 2403–2416.

[184] C. Stehning, P. Börnert, K. Nehrke, H. Eggers, and M. Stuber. “Free-breathing whole-heart coronary MRA with 3D radial SSFP and self-navigated image reconstruction”. In: *Magnetic Resonance in Medicine* 54.2 (2005), pp. 476–480.

[185] T. Sachs, C. Meyer, J. Pauly, B. Hu, D. Nishimura, and A. Macovski. “The real-time interactive 3-D-DVA for robust coronary MRA”. In: *IEEE Transactions on Medical Imaging* 19.2 (2000), pp. 73–79.

[186] A. C. Larson, P. Kellman, A. Arai, G. A. Hirsch, E. McVeigh, D. Li, and O. P. Simonetti. “Preliminary investigation of respiratory self-gating for free-breathing segmented cine MRI”. In: *Magnetic Resonance in Medicine* 53.1 (2004), pp. 159–168.

[187] S. Uribe, V. Muthurangu, R. Boubertakh, T. Schaeffter, R. Razavi, D. L. Hill, and M. S. Hansen. “Whole-heart cine MRI using real-time respiratory self-gating”. In: *Magnetic Resonance in Medicine* 57.3 (2007), pp. 606–613.

[188] J. G. Pipe. “Motion correction with PROPELLER MRI: Application to head motion and free-breathing cardiac imaging”. In: *Magnetic Resonance in Medicine* 42.5 (1999), pp. 963–969.

[189] P. Kellman, C. Chefd’hotel, C. H. Lorenz, C. Mancini, A. E. Arai, and E. R. McVeigh. “Fully automatic, retrospective enhancement of real-time acquired cardiac cine MR images using image-based navigators and respiratory motion-corrected averaging”. In: *Magnetic Resonance in Medicine* 59.4 (2008), pp. 771–778.

[190] M. S. Hansen, T. S. Sørensen, A. E. Arai, and P. Kellman. “Retrospective reconstruction of high temporal resolution cine images from real-time MRI using iterative motion correction”. In: *Magnetic Resonance in Medicine* 68.3 (2011), pp. 741–750.

[191] H. H. Wu, P. T. Gurney, B. S. Hu, D. G. Nishimura, and M. V. McConnell. “Free-breathing multiphase whole-heart coronary MR angiography using image-based navigators and three-dimensional cones imaging”. In: *Magnetic Resonance in Medicine* 69.4 (2012), pp. 1083–1093.

[192] J. Keegan, P. D. Gatehouse, G.-Z. Yang, and D. N. Firmin. “Non-model-based correction of respiratory motion using beat-to-beat 3D spiral fat-selective imaging”. In: *Journal of Magnetic Resonance Imaging* 26.3 (2007), pp. 624–629.

[193] R. B. van Heeswijk, D. Piccini, H. Feliciano, R. Hullin, J. Schwitter, and M. Stuber. “Self-navigated isotropic three-dimensional cardiac T2 mapping”. In: *Magnetic Resonance in Medicine* 73.4 (2014), pp. 1549–1554.

[194] N. O. Addy, R. R. Ingle, H. H. Wu, B. S. Hu, and D. G. Nishimura. “High-resolution variable-density 3D cones coronary MRA”. In: *Magnetic Resonance in Medicine* 74.3 (2015), pp. 614–621.

[195] M. O. Malavé, C. A. Baron, N. O. Addy, J. Y. Cheng, P. C. Yang, B. S. Hu, and D. G. Nishimura. “Whole-heart coronary MR angiography using a 3D cones phyllotaxis trajectory”. In: *Magnetic Resonance in Medicine* 81.2 (2018), pp. 1092–1103.

[196] M. S. Sussman, J. A. Stainsby, N. Robert, N. Merchant, and G. A. Wright. “Variable-density adaptive imaging for high-resolution coronary artery MRI”. In: *Magnetic Resonance in Medicine* 48.5 (2002), pp. 753–764.

[197] C. J. Hardy, M. Saranathan, Y. Zhu, and R. D. Darrow. “Coronary angiography by real-time MRI with adaptive averaging”. In: *Magnetic Resonance in Medicine* 44.6 (2000), pp. 940–946.

[198] P. Lai, A. C. Larson, J. Park, J. C. Carr, and D. Li. “Respiratory self-gated four-dimensional coronary MR angiography: A feasibility study”. In: *Magnetic Resonance in Medicine* 59.6 (2008), pp. 1378–1385.

[199] T. Küstner, A. Bustin, O. Jaubert, R. Hajhosseiny, P. G. Masci, R. Neji, R. Botnar, and C. Prieto. “Fully self-gated free-running 3D Cartesian cardiac CINE with isotropic whole-heart coverage in less than 2 min”. In: *NMR in Biomedicine* 34.1 (2020).

[200] D. Piccini, P. Monney, C. Sierro, S. Coppo, G. Bonanno, R. B. van Heeswijk, J. Chaptinel, G. Vincenti, J. de Blois, S. C. Koestner, T. Rutz, A. Littmann, M. O. Zenge, J. Schwitter, and M. Stuber. “Respiratory Self-navigated Postcontrast Whole-Heart Coronary MR Angiography: Initial Experience in Patients”. In: *Radiology* 270.2 (2014), pp. 378–386.

[201] H. Qi, O. Jaubert, A. Bustin, G. Cruz, H. Chen, R. Botnar, and C. Prieto. “Free-running 3D whole heart myocardial T1 mapping with isotropic spatial resolution”. In: *Magnetic Resonance in Medicine* 82.4 (2019), pp. 1331–1342.

[202] S. Coppo, D. Piccini, G. Bonanno, J. Chaptinel, G. Vincenti, H. Feliciano, R. B. van Heeswijk, J. Schwitter, and M. Stuber. “Free-running 4D whole-heart self-navigated golden angle MRI: Initial results”. In: *Magnetic Resonance in Medicine* 74.5 (2014), pp. 1306–1316.

[203] L. Feng, L. Axel, H. Chandarana, K. T. Block, D. K. Sodickson, and R. Otazo. “XD-GRASP: Golden-angle radial MRI with reconstruction of extra motion-state dimensions using compressed sensing”. In: *Magnetic Resonance in Medicine* 75.2 (2015), pp. 775–788.

[204] N. Seiberlich, P. Ehses, J. Duerk, R. Gilkeson, and M. Griswold. “Improved radial GRAPPA calibration for real-time free-breathing cardiac imaging”. In: *Magnetic Resonance in Medicine* 65.2 (2010), pp. 492–505.

[205] J. Tsao, P. Boesiger, and K. P. Pruessmann. “k-t BLAST and k-t SENSE: Dynamic MRI with high frame rate exploiting spatiotemporal correlations”. In: *Magnetic Resonance in Medicine* 50.5 (2003), pp. 1031–1042.

[206] F. Huang, J. Akao, S. Vijayakumar, G. R. Duensing, and M. Limkeman. “k-t GRAPPA: A k-space implementation for dynamic MRI with high reduction factor”. In: *Magnetic Resonance in Medicine* 54.5 (2005), pp. 1172–1184.

[207] J. Liu, T. D. Nguyen, Y. Zhu, P. Spincemaille, M. R. Prince, J. W. Weinsaft, D. Saloner, and Y. Wang. “Self-Gated Free-Breathing 3D Coronary CINE Imaging with Simultaneous Water and Fat Visualization”. In: *PLoS ONE* 9.2 (2014). Ed. by M. Stuber, e89315.

[208] M. S. Asif, L. Hamilton, M. Brummer, and J. Romberg. “Motion-adaptive spatio-temporal regularization for accelerated dynamic MRI”. In: *Magnetic Resonance in Medicine* 70.3 (2012), pp. 800–812.

[209] Y. Q. Mohsin, S. G. Lingala, E. DiBella, and M. Jacob. “Accelerated dynamic MRI using patch regularization for implicit motion compensation”. In: *Magnetic Resonance in Medicine* 77.3 (2016), pp. 1238–1248.

[210] X. Chen, M. Salerno, Y. Yang, and F. H. Epstein. “Motion-compensated compressed sensing for dynamic contrast-enhanced MRI using regional spatiotemporal sparsity and region tracking: Block low-rank sparsity with motion-guidance (BLOSM)”. In: *Magnetic Resonance in Medicine* 72.4 (2013), pp. 1028–1038.

[211] L. E. Ma, J. Yerly, D. Piccini, L. Di Sopra, C. W. Roy, J. C. Carr, C. K. Rigsby, D. Kim, M. Stuber, and M. Markl. “5D Flow MRI: A Fully Self-gated, Free-running Framework for Cardiac and Respiratory Motion–resolved 3D Hemodynamics”. In: *Radiology: Cardiothoracic Imaging* 2.6 (2020), e200219.

[212] T. Küstner, C. Würslin, M. Schwartz, P. Martirosian, S. Gatidis, C. Brendle, F. Seith, F. Schick, N. F. Schwenzer, B. Yang, and H. Schmidt. “Self-navigated 4D cartesian imaging of periodic motion in the body trunk using partial k-space compressed sensing: Self-Navigated 4D MRI with Compressed Sensing Reconstruction”. In: *Magnetic Resonance in Medicine* 78.2 (2016), pp. 632–644.

[213] D. Piccini, A. Littmann, S. Nielles-Vallespin, and M. O. Zenge. “Spiral phyllotaxis: The natural way to construct a 3D radial trajectory in MRI”. In: *Magnetic Resonance in Medicine* 66.4 (2011), pp. 1049–1056.

[214] J. Pang, B. Sharif, Z. Fan, X. Bi, R. Arsanjani, D. S. Berman, and D. Li. “ECG and navigator/free four/dimensional whole/heart coronary MRA for simultaneous visualization of cardiac anatomy and function”. In: *Magnetic Resonance in Medicine* 72.5 (2014), 1208 –1217.

[215] T. Correia, G. Ginami, G. Cruz, R. Neji, I. Rashid, R. M. Botnar, and C. Prieto. “Optimized respiratory/resolved motion-compensated 3D Cartesian coronary MR angiography”. In: *Magnetic Resonance in Medicine* 80.6 (2018), pp. 2618–2629.

[216] J. Y. Cheng, T. Zhang, N. Ruangwattanapaisarn, M. T. Alley, M. Uecker, J. M. Pauly, M. Lustig, and S. S. Vasanawala. “Free-breathing pediatric MRI with nonrigid motion correction and acceleration: Free-Breathing Pediatric MRI”. In: *Journal of Magnetic Resonance Imaging* 42.2 (2014), pp. 407–420.

[217] H. Xue, P. Kellman, G. LaRocca, A. E. Arai, and M. S. Hansen. “High spatial and temporal resolution retrospective cine cardiovascular magnetic resonance from shortened free breathing real-time acquisitions”. In: *Journal of Cardiovascular Magnetic Resonance* 15.1 (2013).

[218] M. Usman, D. Atkinson, F. Odille, C. Kolbitsch, G. Vaillant, T. Schaeffter, P. G. Batchelor, and C. Prieto. “Motion corrected compressed sensing for free-breathing dynamic cardiac MRI”. In: *Magnetic Resonance in Medicine* 70.2 (2012), pp. 504–516.

[219] J. Royuela-del-Val, L. Cordero-Grande, F. Simmross-Wattenberg, M. Martín-Fernández, and C. Alberola-López. “Nonrigid groupwise registration for motion estimation and compensation in compressed sensing reconstruction of breath/hold cardiac cine MRI”. In: *Magnetic Resonance in Medicine* 75.4 (2015), pp. 1525–1536.

[220] A. Tolouee, J. Alirezaie, and P. Babyn. “Nonrigid motion compensation in compressed sensing reconstruction of cardiac cine MRI”. In: *Magnetic Resonance Imaging* 46 (2018), pp. 114–120.

[221] F. Liu, D. Li, X. Jin, W. Qiu, Q. Xia, and B. Sun. “Dynamic cardiac MRI reconstruction using motion aligned locally low rank tensor (MALLRT)”. In: *Magnetic Resonance Imaging* 66 (2020), pp. 104–115.

[222] A. H. Ahmed, I. M. Qureshi, J. A. Shah, and M. Zaheer. “Motion correction based reconstruction method for compressively sampled cardiac MR imaging”. In: *Magnetic Resonance Imaging* 36 (2017), pp. 159–166.

[223] D. Abergel and A. G. Palmer III. “On the use of the stochastic Liouville equation in nuclear magnetic resonance: application to R1ρ relaxation in the presence of exchange”. In: *Concepts in Magnetic Resonance Part A: An Educational Journal* 19.2 (2003), pp. 134–148.

[224] S. G. Lingala, E. DiBella, and M. Jacob. “Deformation Corrected Compressed Sensing (DC-CS): A Novel Framework for Accelerated Dynamic MRI”. In: *IEEE Transactions on Medical Imaging* 34.1 (2015), pp. 72–85.

[225] S. Roujol, M. Foppa, S. Weingärtner, W. J. Manning, and R. Nezafat. “Adaptive registration of varying contrast-weighted images for improved tissue characterization (ARCTIC): Application to T1 mapping”. In: *Magnetic Resonance in Medicine* 73.4 (2014), pp. 1469–1482.

[226] H. Xue, S. Shah, A. Greiser, C. Guetter, A. Littmann, M.-P. Jolly, A. E. Arai, S. Zuehlsdorff, J. Guehring, and P. Kellman. “Motion correction for myocardial T1 mapping using image registration with synthetic image estimation”. In: *Magnetic Resonance in Medicine* 67.6 (2011), pp. 1644–1655.

[227] A. Bustin, G. Milotta, T. F. Ismail, R. Neji, R. M. Botnar, and C. Prieto. “Accelerated free-breathing whole-heart 3D T2 mapping with high isotropic resolution”. In: *Magnetic Resonance in Medicine* 83.3 (2019), pp. 988–1002.

[228] F. M. Serry, S. Ma, X. Mao, F. Han, Y. Xie, H. Han, D. Li, and A. G. Christodoulou. “Dual flip-angle IR-FLASH with spin history mapping for B1+ corrected T1 mapping: Application to T1 cardiovascular magnetic resonance multitasking”. In: *Magnetic Resonance in Medicine* 86.6 (2021), pp. 3182–3191.

[229] K. Chow, Y. Yang, P. Shaw, C. M. Kramer, and M. Salerno. “Robust free-breathing SASHA T1 mapping with high-contrast image registration”. In: *Journal of Cardiovascular Magnetic Resonance* 18.1 (2016).

[230] J. L. Shaw, Q. Yang, Z. Zhou, Z. Deng, C. Nguyen, D. Li, and A. G. Christodoulou. “Free-breathing, non-ECG, continuous myocardial T1 mapping with cardiovascular magnetic resonance multitasking”. In: *Magnetic Resonance in Medicine* 81.4 (2018), pp. 2450–2463.

[231] C. Kolbitsch, R. Bastkowski, T. Schäffter, C. Prieto Vasquez, K. Weiss, D. Maintz, and D. Giese. “Respiratory motion corrected 4D flow using golden radial phase encoding”. In: *Magnetic Resonance in Medicine* 83.2 (2019), pp. 635–644.

[232] G. Cruz, D. Atkinson, M. Henningsson, R. M. Botnar, and C. Prieto. “Highly efficient nonrigid motion-corrected 3D whole-heart coronary vessel wall imaging”. In: *Magnetic Resonance in Medicine* 77.5 (2016), pp. 1894–1908.

[233] J. Pang, Y. Chen, Z. Fan, C. Nguyen, Q. Yang, Y. Xie, and D. Li. “High efficiency coronary MR angiography with nonrigid cardiac motion correction”. In: *Magnetic Resonance in Medicine* 76.5 (2016), pp. 1345–1353.

[234] T. Correia, G. Cruz, T. Schneider, R. M. Botnar, and C. Prieto. “Technical note: Accelerated nonrigid motion-compensated isotropic 3D coronary MR angiography”. In: *Medical Physics* 45.1 (2017), pp. 214–222.

[235] Y. Chen, W.-C. Lo, J. I. Hamilton, K. Barkauskas, H. Saybasili, K. L. Wright, J. Batesole, M. A. Griswold, V. Gulani, and N. Seiberlich. “Single breath-hold 3D cardiac T1 mapping using through-time spiral GRAPPA”. In: *NMR in Biomedicine* 31.6 (2018).

[236] G. Nordio, A. Bustin, M. Henningsson, I. Rashid, A. Chiribiri, T. Ismail, F. Odille, C. Prieto, and R. M. Botnar. “3D SASHA myocardial T1 mapping with high accuracy and improved precision”. In: *Magnetic Resonance Materials in Physics, Biology and Medicine* 32.2 (2018), pp. 281–289.

[237] R. Guo, Z. Chen, Y. Wang, D. A. Herzka, J. Luo, and H. Ding. “Three-dimensional free breathing whole heart cardiovascular magnetic resonance T1 mapping at 3 T”. In: *Journal of Cardiovascular Magnetic Resonance* 20.1 (2018).

[238] S. Kozerke, M. B. Scheidegger, E. M. Pedersen, and P. Boesiger. “Heart motion adapted cine phase-contrast flow measurements through the aortic valve”. In: *Magnetic Resonance in Medicine* 42.5 (1999), pp. 970–978.

[239] S. Kozerke, J. Schwitter, E. M. Pedersen, and P. Boesiger. “Aortic and mitral regurgitation: Quantification using moving slice velocity mapping”. In: *Journal of Magnetic Resonance Imaging* 14.2 (2001), pp. 106–112.

[240] T. Küstner, A. Bustin, O. Jaubert, R. Hajhosseiny, P. G. Masci, R. Neji, R. Botnar, and C. Prieto. “Isotropic 3D Cartesian single breath-hold CINE MRI with multi-bin patch-based low-rank reconstruction”. In: *Magnetic Resonance in Medicine* 84.4 (2020), pp. 2018–2033.

[241] J. Wetzl, M. Schmidt, F. Pontana, B. Longère, F. Lugauer, A. Maier, J. Hornegger, and C. Forman. “Single-breath-hold 3-D CINE imaging of the left ventricle using Cartesian sampling”. In: *Magnetic Resonance Materials in Physics, Biology and Medicine* 31.1 (2017), pp. 19–31.

[242] X. Feng, S. S. Blemker, J. Inouye, C. M. Pelland, L. Zhao, and C. H. Meyer. “Assessment of velopharyngeal function with dual-planar high-resolution real-time spiral dynamic MRI”. In: *Magnetic Resonance in Medicine* 80.4 (2018), pp. 1467–1474.

[243] C.-Y. Liu, T. A. Bley, O. Wieben, J. H. Brittain, and S. B. Reeder. “Flow-independent T2-prepared inversion recovery black-blood MR imaging”. In: *Journal of Magnetic Resonance Imaging* 31.1 (2010), pp. 248–254.

[244] M. H. Moghari, A. Barthur, M. E. Amaral, T. Geva, and A. J. Powell. “Free-breathing whole-heart 3D cine magnetic resonance imaging with prospective respiratory motion compensation”. In: *Magnetic Resonance in Medicine* 80.1 (2017), pp. 181–189.

[245] P. Spincemaille, J. Liu, T. Nguyen, M. R. Prince, and Y. Wang. “Z intensity-weighted position self-respiratory gating method for free-breathing 3D cardiac CINE imaging”. In: *Magnetic Resonance Imaging* 29.6 (2011), pp. 861–868.

[246] S. Uribe, P. Beerbaum, T. S. Sørensen, A. Rasmusson, R. Razavi, and T. Schaeffter. “Four-dimensional (4D) flow of the whole heart and great vessels using real-time respiratory self-gating”. In: *Magnetic Resonance in Medicine* 62.4 (2009), pp. 984–992.

[247] O. Jaubert, G. Cruz, A. Bustin, T. Schneider, P. Koken, M. Doneva, D. Rueckert, R. Botnar, and C. Prieto. “Free-running cardiac magnetic resonance fingerprinting: Joint T1/T2 map and Cine imaging”. In: *Magnetic Resonance Imaging* 68 (2020), pp. 173–182.

[248] P. G. Batchelor, D. Atkinson, P. Irarrazaval, D. L. G. Hill, J. Hajnal, and D. Larkman. “Matrix description of general motion correction applied to multishot images”. In: *Magnetic Resonance in Medicine* 54.5 (2005), pp. 1273–1280.

[249] F. Odille, P.-A. Vuissoz, P.-Y. Marie, and J. Felblinger. “Generalized Reconstruction by Inversion of Coupled Systems (GRICS) applied to free-breathing MRI”. In: *Magnetic Resonance in Medicine* 60.1 (2008), pp. 146–157.

[250] D. Atkinson, D. L. G. Hill, P. N. R. Stoyle, P. E. Summers, and S. F. Keevil. “An autofocus algorithm for the automatic correction of motion artifacts in MR images”. In: *Information Processing in Medical Imaging*. Springer Berlin Heidelberg, 1997, pp. 341–354.

[251] A. G. Christodoulou, J. L. Shaw, C. Nguyen, Q. Yang, Y. Xie, N. Wang, and D. Li. “Magnetic resonance multitasking for motion-resolved quantitative cardiovascular imaging”. In: *Nature biomedical engineering* 2.4 (2018), pp. 215–226.

[252] F. Ong, X. Zhu, J. Y. Cheng, K. M. Johnson, P. E. Z. Larson, S. S. Vasanawala, and M. Lustig. “Extreme MRI: Large-scale volumetric dynamic imaging from continuous non-gated acquisitions”. In: *Magnetic Resonance in Medicine* 84.4 (2020), pp. 1763–1780.

[253] C. Unterberg-Buchwald, M. Fasshauer, J. M. Sohns, W. Staab, A. Schuster, D. Voit, J. T. Kowallick, M. Steinmetz, J. Frahm, and J. Lotz. “Real time cardiac MRI and its clinical usefulness in arrhythmias and wall motion abnormalities”. In: *Journal of Cardiovascular Magnetic Resonance* 16.S1 (2014).

[254] B. D. Allen, M. L. Carr, M. Markl, M. O. Zenge, M. Schmidt, M. S. Nadar, B. Spottiswoode, J. D. Collins, and J. C. Carr. “Accelerated real-time cardiac MRI using iterative sparse SENSE reconstruction: comparing performance in patients with sinus rhythm and atrial fibrillation”. In: *European Radiology* 28.7 (2018), pp. 3088–3096.

[255] E. C. Bassett, E. G. Kholmovski, B. D. Wilson, E. V. R. DiBella, D. J. Dosdall, R. Ranjan, C. J. McGann, and D. Kim. “Evaluation of highly accelerated real-time cardiac cine MRI in tachycardia”. In: *NMR in Biomedicine* 27.2 (2013), pp. 175–182.

[256] H. Haji-Valizadeh, A. A. Rahsepar, J. D. Collins, E. Bassett, T. Isakova, T. Block, G. Adluru, E. V. R. DiBella, D. C. Lee, J. C. Carr, and D. Kim. “Validation of highly accelerated real-time cardiac cine MRI with radial k-space sampling and compressed sensing in patients at 1.5T and 3T”. In: *Magnetic Resonance in Medicine* 79.5 (2017), pp. 2745–2751.

[257] D. Voit, S. Zhang, C. Unterberg-Buchwald, J. M. Sohns, J. Lotz, and J. Frahm. “Real-time cardiovascular magnetic resonance at 1.5 T using balanced SSFP and 40 ms resolution”. In: *Journal of Cardiovascular Magnetic Resonance* 15.1 (2013).

[258] H. Körperich, J. Gieseke, P. Barth, R. Hoogeveen, H. Esdorn, A. Peterschröder, H. Meyer, and P. Beerbaum. “Flow Volume and Shunt Quantification in Pediatric Congenital Heart Disease by Real-Time Magnetic Resonance Velocity Mapping: A Validation Study”. In: *Circulation* 109.16 (2004), pp. 1987–1993.

[259] J. T. Kowallick, A. A. Joseph, C. Unterberg-Buchwald, M. Fasshauer, K. van Wijk, K. D. Merboldt, D. Voit, J. Frahm, J. Lotz, and J. M. Sohns. “Real-time phase-contrast flow MRI of the ascending aorta and superior vena cava as a function of intrathoracic pressure (Valsalva manoeuvre)”. In: *The British Journal of Radiology* 87.1042 (2014), p. 20140401.

[260] L. Feng, M. B. Srichai, R. P. Lim, A. Harrison, W. King, G. Adluru, E. V. R. Dibella, D. K. Sodickson, R. Otazo, and D. Kim. “Highly accelerated real-time cardiac cine MRI using k–t SPARSE-SENSE”. In: *Magnetic Resonance in Medicine* 70.1 (2012), pp. 64–74.

[261] S. Kozerke, J. Tsao, R. Razavi, and P. Boesiger. “Accelerating cardiac cine 3D imaging using k-t BLAST”. In: *Magnetic Resonance in Medicine* 52.1 (2004), pp. 19–26.

[262] H. Jung, J. Park, J. Yoo, and J. C. Ye. “Radial k-t FOCUSS for high-resolution cardiac cine MRI”. In: *Magnetic Resonance in Medicine* 63.1 (2009), pp. 68–78.

[263] R. Otazo, E. Candès, and D. K. Sodickson. “Low-rank plus sparse matrix decomposition for accelerated dynamic MRI with separation of background and dynamic components: L+S Reconstruction”. In: *Magnetic Resonance in Medicine* 73.3 (2014), pp. 1125–1136.

[264] J. Frahm, A. Haase, and D. Matthaei. “Rapid NMR imaging of dynamic processes using the FLASII technique”. In: *Magnetic Resonance in Medicine* 3.2 (1986), pp. 321–327.

[265] A. Bornstedt, E. Nagel, S. Schalla, B. Schnackenburg, C. Klein, and E. Fleck. “Multi-slice dynamic imaging: Complete functional cardiac MR examination within 15 seconds”. In: *Journal of Magnetic Resonance Imaging* 14.3 (2001), pp. 300–305.

[266] Y.-C. Kim, M. I. Proctor, S. S. Narayanan, and K. S. Nayak. “Improved imaging of lingual articulation using real-time multislice MRI”. In: *Journal of Magnetic Resonance Imaging* 35.4 (2011), pp. 943–948.

[267] K. S. Nayak, J. M. Pauly, D. G. Nishimura, and B. S. Hu. “Rapid ventricular assessment using real-time interactive multislice MRI”. In: *Magnetic Resonance in Medicine* 45.3 (2001), pp. 371–375.

[268] R. Ahmad, H. Xue, S. Giri, Y. Ding, J. Craft, and O. P. Simonetti. “Variable density incoherent spatiotemporal acquisition (VISTA) for highly accelerated cardiac MRI”. In: *Magnetic Resonance in Medicine* 74.5 (2014), pp. 1266–1278.

[269] G. Adluru, L. Chen, S.-E. Kim, N. Burgon, E. G. Kholmovski, N. F. Marrouche, and E. V. DiBella. “Three-dimensional late gadolinium enhancement imaging of the left atrium with a hybrid radial acquisition and compressed sensing”. In: *Journal of Magnetic Resonance Imaging* 34.6 (2011), pp. 1465–1471.

[270] H. Haji-Valizadeh, L. Feng, L. E. Ma, D. Shen, K. T. Block, J. D. Robinson, M. Markl, C. K. Rigsby, and D. Kim. “Highly accelerated, real-time phase-contrast MRI using radial k-space sampling and GROG-GRASP reconstruction: a feasibility study in pediatric patients with congenital heart disease”. In: *NMR in Biomedicine* 33.5 (2020).

[271] M. Krämer, K.-H. Herrmann, J. Biermann, and J. R. Reichenbach. “Retrospective reconstruction of cardiac cine images from golden-ratio radial MRI using one-dimensional navigators”. In: *Journal of Magnetic Resonance Imaging* 40.2 (2013), pp. 413–422.

[272] Y. Y. Li, S. Rashid, Y. J. Cheng, W. Schapiro, K. Gliganic, A.-M. Yamashita, J. Tang, M. Grgas, M. Mendez, E. Haag, J. Pang, B. Stoeckel, C. Leidecker, and J. J. Cao. “Real-time cardiac MRI with radial acquisition and k-space variant reduced-FOV reconstruction”. In: *Magnetic Resonance Imaging* 53 (2018), pp. 98–104.

[273] C. M. Rank, T. Heußer, M. T. A. Buzan, A. Wetscherek, M. T. Freitag, J. Dinkel, and M. Kachelrieß. “4D respiratory motion-compensated image reconstruction of free-breathing radial MR data with very high undersampling”. In: *Magnetic Resonance in Medicine* 77.3 (2016), pp. 1170–1183.

[274] S. Rosenzweig, N. Scholand, H. C. M. Holme, and M. Uecker. “Cardiac and Respiratory Self-Gating in Radial MRI Using an Adapted Singular Spectrum Analysis (SSA-FARY)”. In: *IEEE Transactions on Medical Imaging* 39.10 (2020), pp. 3029–3041.

[275] C. Wang, J. Jang, U. Neisius, M. Nezafat, A. Fahmy, J. Kang, J. Rodriguez, B. Goddu, P. Pierce, S. Berg, *et al.* “Black blood myocardial T 2 mapping”. In: *Magnetic resonance in medicine* 81.1 (2019), pp. 153–166.

[276] X. Wang, S. Rosenzweig, N. Scholand, H. C. M. Holme, and M. Uecker. “Model-based reconstruction for simultaneous multi-slice T1 mapping using single-shot inversion-recovery radial FLASH”. In: *Magnetic Resonance in Medicine* 85.3 (2020), pp. 1258–1271.

[277] T. Shin, M. Lustig, D. G. Nishimura, and B. S. Hu. “Rapid single-breath-hold 3D late gadolinium enhancement cardiac MRI using a stack-of-spirals acquisition”. In: *Journal of Magnetic Resonance Imaging* 40.6 (2013), pp. 1496–1502.

[278] Y. Yang, C. H. Meyer, F. H. Epstein, C. M. Kramer, and M. Salerno. “Whole-heart spiral simultaneous multi-slice first-pass myocardial perfusion imaging”. In: *Magnetic Resonance in Medicine* 81.2 (2018), pp. 852–862.

[279] H. Qi, A. Bustin, G. Cruz, O. Jaubert, H. Chen, R. M. Botnar, and C. Prieto. “Free-running simultaneous myocardial T1/T2 mapping and cine imaging with 3D whole-heart coverage and isotropic spatial resolution”. In: *Magnetic Resonance Imaging* 63 (2019), pp. 159–169.

[280] C. Prieto, M. Doneva, M. Usman, M. Henningsson, G. Greil, T. Schaeffter, and R. M. Botnar. “Highly efficient respiratory motion compensated free-breathing coronary mra using golden-step Cartesian acquisition”. In: *Journal of Magnetic Resonance Imaging* 41.3 (2014), pp. 738–746.

[281] Y. Zhu, Y. Guo, S. G. Lingala, R. M. Lebel, M. Law, and K. S. Nayak. “GOCART: GOlden-angle CArtesian randomized time-resolved 3D MRI”. In: *Magnetic Resonance Imaging* 34.7 (2016), pp. 940–950.

[282] T. Kustner, C. Wurslin, S. Gatidis, P. Martirosian, K. Nikolaou, N. Schwenzer, F. Schick, B. Yang, and H. Schmidt. “MR Image Reconstruction Using a Combination of Compressed Sensing and Partial Fourier Acquisition: ESPReSSo”. In: *IEEE Transactions on Medical Imaging* 35.11 (2016), pp. 2447–2458.

[283] T. Küstner, M. Schwartz, P. Martirosian, S. Gatidis, F. Seith, C. Gilliam, T. Blu, H. Fayad, D. Visvikis, F. Schick, B. Yang, H. Schmidt, and N. Schwenzer. “MR-based respiratory and cardiac motion correction for PET imaging”. In: *Medical Image Analysis* 42 (2017), pp. 129–144.

[284] R. Grimm, S. Fürst, M. Souvatzoglou, C. Forman, J. Hutter, I. Dregely, S. I. Ziegler, B. Kiefer, J. Hornegger, K. T. Block, and S. G. Nekolla. “Self-gated MRI motion modeling for respiratory motion compensation in integrated PET/MRI”. In: *Medical Image Analysis* 19.1 (2015), pp. 110–120.

[285] J. Park, A. C. Larson, Q. Zhang, O. Simonetti, and D. Li. “4D radial coronary artery imaging within a single breath-hold: Cine angiography with phase-sensitive fat suppression (CAPS)”. In: *Magnetic Resonance in Medicine* 54.4 (2005), pp. 833–840.

[286] D. R. Thedens, P. Irarrazaval, T. S. Sachs, C. H. Meyer, and D. G. Nishimura. “Fast magnetic resonance coronary angiography with a three-dimensional stack of spirals trajectory”. In: *Magnetic Resonance in Medicine* 41.6 (1999), pp. 1170–1179.

[287] S. Winkelmann, T. Schaeffter, T. Koehler, H. Eggers, and O. Doessel. “An Optimal Radial Profile Order Based on the Golden Ratio for Time-Resolved MRI”. In: *IEEE Transactions on Medical Imaging* 26.1 (2007), pp. 68–76.

[288] S. Wundrak, J. Paul, J. Ulrici, E. Hell, M.-A. Geibel, P. Bernhardt, W. Rottbauer, and V. Rasche. “Golden ratio sparse MRI using tiny golden angles”. In: *Magnetic Resonance in Medicine* 75.6 (2015), pp. 2372–2378.

[289] S. Ravishankar and Y. Bresler. “MR Image Reconstruction From Highly Undersampled k-Space Data by Dictionary Learning”. In: *IEEE Transactions on Medical Imaging* 30.5 (2011), pp. 1028–1041.

[290] M. Uecker, P. Lai, M. J. Murphy, P. Virtue, M. Elad, J. M. Pauly, S. S. Vasanawala, and M. Lustig. “ESPIRiT—an eigenvalue approach to autocalibrating parallel MRI: Where SENSE meets GRAPPA”. In: *Magnetic Resonance in Medicine* 71.3 (2013), pp. 990–1001.

[291] M. Lustig and J. M. Pauly. “SPIRiT: Iterative self-consistent parallel imaging reconstruction from arbitrary k-space”. In: *Magnetic Resonance in Medicine* 64.2 (2010), pp. 457–471.

[292] A. Bustin, G. Lima da Cruz, O. Jaubert, K. Lopez, R. M. Botnar, and C. Prieto. “High-dimensionality undersampled patch-based reconstruction (HD-PROST) for accelerated multi-contrast MRI”. In: *Magnetic Resonance in Medicine* 81.6 (2019), pp. 3705–3719.

[293] W. Chen. “Artifacts correction for T1rho imaging with constant amplitude spin-lock”. In: *Journal of Magnetic Resonance* 274 (2017), pp. 13–23.

[294] J. P. Haldar. “Low-Rank Modeling of Local k-Space Neighborhoods (LORAKS) for Constrained MRI”. In: *IEEE Transactions on Medical Imaging* 33.3 (2014), pp. 668–681.

[295] S. G. Lingala, Y. Hu, E. DiBella, and M. Jacob. “Accelerated Dynamic MRI Exploiting Sparsity and Low-Rank Structure: k-t SLR”. In: *IEEE Transactions on Medical Imaging* 30.5 (2011), pp. 1042–1054.

[296] X. Miao, S. G. Lingala, Y. Guo, T. Jao, M. Usman, C. Prieto, and K. S. Nayak. “Accelerated cardiac cine MRI using locally low rank and finite difference constraints”. In: *Magnetic Resonance Imaging* 34.6 (2016), pp. 707–714.

[297] S. Moeller, S. Weingartner, and M. Akcakaya. “Multi-scale locally low-rank noise reduction for high-resolution dynamic quantitative cardiac MRI”. In: *2017 39th Annual International Conference of the IEEE Engineering in Medicine and Biology Society (EMBC)*. IEEE, 2017.

[298] U. Nakarmi, Y. Wang, J. Lyu, D. Liang, and L. Ying. “A Kernel-Based Low-Rank (KLR) Model for Low-Dimensional Manifold Recovery in Highly Accelerated Dynamic MRI”. In: *IEEE Transactions on Medical Imaging* 36.11 (2017), pp. 2297–2307.

[299] S. F. Roohi, D. Zonoobi, A. A. Kassim, and J. L. Jaremko. “Multi-dimensional low rank plus sparse decomposition for reconstruction of under-sampled dynamic MRI”. In: *Pattern Recognition* 63 (2017), pp. 667–679.

[300] B. Tremoulheac, N. Dikaios, D. Atkinson, and S. R. Arridge. “Dynamic MR Image Reconstruction–Separation From Undersampled (k, t)-Space via Low-Rank Plus Sparse Prior”. In: *IEEE Transactions on Medical Imaging* 33.8 (2014), pp. 1689–1701.

[301] H. Yoon, K. S. Kim, D. Kim, Y. Bresler, and J. C. Ye. “Motion Adaptive Patch-Based Low-Rank Approach for Compressed Sensing Cardiac Cine MRI”. In: *IEEE Transactions on Medical Imaging* 33.11 (2014), pp. 2069–2085.

[302] Y. Zhu, Y. Liu, L. Ying, X. Peng, Y.-X. J. Wang, J. Yuan, X. Liu, and D. Liang. “SCOPE: signal compensation for low-rank plus sparse matrix decomposition for fast parameter mapping”. In: *Physics in Medicine & Biology* 63.18 (2018), p. 185009.

[303] J. I. Hamilton, Y. Jiang, D. Ma, Y. Chen, W.-C. Lo, M. Griswold, and N. Seiberlich. “Simultaneous multislice cardiac magnetic resonance fingerprinting using low rank reconstruction”. In: *NMR in Biomedicine* 32.2 (2018).

[304] G. Lima da Cruz, A. Bustin, O. Jaubert, T. Schneider, R. M. Botnar, and C. Prieto. “Sparsity and locally low rank regularization for MR fingerprinting”. In: *Magnetic Resonance in Medicine* 81.6 (2019), pp. 3530–3543.

[305] K. M. Becker, J. Schulz-Menger, T. Schaeffter, and C. Kolbitsch. “Simultaneous high-resolution cardiac T1 mapping and cine imaging using model-based iterative image reconstruction”. In: *Magnetic Resonance in Medicine* 81.2 (2018), pp. 1080–1091.

[306] T. Correia, T. Schneider, and A. Chiribiri. “Model-Based Reconstruction for Highly Accelerated First-Pass Perfusion Cardiac MRI”. In: *Medical Image Computing and Computer Assisted Intervention – MICCAI 2019*. Springer International Publishing, 2019, pp. 514–522.

[307] F. Odille, S. Uribe, P. G. Batchelor, C. Prieto, T. Schaeffter, and D. Atkinson. “Model-based reconstruction for cardiac cine MRI without ECG or breath holding”. In: *Magnetic Resonance in Medicine* 63.5 (2010), pp. 1247–1257.

[308] J. Velikina and A. Samsonov. “Reconstruction of dynamic image series from undersampled MRI data using data-driven model consistency condition (MOCCO)”. In: *Magnetic Resonance in Medicine* 74.5 (2014), pp. 1279–1290.

[309] R. J. Kim, E. Wu, A. Rafael, E.-L. Chen, M. A. Parker, O. Simonetti, F. J. Klocke, R. O. Bonow, and R. M. Judd. “The Use of Contrast-Enhanced Magnetic Resonance Imaging to Identify Reversible Myocardial Dysfunction”. In: *New England Journal of Medicine* 343.20 (2000). PMID: 11078769, pp. 1445–1453.

[310] H. W. Kim, A. Farzaneh-Far, and R. J. Kim. “Cardiovascular Magnetic Resonance in Patients With Myocardial Infarction. Current and Emerging Applications”. In: *Journal of the American College of Cardiology* 55 (1 2009), pp. 1–16.

[311] P. Rajiah, M. Y. Desai, D. Kwon, and S. D. Flamm. “MR imaging of myocardial infarction”. In: *Radiographics* 33 (5 2013), pp. 1383–1412.

[312] H. Abdel-Aty, A. Zagrosek, J. Schulz-Menger, A. J. Taylor, D. Messroghli, A. Kumar, M. Gross, R. Dietz, and M. G. Friedrich. “Delayed Enhancement and T2-Weighted Cardiovascular Magnetic Resonance Imaging Differentiate Acute From Chronic Myocardial Infarction”. In: *Circulation* 109.20 (2004), pp. 2411–2416.

[313] T. F. Ismail, W. Strugnell, C. Coletti, M. Božić-Iven, S. Weingärtner, K. Hammernik, T. Correia, and T. Küstner. “Cardiac MR: From Theory to Practice”. In: *Frontiers in Cardiovascular Medicine* 0 (2022), p. 137.

[314] E. Dall’Armellina, S. K. Piechnik, V. M. Ferreira, Q. L. Si, M. D. Robson, J. M. Francis, F. Cuculi, R. K. Kharbanda, A. P. Banning, R. P. Choudhury, T. D. Karamitsos, and S. Neubauer. “Cardiovascular magnetic resonance by non contrast T1-mapping allows assessment of severity of injury in acute myocardial infarction”. In: *Journal of Cardiovascular Magnetic Resonance* 14 (1 2012), pp. 1–13.

[315] D. Carrick, C. Haig, S. Rauhalammi, N. Ahmed, I. Mordi, M. McEntegart, M. C. Petrie, H. Eteiba, S. Hood, S. Watkins, M. Lindsay, A. Mahrous, I. Ford, N. Tzemos, N. Sattar, P. Welsh, A. Radjenovic, K. G. Oldroyd, and C. Berry. “Prognostic significance of infarct core pathology revealed by quantitative non-contrast in comparison with contrast cardiac magnetic resonance imaging in reperfused ST-elevation myocardial infarction survivors”. In: *European Heart Journal* 37 (13 2016), pp. 1044–1059.

[316] S. Nakamori, J. Alakbarli, S. Bellm, S. R. Motiwala, G. Addae, W. J. Manning, and R. Nezafat. “Native T1 value in the remote myocardium is independently associated with left ventricular dysfunction in patients with prior myocardial infarction”. In: *Journal of Magnetic Resonance Imaging* 46 (4 2017), pp. 1073–1081.

[317] M. Ugander, P. S. Bagi, A. J. Oki, B. Chen, L. Y. Hsu, A. H. Aletras, S. Shah, A. Greiser, P. Kellman, and A. E. Arai. “Myocardial Edema as Detected by Pre-Contrast T1 and T2 CMR Delineates Area at Risk Associated With Acute Myocardial Infarction”. In: *JACC: Cardiovascular Imaging* 5 (6 2012), pp. 596–603.

[318] R. H. Stoffers, M. Madden, M. Shahid, F. Contijoch, J. Solomon, J. J. Pilla, J. H. Gorman, R. C. Gorman, and W. R. Witschey. “Assessment of myocardial injury after reperfused infarction by T1rho cardiovascular magnetic resonance”. In: *Journal of Cardiovascular Magnetic Resonance* 19 (1 2017), pp. 1–10.

[319] E. Aherne, K. Chow, and J. Carr. “Cardiac T1 mapping: Techniques and applications”. In: *Journal of Magnetic Resonance Imaging* 51.5 (2020), pp. 1336–1356.

[320] A. F. Martino and R. Damadian. “Improved discrimination of normal and malignant tissue using 1H NMR relaxation time measurements at 2.18 MHz.” In: *Physiological Chemistry and Physics and Medical NMR* 16 (1 1984), pp. 49–55.

[321] R. E. Sepponen, J. A. Pohjonen, J. T. Sipponen, and J. I. Tanttu. “A method for T1 rho imaging”. In: *Journal of computer assisted tomography* 9 (6 1985), pp. 1007–1011.

[322] R. Muthupillai, S. D. Flamm, J. M. Wilson, R. I. Pettigrew, and W. T. Dixon. “Acute myocardial infarction: Tissue characterization with T1 ρ-weighted MR imaging - Initial experience”. In: *Radiology* 232 (2 2004), pp. 606–610.

[323] S. Huber, R. Muthupillai, B. Lambert, M. Pereyra, A. Napoli, and S. D. Flamm. “Tissue characterization of myocardial infarction using T1ρ: Influence of contrast dose and time of imaging after contrast administration”. In: *Journal of Magnetic Resonance Imaging* 24 (5 2006), pp. 1040–1046.

[324] W. R. Witschey, J. J. Pilla, G. Ferrari, K. Koomalsingh, M. Haris, R. Hinmon, G. Zsido, J. H. Gorman, R. C. Gorman, and R. Reddy. “Rotating frame spin lattice relaxation in a swine model of chronic, left ventricular myocardial infarction”. In: *Magnetic Resonance in Medicine* 64 (5 2010), pp. 1453–1460.

[325] H. S. N. Musthafa, G. Dragneva, L. Lottonen, M. Merentie, L. Petrov, T. Heikura, E. Ylä-Herttuala, S. Ylä-Herttuala, O. Gröhn, and T. Liimatainen. “Longitudinal rotating frame relaxation time measurements in infarcted mouse myocardium in vivo”. In: *Magnetic Resonance in Medicine* 69 (5 2013), pp. 1389–1395.

[326] M. Gram, D. Gensler, P. Winter, M. Seethaler, P. A. Arias-Loza, J. Oberberger, P. M. Jakob, and P. Nordbeck. “Fast myocardial T 1ρ mapping in mice using k-space weighted image contrast and a Bloch simulation-optimized radial sampling pattern”. In: *Magnetic Resonance Materials in Physics, Biology and Medicine* 35 (2 2022), pp. 325–340.

[327] M. Gram, D. Gensler, P. Albertova, F. T. Gutjahr, K. Lau, P. A. Arias-Loza, P. M. Jakob, and P. Nordbeck. “Quantification correction for free-breathing myocardial T1ρ mapping in mice using a recursively derived description of a T1ρ* relaxation pathway”. In: *Journal of Cardiovascular Magnetic Resonance* 24 (1 2022), pp. 1–16.

[328] Y. Zhang, W. Zeng, W. Chen, Y. Chen, T. Zhu, J. Sun, Z. Liang, W. Cheng, L. Wang, B. Wu, L. Gong, V. A. Ferrari, J. Zheng, and F. Gao. “MR extracellular volume mapping and non-contrast T1ρ mapping allow early detection of myocardial fibrosis in diabetic monkeys”. In: *European Radiology* 29 (6 2019), pp. 3006–3016.

[329] J. W. van Oorschot, H. E. Aidi, S. J. J. of Lorkeers, J. M. Gho, M. Froeling, F. Visser, S. A. Chamuleau, P. A. Doevendans, P. R. Luijten, T. Leiner, and J. J. Zwanenburg. “Endogenous assessment of chronic myocardial infarction with T(1rho)-mapping in patients”. In: *Journal of cardiovascular magnetic resonance : official journal of the Society for Cardiovascular Magnetic Resonance* 16 (1 2014), p. 104.

[330] S. Berisha, J. Han, M. Shahid, Y. Han, and W. R. Witschey. “Measurement of Myocardial T1ρ with a Motion Corrected, Parametric Mapping Sequence in Humans”. In: *PLOS ONE* 11 (3 2016), e0151144.

[331] J. W. Van Oorschot, F. Visser, A. L. Eikendal, E.-j. P. Vonken, P. R. Luijten, S. A. Chamuleau, T. Leiner, and J. J. Zwanenburg. “Single breath-hold T1*ρ*-mapping of the heart for endogenous assessment of myocardial fibrosis”. In: *Investigative Radiology* 51.8 (2016), pp. 505–512.

[332] H. Qi, A. Bustin, T. Kuestner, R. Hajhosseiny, G. Cruz, K. Kunze, R. Neji, R. M. Botnar, and C. Prieto. “Respiratory motion-compensated high-resolution 3D whole-heart T1ρ mapping”. In: *Journal of Cardiovascular Magnetic Resonance* 22 (1 2020), pp. 1–13.

[333] E. W. Thompson, S. K. Iyer, M. P. Solomon, Z. Li, Q. Zhang, S. Piechnik, K. Werys, S. Swago, B. F. Moon, Z. B. Rodgers, A. Hall, R. Kumar, N. Reza, J. Kim, A. Jamil, B. Desjardins, H. Litt, A. Owens, W. R. Witschey, and Y. Han. “Endogenous T1ρ cardiovascular magnetic resonance in hypertrophic cardiomyopathy”. In: *Journal of Cardiovascular Magnetic Resonance* 23 (1 2021), pp. 1–9.

[334] C. Wang, J. Zheng, J. Sun, Y. Wang, R. Xia, Q. Yin, W. Chen, Z. Xu, J. Liao, B. Zhang, and F. Gao. “Endogenous contrast T1rho cardiac magnetic resonance for myocardial fibrosis in hypertrophic cardiomyopathy patients”. In: *Journal of Cardiology* 66 (6 2015), pp. 520–526.

[335] L. Wang, J. Yuan, S. J. Zhang, M. Gao, Y. C. Wang, Y. X. Wang, and S. Ju. “Myocardial T1rho mapping of patients with end-stage renal disease and its comparison with T1 mapping and T2 mapping: A feasibility and reproducibility study”. In: *Journal of Magnetic Resonance Imaging* 44 (3 2016), pp. 723–731.

[336] K. Wang, W. Zhang, S. Li, H. Jin, Y. Jin, L. Wang, R. Li, Y. Yang, J. Zheng, and J. Cheng. “Noncontrast $T1_\rho$ dispersion imaging is sensitive to diffuse fibrosis: A cardiovascular magnetic resonance study at 3T in hypertrophic cardiomyopathy”. In: *Magnetic Resonance Imaging* 91 (2022), pp. 1–8.

[337] W. R. Witschey, A. Borthakur, M. A. Elliott, E. Mellon, S. Niyogi, D. J. Wallman, C. Wang, and R. Reddy. “Artifacts in T1rho-weighted imaging: Compensation for B1 and B0 field imperfections”. In: *Journal of Magnetic Resonance* 186 (1 2007), pp. 75–85.

[338] Q. Han, Y. Han, R. C. Gorman, and W. R. Witschey. “The influence of static and RF field heterogeneity on T1rho cardiovascular MRI”. In: *Journal of Cardiovascular Magnetic Resonance 2014 16:1* 16 (1 2014), pp. 1–3.

[339] S. R. Charagundla, A. Borthakur, J. S. Leigh, and R. Reddy. “Artifacts in $T1_\rho$-weighted imaging: correction with a self-compensating spin-locking pulse”. In: *Journal of Magnetic Resonance* 162 (1 2003), pp. 113–121.

[340] M. Garwood and L. Delabarre. “The Return of the Frequency Sweep: Designing Adiabatic Pulses for Contemporary NMR”. In: *Journal of Magnetic Resonance* 153 (2001), pp. 155–177.

[341] R. Nezafat, M. Stuber, R. Ouwerkerk, A. M. Gharib, M. Y. Desai, and R. I. Pettigrew. “B1-insensitive T2 preparation for improved coronary magnetic resonance angiography at 3 T”. In: *Magnetic Resonance in Medicine* 55 (4 2006), pp. 858–864.

[342] D. J. Sorce, S. Michaeli, and M. Garwood. “Relaxation During Adiabatic Radiofrequency Pulses”. In: *Current Analytical Chemistry* 3 (3 2007), pp. 239–251.

[343] S. Michaeli, D. J. Sorce, and M. Garwood. “T2rho and T1rho Adiabatic Relaxations and Contrasts”. In: *Current Analytical Chemistry* 4 (1 2008), pp. 8–25.

[344] S. Jerban, Y. Ma, A. Kasibhatla, M. Wu, N. Szeverenyi, M. Guma, D. Covey, D. D'lima, S. R. Ward, R. L. Sah, E. Y. Chang, J. Du, and C. B. Chung. "Ultrashort echo time adiabatic T1ρ (UTE-Adiab-T1ρ) is sensitive to human cadaveric knee joint deformation induced by mechanical loading and unloading". In: *Magnetic Resonance Imaging* 80 (2021), pp. 98–105.

[345] T. Okuaki, Y. Takayama, A. Nishie, T. Ogino, M. Obara, H. Honda, T. Miyati, and M. Van Cauteren. "T1*ρ* mapping improvement using stretched-type adiabatic locking pulses for assessment of human liver function at 3 T". In: *Magnetic Resonance Imaging* 40 (2017), pp. 17–23.

[346] S. Weingärtner, N. M. Meßner, F. G. Zöllner, M. Akçakaya, and L. R. Schad. "Black-blood native T 1 mapping: Blood signal suppression for reduced partial voluming in the myocardium". In: *Magnetic resonance in medicine* 78.2 (2017), pp. 484–493.

[347] R. Noeske, F. Seifert, K.-H. Rhein, and H. Rinneberg. "Human cardiac imaging at 3 T using phased array coils". In: *Magnetic Resonance in Medicine* 44.6 (2000), pp. 978–982.

[348] M. Schär, E.-J. Vonken, and M. Stuber. "Simultaneous B0- and B1+-Map acquisition for fast localized shim, frequency, and RF power determination in the heart at 3 T". In: *Magnetic Resonance in Medicine* 63.2 (2010), pp. 419–426.

[349] M. Akçakaya, T. A. Basha, S. Weingärtner, S. Roujol, S. Berg, and R. Nezafat. "Improved quantitative myocardial T2 mapping: Impact of the fitting model". In: *Magnetic Resonance in Medicine* 74 (1 2015), pp. 93–105.

[350] R. J. Ogg, R. Kingsley, and J. S. Taylor. "WET, a T1-and B1-insensitive water-suppression method for in vivo localized 1H NMR spectroscopy". In: *Journal of Magnetic Resonance, Series B* 104.1 (1994), pp. 1–10.

[351] G. Captur, P. Gatehouse, K. E. Keenan, F. G. Heslinga, R. Bruehl, M. Prothmann, M. J. Graves, R. J. Eames, C. Torlasco, G. Benedetti, J. Donovan, B. Ittermann, R. Boubertakh, A. Bathgate, C. Royet, W. Pang, R. Nezafat, M. Salerno, P. Kellman, and J. C. Moon. "A medical device-grade T1 and ECV phantom for global T1 mapping quality assurance - the T1 Mapping and ECV Standardization in cardiovascular magnetic resonance (T1MES) program". In: *Journal of Cardiovascular Magnetic Resonance* 18 (1 2016), pp. 1–20.

[352] A. M. Sprinkart, J. A. Luetkens, F. Träber, J. Doerner, J. Gieseke, B. Schnackenburg, G. Schmitz, D. Thomas, R. Homsi, W. Block, *et al.* "Gradient Spin Echo (GraSE) imaging for fast myocardial T2 mapping". In: *Journal of Cardiovascular Magnetic Resonance* 17 (2015), pp. 1–9.

[353] S. Weingärtner, K. L. Desmond, N. A. Obuchowski, B. Baessler, Y. Zhang, E. Biondetti, D. Ma, X. Golay, M. A. Boss, J. L. Gunter, K. E. Keenan, and D. Hernando. “Development, validation, qualification, and dissemination of quantitative MR methods: Overview and recommendations by the ISMRM quantitative MR study group”. In: *Magnetic Resonance in Medicine* 87 (3 2022), pp. 1184–1206.

[354] F. Isensee, P. F. Jaeger, S. A. Kohl, J. Petersen, and K. H. Maier-Hein. “nnU-Net: a self-configuring method for deep learning-based biomedical image segmentation”. In: *Nature Methods 2020 18:2* 18 (2 2020), pp. 203–211.

[355] Y. Zhao, C. Yang, A. Schweidtmann, and Q. Tao. “Efficient Bayesian uncertainty estimation for nnU-Net”. In: *International Conference on Medical Image Computing and Computer Assisted Intervention* (2022).

[356] T. A. Treibel, M. Fontana, V. Maestrini, S. Castelletti, S. Rosmini, J. Simpson, A. Nasis, A. N. Bhuva, H. Bulluck, A. Abdel-Gadir, *et al.* “Automatic measurement of the myocardial interstitium: synthetic extracellular volume quantification without hematocrit sampling”. In: *JACC: Cardiovascular Imaging* 9.1 (2016), pp. 54–63.

[357] Q. Tao, P. van der Tol, F. F. Berendsen, E. H. Paiman, H. J. Lamb, and R. J. van der Geest. “Robust motion correction for myocardial T1 and extracellular volume mapping by principle component analysis-based groupwise image registration”. In: *Journal of Magnetic Resonance Imaging* 47.5 (2018), pp. 1397–1405.

[358] S. Weingärtner, N. M. Meßner, J. Budjan, D. Loßnitzer, U. Mattler, T. Papavassiliu, F. G. Zöllner, and L. R. Schad. “Myocardial T1-mapping at 3T using saturation-recovery: reference values, precision and comparison with MOLLI”. In: *Journal of Cardiovascular Magnetic Resonance* 18.1 (2016).

[359] N. Hänninen, J. Rautiainen, L. Rieppo, S. Saarakkala, and M. J. Nissi. “Orientation anisotropy of quantitative MRI relaxation parameters in ordered tissue”. In: *Scientific reports* 7.1 (2017), p. 9606.

[360] E. Aliotta, K. Moulin, P. Magrath, and D. B. Ennis. “Quantifying precision in cardiac diffusion tensor imaging with second-order motion-compensated convex optimized diffusion encoding”. In: *Magnetic Resonance in Medicine* 80 (3 2018), pp. 1074–1087.

[361] J. W. van Oorschot, F. Güçlü, S. de Jong, S. A. Chamuleau, P. R. Luijten, T. Leiner, and J. J. Zwanenburg. “Endogenous assessment of diffuse myocardial fibrosis in patients with $T1_\rho$-mapping”. In: *Journal of Magnetic Resonance Imaging* 45.1 (2017), pp. 132–138.

[362] I. Mordi, A. Radjenovic, T. Stanton, R. S. Gardner, A. McPhaden, D. Carrick, C. Berry, and N. Tzemos. “Prevalence and prognostic significance of lipomatous metaplasia in patients with prior myocardial infarction”. In: *JACC: Cardiovascular Imaging* 8.9 (2015), pp. 1111–1112.

[363] S. K. Iyer, B. Moon, E. Hwuang, Y. Han, M. Solomon, H. Litt, and W. R. Witschey. “Accelerated free-breathing 3D T1ρ cardiovascular magnetic resonance using multicoil compressed sensing”. In: *Journal of Cardiovascular Magnetic Resonance* 21 (1 2019), pp. 1–11.

[364] C. Velasco, G. Cruz, O. Jaubert, B. Lavin, R. M. Botnar, and C. Prieto. “Simultaneous comprehensive liver T1, T2, , T1ρ, and fat fraction characterization with MR fingerprinting”. In: *Magnetic Resonance in Medicine* 87 (4 2022), pp. 1980–1991.

[365] A. Bustin, X. Pineau, S. Sridi, R. B. van Heeswijk, P. Jaıs, M. Stuber, and H. Cochet. “Assessment of myocardial injuries in ischemic and non-ischemic cardiomyopathies using magnetic resonance T1-rho mapping”. In: *European Heart Journal-Cardiovascular Imaging* (2023), jead319.

[366] Z. Lyu, S. Hua, J. Xu, Y. Shen, R. Guo, P. Hu, and H. Qi. “Free-breathing simultaneous native myocardial T1, T2 and T1ρ mapping with Cartesian acquisition and dictionary matching”. In: *Journal of Cardiovascular Magnetic Resonance* 25.1 (2023), p. 63.

[367] C. Coletti, A. Fotaki, J. Tourais, Y. Zhao, C. van de Steeg-Henzen, M. Akçakaya, Q. Tao, C. Prieto, and S. Weingärtner. “Robust cardiac T 1 ρ mapping at 3T using adiabatic spin-lock preparations”. In: *Magnetic Resonance in Medicine* (2023).

[368] M. Henningsson, S. Malik, R. Botnar, D. Castellanos, T. Hussain, and T. Leiner. “Black-Blood Contrast in Cardiovascular MRI”. In: *Journal of Magnetic Resonance Imaging* 55 (1 2022), pp. 61–80.

[369] R. Francis, P. Kellman, T. Kotecha, A. Baggiano, K. Norrington, A. Martinez-Naharro, S. Nordin, D. S. Knight, R. D. Rakhit, T. Lockie, *et al.* “Prospective comparison of novel dark blood late gadolinium enhancement with conventional bright blood imaging for the detection of scar”. In: *Journal of Cardiovascular Magnetic Resonance* 19.1 (2017), pp. 1–12.

[370] C. Farrelly, W. Rehwald, M. Salerno, A. Davarpanah, A. N. Keeling, J. T. Jacobson, and J. C. Carr. “Improved detection of subendocardial hyperenhancement in myocardial infarction using dark blood – pool delayed enhancement MRI”. In: *American Journal of Roentgenology* 196.2 (2011), pp. 339–348.

[371] S. A. Peel, G. Morton, A. Chiribiri, A. Schuster, E. Nagel, and R. M. Botnar. “Dual inversion-recovery MR imaging sequence for reduced blood signal on late gadolinium-enhanced images of myocardial scar”. In: *Radiology* 264.1 (2012), pp. 242–249.

[372] R. J. Holtackers, A. Chiribiri, T. Schneider, D. M. Higgins, and R. M. Botnar. “Dark-blood late gadolinium enhancement without additional magnetization preparation”. In: *Journal of Cardiovascular Magnetic Resonance* 19.1 (2017), pp. 1–10.

[373] R. J. Holtackers, C. M. V. D. Heyning, M. S. Nazir, I. Rashid, I. Ntalas, H. Rahman, R. M. Botnar, and A. Chiribiri. “Clinical value of dark-blood late gadolinium enhancement cardiovascular magnetic resonance without additional magnetization preparation”. In: *Journal of Cardiovascular Magnetic Resonance* 21 (1 2019), pp. 1–11.

[374] P. Kellman, H. Xue, L. J. Olivieri, R. R. Cross, E. K. Grant, M. Fontana, M. Ugander, J. C. Moon, and M. S. Hansen. “Dark blood late enhancement imaging”. In: *Journal of Cardiovascular Magnetic Resonance* 18 (2017), pp. 1–11.

[375] T. A. Basha, M. C. Tang, C. Tsao, C. M. Tschabrunn, E. Anter, W. J. Manning, and R. Nezafat. “Improved dark blood late gadolinium enhancement (DB-LGE) imaging using an optimized joint inversion preparation and T2 magnetization preparation”. In: *Magnetic Resonance in Medicine* 79.1 (2018), pp. 351–360.

[376] A. S. Fahmy, U. Neisius, C. W. Tsao, S. Berg, E. Goddu, P. Pierce, T. A. Basha, L. Ngo, W. J. Manning, and R. Nezafat. “Gray blood late gadolinium enhancement cardiovascular magnetic resonance for improved detection of myocardial scar”. In: *Journal of Cardiovascular Magnetic Resonance* 20.1 (2018), pp. 1–11.

[377] G. Muscogiuri, W. G. Rehwald, U. J. Schoepf, P. Suranyi, S. E. Litwin, C. N. D. Cecco, J. L. Wichmann, S. Mangold, D. Caruso, S. R. Fuller, R. R. Bayer, and A. Varga-Szemes. “T(Rho) and magnetization transfer and INvErsion recovery (TRAMINER)-prepared imaging: A novel contrast-enhanced flow-independent dark-blood technique for the evaluation of myocardial late gadolinium enhancement in patients with myocardial infarction”. In: *Journal of Magnetic Resonance Imaging* 45 (5 2017), pp. 1429–1437.

[378] H. W. Kim, W. G. Rehwald, E. R. Jenista, D. C. Wendell, P. Filev, L. van Assche, C. J. Jensen, M. A. Parker, E.-l. Chen, A. L. C. Crowley, *et al.* “Dark-blood delayed enhancement cardiac magnetic resonance of myocardial infarction”. In: *JACC: Cardiovascular Imaging* 11.12 (2018), pp. 1758–1769.

[379] S. Sridi, M. Nuñez-Garcia, M. Sermesant, A. Maillot, D. E. Hamrani, J. Magat, J. Naulin, F. Laurent, M. Montaudon, P. Jaïs, M. Stuber, H. Cochet, and A. Bustin. “Improved myocardial scar visualization with fast free-breathing motion-compensated black-blood T1-rho-prepared late gadolinium enhancement MRI”. In: *Diagnostic and Interventional Imaging* 103.12 (2022), pp. 607–617.

[380] T. He, P. D. Gatehouse, P. Kirk, M. A. Tanner, G. C. Smith, J. Keegan, R. H. Mohiaddin, D. J. Pennell, and D. N. Firmin. “Black-blood T2* technique for myocardial iron measurement in thalassemia”. In: *Journal of Magnetic Resonance Imaging: An Official Journal of the International Society for Magnetic Resonance in Medicine* 25.6 (2007), pp. 1205–1209.

[381] G. C. Smith, J. P. Carpenter, T. He, M. H. Alam, D. N. Firmin, and D. J. Pennell. “Value of black blood T2* cardiovascular magnetic resonance”. In: *Journal of Cardiovascular Magnetic Resonance* 13.1 (2011), pp. 1–6.

[382] C. Liguori, I. Di Giampietro, F. Pitocco, A. E. De Vivo, E. Schena, L. Mortato, F. Pirro, P. Cianciulli, and B. B. Zobel. “Dark blood versus bright blood T2* acquisition in cardiovascular magnetic resonance (CMR) for thalassaemia major (TM) patients: Evaluation of feasibility, reproducibility and image quality”. In: *European Journal of Radiology* 83.1 (2014), e8–e14.

[383] B. Baeßler, F. Schaarschmidt, C. Stehning, B. Schnackenburg, D. Maintz, and A. C. Bunck. “Cardiac T2-mapping using a fast gradient echo spin echo sequence-first in vitro and in vivo experience”. In: *Journal of Cardiovascular Magnetic Resonance* 17.1 (2015), pp. 1–8.

[384] B. Baeßler, F. Schaarschmidt, C. Stehning, B. Schnackenburg, A. Giolda, D. Maintz, and A. C. Bunck. “Reproducibility of three different cardiac T2-mapping sequences at 1.5 T”. In: *Journal of Magnetic Resonance Imaging* 44.5 (2016), pp. 1168–1178.

[385] P. Kellman and M. S. Hansen. “T1-mapping in the heart: Accuracy and precision”. In: *Journal of Cardiovascular Magnetic Resonance* 16.1 (2014).

[386] G. J. Stanisz, E. E. Odrobina, J. Pun, M. Escaravage, S. J. Graham, M. J. Bronskill, and R. M. Henkelman. “T1, T2 relaxation and magnetization transfer in tissue at 3T”. In: *Magnetic Resonance in Medicine: An Official Journal of the International Society for Magnetic Resonance in Medicine* 54.3 (2005), pp. 507–512.

[387] F. von Knobelsdorff-Brenkenhoff, M. Prothmann, M. A. Dieringer, R. Wassmuth, A. Greiser, C. Schwenke, T. Niendorf, and J. Schulz-Menger. “Myocardial T 1 and T 2 mapping at 3 T: reference values,

influencing factors and implications". In: *Journal of Cardiovascular Magnetic Resonance* 15 (2013), pp. 1–11.

[388] C. Hu, S. Huber, V. Nguyen, L. Baldassarre, H. Mojibian, and D. Peters. "Fat-saturated dark-blood cardiac T2 mapping in a single breath-hold". In: *Magnetic Resonance Imaging* 81 (2021), pp. 24–32.

[389] A. J. Wheaton, A. Borthakur, M. T. Corbo, G. Moonis, E. Melhem, and R. Reddy. "T2ρ-weighted contrast in MR images of the human brain". In: *Magnetic Resonance in Medicine: An Official Journal of the International Society for Magnetic Resonance in Medicine* 52.6 (2004), pp. 1223–1227.

[390] I. Nestrasil, S. Michaeli, T. Liimatainen, C. Rydeen, C. M. Kotz, J. Nixon, T. Hanson, and P. J. Tuite. "T 1ρ and T 2ρ MRI in the evaluation of Parkinson's disease". In: *Journal of neurology* 257 (2010), pp. 964–968.

[391] M. Gram, T. Williams, P. Albertova, P. Jakob, B. Gerull, W. Bauer, P. Nordbeck, and M. Christa. "T1rho and T2rho based myocardial tissue characterisation in small animals at high-field MRI". In: *European Heart Journal* 44.Supplement_2 (2023), ehad655–163.

[392] M. Banjar, S. Horiuchi, D. N. Gedeon, and H. Yoshioka. "Review of quantitative knee articular cartilage MR imaging". In: *Magnetic Resonance in Medical Sciences* 21.1 (2022), pp. 29–40.

[393] K. Emanuel, L. Kellner, M. J. Peters, M. J. Haartmans, M. T. Hooijmans, and P. J. Emans. "The relation between the biochemical composition of knee articular cartilage and quantitative MRI: a systematic review and meta-analysis". In: *Osteoarthritis and Cartilage* 30.5 (2022), pp. 650–662.

[394] G. Cao, S. Gao, and B. Xiong. "Application of quantitative T1, T2 and T2* mapping magnetic resonance imaging in cartilage degeneration of the shoulder joint". In: *Scientific Reports* 13.1 (2023), p. 4558.

[395] A. G. Palmer and F. Massi. "Characterization of the dynamics of biomacromolecules using rotating-frame spin relaxation NMR spectroscopy". In: *Chemical reviews* 106.5 (2006), pp. 1700–1719.

[396] Y. Wang, A. E. Wluka, F. M. Cicuttini, G. Jones, and C. Ding. *Use magnetic resonance imaging to assess articular cartilage*. 2012.

[397] Y. Han, T. Liimatainen, R. C. Gorman, and W. R. Witschey. "Assessing Myocardial Disease Using T1$_\rho$ MRI". In: *Current Cardiovascular Imaging Reports* 7 (2 2014), pp. 1–9.

[398] M. Boudreau, K. E. Keenan, and N. Stikov. "Quantitative T1 and T1ρ Mapping". In: 1 (2020), pp. 19–45.

[399] J. Rautiainen, M. J. Nissi, T. Liimatainen, W. Herzog, R. K. Korhonen, and M. T. Nieminen. “Adiabatic rotating frame relaxation of MRI reveals early cartilage degeneration in a rabbit model of anterior cruciate ligament transection”. In: *Osteoarthritis and Cartilage* 22.10 (2014).

[400] Y.-X. J. Wáng, Q. Zhang, X. Li, W. Chen, A. Ahuja, and J. Yuan. “T1ρ magnetic resonance: basic physics principles and applications in knee and intervertebral disc imaging”. In: *Quantitative imaging in medicine and surgery* 5.6 (2015), p. 858.

[401] T. Liimatainen, D. J. Sorce, R. O’Connell, M. Garwood, and S. Michaeli. “MRI contrast from relaxation along a fictitious field (RAFF)”. In: *Magnetic Resonance in Medicine* 64 (4 2010), pp. 983–994.

[402] T. Liimatainen, S. Mangia, W. Ling, J. Ellermann, D. J. Sorce, M. Garwood, and S. Michaeli. “Relaxation dispersion in MRI induced by fictitious magnetic fields”. In: *Journal of magnetic resonance* 209.2 (2011), pp. 269–276.

[403] J. Rautiainen, M. J. Nissi, E. N. Salo, V. Tiitu, M. A. Finnilä, O. M. Aho, S. Saarakkala, P. Lehenkari, J. Ellermann, and M. T. Nieminen. “Multiparametric MRI assessment of human articular cartilage degeneration: Correlation with quantitative histology and mechanical properties”. In: *Magnetic Resonance in Medicine* 74.1 (2015).

[404] E. Yla-Herttuala, S. Laidinen, H. Laakso, and T. Liimatainen. “Quantification of myocardial infarct area based on T RAFFn relaxation time maps-comparison with cardiovascular magnetic resonance late gadolinium enhancement, T 1ρ and T 2 in vivo”. In: *Journal of Cardiovascular Magnetic Resonance* 20 (2018), pp. 1–10.

[405] H. Hakkarainen, A. Sierra, S. Mangia, M. Garwood, S. Michaeli, O. Gröhn, and T. Liimatainen. “MRI relaxation in the presence of fictitious fields correlates with myelin content in normal rat brain”. In: *Magnetic resonance in medicine* 75.1 (2016), pp. 161–168.

[406] C. P. Johnson, L. Wang, F. Tóth, O. Aruwajoye, C. S. Carlson, H. K. Kim, and J. M. Ellermann. “Quantitative MRI helps to detect hip ischemia: preclinical model of Legg-Calve-Perthes disease”. In: *Radiology* 289.2 (2018), pp. 386–395.

[407] S. A. Mirmojarabian, E. Lammentausta, E. Liukkonen, L. Ahvenjärvi, J. Junttila, M. T. Nieminen, and T. Liimatainen. “Myocardium Assessment by Relaxation along Fictitious Field, Extracellular Volume, Feature Tracking, and Myocardial Strain in Hypertensive Patients with Left Ventricular Hypertrophy”. In: *International Journal of Biomedical Imaging* 2022 (2022).

[408] J. Tourais, T. Ploem, T. A. van Zadelhoff, C. van de Steeg-Henzen, E. H. Oei, and S. Weingärtner. “Rapid Whole-Knee Quantification of Cartilage using T_1, T_2^*, and T_{RAFF2} mapping with Magnetic Resonance Fingerprinting”. In: *IEEE Transactions on Biomedical Engineering* (2023).

[409] P. Filip, A. Svatkova, A. F. Carpenter, L. E. Eberly, I. Nestrasil, M. J. Nissi, S. Michaeli, and S. Mangia. “Rotating frame MRI relaxations as markers of diffuse white matter abnormalities in multiple sclerosis”. In: *NeuroImage: Clinical* 26 (2020), p. 102234.

[410] T. Liimatainen, H. Hakkarainen, S. Mangia, J. M. Huttunen, C. Storino, D. Idiyatullin, D. Sorce, M. Garwood, and S. Michaeli. “MRI contrasts in high rank rotating frames”. In: *Magnetic Resonance in Medicine* 73.1 (2015).

[411] G. Van Rossum, F. L. Drake, C. R. Harris, K. J. Millman, S. J. van der Walt, R. Gommers, P. Virtanen, D. Cournapeau, E. Wieser, J. Taylor, S. Berg, N. J. Smith, R. Kern, M. Picus, S. Hoyer, M. H. van Kerkwijk, M. Brett, A. Haldane, J. F. Del Río, M. Wiebe, P. Peterson, P. Gérard-Marchant, K. Sheppard, T. Reddy, W. Weckesser, H. Abbasi, C. Gohlke, and T. E. Oliphant. *Python 3 Reference Manual*. Vol. 585. 7825. 2009.

[412] J. Kim, Q. Peng, C. Wu, and X. Li. “MR T1ρ preparations: B1 and B0 inhomogeneity response on 3T and 7T systems”. In: *Poreceedings of the International Society of Magnetic Resonance in Medicine (ISMRM) 2021*. ISMRM. 2021.

[413] N. E. Hänninen, T. Liimatainen, M. Hanni, O. Gröhn, M. T. Nieminen, and M. J. Nissi. “Relaxation anisotropy of quantitative MRI parameters in biological tissues”. In: *Scientific Reports* 12.1 (2022), p. 12155.

[414] J. Ellermann, W. Ling, M. J. Nissi, E. Arendt, C. S. Carlson, M. Garwood, S. Michaeli, and S. Mangia. “MRI rotating frame relaxation measurements for articular cartilage assessment”. In: *Magnetic Resonance Imaging* 31.9 (2013).

[415] L. Wang, M. J. Nissi, F. Tóth, J. Shaver, C. P. Johnson, J. Zhang, M. Garwood, C. S. Carlson, and J. M. Ellermann. “Multiparametric MRI of epiphyseal cartilage necrosis (osteochondrosis) with histological validation in a goat model”. In: *PloS one* 10.10 (2015), e0140400.

[416] N. T. Roberts, L. A. Hinshaw, T. J. Colgan, T. Ii, D. Hernando, and S. B. Reeder. “B0 and B1 inhomogeneities in the liver at 1.5 T and 3.0 T”. In: *Magnetic resonance in medicine* 85.4 (2021), pp. 2212–2220.

[417] C. A. Azlan, P. Di Giovanni, T. S. Ahearn, S. I. Semple, F. J. Gilbert, and T. W. Redpath. “B1 transmission-field inhomogeneity and enhancement ratio errors in dynamic contrast-enhanced MRI (DCE-MRI) of the breast at 3T”. In: *Journal of Magnetic Resonance Imaging* 31.1 (2010), pp. 234–239.

[418] S. Weingärtner, F. Zimmer, G. J. Metzger, K. Uğurbil, P.-F. Van de Moortele, and M. Akçakaya. “Motion-robust cardiac mapping at 3T using interleaved Bloch-Siegert shifts”. In: *Magnetic resonance in medicine* 78.2 (2017), pp. 670–677.

[419] C. Coletti, C. Van De Steeg-Henzen, and S. Weingärtner. “Adiabatic T2ρ Mapping in the Human Myocardium at 3T”. In: *Journal of Cardiovascular Magnetic Resonance* 26 (2024).

[420] M. Goldman. “Formal theory of spin-lattice relaxation”. In: *Journal of Magnetic Resonance* 149.2 (2001), pp. 160–187.

[421] A. Singh, D. Reddy, M. Haris, K. Cai, K. Rajender Reddy, H. Hariharan, and R. Reddy. “T1ρ MRI of healthy and fibrotic human livers at 1.5 T”. In: *Journal of Translational Medicine* 13 (2015), pp. 1–7.

[422] S. Xie, Q. Li, Y. Cheng, Y. Zhang, Z. Zhuo, G. Zhao, and W. Shen. “Impact of liver fibrosis and fatty liver on T1rho measurements: a prospective study”. In: *Korean Journal of Radiology* 18.6 (2017), pp. 898–905.

[423] A. Sharafi, D. Xia, G. Chang, and R. R. Regatte. “Biexponential T1ρ relaxation mapping of human knee cartilage in vivo at 3 T”. In: *NMR in Biomedicine* 30.10 (2017), e3760.

[424] S. V. Akella, R. Reddy Regatte, A. J. Gougoutas, A. Borthakur, E. M. Shapiro, J. B. Kneeland, J. S. Leigh, and R. Reddy. “Proteoglycan-induced changes in T1ρ-relaxation of articular cartilage at 4T”. In: *Magnetic Resonance in Medicine: An Official Journal of the International Society for Magnetic Resonance in Medicine* 46.3 (2001), pp. 419–423.

[425] A. J. Wheaton, G. R. Dodge, A. Borthakur, J. B. Kneeland, H. R. Schumacher, and R. Reddy. “Detection of changes in articular cartilage proteoglycan by T1ρ magnetic resonance imaging”. In: *Journal of Orthopaedic Research* 23.1 (2005), pp. 102–108.

[426] B. S. Kester, P. M. Carpenter, J. Y. Hon, T. Nozaki, Y. Kaneko, H. Yoshioka, and R. Schwarzkopf. “T1ρ/T2 mapping and histopathology of degenerative cartilage in advanced knee osteoarthritis”. In: *World journal of orthopedics* 8.4 (2017), p. 350.

[427] L. N. Heckelman, W. A. Smith, A. D. Riofrio, E. N. Vinson, A. T. Collins, O. R. Gwynn, G. M. Utturkar, A. P. Goode, C. E. Spritzer, and L. E. DeFrate. “Quantifying the biochemical state of knee cartilage in response to running using T1rho magnetic resonance imaging”. In: *Scientific reports* 10.1 (2020), p. 1870.

[428] A. Borthakur, M. Sochor, C. Davatzikos, J. Q. Trojanowski, and C. M. Clark. “T1ρ MRI of Alzheimer’s disease”. In: *Neuroimage* 41.4 (2008), pp. 1199–1205.

[429] M. Haris, A. Singh, K. Cai, C. Davatzikos, J. Q. Trojanowski, E. R. Melhem, C. M. Clark, and A. Borthakur. “T1rho (T 1ρ) MR imaging in Alzheimer’disease and Parkinson’s disease with and without dementia”. In: *Journal of neurology* 258 (2011), pp. 380–385.

[430] L. Wang, X. Wang, F. Jiang, Y. Cao, S. Liu, H. Chen, J. Yang, X. Zhang, T. Yu, H. Xu, *et al.* “Adding quantitative T1rho-weighted imaging to conventional MRI improves specificity and sensitivity for differentiating malignant from benign breast lesions”. In: *Magnetic Resonance Imaging* (2024).

[431] U. Duvvuri, H. Poptani, M. Feldman, L. Nadal-Desbarats, M. S. Gee, W. M. Lee, R. Reddy, J. S. Leigh, and J. D. Glickson. “Quantitative T1ρ magnetic resonance imaging of RIF-1 tumors in vivo: detection of early response to cyclophosphamide therapy”. In: *Cancer research* 61.21 (2001), pp. 7747–7753.

[432] J. Villanueva-Meyer, R. Barajas Jr, M. Mabray, W. Chen, A. Shankaranarayanan, P. Koon, I. Barani, T. Tihan, and S. Cha. “Differentiation of brain tumor-related edema based on 3D T1rho imaging”. In: *European journal of radiology* 91 (2017), pp. 88–92.

[433] Q. Ai, W. Chen, T. So, W. Lam, B. Jiang, D. Poon, S. Qamar, F. Mo, T. Blu, Q. Chan, *et al.* “Quantitative T1ρ MRI of the head and neck discriminates carcinoma and benign hyperplasia in the nasopharynx”. In: *American Journal of Neuroradiology* 41.12 (2020), pp. 2339–2344.

[434] M. T. Cashmore, A. J. McCann, S. J. Wastling, C. McGrath, J. Thornton, and M. G. Hall. *Clinical quantitative MRI and the need for metrology*. 2021.

[435] R. B. Souza, D. Kumar, N. Calixto, J. Singh, J. Schooler, K. Subburaj, X. Li, T. M. Link, and S. Majumdar. “Response of knee cartilage T1rho and T2 relaxation times to in vivo mechanical loading in individuals with and without knee osteoarthritis”. In: *Osteoarthritis and cartilage* 22.10 (2014), pp. 1367–1376.

[436] R. Watts, T. Andrews, S. Hipko, J. V. Gonyea, and C. G. Filippi. “In vivo whole-brain T1-rho mapping across adulthood: Normative values and age dependence”. In: *J. Magn. Reson. Imag.* 40 (1999), pp. 376–382.

[437] M. Haris, S. K. Yadav, A. Rizwan, A. Singh, K. Cai, D. Kaura, E. Wang, C. Davatzikos, J. Q. Trojanowski, E. R. Melhem, F. M. Marincola, and A. Borthakur. “T1rho MRI and CSF biomarkers in diagnosis of Alzheimer’s disease”. In: *NeuroImage: Clinical* 7 (2015).

[438] Y. Lu, Q. Wang, T. Zhang, J. Li, H. Liu, D. Yao, L. Hou, B. Tu, and D. Wang. “Staging Liver Fibrosis: Comparison of Native T1 Mapping, T2 Mapping, and T1ρ: An Experimental Study in Rats With Bile Duct Ligation and Carbon Tetrachloride at 11. 7 T MRI”. In: *Journal of Magnetic Resonance Imaging* 55.2 (2022), pp. 507–517.

[439] Y. Takayama, A. Nishie, K. Ishimatsu, Y. Ushijima, N. Fujita, Y. Kubo, T. Yoshizumi, K.-i. Kouhashi, J. Maehara, Y. Akamine, *et al.* “Diagnostic potential of T1ρ and T2 relaxations in assessing the severity of liver fibrosis and necro-inflammation”. In: *Magnetic resonance imaging* 87 (2022), pp. 104–112.

[440] V. Casula, J. Autio, M. J. Nissi, E. J. Auerbach, J. Ellermann, E. Lammentausta, and M. T. Nieminen. “Validation and optimization of adiabatic T1ρ and T2ρ for quantitative imaging of articular cartilage at 3 T”. In: *Magnetic resonance in medicine* 77.3 (2017), pp. 1265–1275.

[441] J. Kowalewski and L. Maler. *Nuclear spin relaxation in liquids: theory, experiments, and applications*. CRC press, 2017.

[442] S. Ogawa and T. M. a. Lee. “Brain magnetic resonance imaging with contrast dependent on blood oxygenation”. In: *Proc. Nat. Acad. Sc* 87.24 (1990), pp. 9868–9872.

[443] R. S. Menon and S. G. Kim. “Spatial and temporal limits in cognitive neuroimaging with fMRI”. In: *Tr* 3.6 (1999), pp. 207–216.

[444] G. C. Scott and M. L. G. a. Joy. “Rotating Frame RF Current Density Imaging”. In: *Magn*. Reson. Med., 33, 1995, pp. 355–369.

[445] N. Petridou and D. a. Plenz. “Direct magnetic resonance detection of neuronal electrical activity”. In: *Proc. Nat. Acad. Sc* 103.43 (2006), pp. 16015–16020.

[446] R. H. Kraus and V. Jr. “P. et al”. In: *Toward direct neural current imaging by resonant mechanisms at ultra-low field* 39 (2008), pp. 310–317.

[447] R. Chu and J. A. a. de Zwart. “Hunting for neuronal currents: absence of rapid MRI signal changes during visual-evoked response”. In: *Neuroimage* 23.3 (2004), pp. 1059–1067.

[448] L. Tang and M. J. a. Avison. “Failure to direct detect magnetic field dephasing corresponding to ERP generation”. In: *Magn. Res* 24.4 (2008), pp. 484–489.

[449] Q. Luo and H. a. Lu. “Physiologically evoked neuronal current MRI in a bloodless turtle brain: detectable or not?” In: *NeuroImage* 47.4 (2009), pp. 1268–1276.

[450] N. Logothetis and J. a. Pauls. “Neurophysiological investigation of the basis of the fMRI signal”. In: *Nature* 412 (2001), pp. 150–157.

[451] T. Witzel, F. H. Lin, B. R. Rosen, and L. L. Wald. “Stimulus-induced Rotary Saturation (SIRS): a potential method for the detection of neuronal currents with MRI”. In: *NeuroImage* 42.4 (2008), pp. 1357–1365.

[452] N. W. Halpern-Manners, V. S. Bajaj, T. Z. Teisseyre, and A. Pines. “Magnetic resonance imaging of oscillating electrical currents”. In: *Proc. Nat. Acad. of Sc* 107.19 (2010), pp. 8519–8524.

[453] T. K. Truong, K. C. Roberts, M. G. Woldorff, and A. W. Song. “Toward direct MRI of neuro-electro-magnetic oscillations in the human brain”. In: *Magn*. Res. Med., 81(6), 2019, pp. 3462–3475.

[454] J. Bodurka and P. A. Bandettini. “Toward direct mapping of neuronal activity: MRI detection of ultraweak, transient magnetic field changes”. In: *Magn*. Reson. Med., 47, 2002, pp. 1052–1058.

[455] S. Domsch, J. Zapp, L. R. Schad, F. Nees, H. Hill, D. Hermann, K. Mann, and S. Vollst"adt-Klein. “Optimized protocol for high resolution functional magnetic resonance imaging at 3T using single-shot echo planar imaging”. In: *Journ. Neurosc. Meth* 239 (2015), pp. 170–182.

[456] K. J. Friston, A. P. Holmes, K. J. Worsley, J.-P. Poline, C. D. Frith, and R. S. J. Frackowiak. “Statistical parametric maps in functional imaging: A general linear approach”. In: *Human Brain Mapping* 2 (1994), pp. 189–210.

[457] B. Fischl, A. van der Kouwe, C. Destrieux, E. Halgren, F. Ségonne, D. H. Salat, E. Busa, L. J. Seidman, J. Goldstein, D. Kennedy, V. Caviness, N. Makris, B. Rosen, and A. M. Dale. “Automatically parcellating the human cerebral cortex”. In: *Cerebr. Cortex* 14.1 (2004), pp. 11–22.

[458] M. J. Graves. “3 T: the good, the bad and the ugly”. In: *The British Journal of Radiology* 95.1130 (2022), p. 20210708.

[459] M. Crabb, K. Kunze, C. Castillo-Passi, C. Munoz, C. Velasco, R. Neji, C. Prieto, and R. Botnar. “3D whole-heart joint T1/T1$_\rho$ mapping and water/fat imaging at low-field 0.55T scanner”. In: *ISMRM 2023*. 2023.

[460] B. Lena, C. Najac, L. Vaclavu, T. O’Reilly, and A. Webb. “$T_{1\rho}$ and magnetization transfer experiments on a point-of-care 46 mT MRI system”. In: *Poreceedings of the International Society of Magnetic Resonance in Medicine (ISMRM) 2023*. ISMRM. 2023, p. 0300.

[461] J. Yuan, Y. Li, F. Zhao, Q. Chan, A. T. Ahuja, and Y.-X. J. Wang. “Quantification of T1ρ relaxation by using rotary echo spin-lock pulses in the presence of B0 inhomogeneity”. In: *Physics in Medicine & Biology* 57.15 (2012), p. 5003.

[462] R. G. Menon, A. Sharafi, J. Windschuh, and R. R. Regatte. “Bi-exponential 3D-T1ρ mapping of whole brain at 3 T”. In: *Scientific reports* 8.1 (2018), p. 1176.

[463] G. E. Santyr, E. J. Fairbanks, F. Kelcz, and J. A. Sorenson. “Off-resonance spin locking for MR imaging”. In: *Magnetic resonance in medicine* 32.1 (1994), pp. 43–51.

[464] B. Jiang and W. Chen. “On-resonance and off-resonance continuous wave constant amplitude spin-lock and T1ρ quantification in the presence of B1 and B0 inhomogeneities”. In: *NMR in Biomedicine* 31.7 (2018), e3928.

[465] Y. Pang. “A self-compensated spin-locking scheme for quantitative R1ρ dispersion MR imaging in ordered tissues”. In: *Magnetic Resonance Imaging* 94 (2022), pp. 112–118.

[466] Y. Yang, C. Wang, Y. Liu, Z. Chen, X. Liu, H. Zheng, D. Liang, and Y. Zhu. “A robust adiabatic constant amplitude spin-lock preparation module for myocardial T1ρ quantification at 3 T”. In: *NMR in Biomedicine* 36.2 (2023), e4830.

[467] S. Pala, N. E. Hänninen, O. Nykänen, T. Liimatainen, and M. J. Nissi. “New methods for robust continuous wave T1ρ relaxation preparation”. In: *NMR in Biomedicine* 36.2 (2023), e4834.

[468] Y. Pang. “An adiabatic RF pulse in spin-lock preparations: A double-edged sword for quantitative R 1 ρ imaging in clinical applications”. In: *NMR in Biomedicine* 36.9 (2023), e4953.

[469] I. Jambor, A. Steiner, M. Pesola, T. Liimatainen, M. Sucksdorff, E. Rissanen, L. Airas, H. J. Aronen, and H. Merisaari. “Whole Brain Adiabatic T1rho and Relaxation Along a Fictitious Field Imaging in Healthy Volunteers and Patients With Multiple Sclerosis: Initial Findings”. In: *Journal of Magnetic Resonance Imaging* 54.3 (2021), pp. 866–879.

[470] Y. Ma, M. Carl, Q. Tang, D. Moazamian, J. S. Athertya, H. Jang, S. V. Bukata, C. B. Chung, E. Y. Chang, and J. Du. “Whole knee joint mapping using a phase modulated UTE adiabatic T1ρ (PM-UTE-AdiabT1ρ) sequence”. In: *Magnetic Resonance in Medicine* 91.3 (2024), pp. 896–910.

[471] J. Tourais, I. Hermann, R. Voncken, O. B. Demirel, S. Weingärtner, and M. Akcakaya. “2D High Resolution Myocardial TRAFF2 Mapping: Reproducibility and Accuracy”. In: *Poreceedings of the International Society of Magnetic Resonance in Medicine (ISMRM) 2021*. ISMRM. 2021.

[472] K. Chow, L. Pearce, C. Coletti, J. Flewitt, A. Howarth, C. Lydell, J. A. Whithe, and S. Weingärtner. “Multi-parametric T1, T2, and T1ρ mapping with mSASHA at 1.5T and 3T”. In: *Poreceedings of the Society for Cardiovascular Magnetic Resonance 26th Annual Scientific Session*. SCMR. 2023.

[473] L. Pearce, C. Coletti, J. Flewitt, J. Nong, R. Lam, A. Howarth, C. Lydell, J. A. Whithe, S. Weingärtner, and k. Chow. “Clinical evaluation of multiparametric with T1, T2, and T1rho with mSASHA at 3T”. In: *Poreceedings of the Society for Cardiovascular Magnetic Resonance 26th Annual Scientific Session*. SCMR. 2023.

[474] A. Tyler, K. Kunze, R. Neji, P. G. Masci, R. Razavi, A. Chiribiri, and S. Roujol. “Fast cardiac T 1ρ, adiab mapping using slice-selective adiabatic spin-lock preparation pulses”. In: *Magnetic resonance in medicine* (2024).

[475] A. G. Redfield. “On the theory of relaxation processes”. In: *IBM Journal of Research and Development* 1.1 (1957), pp. 19–31.

[476] J. Jacquinot and M. Goldman. “Nuclear spin-lattice relaxation in the rotating frame”. In: *Physical Review B* 8.5 (1973), p. 1944.

[477] A. Lamminen, J. I. Tanttu, R. Sepponen, H. Pihko, and O. A. Korhola. “T1ρ dispersion imaging of diseased muscle tissue”. In: *The British Journal of Radiology* 66.789 (1993), pp. 783–787.

[478] F. Adelnia, Z. Zu, J. T. Spear, F. Wang, K. D. Harkins, and J. C. Gore. “Tissue characterization using R1rho dispersion imaging at low locking fields”. In: *Magnetic Resonance Imaging* 84 (2021), pp. 1–11.

[479] J. G. Cobb, J. Xie, and J. C. Gore. “Contributions of chemical exchange to T1ρ dispersion in a tissue model”. In: *Magnetic resonance in medicine* 66.6 (2011), pp. 1563–1571.

[480] J. T. Spear and J. C. Gore. “New insights into rotating frame relaxation at high field”. In: *NMR in Biomedicine* 29.9 (2016), pp. 1258–1273.

[481] J. T. Spear, Z. Zu, and J. C. Gore. “Dispersion of relaxation rates in the rotating frame under the action of spin-locking pulses and diffusion in inhomogeneous magnetic fields”. In: *Magnetic resonance in medicine* 71.5 (2014), pp. 1906–1911.

[482] E. S. Kooreman, M. Tanaka, L. C. Ter Beek, F. P. Peters, C. A. Marijnen, U. A. van der Heide, and P. J. van Houdt. “T1ρ for radiotherapy treatment response monitoring in rectal cancer patients: a pilot study”. In: *Journal of Clinical Medicine* 11.7 (2022), p. 1998.

[483] C. Velasco, G. Cruz, B. Lavin, A. Hua, A. Fotaki, R. M. Botnar, and C. Prieto. “Simultaneous T1, T2, and T1ρ cardiac magnetic resonance fingerprinting for contrast agent–free myocardial tissue characterization”. In: *Magnetic Resonance in Medicine* 87 (4 2022), pp. 1992–2002.

[484] H. Qi, Z. Lv, J. Hu, J. Xu, R. Botnar, C. Prieto, and P. Hu. “Accelerated 3D free-breathing high-resolution myocardial T 1 *ρ* mapping at 3 Tesla”. In: *Magnetic Resonance in Medicine* 88.6 (2022), pp. 2520–2531.

[485] L. Di Sopra, D. Piccini, S. Coppo, M. Stuber, and J. Yerly. “An automated approach to fully self-gated free-running cardiac and respiratory motion-resolved 5D whole-heart MRI”. In: *Magnetic resonance in medicine* 82.6 (2019), pp. 2118–2132.

[486] P. T. Toi, H. J. Jang, K. Min, S.-P. Kim, S.-K. Lee, J. Lee, J. Kwag, and J.-Y. Park. “In vivo direct imaging of neuronal activity at high temporospatial resolution”. In: *Science* 378.6616 (2022), pp. 160–168.

[487] S.-H. Choi, G. H. Im, S. Choi, X. Yu, P. A. Bandettini, R. S. Menon, and S.-G. Kim. “No Replication of Direct Neuronal Activity-related (DIANA) fMRI in Anesthetized Mice”. In: *bioRxiv* (2023), pp. 2023–05.

[488] M. Capiglioni, C. Turco Federico nd Kiefer, and R. Wiest. “Analysis of spin-lock techniques for the non-invasive detection of neuronal currents with magnetic resonance”. In: *Poreceedings of the International Society of Magnetic Resonance in Medicine (ISMRM) 2022*. ISMRM. 2022.

[489] M. Capiglioni, F. Turco, R. Wiest, and C. Kiefer. “Analysis of the robustness and dynamics of spin-locking preparations for the detection of oscillatory magnetic fields”. In: *Scientific reports* 12.1 (2022), p. 16965.

[490] M. Gram, P. Albertova, V. Schirmer, M. Blaimer, M. Gamer, M. J. Herrmann, P. Nordbeck, and P. Jakob. “Towards robust in vivo quantification of oscillating biomagnetic fields using Rotary Excitation based MRI”. In: *Scientific Reports* 12.1 (2022), p. 15375.

[491] P. Albertova, M. Gram, M. Blaimer, W. R. Bauer, P. M. Jakob, and P. Nordbeck. “Rotary Excitation of peak-like magnetic field fluctuations: Towards non-invasive direct detection of cardiac conduction”. In: *arXiv preprint arXiv:2311.14416* (2023).

Acknowledgements

Exactly 10 years ago I was graduating from high school and my then Maths and Physics teacher, prof. Cialdella, vehemently insisted on the fact that I should have chosen Physics as my University major. At the time, however, I was lured into Biomedical Engineering by an Open Yale course on YouTube, "Frontiers of Biomedical Engineering", promising I would work on things such as shiny new robotics arms, artificial organs, or genetic expression control. Many years later, I can say that prof. Cialdella was probably right.

Luckily, time gave me a second opportunity to adjust my path and steer a bit closer to Physics again. For this, I have to thank first and foremost my supervisor and co-promotor, Sebastian. Thank you for taking a chance on a graduating Biomedical Engineering student with little to no knowledge about MR Physics, and guiding me to where I am today, proudly presenting the work in this dissertation. It was a pleasure working every day with someone who is incredibly passionate about scientific research and "advancing the edge of human knowledge". The most inspiring moments of this PhD were undoubtedly our long discussions/brainstorming sessions. In the first months, I think I could understand 5% of your reasoning. Now I can confidently say I get maybe a good 75% of your deductions, and this to me is a greater achievement than any paper or award. I also had the privilege of seeing MarsLab blossom from nothing into the vibrant lab that it is today. You put together and guided a group of people who strive to do cool meaningful science day after day, who will never submit a conference abstract more than a few minutes before the deadline, and, most importantly, who have fun doing it together.

I am also beyond grateful to my promotor, Frans. First, for forwarding my application for an already filled PhD position in his lab to Sebastian. Second, but definitely more importantly, for his unwavering support over the years, and for always having a kind encouraging word in the many difficult moments along this path. Your commitment to fostering a nurturing environment in the department is truly inspiring. The TU Delft students are lucky to have you as their teacher and mentor. I would also like to thank my former mentor from Politecnico di Milano, universally known as "*il Santa*", for his selfless dedication to forming great engineers that allowed me to have unique academic opportunities that made me the scientist I am. Thank you for teaching me that there is no one way to be an academic, that "this has never been done before" is not a good

excuse not to do something, and that "this has been done before" is not a good excuse not to try to do it radically better.

A most heartfelt thank you also goes to the MarsLab team. To Paulina and Maša, there was one moment when we all knew we would become so much more than colleagues. That first dinner together when, after some small talk, we all kind of paused for a second, looked at each other, and started sharing how we honestly all felt like big impostors, how we feared never amounting to anything (in pulse programming and) in PhD life. Well, look at us now, two - almost three - PhDs later (still desperately pulse programming, but occasionally from the cliffs of Bali). Thank you for helping me to keep some shred of sanity in the last years, or for laughing/crying with me in lack of it. To Joao, for accepting and tolerating our messy selves and the fact we would never learn to pronounce his name right. For all the help and guidance throughout the years, and for his immeasurable patience. MarsLab would have crumbled on day 2 without you. To Ayda, for being the kindest colleague and friend, and for always bringing emergency chocolate to long days at the scanner. We also shared a big part of this path; the next year will be tough for you but I am sure you will thrive and have a great professional future ahead (hopefully, with less unfair visa restrictions). To Martina, the newest addition to the lab. Thank you for bringing a much-needed breath of fresh air into the lab, while we struggled with the last months of our PhD, and for always being up for a drink. Berat and Niccolò, you are in for a great ride with these people. A big thank you to the students I supervised, Ties, Hülya, Roeland, Mark, and Maaike. With some of you, I spent several months, full of highs and lows. Thank you for trusting me through them. I learned a lot from each of you and I am very proud of what we achieved together. Last, but definitely not least, a deep thank you to Christal. Even though you are not part of the lab officially, it really feels like you should be. Thank you for your unparalleled support at HPTC over the years, and for making sure all of our experiments ran smoothly, even if that sometimes meant working extra hours and personally recruiting volunteers to make sure we had enough data for our deadlines.

Then, I want to thank everyone in the ImPhys department for contributing to a great research environment. To Angela, Henry, Annelies, and Ronald for making all of our lives so much easier. Not only MarsLab, but the whole department would crumble without your constant support. A special thanks to Angela for opening the doors of her house to our department when we needed a place to come together during covid and to Henry, for supporting all of my and my students' weird phantom-building efforts, as well as inspiring my next non-academic adventure. To Martijn and Chih-Hsien, for sharing a common MRI interest, but enriching it through new perspectives. To Yidong and Yi, for their incredible help in making sure our MRI datasets looked their best through state-of-the-art registration and segmentation techniques. To the "Beach people",

Djalma, Agis, Eszter (and Jazmine), Xiufeng, Rik, Victor, Moein, Fabian, Baptiste, Gabrielle, Eleonora, Hugues, Lorenzo, Dion, Liam, and Jack. Never was there a more inappropriate name for a WhatsApp group, considering we went to the beach once in four years (thanks Dutch weather), but the many beers, coffees, lunches, and dinners we shared were a crucial -and chaotic, when Agis was there- part of this PhD. To David, Qian, Guillaume, Rik, Miriam, Bernd, Martin, Sjoerd, thank your for your support over the years and the stimulating discussions.

I am very grateful for the MRI people that I was lucky enough to meet during my PhD. A heartfelt thank you goes to Claudia and René for being early supporters of my work and opening the doors of their welcoming lab when I needed to scan patients. Thank you to Anastasia, for all the help in London, for being an amazing and inspiring colleague, and a dear friend. To Alina, Carlos, and Carlos for being the best conference partners one could ask for. To Chiara, for being the most unexpected friend SMRA gave me. I am forever grateful for ending up in that particular dorm room in Santa Monica. To Teresa and Thomas, for all the laughs (and drinks) we shared after many conferences - and for recording the Korean BBQ song so we can forever keep it in our hearts. To Pierre, Gastao, Camila, Ludovica, Olivier, and Felicia for being enthusiastic fellow members of the Fiesta groups at every ISMRM.

Finally, I would like to thank my friends and family, who were there long before the start of this PhD and will hopefully continue to be the roots of my existence, no matter where science brings me. Sara and Anita, we share a bond that has grown and strengthened over all the stages of our lives. We have all taken different paths, but it is always nice to go back to the *condominio* (and sometimes, the *condominio* comes to you!). To the Cuppons, who have been my adoptive family for my university years in Milan and keep making my life much fuller, despite the distance. To Chiara, for sharing this crazy PhD ride with me from across the Channel, and for always finding time for me in any random city we are coincidentally both in. To Marta, for finally coming to an Alt-J concert with me, for joining many post-conference adventures, and for simply being the best Brunilde. To Bea, for being the wise friend everyone needs in their life. During these years our lives took very different ways, but anything can be shared during our hours-long calls or sofa chats in Affori. To Tommi, for always casually following me around the world (are you ready for the next move?), and literally there when you need him. To Fil, for being the friend I can laugh with, and share *sfighe* with, as if not a single day had passed since we sat next to each other for that first Polimi lecture. To Cic, for always coming to listen to every single one of my talks at ISMRM, despite not being at all interested in my side of MRI research. To Nico, who, despite now being a grown married man, never loses the silly side we all love him for. To Gian, for being probably the most invested friend in my post-doc choice, and for never losing his

acidello side. To Fra, for lending me the most epic quote "*Non interagisco ma capisco*". To Fello, for being the friend that just gets me, no matter the situation or the time we spent apart. To David, for saving me during covid through many hallway drinks.

To *la Zia con la Z maiuscola*, thank you for supporting me always, and spoiling me very often. You are a great source of inspiration and the coolest aunt one could ask for. To Bruno, for being the only person who could ever *sopportare la Zia*, so she can *supportare* us. To my sister Sere, who I love more than my cold heart often shows. Knowing that you are there and care for our family when I can't allows me to follow my dreams with some peace of mind. To my mum and dad, for giving me every opportunity to realize my dreams. I am sorry I will still not get a "real job" after this, but I hope you know I am doing what makes me happy.

Curriculum Vitae

CHIARA COLETTI

Education

2014 – 2017 Bachelor of Science in Biomedical Engineering
Politecnico di Milano
Milan, Italy

2017 – 2019 Master of Science in Biomedical Engineering
Politecnico di Milano
Milan, Italy

Thesis: ECCO: an electron counting implementation for image compression and optimization of Cryo-EM data management
Promotor: Dr. M. D. Santambrogio

2018 Erasmus+ International Exchange Program
KTH Royal Institute of Technology
Stockholm, Sweden

2017 – 2020 Alta Scuola Politecnica Honours Programme
Honorary Double Degree in Biomedical Engineering
Politecnico di Milano, Politecnico di Torino
Milan and Turin, Italy

2020 – 2024 Ph.D. in Applied Physics
Delft University of Technology
Delft, The Netherlands

Thesis: Radiofrequency Pulse Design for Robust Quantitative Spin-Lock MRI
Promotor: Dr. F. M. Vos
Co-promotor: Dr. S. D. Weingärtner

Experience

Jun-Dec 2019 Graduate Research Assistant
Computational Research Division
Lawrence Berkeley National Laboratory
Berkeley, California, USA

Feb-Sep 2024	Post-doctoral researcher in MRI Physics *Delft University of Technology* Delft, The Netherlands

Awards

2021 – 2024	3x ISMRM Educational Stipend
2023 – 2024	2x SCMR Travel Award
2022	ISMRM Magna cum Laude
2022	ISMRM Cardiac Study Group Best Abstract Award
2022	SMRA Travel Award
2017 – 2019	Alta Scuola Politecnica full Scholarship
2016	Best Freshman Award 2014/2015 Politecnico di Milano
2014	National Excellence Registry Scholarship Italian Ministry of Education, University and Research

Service

2023 – 2024	Ad-Hoc Reviewer *Journal of Cardiovascular Magnetic Resonance, European Hearth Journal, International Journal of Cardiology*
2023 – 2024	ISMRM Cardiac MR Study Group *Trainee Representative*
2021 – 2021	ISMRM Benelux Annual Meeting *Organizing Committee Member*

List of Publications

Journal Publications

1. **Chiara Coletti**, Joao Tourais, Anastasia Fotaki, Yidong Zhao, Yi Zhang, Christal van de Steeg-Henzen, Qian Tao, Claudia Prieto, Sebastian Weingärtner. "Dark-blood adiabatic $T_{1\rho}$ mapping of the heart using combined non-selective and slice-selective RF pulses at 3T". *Under review at Journal of Journal of Cardiovascular Magnetic Resonance*.

2. **Chiara Coletti**[†], Roeland Naaktgeboren[†], Joao Tourais, Christal van de Steeg-Henzen, Sebastian Weingärtner. "Generalized inhomogeneity-resilient relaxation along a fictitious field (girRAFF) for improved robustness in rotating frame relaxometry at 3T". *Magnetic Resonance in Medicine, (2024): pp. 1-19, doi: 10.1002/mrm.30219*.

3. Paulina Šiurytė, Joao Tourais, Yi Zhang, **Chiara Coletti**, Christal van de Steeg-Henzen, Stefano Mandija, Qian Tao, Markus Henningsson, Sebastian Weingärtner. "Preparation-based $B_1{}^+$ mapping in the heart using Bloch–Siegert shifts". *Magnetic Resonance in Medicine, (2024): pp. 1-11, doi: 10.1002/mrm.30232*.

4. **Chiara Coletti**, Anastasia Fotaki, Joao Tourais, Yidong Zhao, Christal van de Steeg-Henzen, Mehmet Akçakaya, Qian Tao, Claudia Prieto, Sebastian Weingärtner. "Robust cardiac $T_{1\rho}$ mapping at 3T using adiabatic spin-lock preparations". *Magnetic Resonance in Medicine, Vol. 90.4 (2023): pp. 1363-1379, doi: 10.1002/mrm.29713*.

5. Nasim Bakhshaee Babaroud, Merlin Palmar, Andrada Iulia Velea, **Chiara Coletti**, Sebastian Weingärtner, Frans Vos, Wouter A Serdijn, Sten Vollebregt, Vasiliki Giagka. "Multilayer CVD graphene electrodes using a transfer-free process for the next generation of optically transparent and MRI-compatible neural interfaces". *Nature Microsystems and Nanoengineering, Vol. 8.1 (2022): pp. 107-123, doi:10.1038/s41378-022-00430-x*.

6. Tevfik Ismail[†], Wendy Strugnell[†], Sebastian Weingärtner[†], **Chiara Coletti**[†], Maša Božić-Iven[†], Kerstin Hammernik[†], Teresa Correia[‡], Thomas Küstner[‡]. "Cardiac MR: From Theory to Practice". *Frontiers in Cardiovascular Medicine, Vol. 9 (2022): p.826283, doi: 10.3389/fcvm.2022.826283*.

[†]These authors contributed equally
[‡]These authors contributed equally

Conference Contributions

1. Maaike Smit†, **Chiara Coletti**†, Kathleen Allyson Harrison†, Sebastian Weingärtner. “Phantom evaluation of sensitivity and specificity of spin-lock MRI for oscillating current imaging”. *Accepted for oral presentation at the European Society for Magnetic Resonance in Medicine and Biology 40th Annual Scientific Meeting (2024)*.

2. **Chiara Coletti**†, Mark Vermeulen†, Sebastian Weingärtner. "Optimising dipole-dipole relaxation resilience to off-resonance Fields during adiabatic $T_{1\rho}$". *Proceedings of the 46th Annual International Conference of the IEEE Engineering in Medicine and Biology Society, (2024)*. Oral presentation.

3. **Chiara Coletti**, Joao Tourais, Christal van de Steeg-Henzen, Sebastian Weingärtner. "Adiabatic spin-lock preparations for myocardial $T_{2\rho}$ mapping at 3T". *Proceedings of the International Society of Magnetic Resonance in Medicine 32 (2024)*. Oral presentation.

4. **Chiara Coletti**, Christal van de Steeg-Henzen, Sebastian Weingärtner. "Adiabatic $T_{2\rho}$ mapping in the human myocardium at 3T". *Proceedings of the Cardiovascular Magnetic Resonance Conference (2024), doi: 10.1016/j.jocmr.2024.100223*. Oral presentation.

5. **Chiara Coletti**, Maša Božić-Iven, Joao Tourais, Christal van de Steeg-Henzen, Mehmet Akçakaya, Sebastian Weingärtner. "Suppressing blood signal in myocardial $T_{1\rho}$ mapping at 3T through novel dark-blood adiabatic spin-lock preparations". *Proceedings of the International Society of Magnetic Resonance in Medicine 31 (2023), doi: 10.58530/2023/1367*. Power Pitch.

6. Roeland Naaktgeboren†, **Chiara Coletti**†, Christal van de Steeg-Henzen, Sebastian Weingärtner. "Off-resonance and $B_1{}^+$ Resilience of Relaxation Along a Fictitious Field (RAFF) pulses". *Proceedings of the International Society of Magnetic Resonance in Medicine 31 (2023), doi: 10.58530/2023/2386*. Poster presentation.

7. Merijn Berendsen, Maša Bozic-Iven, Joao Tourais, **Chiara Coletti**, Ingo Hermann, Sebastian Weingärtner. "Phase-based T_2 mapping using dual phase-cycled balanced SSFP imaging". *Proceedings of the International Society of Magnetic Resonance in Medicine 31 (2023), doi: 10.58530/2023/2205*. Power Pitch.

8. **Chiara Coletti**, Maša Božić-Iven, Joao Tourais, Christal van de Steeg-Henzen, Mehmet Akçakaya, Kelvin Chow, Sebastian Weingärtner. "Adiabatic dark-blood $T_{1\rho}$-mapping for blood signal suppression in myocardial tissue characterization at 3T". *Proceedings of the Society of Cardiovascular Magnetic Resonance Annual Meeting(2023)*. Oral presentation.

9. Lauren Pearce, **Chiara Coletti**, Jaqueline Flewitt, Jian Nong, Rita Lam, Andrew Howarth, Carmen Lydell, James A. Whithe, Sebastian Weingärtner, Kelvin Chow.

†These authors contributed equally

"Clinical evaluation of multiparametric with T1, T2, and $T_{1\rho}$ with mSASHA at 3T". *Proceedings of the Society of Cardiovascular Magnetic Resonance Annual Meeting(2023)*. Oral presentation.

10. Kelvin Chow, Lauren Pearce, **Chiara Coletti**, Jaqueline Flewitt, Andrew Howarth, Carmen Lydell, James A. Whithe, Sebastian Weingärtner. "Multi-parametric T1, T2, and $T_{1\rho}$ mapping with mSASHA at 1.5T and 3T". *Proceedings of the Society of Cardiovascular Magnetic Resonance Annual Meeting(2023)*. Oral presentation.

11. **Chiara Coletti**, Joao Tourais, Christal van de Steeg-Henzen, Mehmet Akçakaya, Sebastian Weingärtner. "Adiabatic spin-lock preparations for robust in-vivo myocardial $T_{1\rho}$ mapping at 3T". *Proceedings of the 34th Annual International Conference of the Society for Magnetic Resonance Angiography (2022)*. Oral presentation.

12. **Chiara Coletti**, Joao Tourais, Christal van de Steeg-Henzen, Mehmet Akçakaya, Sebastian Weingärtner. "Adiabatic $T_{1\rho}$ mapping in the human myocardium at 3T". *Proceedings of the International Society of Magnetic Resonance in Medicine 30 (2022), doi: 10.58530/2022/0273*. Oral presentation, Magna cum Laude, and Best Abstract Award of the Cardiac MR Study Group.

13. Ties Tensen[†], Maša Božić-Iven[†], **Chiara Coletti**[†], Sebastian Weingärtner. "E-MaRSSim: A Python-based open-source MRI pulse sequence simulation tool". *Proceeding of the ESMRMB MRI Together Workshop (2021).*

14. **Chiara Coletti**, Sebastian Domsch, Frans Vos, Sebastian Weingärtner. "Functional MRI of neuro-electro-magnetic oscillations: Statistical processing in the presence of system imperfections". *Proceedings of the 2020 IEEE-EMBS Conference on Biomedical Engineering and Sciences (2021)*. Oral presentation.

15. **Chiara Coletti**, Sebastian Domsch, Frans Vos, Sebastian Weingärtner. "Towards direct neuronal-current MRI: a novel statistical processing technique for measurements in the presence of system imperfections". *Proceedings of the International Society of Magnetic Resonance in Medicine 29 (2021)*. Poster presentation.

16. **Chiara Coletti**, Sebastian Domsch, Frans Vos, Sebastian Weingärtner. "Understanding limitations of neuronal-current MRI for functional imaging of brain activation: A simulation study". *Proceedings of the 37th Annual Scientific Meeting of the European Society of Magnetic Resonance in Medicine and Biology (2020)*. Oral presentation.

Book Chapters

1. Joao Tourais[†], **Chiara Coletti**[†], Sebastian Weingärtner. "Brief Introduction to MRI Physics", in *Mariya Doneva, Mehmet Akcakaya and Claudia Prieto, "Magnetic Resonance Image Reconstruction"*, Elsevier (2021).

[†]These authors contributed equally

Supervised Student Projects

Bachelor Thesis

1. Hülya Falkena. "Tissue Mimicking Phantoms for Quantitative MRI". September 2022 - November 2022. *TU Delft Applied Physics*.
2. Ties O. Tensen. "E-MaRSSim: A Python-based open-source MRI pulse sequence simulation tool". September 2021 - December 2021 (co-supervised with Maša Božić-Iven). *TU Delft Applied Physics*

Master Thesis

1. Maaike Smit. "In Situ Evaluation of Spin-Lock Methods for Direct Detection of Oscillating Currents using MRI". November 2023 - July 2024. *TU Delft Applied Physics*.
2. Mark M. Vermeulen. "Rotating Frame Relaxation Times for Off-Resonant MRI Pulses". July 2023 - March 2024. *TU Delft Applied Physics*.
3. Roeland C. Naaktgeboren. "Parametric Relaxation Along a Fictitious Field (pRAFF) Pulse for Robust Quantitative MRI". June 2022 - March 2023. *TU Delft Applied Physics*.

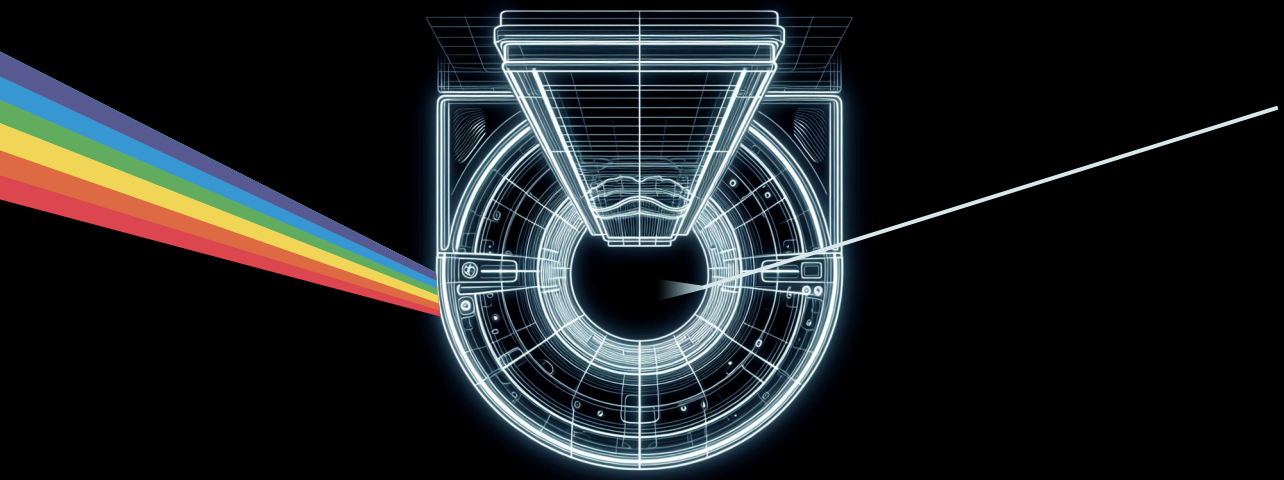

Propositions

accompanying the dissertation

Radiofrequency Pulse Design for Robust Quantitative Spin-Lock MRI

by

Chiara COLETTI

1. There is no universally agreed formal definition of rotating-frame relaxation values. (*This dissertation*)
2. MRI physicists must always consider replacing standard RF pulses with adiabatic pulses. (*This dissertation*)
3. Solely relying on the choices made in previously published work for the selection of RF pulse design parameters is shortsighted. (*This dissertation*)
4. The lack of sequence standardization and comprehensive reference values for healthy and diseased tissues hinders the clinical application of quantitative MRI methods.
5. An academic system basing promotions exclusively on scholar merit is biased in favor of people with higher economical status.
6. Colleagues making remarks on the composition of an all-female lab, but not all-male labs, are sexists.
7. Stating a skirt or dress needs to be of "knee-length minimum" in the Doctoral Defence Regulations is sexist.
8. The introduction of a C2 proficiency level requirement in Dutch language for promotion of TU Delft professors will negatively affect the quality of teaching and research in the university.
9. A crucial skill one should possess as a PhD candidate in a foreign university is the ability to recommend restaurants in their country of origin.
10. The most effective way to rebut skeptics arguing that someone does not have a heart is to undergo cardiac MRI.

These propositions are regarded as opposable and defendable, and have been approved as such by the promotor Dr. F. M. Vos.